9-1-2019

Investigations of Point Defects in KH_2PO_4 Crystals Using *Ab Initio* Quantum Methods

Tabitha E. R. Dodson

INVESTIGATIONS OF POINT DEFECTS IN KH_2PO_4 CRYSTALS USING *AB INITIO* QUANTUM METHODS

DISSERTATION

Tabitha E.R. Dodson, PhD

AFIT-ENP-DS-19-S-021

DEPARTMENT OF THE AIR FORCE
AIR UNIVERSITY

AIR FORCE INSTITUTE OF TECHNOLOGY

Wright-Patterson Air Force Base, Ohio

AFIT-ENP-DS-19-S-021

INVESTIGATIONS OF POINT DEFECTS IN KH_2PO_4 CRYSTALS USING *AB INITIO* QUANTUM METHODS

DISSERTATION

Presented to the Faculty

Department of Engineering Physics

Graduate School of Engineering and Management

Air Force Institute of Technology

Air University

Air Education and Training Command

In Partial Fulfillment of the Requirements for the

Degree of Doctor of Philosophy

Tabitha E.R. Dodson, BA, BA, MA, PhD

September 2019

AFIT-ENP-DS-19-S-021

INVESTIGATIONS OF POINT DEFECTS IN KH_2PO_4 CRYSTALS USING *AB INITIO* QUANTUM METHODS

Tabitha E.R. Dodson, BA, BA, MA, PhD

Committee Membership:

Dr. Nancy C. Giles
Chair

Dr. Gary S. Kedziora
Member

Dr. Matthew C. Fickus
Member

ADEDEJI B. BADIRU, PhD
Dean, Graduate School of Engineering and Management

ABSTRACT

Potassium dihydrogen phosphate (KH_2PO_4, or commonly called KDP) crystals can be grown to large sizes and are used for many important devices (fast optical switches, frequency conversion, polarization rotation) for high powered lasers. The nonlinear optical material has a wide intrinsic transparency range. Intrinsic point defects are responsible for several short-lived absorption bands in the visible and ultraviolet regions that affect high-power pulsed laser propagation. The primary intrinsic defects have been experimentally detected in KDP using electron paramagnetic resonance (EPR) experiments. The defect models established thus far include (i) self-trapped holes, (ii) oxygen vacancies, and (iii) hydrogen vacancies. In this research, the quantum chemistry Gaussian software program was successfully used to establish the atomic displacements forming the potential well to "self-trap" the hole in an otherwise perfect region of the crystal. The Gaussian results provide isotropic and anisotropic hyperfine predictions for the self-trapped hole and simulated EPR spectra (using EasySpin) are in excellent agreement with prior experimental work. A cluster approach was used in this work and discussion of cluster size and approach for modeling of defects in KDP will be presented. This research further develops the understanding of the overlap of spin density on neighboring ions in KDP and the resulting nuclear hyperfine values which can be compared to EPR data. The best approach determined by the modeling of self-trapped holes is also applied to the cation and anion vacancy problems. Work was performed on the DOD's High Performance Computer (WPAFB).

ACKNOWLEDGEMENTS

I want to acknowledge all three of my children. My “AFIT babies” were all born in the course of this dissertation research, within a span of five years. They learned a lot about potassium dihydrogen phosphate and had fun “playing” in GaussView with me, in their young toddler years. I love to share the wonders of physics with them and look forward to sharing more with them as they grow.

Nancy Giles and her husband Larry Halliburton deserve a very special thanks. Their infinite patience and kindness, insights, and persistence to seek truth were inspirational. It was an honor to be transformed into the physicist that I am today under their tutelage.

Table of Contents

List of Figures

List of Tables

INVESTIGATIONS OF POINT DEFECTS IN KH_2PO_4 CRYSTALS USING *AB INITIO* QUANTUM METHODS

I. Introduction

This dissertation describes a computational *ab initio* investigation of point defects in potassium dihydrogen phosphate (KH_2PO_4) crystals. The short notation of KDP is often used for these crystals. Quantum chemistry software from Gaussian, Inc. [1] is used to model several point defects in KDP, including self-trapped holes, oxygen vacancies, and hydrogen vacancies. The problems of modeling defects in KDP are explored by comparing results obtained using the unrestricted Hartree-Fock (UHF) method, Moeller-Plesset (MP) perturbation method, and density-functional theory (DFT) methods available in Gaussian. A primary goal of these investigations is to determine hyperfine parameters, both isotropic Fermi contact values and anisotropic dipole-dipole matrices, and determine the local lattice relaxation and bond-distance changes that occur due to the localized defect.

KDP is a nonlinear optical material often used to produce the second, third, and fourth harmonics of high-power near-infrared lasers. A few characteristics that make KDP crystals a suitable candidate for frequency conversion are a transparency range extending from 0.1765 to 1.7 μm, birefringence resulting in a negative uniaxial crystal $n_o > n_e$, and suitable magnitudes of the nonlinear optical coefficients [2]. Fourth-harmonic frequency generation has been achieved with KDP when exposing it to a 1.053 micron laser [3]. Harmonics of a 1.064 micron Nd:YAG laser may also be produced with KDP, at 2ω (532 nm), 3ω (355 nm), and 4ω (266 nm). These capabilities make KDP an ideal crystal for shifting laser light from near-infrared to visible and ultraviolet wavelengths [4]. Because

they can be grown to large sizes, KDP crystals are used for frequency conversion of large-diameter, high-power laser beams [5-10].

The presence of optically active defects in KDP crystals can negatively impact their performance in nonlinear applications. Thus, it is important to identify and characterize the types of defects that occur in KDP crystals. When exposed to intense laser beams, defects in KDP can change their charge state and produce broad transient optical absorption bands in the visible and ultraviolet regions of the spectrum. This darkens the crystal and hinders device performance [11]. Point defects in specific charge states are thought to be responsible for initiating damage in KDP crystals during illumination with intense femtosecond and nanosecond laser pulses [12-18].

The self-trapped hole is the primary focus of this dissertation because it is the most fundamental intrinsic defect in KDP crystals. This defect was challenging to correctly model using quantum chemistry methods, and it took a considerable amount of trial and error before acceptable results were obtained and understood. EPR experiments suggested that a self-trapped hole could be produced during an x-ray irradiation at 77 K [19-22]. The hyperfine results from these EPR experiments led to a proposed model for the self-trapped hole in which the hole is primarily shared by two oxygen ions, with overlap onto their two nearest-neighbor hydrogen ions and one nearest-neighbor phosphorus ion [19-22]. Having two oxygen ions share a self-trapped hole was not the only possible explanation of the EPR spectra, thus the model proposed by the experimentalists needed to be verified using quantum chemistry methods. Modeling this defect determines which oxygen ions share the hole and reveals the nature of the lattice relaxation that allows the hole to be self-trapped. Self-trapped holes, localized on one oxygen ion, have been reported in TiO_2 and

β-Ga_2O_3 crystals. Self-trapped holes shared by two oxygen ions have been reported in $CdWO_4$ crystals and amorphous SiO_2 [23-25]. In this dissertation, additional modeling efforts of defects in KDP include a hydrogen vacancy, and different oxygen vacancies. Experimental EPR results are available for each of these defects, thus allowing comparisons with computational outputs [19-22].

Chapter 2 reviews the literature on past investigations that experimentally characterized KDP defects using EPR, including proposed specific models. Prior KDP defect simulations using quantum chemistry methods are presented. Chapter 3 describes the Gaussian, Inc. software package and the various *ab initio* quantum chemistry methods that were utilized in this work to model the defects in KDP. Chapter 4 presents the results of the computational simulations that modeled small and large KDP clusters for the self-trapped hole. A variety of methods and basis sets were attempted for small and large clusters. This dissertation research began by exploring, for the self-trapped hole, the relative magnitudes of the predicted Fermi contact hyperfine values associated with hole localization and assessing the degree to which these hyperfine values agree or disagree with EPR experiments. Two different MATLAB programs were explored to convert the isotropic and anisotropic outputs produced by the Gaussian DFT program to hyperfine splittings when the magnetic field is along the *c* direction in the crystal. These *c*-direction splittings can then be directly compared to experimentally observed EPR spectra.

The computational modeling of the self-trapped hole in KDP demonstrated that the hole was equally shared between two oxygen ions on one PO_4 unit with overlap onto the two far hydrogen ions. This is in contrast to the empirical model proposed by Stevens *et al*. [19] that placed the self-trapped hole on the two oxygen ions that had the close hydrogen

ions. It was not possible for Stevens *et al*. to say with great certainty, via experiment, which oxygen-hydrogen pairs the self-trapped hole was located on. With electronic structure methods, in this dissertation, it was possible to visualize and quantify on an individual atom basis which oxygen-hydrogen pairs the defect was localized on.

The distribution of atoms, electrons, molecular orbitals, the spin density, and the relaxation that defects have within a material can be visualized and understood with computational methods. Chapter 5 provides a discussion of the graphical depiction of the electronic structure of KDP, primarily using the tool GaussView to visualize molecular orbitals and the electron density from the spin SCF density. Chapter 6 describes preliminary hydrogen and oxygen vacancy simulations using the lessons learned from Chapter 4. The research described in this dissertation was successful in modeling the self-trapped hole defect, the hydrogen-vacancy defect, and a variety of oxygen-vacancy defects. The appendices provide mathematical derivations, MATLAB code used in analyzing hyperfine spectra, example input files for Gaussian, and hyperfine output from completed simulations.

II. Potassium Dihydrogen Phosphate (KDP)

2.1 Crystal Structure and Ferroelectricity

Potassium dihydrogen phosphate (KDP) crystals have a structural phase transition at 123 K which affects their ferroelectric properties. Ferroelectric materials exhibit spontaneous electric polarization which may be influenced by an externally applied electric field. The KDP crystals are paraelectric (meaning, they exhibit a nonlinear polarization with an applied electric field) above 123 K and are ferroelectric (the polarization will exhibit hysteresis as a function of applied electric field) below 123 K. The terms paraelectric and ferroelectric also go by the terms disorder-phase and order-phase, respectively. Modeling the wave functions and vibrational properties of the hydrogen ions in KDP using quantum chemistry methods has been an active area of research in recent years [21, 26-28]. The goal of these efforts has been to explain the origin and nature of the ferroelectricity in KDP. There have also been numerous experimental studies at various temperatures using x-ray and neutron diffraction [29-31]. The focus of these studies, above and below the phase change at 123 K, was on the behavior of the hydrogen ions that connect the basic PO_4 units. These units consist of a central phosphorus ion surrounded by four oxygen ions. There is a hydrogen ion near each oxygen ion. The hydrogen ion is located along the line joining two oxygen ions, with the two oxygen ions being on neighboring PO_4 units. This hydrogen ion links the two adjacent PO_4 units, as seen in Figure 2.1.

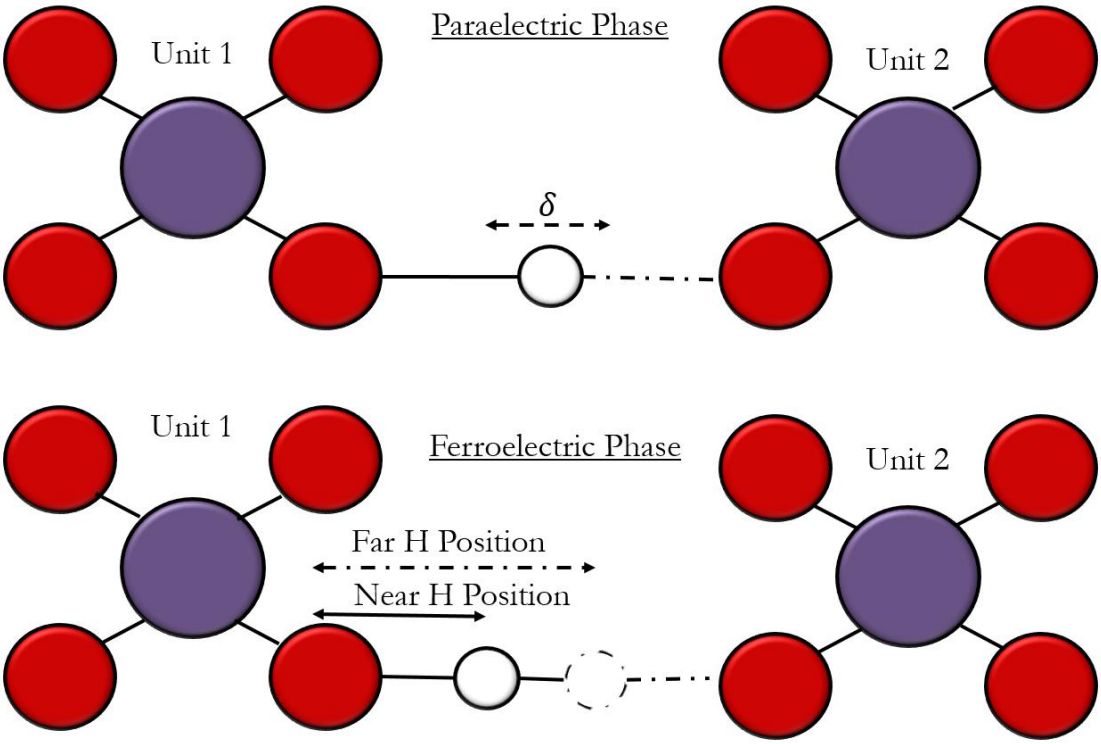

Figure 2.1. Two neighboring PO_4 units and the hydrogen ion that connects them are depicted looking along the z direction at the x,y plane for the (a) paraelectric and (b) ferroelectric phase. The image in (a) demonstrates the $\boldsymbol{\delta}$ separation between the distance between the two potential wells that can be occupied by the hydrogen ion. The image in (b) depicts the two possible locations for the hydrogen after settling into either its near or far position at low temperatures.

A unique feature of the KDP crystal is the probabilistic nature of the wave function describing the bonds between a hydrogen ion and the two oxygen ions that it links. A hydrogen ion located between two oxygen ions associated with different PO_4 units will have equal probability of occupying either side of a double potential well above 123 K, which ascribes a distance of 1.26 Å between the hydrogen ion and either one of its neighboring oxygen ions [26]. This corresponds to the top two units in Figure 2.1.a. Below this temperature, the hydrogen ion will remain in one of the wells, i.e., close to one oxygen

ion at a distance of 1.06 Å or far from the other oxygen ion at a distance of 1.44 Å. This corresponds to the bottom two units in Figure 2.1.b. Minimizing the energy requires that two hydrogen ions are close to two of the oxygen ions within a PO_4 unit and two hydrogen ions are far from the remaining two oxygen ions. Below 123 K, the KDP crystal has an orthorhombic structure with space group Fdd2 (C_{2v}^{19}). Above this temperature the KDP crystal has a tetragonal structure with space group $I\bar{4}2d$ (D_{2d}^{12}).

When KDP goes from its high temperature paraelectric phase to its low temperature ferroelectric phase, it develops an electric polarization along the *c* axis [30, 31]. The direction of the polarization depends on which two of the four neighboring hydrogen ions have bonded with the oxygen ions in the PO_4 unit. There are competing theories as to the mechanism that allows the hydrogen ions to assign themselves to their particular quantum well, both during the paraelectric and ferroelectric phase, with one of the theories suggesting that quantum tunneling is occurring. Studies have also been conducted on the influence of the host lattice on the settlement of the hydrogen ions with ammonium dihydrogen phosphate ($NH_4H_2PO_4$ or ADP), which is the ammonia analogue of KDP [27]. Similar to KDP, ADP has a hydrogen bridge that exhibits ordering at low temperature thus bringing the ADP structure to a ferroelectric geometry. Isotope effects were observed for both materials when substituting deuterium for hydrogen, thus supporting the "geometrical model" that demonstrates the settlement of hydrogen ions into their respective positions as a direct function of temperature and its effect on the vibrational properties of the lattice [27].

Koval *et al*. [26] performed *ab initio* DFT calculations and customized self-consistent model calculations (whereby they added a quadratic wave-function dependent

term to the hydrogen potential) to observe the different quantum well structures of KDP and DKDP (deuterated KDP, with deuterium substituting for the hydrogen ions). Their findings demonstrated the importance of mass on the location of the hydrogen or deuterium ion within the quantum well. The deuterium ion, which is heavier than the hydrogen ion, is much more likely to be situated within a well-defined double peak probability distribution, whereas a hydrogen's probability distribution is more localized with a central peak. The lighter hydrogen can move more quickly between the two closely spaced locations as a function of time, thus "smearing" the probability density between the two potential wells. This is seen in Figure 2.2 which demonstrates the different wave functions for the hydrogen and deuterium ions in KDP and DKDP as a function of distance, δ, in units of Angstroms.

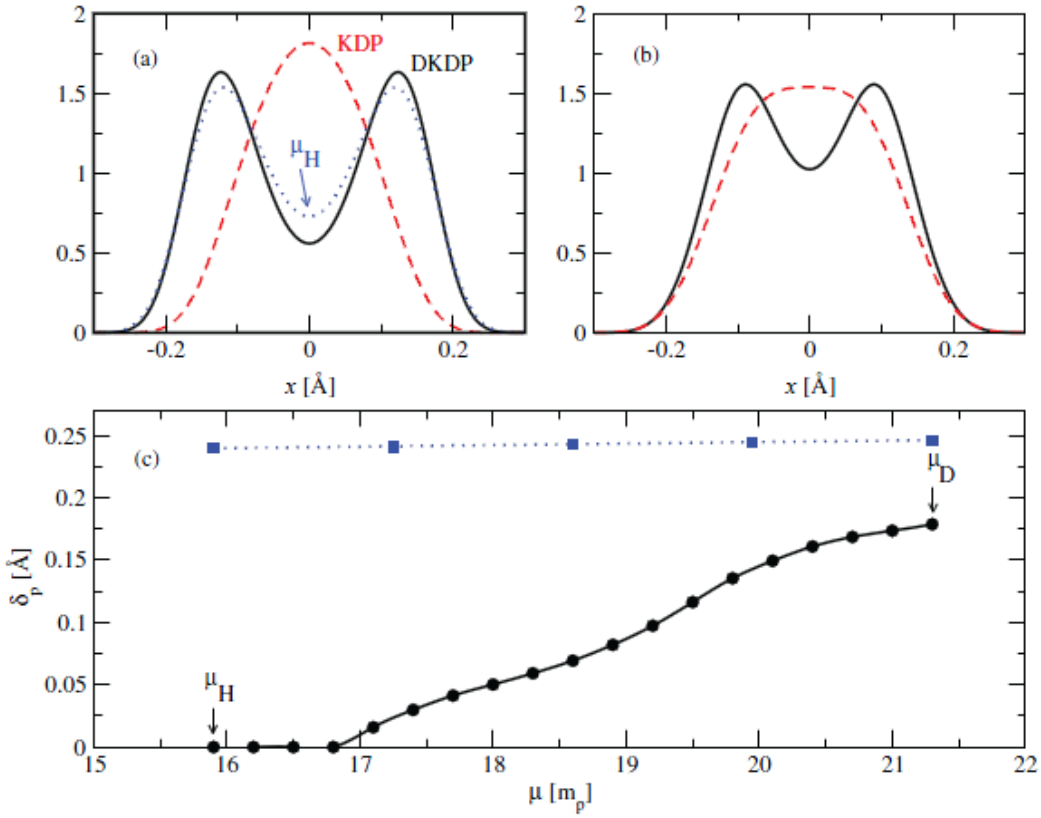

Figure 2.2. Calculated wave functions for hydrogen (red dashed lines) and deuterium (solid black lines) in a paraelectric $P_2O_8H_7$ KDP cluster, representing the dual potential well of deuterium and the smeared potential well of the hydrogen ion that connects the two PO_4 units. (a) The top left was from an *ab initio* DFT simulation, and the (b) top right figure is from a customized self-consistent model. (c) The bottom plot is the wave function peak separation distance $\boldsymbol{\delta}$ as a function of effective mass μ [26, 27]. Figure reprinted with permission from the publisher of Reference [26].

Sub-plot (c) in Figure 2.2 is depicted for a fixed DKDP potential and geometry (blue squares), and the circles represent the gradual increase in separation distance as mass increases, with subscript H representing hydrogen and D representing deuterium. The effective mass μ is given in units of proton mass, m_p.

When considering the low-temperature orthorhombic KDP crystal structure in the present dissertation, the hydrogen ions are rigidly held in place either in the near position

or far position. In other words, these ions are locked into a potential well at zero degrees Kelvin and are not jumping between two positions. For the high-temperature tetragonal cluster where the hydrogen ion probability is smeared in a potential well between two locations, the hydrogen ion is taken to be at the mid-point position, which is the averaged position between the two oxygen ions under thermal motion.

2.2 Previous Studies of Point Defects in KDP Crystals (1963-1998)

For KDP crystals to be successfully used in nonlinear applications involving high-power lasers such as those at the National Ignition Facility (NIF) (a facility located at Lawrence Livermore National Laboratory) they must be able to survive intense laser pulses without incurring surface and bulk damage. The presence of defects in the crystals will initiate laser-induced damage. Free electrons and holes generated by incident photons can be trapped at existing defects or can form new defects. These point defects formed by intense laser beams will lead to the formation of unwanted absorption bands in the visible and ultraviolet regions [11].

One of the earliest electron paramagnetic resonance (EPR) studies that investigated defects in KDP was by Hughes and Moulton [32]. After an x-ray irradiation at 77 K, they observed an EPR spectrum with a g value near 2.0 and a pair of EPR lines with an isotropic hyperfine splitting of 32 Gauss attributed to a 100% abundant I = 1/2 nucleus. The responsible nucleus was identified as ^{31}P. These defects were found to be unstable above 77 K. An earlier study of this same defect by DuVarney and Kohin [33] used EPR on x-ray irradiated KDP to attribute the anisotropy of the g factor to the localization of the spin density on an oxygen ion with 1% of the spin density in the *3s* orbital of the adjacent phosphorus atom. McMillan and Clemens [34] also measured a 32 Gauss hyperfine

splitting with EPR for this defect in KDP and suggested that 0.9% of the unpaired spin was in a phosphorus atom *3s* orbital. Exchange core polarization was postulated to be the dominant contribution to this hyperfine interaction [34]. In Chapter 4 of this dissertation, this estimate is validated by comparing the calculated Fermi contact value of the phosphorus to the expected value for a Fermi interaction if the electron had been located 100% within a *3s* orbital, supporting the theory that exchange core polarization is a primary contributor.

Demos *et al*. subjected KDP crystals to pulsed 355 nm laser irradiation [35] and used Raman spectroscopy to observe a transient change in the internal vibration mode of the PO_4 units at 915 cm^{-1}. This effect was attributed to the generation of defects or localized impurity clusters which cause transient absorption on the time scale of 1.6 ±0.4 ps. Time measurements done by Davis *et al*. [11] demonstrated the relevance of the hydrogen ions that link the PO_4 units to these defects. They explored the defect physics associated with hydrogen in KDP and illustrated proton transport processes [11]. Their experiments used gigawatt-power UV irradiation at 266 nm from a Nd^{3+}:YAG regenerative amplifier, a Q-switched Nd^{3+}:YAG laser, and sub-picosecond probe pulses at 308 nm to investigate both KDP and DKDP crystals. The 266 nm light caused two-photon inter band absorption and the generation of electron-hole pairs. Frequency conversion to 4ω and two-photon-induced absorption between 200–700 nm was investigated by Marshall *et al*. using the same experimental methods [37].

According to Davis *et al*., the induced defects have a non-exponential decay behavior which can be described by one-dimensional or semi-one-dimensional transport models. Their results had an $\mathrm{erf}\left(\sqrt{\tau_d/t}\right)$ behavior where τ_d is a decay time constant and t

is time [11]. Defects in DKDP decayed slower than defects in KDP, on the order of 42.2 ms versus 20.5 ms, respectively. This difference in decay time was attributed to isotope effects. These investigators refer to Defect A and Defect B (after having been initially labeled as π–type and σ-type polarized optical absorption, respectively). Defect A is a hole trapped adjacent to a hydrogen vacancy, and Defect B is the self-trapped hole. The Defect A (the π–type polarized defect) had a broad peak centered near 510-550 nm, and Defect B (the σ–type polarized defect) had two broad peaks centered near 390-410 nm and 510-550 nm. Additional results describe similar behaviors in rubidium dihydrogen phosphate (RDP), ADP, and potassium dihydrogen arsenate (KDA) [11].

The intrinsic nature of the point defects was suggested in the studies of the optical properties by Dieguez *et al*. [37]. They conducted optical absorption and luminescence experiments on KDP and DKDP that had been by subjected to an x-ray irradiation. They used the annotation "π polarized defect" in KDP for a "proton vacancy hole center". This was assigned for absorption bands at 510 nm and 550 nm and a thermoluminescence glow peak at 123 K. They assigned the annotation "σ polarized defect" in KDP for absorption bands at 390 and 550 nm and a glow peak at 73 K.

Understanding defects in KDP can assist crystal growers in eliminating or neutralizing the mechanisms associated with defect formation. The high-power lasers that are used for inertial confinement fusion research require large KDP crystals that are grown to at least 50 cm x 50 cm x 50 cm. The KDP crystals can be grown at fast rates, such as 40 mm/day, or slow rates, such as 5 mm/day, although the faster growth of KDP tends to introduce more defects than the slower growth rate [38].

2.3 Previous Studies of Point Defects in KDP Crystals (1998-2003)

Extensive research identifying defects in KDP has been reported [19-22, 39] using EPR at West Virginia University. Defects identified in these studies include the self-trapped hole, an interstitial hydrogen atom, a hole trapped next to a hydrogen vacancy, a silicon impurity, and an oxygen vacancy. The oxygen vacancy can take on several variants, and each one is thought to be due to the different positions of nearby cation vacancies, such as a missing hydrogen or potassium ion. The oxygen vacancy combined with a cation vacancy is known as a divacancy complex.

The hole next to a hydrogen vacancy and the self-trapped hole are created in the KDP crystals by exposure to x rays or a 266 nm laser. As demonstrated by Setzler *et al*. [39], free electrons and holes are generated during the irradiation. A portion of these electrons and holes immediately recombine to restore the original lattice, but a few of these electrons allow a hydrogen ion to move into an interstitial position and become a hydrogen atom by trapping an electron. At the same time, a similar number of holes are trapped on oxygen ions and form the defects referred to as a hole next to a hydrogen vacancy and a self-trapped hole. The crystal remains electrically neutral during these processes, as the number of trapped electrons must equal the number of trapped holes. Chirila *et al*. [21, 22] show that the appearance of these defects in KDP are responsible for the broad, transient (less than one second) optical absorption bands in the visible and ultraviolet regions of the electromagnetic spectrum.

The self-trapped hole is given the designation $(H_2PO_4)^0$ and corresponds to "Defect B" or "σ–type polarized defect" mentioned in Section 2.2 of this dissertation. EPR spectra for the self-trapped hole in KDP and DKDP are shown below in Figure 2.3. This figure

also shows the 31 Gauss phosphorus hyperfine interaction due to a hole trapped on an oxygen ion adjacent to a hydrogen vacancy. This defect is given the designation $(HPO_4)^-$ and corresponds to the notations "Defect A" or "π–type polarized defect" mentioned in Section 2.2 of this dissertation.

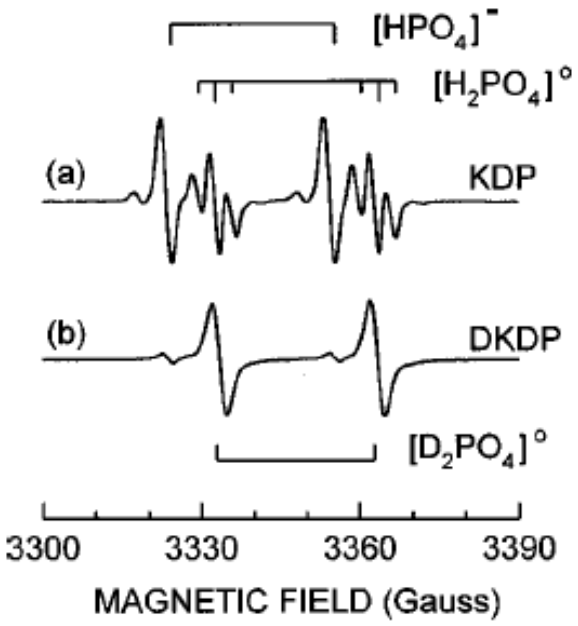

Figure 2.3. EPR spectra of the self-trapped hole for KDP and DKDP and the hydrogen vacancy for KDP. The 31 Gauss hyperfine separation is due to the adjacent phosphorus atom, and the pair of triplets is due to the two neighboring hydrogen ions which each have 3.2 Gauss hyperfine values. Figure reprinted with permission from the publisher of Reference [19].

Self-trapped holes shared by two anions have been observed in alkali-halide crystals, where two adjacent halide ions trap a hole in the resulting σ antibonding orbital (σ orbitals are explained in detail in Chapter 5 of this dissertation) at cryogenic temperatures, after having relaxed towards one another to produce a shallow potential well

[40]. The halide ions, such as fluorine or chlorine, have a single negative (1-) charge. A hole trapped by a single halide, thus forming a halide atom, has not been experimentally observed or computationally predicted for these types of crystals, such as for LiF, NaCl, KCl or KBr [41]. This behavior is different for oxides, where the oxygen ions have a doubly negative (2-) charge. It is common to observe a trapped hole on one oxygen, and it is uncommon to have a self-trapped hole between two oxygen atoms [42]. An exception to this, other than KDP, is amorphous SiO_2, where the hole is shared by two oxygen ions [42].

In previous research [21], preliminary quantum chemistry simulations using unrestricted Hartree Fock and Moeller-Plesset perturbation theory for small, 41-atom, KDP clusters were performed. These efforts used the limited processing capability of a personal computer to run simulations with small basis sets (ie: STO-3G and 6-31G – an explanation of basis sets follows in Chapter 3), along with the small cluster, due to the limitations in computational processing capabilities. Only tetragonal (ie: paraelectric phase) KDP clusters were considered, and potassium ions were not included, thus limiting the usefulness of the results. The self-trapped hole is only stable at very low temperatures when the KDP crystal is in the orthorhombic state. Realistic modeling of the self-trapped hole must start with the orthorhombic KDP structure.

The results of the 41-atom tetragonal cluster electronic structure calculations conducted in Reference [22] demonstrated a localization of the self-trapped hole on two oxygen ions and their neighboring hydrogen ions, for the self-trapped hole. This research also demonstrated Fermi contact values ranging from -45 to -306 Gauss for the central phosphorus ion and Fermi contact values for both of the hydrogen ions that shared the hole as equally ranging from -3 to -13 Gauss. As a beginning point for the present research, the

tetragonal cluster results of Reference [22] were verified in Chapter 4, Section 4.1. Significant advances were then made by considering orthorhombic clusters, large structures including potassium ions, and various quantum methods including DFT. Most important, lattice relaxation was allowed in the present work.

The oxygen vacancy is a trapped-electron defect in KDP crystals, and thus is very different from the trapped-hole defects previously investigated in this dissertation. Garces *et al.* [20] has described experimental EPR observations of oxygen-vacancy defects in KDP with phosphorus hyperfine splitting values ranging between 552 to 757 Gauss. Figure 2.4 shows the EPR spectra for the defects with hyperfine splittings of 757, 733, 690, 647, and 552 Gauss. These different oxygen vacancy spectra are attributed to an additional vacancy being located near the oxygen vacancy, such as a missing hydrogen. A potassium vacancy could also be near the oxygen vacancy, since there are six different potassium positions nearby. The $(PO_4)^{3-}$ units are replaced by a unit with an oxygen vacancy during the growth process of the KDP crystal to form a $(PO_3)^{-}$ unit, and once the atom is removed, an electron becomes trapped after an x-ray irradiation, forming a $(PO_3)^{2-}$ unit.

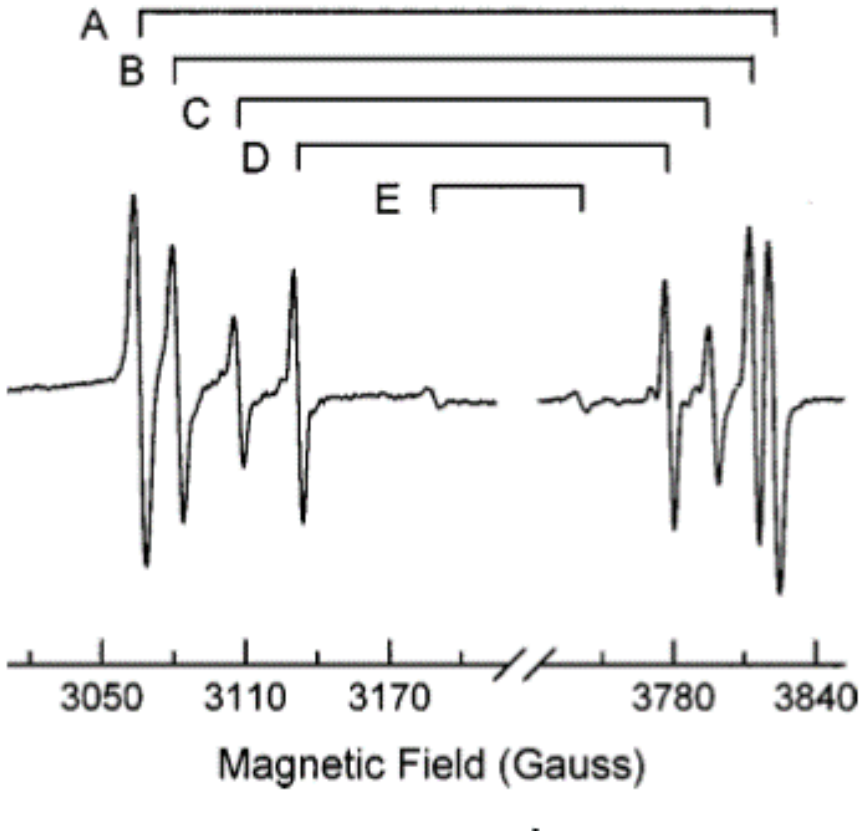

Figure 2.4. Five variations of the $(PO_3)^{2-}$ oxygen vacancy, with ^{31}P hyperfine splittings of 757, 733, 690, 647, and 552 Gauss. Figure reprinted with permission from the publisher of Reference [20].

The research introduced from Reference [22] in the preceding pages also pursued preliminary efforts to model the oxygen vacancy defect using the same 41-atom tetragonal cluster that was used for the self-trapped hole, described previously. The document does not specify what method and basis set were used. The results documented Fermi contact terms before and after optimization for the central phosphorus and the remaining three oxygen ions of the central PO_4 unit. These results gave Fermi contact values of 586 and 619 Gauss for the central phosphorus ion, -23 and -18 Gauss for the oxygen ion "paired"

with the oxygen vacancy, -26 and -22 Gauss for the oxygen ion located “beneath” the oxygen vacancy, and -13 and -9 Gauss for the remaining oxygen of the central unit [22]. These values are all listed before and after geometry optimization respectively, and the geometry optimization had allowed the three oxygen ions in the central unit to move.

III. Quantum Chemistry Using Gaussian

Gaussian is quantum chemistry software used to calculate the electronic structure of molecules and solids. Wave functions are described using Gaussian orbitals (as opposed to Slater-type orbitals), and a wide variety of physical phenomena, such as molecular orbital distributions for crystal defects and intermolecular bonds in biological structures, can be simulated. Examples of a *1s* Slater-type function and *1s* Gaussian-type function, centered at R_A, are shown in Equation 3.1 and Equation 3.2,

$$\boldsymbol{\phi_{1s}^{SF}(\zeta, r - R_A)} = \left(\frac{\zeta^3}{\pi}\right)^{\frac{1}{2}} \boldsymbol{e^{-\zeta|r-R_A|}}, \qquad \textit{Eq. 3.1}$$

$$\boldsymbol{\phi_{1s}^{GF}(\alpha, r - R_A)} = \left(\frac{2\alpha}{\pi}\right)^{\frac{3}{4}} \boldsymbol{e^{-\alpha|r-R_A|^2}}, \qquad \textit{Eq. 3.2}$$

where ζ and α are the Slater and Gaussian orbital type exponents, respectively [43]. The exponents of each function will determine the physical nature of the wave function, with a Gaussian-shaped distribution being defined for ϕ^{GF} and a shape given by double-sided exponential decay curves meeting in the middle to give a sharp peak for the Slater-type function. Problems are set up by defining an initial spatial arrangement of the participating atoms and then choosing an appropriate quantum method and a specific basis set. Generally, multiple functions (*1s*, and/or *2p*, *3d*, etc.) are represented in a basis set $\{\phi_\mu\}$. The orbital type exponents are numbers that are greater than zero, which vary depending on the selected basis set, and are a way to define whether a basis function is small and dense (with a large orbital type exponent) or large and diffuse (with a small orbital type exponent). A primary feature of the present research is a comparison of results from

ENDOR and EPR experiments with hyperfine values calculated using electronic structure methods. These comparisons lead to a better understanding of the defect's electronic structure.

The three main quantum methods that have been considered in the present investigations of defects in KDP are density functional theory (DFT), unrestricted Hartree Fock (UHF), and unrestricted Moeller Plesset (UMP) theory. "Unrestricted" means that an open shell model is utilized versus a closed shell approach, which then allows the study of defects with an unpaired spin. The closed shell approach places two electrons (one spin-up and one spin-down) into a single orbital, whereas the open shell approach places each spin-up electron into an alpha orbital and each spin-down electron into a separate beta orbital. Spin up is associated with positive spin density, and spin down is associate with negative spin density.

As the quantum methods increase in complexity, their implementation requires increasing amounts of computational time and resources, in particular when larger basis sets are used. The basis sets that were considered in this research project include 6-31G, 6-31++G, 6-31+G(d), and 6-31++G(d,p) [44-53] for UHF, UMP, and DFT simulations [54-58], and for DFT, various iterations of the hybrid functional B3LYP and ωB97XD [59-61] were attempted. A variety of additional basis sets optimized for DFT were tested, but their results were not optimal, and they are not elaborated on in the later sections of this dissertation. For instance, EPR-II and EPR-III were used on specific ions of interest, such as hydrogen, while keeping basis sets like 6-31G on the remaining ions. Additionally, basis sets optimized for DFT such as N07 [62] for EPR calculations and correlation consistent basis sets Aug-cc-pV*Z [63] were tested.

Basis sets are used to represent the electronic wave functions that the quantum chemistry program uses to compute eigenvalues and to spatially restrict or distribute electrons. The basis set 6-31G can be used with either UHF, UMP, or DFT methods. 6-31G is considered to be a split valence basis set, in which two or more functions are used for a valence orbital. 6-31G specifically has two valence orbitals represented by a contraction of three and one primitive Gaussian function, as indicated by the "31G". This is referred to as a valence double-zeta basis set. The "6" represents the contraction of 6 primitives for the core (a primitive is another word for an uncontracted Gaussian exponent, as depicted by Equation 3.2). The 6-31++G basis set includes doubly diffuse functions, indicated by the "++", which increase the spatial extent for a given ion by adding a diffuse Gaussian function to both heavy atoms and hydrogen atoms. Lastly, 6-31++G(d,p) represents a polarized basis set that adds p-functions to hydrogen atoms and d-functions to heavy atoms. Increasing the size of basis sets by including more polarization and diffuse functions may increase the accuracy of the calculations by lowering the overall energy of the cluster [64].

The Department of Defense High Performance Computing Modernization Program (HPCMP) supercomputers were used to effectively run Gaussian with sufficiently large atomic clusters in combination with computationally intensive methods and basis sets. The majority of the simulations on the high-performance computers (HPC) were run on the servers referred to as Thunder and Garnet, although Garnet was decommissioned during the course of this research. Thunder is an SGI ICE X 5.62 petaflops server with 3,216 standard memory nodes with 36 cores per node [65]. Before proper utilization of all 36 processors on a node of Thunder, the jobs had typically required at least 24 hours of

computational time, in particular when utilizing the UMP method, and up to a week or longer when the size of the cluster is larger than 100 atoms. This is still an improvement over using a personal computer, which would comparatively take six months for a job and could only run one job at a time. In addition to being faster (i.e., three days for a job versus six months), the HPC can run hundreds of jobs at a time.

Time requirements scale on the order of n^5, with "n" being the number of basis functions for jobs using the UMP2 method [66]. Additionally, memory requirements for UMP2 can scale on the order of n^3 to n^4, and an increase in memory requirement may be specified in the header of the Gaussian input files. Gaussian uses one of three algorithms depending on the situation: in-core, direct, or semi-direct, each with different memory requirements. Memory was manually set to an optimum value of %mem=96GB, or 90% of free user memory for a given computer, keeping in mind that the default memory setting for Gaussian is 800 MB. The number of nodes had initially ranged between one to ten with all 36 processors on each node being utilized. After discovering that Gaussian does not scale across nodes, the number of nodes for jobs was set back to one. Previous literature indicates that the accuracy of Gaussian simulations increases with increasing size and complexity of the quantum method and basis set used [67]. However, lack of parallel efficiency limits the ability to use the more complex methods in a timely manner. Therefore, for this research the number of nodes was generally less than three nodes, with the optimum number of nodes being one in terms of computational efficiency. The default number of processors used per node on the HPC is all 36 of the processors, and thus all 36 processors are used for each node by default. This is specified in the input file by using the "%CPU" keyword, and the input files in Appendix C demonstrate the use of this keyword.

3.1 Hyperfine Parameters: Measured in Experiment and Calculated by Gaussian

Spectra obtained in EPR experiments often provide g values and hyperfine values. The g values are dimensionless, and the hyperfine parameters are typically expressed in units of Gauss (G), MHz, or cm^{-1}. For g = 2.0, 1 G is equivalent to 2.8 MHz. The basic EPR experiment consists of placing a crystal in a microwave cavity resonating at a fixed microwave frequency (usually near 9.4 GHz) and then applying a varying magnetic field [68]. In most cases, the sample is cooled to a temperature in the 20-50 K region to maximize the signal strength and reduce the effects of unfavorable spin-lattice relaxation times. Because of the electron Zeeman effect, the spin-up and the spin-down electrons associated with a defect have different energies and populations (for a concentration n of spins) at a given temperature T, as illustrated in Figure 3.1.

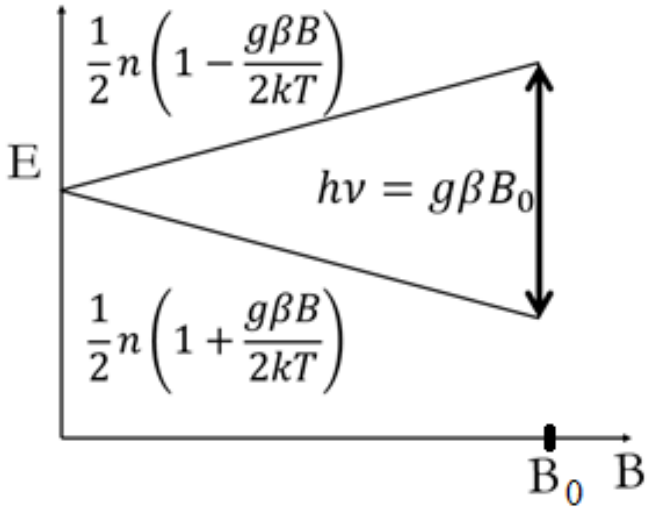

Figure 3.1. Energy diagram (energy E vertical versus magnetic field B horizontal) illustrating the electron Zeeman effect for an S = 1/2 spin system. The ΔM = ±1 transition between populations is denoted by the vertical double arrow. The populations are indicated on the diagram as well.

As the magnetic field is slowly swept across a pre-selected region at a constant rate, the spin system will pass through the resonance condition $h\nu = g\beta B_0$. In this resonance condition, h is Planck's constant, ν is the fixed microwave frequency, g is the "g value" that is unique for each defect, the constant β is the Bohr magneton, and B_0 is the magnetic field at resonance. The resonance condition corresponds to the "flipping" of the spin as the microwave photons drive the $\Delta M = \pm 1$ transition, denoted by the double vertical arrow in Figure 3.1. For most EPR studies, the concentrations of defects are less than 10^{19} cm^{-3} and thus the individual defects are well isolated and Boltzmann statistics apply. This means that the populations of the spin-up and spin-down states are different, as shown in Figure 3.1 with the lower energy having a larger population. The different populations cause a net absorption of microwave energy when the system passes through the resonance condition.

When the unpaired electron spin interacts with the spin of a magnetic nucleus (i.e., a nucleus with a nuclear spin quantum number $I > 0$), the spin Hamiltonian must be expanded to include these additional hyperfine interactions. This is the case in KDP when an unpaired spin primarily localized on the oxygen ions interacts with the nuclear magnetic moments of the neighboring phosphorus and hydrogen ions. The total Hamiltonian in Equation 3.3 includes the electron Zeeman term, the hyperfine term, and the nuclear Zeeman term, where the subscript *N* represents the nucleus, and g_N is the nuclear g value:

$$H = \beta \boldsymbol{S} \cdot \boldsymbol{g} \cdot \boldsymbol{B} + \sum_i (\boldsymbol{I_i} \cdot \boldsymbol{A_i} \cdot \boldsymbol{S} - \beta_N g_N \boldsymbol{I_i} \cdot \boldsymbol{B}) \,. \qquad \textit{Eq. 3.3}$$

The resulting energy level diagram for an S = 1/2, I = 1/2 spin system is shown in Figure 3.2. Lowercase b_α or b_β in this case, are values for the magnitude of the effective magnetic field seen by the nucleus, with magnetic quantum numbers $m \pm \frac{1}{2}$.

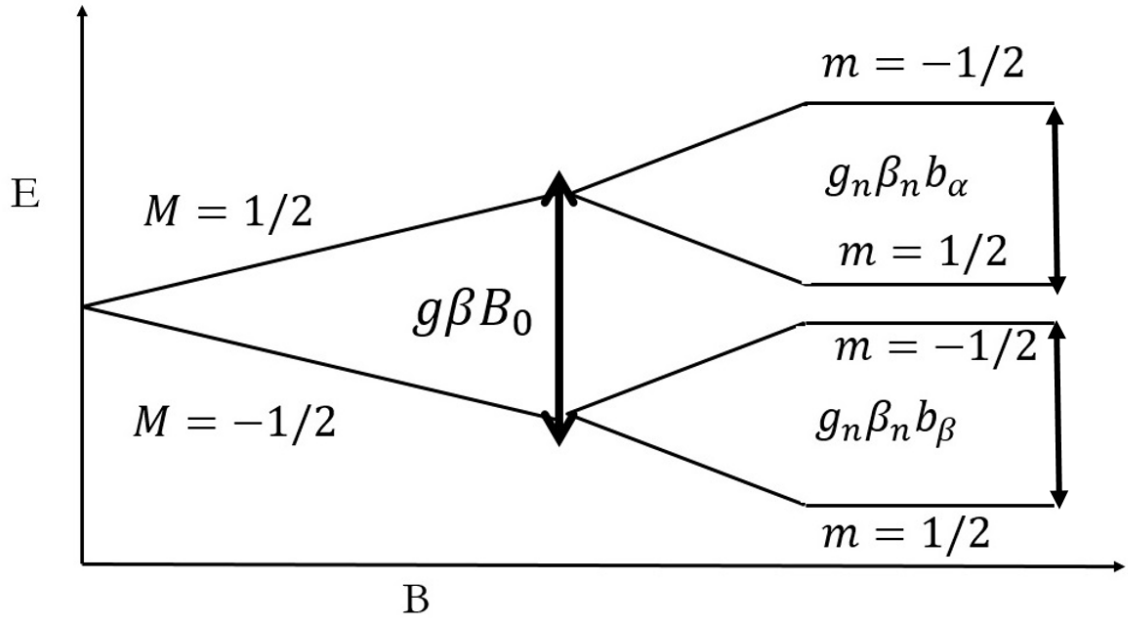

Figure 3.2. Energy diagram for an unpaired electron interacting with the nucleus of a neighboring ion (S = 1/2, I = 1/2), two-spin system.

The **A** matrix represents the hyperfine interactions with a specific nucleus and can be separated into two parts. These are the isotropic Fermi contact interaction term, a_{iso}, multiplied by the identity matrix I, and the anisotropic dipole-dipole interaction A_{aniso} matrix:

$$\boldsymbol{A = a_{iso} I + A_{aniso}}\,. \qquad \textit{Eq. 3.4}$$

The isotropic component (the Fermi contact interaction) of the hyperfine term [42, 69, 70] a_{iso} is directly proportional to the net unpaired electron spin density at the position of the nucleus, $\rho(r_N)$,

$$\boldsymbol{a_{iso} = \left(\frac{8\pi}{3}\right) g\beta g_N \beta_N \rho(r_N)} \, . \qquad \textit{Eq. 3.5}$$

The components of the anisotropic matrix $\boldsymbol{A_{aniso}}$ depend on the spatial distribution of the unpaired spin's wave function relative to the nuclear magnetic moment, representing a classic dipole-dipole interaction:

$$\boldsymbol{A_{aniso} = -g\beta g_N \beta_N \left(\frac{I}{R^3} - \frac{3R \cdot R}{R^5}\right) \rho(r) d\tau} \, . \qquad \textit{Eq. 3.6}$$

The vector $\boldsymbol{R}$ is $\boldsymbol{R = r - R_N}$; the vector $\boldsymbol{r}$ is the location of the electron spin density relative to the nucleus at the vector $\boldsymbol{R_N}$; $\boldsymbol{\tau}$ is the direction of the applied magnetic field; and $\boldsymbol{\rho(r)}$ is the spin density matrix [43]. When the anisotropic matrix is diagonalized, it takes the following form:

$$\boldsymbol{A_{aniso} = \begin{bmatrix} -b & 0 & 0 \\ 0 & -b & 0 \\ 0 & 0 & 2b \end{bmatrix}} \quad . \qquad \textit{Eq. 3.7}$$

In the Gaussian output, the anisotropic hyperfine matrix is presented in the recognizable format of Equation 3.6, as three specified diagonal elements, which Gaussian labels as: $3XX - RR$, $3YY - RR$, and $3ZZ - RR$ and three off-diagonal elements, XY, XZ, and YZ which are generally non-zero. An example of the anisotropic portion of the Gaussian output, reformatted into a table for demonstration purposes, is given in Table 3.1.

Table 3.1. Output from Gaussian showing the spin dipole couplings data from which the anisotropic component of the hyperfine A matrix is constructed in atomic units. This is a three atom subset of data, from a larger set of atoms, meant for illustration purposes.

Center	Spin Dipole Couplings					
	$3XX - RR$	$3YY - RR$	$3ZZ - RR$	XY	XZ	YZ
Atom 1	-0.000363	0.000278	0.00084	0.000254	0.000228	0.000637
Atom 2	0.000071	-0.000008	-0.000063	-0.000254	-0.000220	0.000189
Atom 3	-0.000234	0.000096	0.000138	-0.000077	-0.000078	0.000367

Using the data from Table 3.1, the anisotropic matrix for Atom 1 becomes:

$$\boldsymbol{A_{aniso}} = \begin{bmatrix} -0.000363 & 0.000254 & 0.000228 \\ 0.000254 & 0.000278 & 0.000637 \\ 0.000228 & 0.000637 & 0.000084 \end{bmatrix}.$$

This matrix is then diagonalized by Gaussian, thus finding its eigenvalues, also known as the three principal values of the anisotropic matrix in the direction of the principal axis, for each principal value. These principal values and directions of the principal axes are listed in the Gaussian output section called "Anisotropic Spin Dipole Couplings in the Principal Axis System". The directional cosines of the anisotropic spin dipole couplings are given in columns for each principal component of the diagonalized anisotropic matrix elements and are labeled Baa, Bbb, and Bcc in the Gaussian output file. This notation is used in Chapter 4 of this dissertation. These values of the directional cosines represent the orientation of the anisotropic hyperfine matrix relative to the crystal axes. Additional steps are described in Chapter 4, Section 4.2.2 to address significant off-diagonal elements of

the $\boldsymbol{A_{aniso}}$ matrix and how to utilize these values for computationally simulating hyperfine spectra in the same rotated reference frame as EPR experiment.

A key feature of Gaussian is geometry optimization, where the energy of the system is minimized by finding local minima by varying the positions of atoms. This process was used to predict an equilibrium geometry for some of the KDP clusters in this dissertation. Two or more of the ions that comprise the central PO_4 unit are allowed to move, or relax, in order to observe how changes in position affect the electronic structure of the defect. This geometry optimization provides a solution that has converged on an energy minimum located on the potential energy surface. As the atoms move during the optimization, the second derivative of the energy with respect to the cluster coordinates is either estimated using quasi Newton methods or optionally calculated analytically. At the minimum energy the gradient or forces should be zero, and an optimization to a local minimum is considered complete when four convergence criteria are met. These four criteria which must all be below appropriately set thresholds are first, the root mean square (rms) of the force; second, the displacement for the next step; third, the rms of the displacement of the next step; and fourth, the force itself.

3.2 Discussion of the UHF, UMP2, and DFT Quantum Methods

Pacchioni *et al*. [71-73] and others [74, 75] have explored the merits of using Moeller Plesset perturbation theory to localize defects, such as the AlO_4 defects in SiO_2 crystals, as well as examining the demerits of using DFT for these simulations. Their unrestricted 2nd order Moeller Plesset (UMP2) calculations predicted a localized hole on one oxygen ion for the AlO_4 defect, thus matching experimental hyperfine coupling data. In contrast, their DFT simulations using functionals incorrectly predicted the hole would

be localized on two oxygen ions for AlO_4, which did not agree with the data from experiments. This significant difference in predicted models was attributed to the fact that Moeller Plesset perturbation theory does explicit electron correlation calculations, whereas DFT approximates these effects through functionals. Another example is the delocalization by DFT of excess electron density over all surface cerium atoms in CeO_2, which disagrees with experiment [73]. The correct spin localization in this latter case is achieved by implementing UHF and UMP2 theory [73].

The research described in this dissertation initially started by utilizing the UHF method, and then once access to the HPC was granted, the more computationally intensive UMP2 method was included and shown to perform well. The UMP2 method consistently demonstrated spin density localization results that matched expectations from experimental results as opposed to various DFT methods, which was consistent with the published literature of Pacchioni and coworkers discussed in the previous paragraph. Near the end of the research conducted in this dissertation, a suitable DFT functional was identified, known as ωB97XD, that gave correct hyperfine values and defect localization. This was an encouraging development and validated the use of the DFT method. A description of the UHF and UMP2 methods are discussed below, and the section concludes with a description of the successful ωB97XD functional.

3.2.1 Hartree Fock and Moeller Plesset Theory

The unrestricted Moeller Plesset theory is based on unrestricted Hartree Fock (UHF). The HF energy equation is represented in Equation 3.8, where the "< >" denote bra-kets:

$$\boldsymbol{E_{HF} = E_{NUCL} + < hP > + \frac{1}{2} < PJ(P) > - \frac{1}{2} < PK(P) > .} \qquad \textit{Eq. 3.8}$$

The nuclear repulsion energy E_{NUCL}, the electron density matrix $\boldsymbol{P}$, the classical Coulomb repulsion term $\boldsymbol{J(P)}$, and the exchange energy from electrons $\boldsymbol{K(P)}$ are included. The HF Hamiltonian shown in Equation 3.9 is a summation over all electrons indexed by i, where $v^{HF}(i)$ represents the electron-electron repulsion which leads to the Coulomb and exchange terms,

$$\boldsymbol{H_0 = \sum_i [h(i) + v^{HF}(i)] .} \qquad \textit{Eq. 3.9}$$

A simple way to describe Moeller Plesset theory for UMP2 is that it incorporates the 2nd order perturbation energy correction E_2 for the solution to Schrodinger's equation ($E = E_0 + E_1 + E_2$). It is a post Hartree Fock method (where the HF energy is $E = E_0 + E_1$). A more general Hamiltonian [76] includes the original Hartree Fock Hamiltonian term H_0 from Equation 3.9 and the expanded form of the Moeller Plesset perturbation, P:

$$\boldsymbol{H = H_0 + P,} \qquad \textit{Eq. 3.10}$$

$$\boldsymbol{P = \sum_{i<j} r_{ij}^{-1} - \sum_i v^{HF}(i) ,} \qquad \textit{Eq. 3.11}$$

$$\boldsymbol{H_0 |\Psi_0> = E_0^0 |\Psi_0> .} \qquad \textit{Eq. 3.12}$$

The eigenvalue $E_0^{(0)}$ represents the zeroth-order perturbation energy as a sum of orbital energies, $E_0^0 = \sum_a \varepsilon_a$. The calculation for the first order energy is as follows:

$$\boldsymbol{E_0^{(1)} = < \Psi_0 | P | \Psi_0 >} \qquad \textit{Eq. 3.13}$$

$$\boldsymbol{E_0^{(1)}} = < \boldsymbol{\Psi_0} \left| \sum_{i<j} \boldsymbol{r_{ij}^{-1}} - \sum_i \boldsymbol{v^{HF}(i)} \right| \boldsymbol{\Psi_0} > \qquad \textit{Eq. 3.14}$$

$$\boldsymbol{E_0^{(1)}} = < \boldsymbol{\Psi_0} | \sum_{i<j} \boldsymbol{r_{ij}^{-1}} | \boldsymbol{\Psi_0} > - < \boldsymbol{\Psi_0} | \sum_i \boldsymbol{v^{HF}(i)} | \boldsymbol{\Psi_0} >. \qquad \textit{Eq. 3.15}$$

The Hartree-Fock potential v^{HF} may be re-written in terms of its Coulomb operator J and exchange operator K. For example, Equation 3.16 demonstrates v^{HF} as an effective one-electron potential operator, with the electron in question being labeled with a number "1"

$$\boldsymbol{v^{HF}(1)} = \sum_b \boldsymbol{J_b(1)} - \boldsymbol{K_b(1)} \, . \qquad \textit{Eq. 3.16}$$

The Coulomb operator (here, expressed in its closed-shell form) takes after the equation for a one-electron Coulomb potential r_{ij}^{-1} by representing the two-electron operator as the two-electron potential of electron 1 felt by the relative position of electron 2, r_{12}^{-1} [43]:

$$\boldsymbol{J_b(1)} = \int \boldsymbol{dx_2} |\boldsymbol{\chi_b(2)}|^2 \, \boldsymbol{r_{12}^{-1}} \, . \qquad \textit{Eq. 3.17}$$

In Equation 3.17, the symbol χ_b represents a spin orbital that is part of a set of spin orbitals, from which the single determinant $|\Psi_0> = |\chi_1 \chi_2 \cdots \chi_a \chi_b \cdots \chi_N>$ is formed. In the above case, electron 2 is occupying $\chi_b(2)$.

In order to define the exchange operator in Equation 3.16, it is useful to have it operating on a spin orbital $\chi_a(1)$, because the exchange operator does not have a straightforward classical analog as the Coulomb potential does. Electron 2 in this example is "exchanged" with electron 1 and now occupies $\chi_a(2)$, as seen in Equation 3.18 [43]. For comparison, the Coulomb operator is operating on the same spin orbital in Equation 3.19, but it keeps electron 1 in $\chi_a(1)$ and electron 2 in $\chi_b(2)$:

$$\boldsymbol{K_b(1)\chi_a(1)} = \left[\int \boldsymbol{dx_2} \boldsymbol{\chi_b^*(2)} \, \boldsymbol{r_{12}^{-1}} \boldsymbol{\chi_a(2)} \right] \boldsymbol{\chi_b(1)} \, , \qquad \textit{Eq. 3.18}$$

$$\boldsymbol{J_b(1)\chi_a(1) = \left[\int dx_2 |\chi_b(2)|^2 \, r_{12}^{-1}\right]\chi_a(1).}$$ *Eq. 3.19*

Re-writing Equation 3.15 in the same "ab" spin notation in bra-ket form gives:

$$\boldsymbol{E_0^1 = \frac{1}{2}\sum_{ab} < ab|ab > - < ab|ba > - \sum_a < a|v^{HF}|a >.}$$ *Eq. 3.20*

The first pair of "single-bar" bra-kets may be combined into a "double-bar" bra-ket, of the form <ab| |ab> and will be shown in Equation 3.24. But first, a mathematical explanation for this notation is explained in the following paragraphs and in Equations 3.21-3.23.

Equations 3.18 and 3.19 demonstrate one-electron integrals which are integrated over the coordinates of one electron. A two-electron integral [77], where the *i* and *k* spin orbitals are occupied by electron 1, and *j* and *l* spin orbitals are occupied by electron 2, is shown in Equation 3.21:

$$< ik \left|\frac{1}{r_{12}}\right| jl > = < ik|jl > = \iint d\boldsymbol{x_1} d\boldsymbol{x_2} \chi_i^*(\boldsymbol{x_1})\chi_j^*(\boldsymbol{x_2}) r_{12}^{-1} \chi_k(\boldsymbol{x_1})\chi_l(\boldsymbol{x_2}).$$ *Eq. 3.21*

This four letter notation will be useful for completing the analysis of the 2nd order Moeller Plesset energy perturbation correction, at the end of this section [43].

Antisymmetry is a means to satisfy the Pauli exclusion principal, and it is a way of coping with the interchange of space and spin coordinates of any two electrons that may occur within the matrix of a wave function. The antisymmetric wave function is displayed as a Slater determinant in Equation 3.22 for two electrons and requires that $\Psi(x_1, x_2) = -\Psi(x_2, x_1)$, such that the Slater determinant will not equal zero if exchange (ie:, index $i = j$) should occur [43]. "Exchange correlation" is a term used to describe what happens when two electrons have the same spin. The determinant in Equation 3.22 will be uncorrelated when electrons 1 and 2 occupy their own spin orbitals, χ_i and χ_j:

$$\boldsymbol{\Psi(x_1, x_2) = 2^{-\frac{1}{2}} \begin{vmatrix} \chi_i(x_1) & \chi_j(x_1) \\ \chi_i(x_2) & \chi_j(x_2) \end{vmatrix}} . \qquad \textit{Eq. 3.22}$$

Re-writing in terms of bra-ket notation, an antisymmetrized two electron integral can be represented as:

$$\boldsymbol{< ij| \, |kl > = < ij \, |kl > \, - < ij|lk >.} \qquad \textit{Eq. 3.23}$$

Equation 3.23 (with four different letters) is for the case when two determinants differ by two spin orbitals. Equation 3.20 (with two letters) is for the case in which two determinants are equal, and the equation $< ab \, | \, | \, ab > = < ab|ab > - < ab|ba >$ is used. The final form of Equation 3.20 may now be written using this case (still considering letters "ab" from Equation 3.20) as

$$E_0^{(1)} = \frac{1}{2}\sum_{ab} < ab| \, |ab > - \sum_a < a|v^{HF}|a >,$$
$$E_0^{(1)} = -\tfrac{1}{2}\textstyle\sum_{ab} < ab| \, |ab >. \qquad \textit{Eq. 3.24}$$

The second order perturbation term $E_0^{(2)}$ will only include doubly excited determinants [78]; this is due to the Brillouin theorem, in which single substitutions in the determinant make the expression zero and are representative of pairwise interactions between electrons. The second order energy equation may be written as

$$\boldsymbol{E_0^{(2)} = < \Psi_0 | P | \Psi_0^{(1)} >,} \qquad \textit{Eq. 3.25}$$

which can be further reduced using the expanded form of $|\Psi_0^{(1)}>$ in terms of "n" eigenfunctions, $|\Psi_0^{(1)}> = \sum_n |n><n|\Psi_0^{(1)}>$, and using the following relationship for the zeroth order energy:

$$\left(\boldsymbol{E_0^{(0)} - E_n^{(0)}}\right) < \boldsymbol{n}|\, \boldsymbol{\Psi_0^{(1)}} > = < \boldsymbol{n} \mid \boldsymbol{P} \mid \boldsymbol{0} >, \qquad \textit{Eq. 3.26}$$

$$\boldsymbol{E_0^{(2)}} = < \boldsymbol{\Psi_0}|\boldsymbol{P}|\boldsymbol{\Psi_0^{(1)}} > = \sum_{\boldsymbol{n}} < \boldsymbol{0}|\boldsymbol{P}|\boldsymbol{n} >< \boldsymbol{n}\,|\boldsymbol{\Psi_0^{(1)}} >, \qquad \textit{Eq. 3.27}$$

$$\boldsymbol{E_0^{(2)}} = \sum_{\boldsymbol{n}} \frac{|<\boldsymbol{0}|\boldsymbol{P}|\boldsymbol{n}>|^2}{\boldsymbol{E_0^{(0)} - E_n^{(0)}}}. \qquad \textit{Eq. 3.28}$$

Using the bra-ket notation for a two electron integral with double excitations notated by the wave function, $|\Psi_{ab}^{rs}>$, the second order energy term takes on the familiar form:

$$\boldsymbol{E_0^{(2)}} = \sum_{\substack{\boldsymbol{a<b} \\ \boldsymbol{r<s}}} \frac{|<\boldsymbol{ab}||\boldsymbol{rs}>|^2}{\boldsymbol{\varepsilon_a - \varepsilon_b - \varepsilon_r - \varepsilon_s}}. \qquad \textit{Eq. 3.29}$$

The ε terms in the denominator are orbital energies (as expanded in the text below Equation 3.12). In summary, the MP2 theory differs from HF by incorporating electron correlation, in this case up to the 2nd order correction. The second order correction will be negative and therefore lowers the total energy, which is more representative of the structure's equilibrium state.

3.2.2 Density Functional Theory

Instead of having the final term which represents the exact HF exchange, many DFT methods replace it with an approximate exchange functional E_X and an approximate correlation term E_C:

$$\boldsymbol{E_{DFT} = E_{NUCL} + < hP > + \frac{1}{2} < PJ(P) > + E_X + E_C} \ . \qquad \textit{Eq. 3.30}$$

Previous research reported that, Hartree Fock exchange is useful for correcting the limitations that DFT has in handling self-interaction [71-73]. Initially the research conducted in this dissertation supported the reports of advantages [71-73] of UMP2 simulations over DFT methods in localizing the self-trapped hole defect for KDP. An exception to this was ωB97XD which is explained further in the following paragraphs. Analysis was conducted by comparing the Fermi contact and anisotropic terms to hyperfine coupling constants obtained during EPR experiments. Specifically, when attempting to correctly model the self-trapped hole defect for KDP, the UMP2 simulations correctly localized the defect on two oxygen ions with their respective hydrogen ions, whereas most of the DFT results predicted the hole to be spread between the four oxygen ions and their respective hydrogen ions. These data are briefly summarized in Appendix A.

The ωB97XD range-separated functional was utilized, and it had satisfactory results. The resultant calculations using this functional had spin densities that matched expectations based on experiment, beginning with the small 41-atom cluster (see Figure 4.4 for a depiction of this cluster). This functional, ωB97XD, utilizes a long-range correction by incorporating Hartree Fock exchange using the term $\mathrm{erf}(\omega r)/r$ and maintaining the exchange functional using $erfc(\omega r)/r$ for short ranges [79]. The "XD" in ωB97XD stands for HF exchange and dispersion correction, with the dispersion correction term E_{disp} adding to the original Kohn-Sham DFT energy equation:

$$\boldsymbol{E_{DFT,D} = E_{KS,DFT} + E_{disp},} \qquad \textit{Eq. 3.31}$$

$$\boldsymbol{E_{disp}} = -\sum_{i=1}^{N-1}\sum_{j=i+1}^{N}\frac{C_6^{ij}}{R_{ij}^6}\boldsymbol{f_{damp}}(\boldsymbol{R_{ij}}). \qquad \textit{Eq. 3.32}$$

The variables within the dispersion correction term for the energy are: N, the number of atoms in the system, C_6^{ij}, the dispersion coefficient for atom pair ij, and interatomic distance R_{ij}. The damping function is represented as:

$$\boldsymbol{f_{damp}}(\boldsymbol{R_{ij}}) = \frac{1}{1+a\left(\frac{R_{ij}}{R_r}\right)^{-12}}. \qquad \textit{Eq. 3.33}$$

The variable R_r is the sum of van der Waals (vdW) radii between ij atomic pairs, and the variable "a" is a parameter that controls the strength of dispersion corrections. The vdW radius refers to an spherical area surrounding each atom that indicates the region of occupation for a particular atom and the region of closest, physically allowable approach by a separation atom. The damping factor corrects the dispersion energy term at short interatomic distances.

3.3 Information Included In Gaussian Outputs

A few issues were encountered with Gaussian when conducting simulations, in particular for the computationally intensive jobs. For instance, the Gaussian software is programmed to omit the electron density calculations, and thus the hyperfine output, for the larger UMP2 theory and for structures of 100 atoms or more, regardless of the theory. This is to save on computational cost. In order to circumvent this, when conducting a UMP2 simulation of less than 100 atoms which does not include optimization, one must specify the keyword and option combination of "density=current". An important keyword to include for structures of 100 atoms or more when using SCF-based methods, is

Iop(6/82=1, 10/47=1), which will guarantee that Gaussian prints the hyperfine terms for structures with 100 atoms or more, in particular for UHF jobs. The keyword “Iop” stands for internal options, and there are a variety of ways to use Iop settings that may be typed into the header of the input files to bypass default Gaussian settings. The header in the example code of Appendix C demonstrates the use of the “density” and “Iop” keywords.

Additionally, the population analysis in Gaussian defaults to the self-consistent field (SCF) density unless the “density” keyword is specified. The use of the “density” keyword affects two parts of the Gaussian output: first, the population analysis which consists of the Mulliken analysis, dipole moment, quadrupole moments, and higher order moments. Secondly, the hyperfine couplings which are the Fermi contact terms and anisotropic couplings. During an optimization job, MP2 uses analytic gradients, and the “density” keyword is not necessarily needed. In a geometry optimization, the energy’s first derivatives need to be computed. These are needed so one can have the forces on the atoms to indicate whether the structure is a stationary point or not, and if not, which direction to take a geometry optimization step. For methods such as MP2, analytic expressions are coded into Gaussian to be used for the first derivatives of the energy. Analytic gradients involve taking the derivative of the second order perturbation energy term to calculate the forces on the atoms as a step in trying to locate a stationary point.

IV. KDP Point Defect Simulations

This dissertation includes the quantum chemistry results obtained for three different point defects in KDP. This chapter focuses on the efforts and methods used to model a self-trapped hole in KDP and how to optimize the use of Gaussian for doing these electronic structure calculations. Chapter 5 depicts molecular orbitals and spin density plots for the self-trapped hole defect in KDP, and Chapter 6 discusses preliminary results on the hydrogen vacancy and oxygen vacancy defect in KDP. EPR data was available for all three of these defect types [19-22]. The self-trapped hole and the hydrogen vacancy were assigned to EPR spectra observed at low temperatures, therefore the orthorhombic, order-phase structure of KDP was utilized for these defects. The oxygen vacancy spectra can be observed at room temperature, therefore the tetragonal, disorder-phase structure of KDP was used for these defects. The crystal structures were modeled with a range of atom cluster sizes that varied between 41 atoms to 185 atoms.

The first step in using quantum chemistry methods to model a defect using a cluster approach is to determine the excess charge and the total spin on the specific cluster being studied. Values for the net charge and the spin multiplicity, an indicator of the number of unpaired spins and defined as 2S+1, are required inputs when starting a Gaussian run. As an example, consider the 41-atom cluster $H_{16}P_5O_{20}$ used to model the self-trapped hole. Visualize the cluster as composed of closed shell ions, i.e., K^+, H^+, P^{5+} and O^{2-} ions. In the 41-atom cluster $H_{16}P_5O_{20}$, the sixteen H^+ ions, and the five P^{5+} ions give a charge of +41, whereas the twenty O^{2-} ions give a charge of –40. Thus the net charge on the cluster, without the defect, is +1, with all the electrons in spin-up, spin down pairs. The 47-atom

cluster $K_6H_{16}P_5O_{20}$ provides another example. The six K^+ ions, sixteen H^+ ions, and the five P^{5+} ions give a charge of +47 and the twenty O^{2-} ions give a charge of –40. The net charge on this latter cluster, without a defect, is +7.

By introducing the hole (a positive entity) on the 41-atom cluster, the net charge is brought to +2 and results in an unpaired electron. Similarly, introducing the self-trapped hole for the 47-atom cluster increases the total charge to +8 and results in one unpaired electron. The unpaired electron on each cluster is represented by its unpaired spin through the spin multiplicity. For the clusters with a self-trapped hole, S = 1/2 and $2\left(\frac{1}{2}\right)+1$ gives a spin multiplicity of 2. Therefore, the 41-atom cluster has net charge and spin multiplicity values of +2 and 2. These values are stated in the Gaussian code in the line immediately preceding the atom specifications (see input code Appendix C.1 and line with "2 2"). The 47-atom cluster has +8 for the net charge and a multiplicity of 2, which would give a Gaussian input line of “8 2”.

The electrons within the KDP crystal will distribute themselves among the atoms to form a minimum energy, thus forming a stable structure. Some atoms gain electrons and other atoms lose electrons to their neighbors as bonds are formed. A useful technique to visualize the way that electrons are split up and shared between atoms in a molecule is to apply Valence Shell Electron Pair Repulsion (VSEPR) theory. By themselves, the atoms within KDP have the following atomic numbers: potassium is number nineteen; oxygen is atomic number eight; phosphorus is fifteen; and hydrogen is one. Potassium atoms have just one valence electron in the outer *4s* shell; oxygen atoms have six electrons in the outer *2s2p* shell; hydrogen atoms have one electron in the outer *1s* shell; and phosphorus atoms

have five electrons in the outer *3s3p* shell. In the PO_4H_4 unit, each of the atoms are bonded to one another by their valence electrons. Two electrons of the phosphorus and an electron from each hydrogen atom is primarily shared with their neighboring oxygen, thereby filling the outermost shell of the four oxygen atoms with a total of eight electrons.

The figures graphically depicting KDP in Chapters 4 and 5 share the same color scheme. Small white spheres are used for hydrogen, red spheres for oxygen, purple spheres for phosphorus, and large white spheres for potassium. The electrons of each atom will combine into shared molecular orbitals which can also be visualized using Gaussian, and this process is described in Chapter 5 of this dissertation. Besides demonstrating the way in which electrons are shared in order to fill the outer shells, VSEPR describes how each electron is paired. Electrons occur in pairs of spin up and spin down, as consistent with the Pauli Exclusion Principle. Once the appropriate charge and multiplicity is determined for a cluster, and the single point energy calculations are performed, the hyperfine values for a variety of defects are extracted from the Gaussian outputs and compared to experimental EPR results.

The EPR spectrum from the self-trapped hole defect was described in Chapter 2 and shows six lines representing a 31.0 Gauss hyperfine interaction with the central phosphorus nucleus and two 3.2 Gauss hyperfine interactions with the two nearby hydrogen nuclei. The EPR spectrum from the hydrogen-vacancy defect introduced in Chapter 2 also has two lines separated by 31.0 Gauss, attributed to a phosphorus hyperfine interaction. The computationally modeled self-trapped hole is presented in this chapter, and the hydrogen vacancy defects are presented and compared with EPR results in Chapter 6. Lastly, there are five similar, yet distinct, EPR spectra from oxygen vacancies

with hyperfine splittings from phosphorus that range from 600 to 800 Gauss. These oxygen vacancies are discussed further in Chapter 6.

4.1 Introduction to the Self-Trapped Hole

This section describes how the optimum combination of quantum method and basis set, combined with the optimum geometry, was determined for performing the KDP self-trapped hole defect calculations. These results also helped to set up the inputs for the oxygen vacancy and hydrogen vacancy simulations. The development of the approach began by comparing to previous [22] computational results using the tetragonal crystal structure, and this is discussed in Section 4.1.1. The subsequent Sections 4.1.2-4.1.7 present results for the orthorhombic crystal structure, which is the physically realistic structure for the self-trapped hole defect.

4.1.1 Validation of Previous Tetragonal Cluster Results without Potassium Ions

Before modeling the self-trapped hole in an orthorhombic cluster, this defect was studied in a 41-atom tetragonal cluster (shown in Figure 4.1) which was constructed using the lattice constants from Nelmes *et al.* [80]. The reason for initially using a tetragonal cluster was to confirm the computational results presented in Chirila's dissertation which used a tetragonal $H_{16}P_5O_{20}$ cluster for point defects [22]. In order to precisely duplicate the prior study, the cluster does not include potassium ions. Additionally, the prior study only focused on the isotropic Fermi contact values and not the anisotropic dipole-dipole hyperfine values. For this initial task, only the computed isotropic hyperfine parameters are considered. The isotropic Fermi contact values before and after a geometry optimization using UHF and the 6-31++G(d,p) basis set are displayed in Table 4.1 below

and are in agreement with previously published optimization results which also used UHF and 6-31++G(d,p) [22].

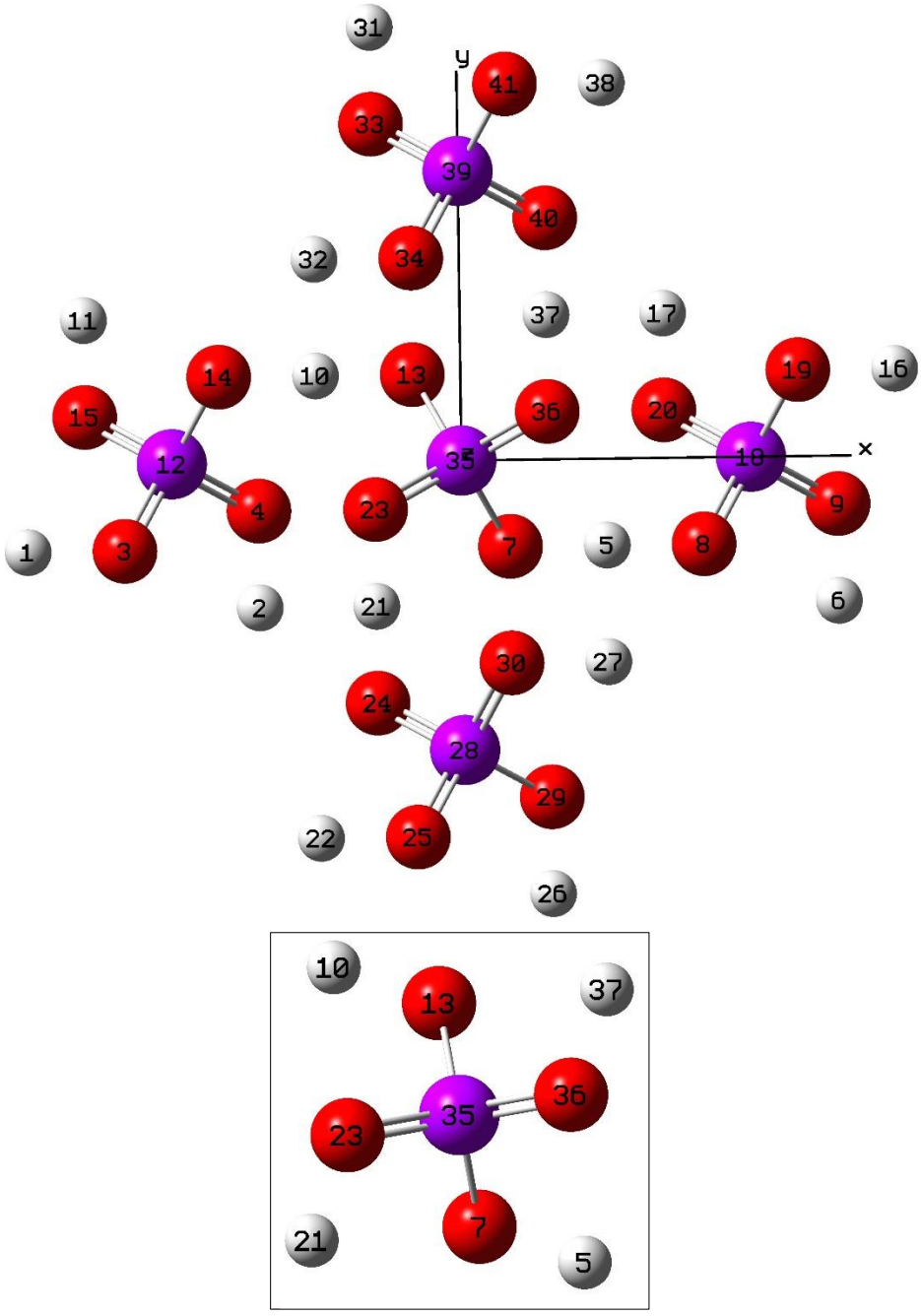

Figure 4.1. 41-atom tetragonal KDP cluster before optimization, with the Cartesian axis overlaid. The top image shows all 41 atoms (z-axis pointing out) with the Cartesian axis. The bottom shows the central PO_4H_4 unit of interest, zoomed in. Atoms H21, O23, P35, O36 and H37 share the self-trapped hole.

The results in Table 4.1 indicate that two out of the four oxygen ions in the central PO_4 unit share the hole, oxygen number 23 and 36, and their Fermi contact values are shown in the first row of Table 4.1. The other two oxygen ions have a comparatively small amount of the spin density, oxygen number 13 and 7, and their Fermi contact values are listed in the second row of Table 4.1. The results for the hydrogen atoms are also listed. The hydrogen atoms with the hole are number 21 and 37 and are listed in the third row of Table 4.1, and the hydrogens without the hole, number 10 and 5, are the fourth row of Table 4.1. The two hydrogens with larger Fermi contact values are located next to the two oxygen ions (H21, O23 and O36, H37 in Figure 4.1) with larger Fermi contact values, and the two hydrogens with smaller Fermi contact values are next to the oxygen ions with smaller Fermi contact values (H10, O13 and O7, H5 in Figure 4.1). The Fermi contact values for the cluster help to obtain a preliminary understanding of how the self-trapped hole's unpaired spin is distributed among the atoms, before delving fully into a calculation of the anisotropic hyperfine values.

Table 4.1. Isotropic hyperfine values for atoms with (O23, O36, H21, H37) and without the hole (O13, O7, H10, H5) for the 41-atom tetragonal cluster before and after optimization, allowing all nine atoms in the central PO_4H_4 to move. The results are also compared to previous work [22] which allowed the two hydrogen atoms and two oxygen atoms that shared the self-trapped hole to move during optimization. All results are in Gauss units and used the UHF/6-31++G(d,p) method and basis set.

Atom	Fermi Contact Value, pre-optimization	Fermi Contact Value for Atoms with hole, from [22]	Fermi Contact Value, post-optimization
Oxygen 23, 36	-29.43		-29.38
Oxygen 13, 7	0.57		1.06
Hydrogen 21, 37	-6.84	-10	-1.03
Hydrogen 10, 5	0.05		0.12
Phosphorus 35	-87.05	-46	-78.70

The Fermi contact values before optimization for the atoms that shared the self-trapped hole were -1.03 Gauss for both of the hydrogen ions (H37 and H21) and -29.43 Gauss for both of the oxygen ions (O23 and O36). The relative location of these ions to the central PO_4H_4 unit and the atoms in the rest of the surrounding cluster (minus potassium atoms) are seen in Figure 4.1. After optimization, the Fermi contact value for the hydrogen ions became -6.84 Gauss, and the Fermi contact values for the oxygen ions changed very slightly, to -29.38 Gauss. The isotropic hyperfine values for the phosphorus ion (P35) were -87.05 Gauss before optimization and -78.70 Gauss after optimization, as seen in Table 4.1. The hyperfine values for the phosphorus and hydrogen ions are on the same order of the experimental EPR results, namely 31.0 Gauss for the phosphorus and 3.2 Gauss for the hydrogen atoms [19-21]. The relative difference in signs, negative for the output from Gaussian and positive from EPR experiments, are not directly comparable, because the choice of the sign is chosen arbitrarily in experiment. A discussion on the significance of relative signs from *ab-initio* calculations is introduced in Section 4.1.7 in order to examine the distribution of spin density for the isotropic versus anisotropic hyperfine values, post geometry optimization.

The geometric displacement of the atoms that share the self-trapped hole is seen in Table 4.2. Specifically, the distance between the hydrogen atoms and their neighboring oxygen atoms increases from 1.26 Angstroms to 1.64 Angstroms. The other significant geometry change is the angle between the central phosphorus atom and the two oxygen atoms. This angle decreases from the perfect lattice placement of 103.44 degrees to 97.06 degrees after geometry optimization. This demonstrates the “trapping” of the self-trapped hole, and this geometric phenomenon is explored in more detail later in this chapter.

Table 4.2. Interatomic, oxygen hydrogen (O-H) and oxygen phosphorus (O-P), distances and oxygen-phosphorus-oxygen (OPO) angle measurements before and after optimization for the atoms that shared the self-trapped hole in the 41-atom cluster.

Atom	Pre-optimization	Post-optimization
O-H distance	1.26 Å	1.64 Å
O-P distance	1.56 Å	1.54 Å
OPO angle	103.44 deg	97.06 deg

4.2 Results from a 41-atom Orthorhombic Cluster without Potassium Ions

The self-trapped hole is an unstable defect when the crystal is in the high-temperature tetragonal phase, and thus the results from the previous tetragonal clusters are not truly representative of the actual defect. To accurately model the self-trapped hole defect, a cluster was created using the low temperature orthorhombic lattice constants from a 2001 paper by Miyoshi and coworkers who performed single crystal neutron diffraction experiments at 10 K [81]. Figures 4.2-4.4 demonstrate a typical procedure for how GaussView (a software component compatible with Gaussian) was used to create the orthorhombic clusters. First, the space group is chosen, and the unit cell parameters are entered. The appropriate Fdd2 orthorhombic space group was selected for KDP with unit cell parameters based on fractional coordinates reported in [81] and given in Table 4.3. These unit cell parameters were determined by converting the a, b, c lattice constants from the fractional coordinates to regular Cartesian coordinates in order to input them to GaussView. This was done by multiplying the unit cell parameters by the fractional cell parameters, and the results are seen in Table 4.3 for five central atoms.

After entering the Cartesian coordinates and unit cell parameters from Table 4.3 into GaussView, it automatically creates a cell with the atoms duplicated the appropriate amount of times depending on where they are in the lattice for the pre-defined space group. A KDP unit cell is 32 atoms, comprised of four formula units. The cell depicted in Figure 4.2 is a 64 atom cell. The cell may be grown by utilizing the periodic boundary cell editor, which is a tool within GaussView. As seen in Figures 4.3, the cell is duplicated in the x, y, and z directions once for each axis. Figure 4.4 is the result after trimming away extra atoms from Figure 4.3.

Table 4.3. Cartesian coordinates (x,y,z) for the central atoms calculated from the fractional coordinates measured by Miyoshi and coworkers for the orthorhombic KDP cluster [81].

Atom	X	Y	Z	Unit Cell Parameters (Å)	
K	0	0	3.347792	a	10.5447
P	0	0	0	b	10.4816
O	0.358509	1.210614	-0.94762	c	6.9205
O	1.225073	-0.36067	0.809283		
H	2.243069	0.662647	0.787968		

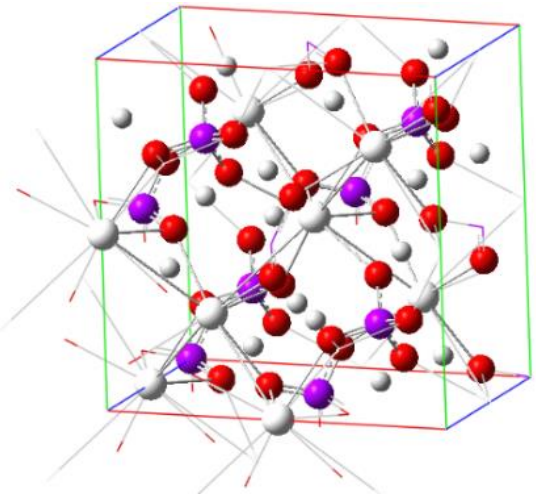

Figure 4.2. A 64-atom cell for the orthorhombic KDP cluster. The lines indicate dangling bonds that are ready to have atoms affixed to them, if the user specifies to grow the cell.

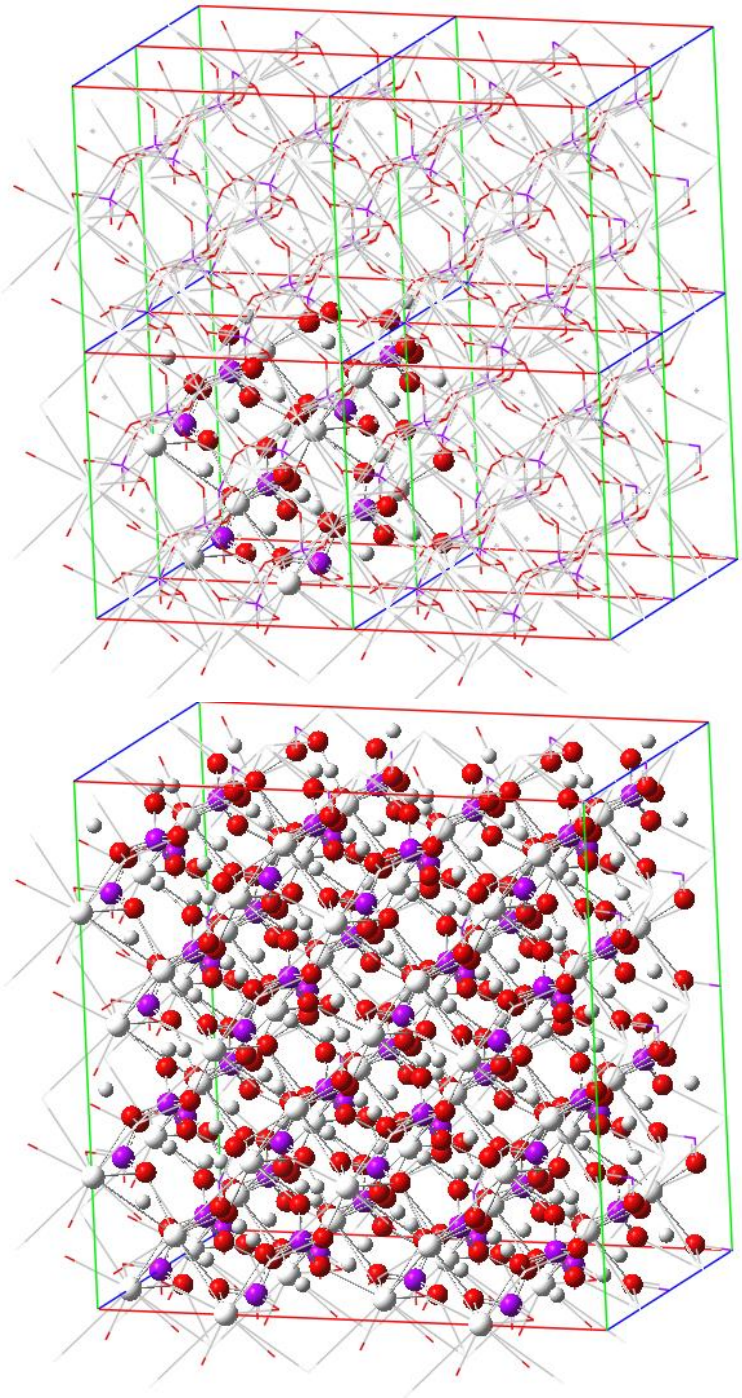

Figure 4.3. (Top) Expanding the 64 atom cell in the (x,y,z) direction by one unit along each axis utilizing the periodic boundary condition tool in GaussView. (Bottom) The supercell corresponding to the replicated atoms in the top panel.

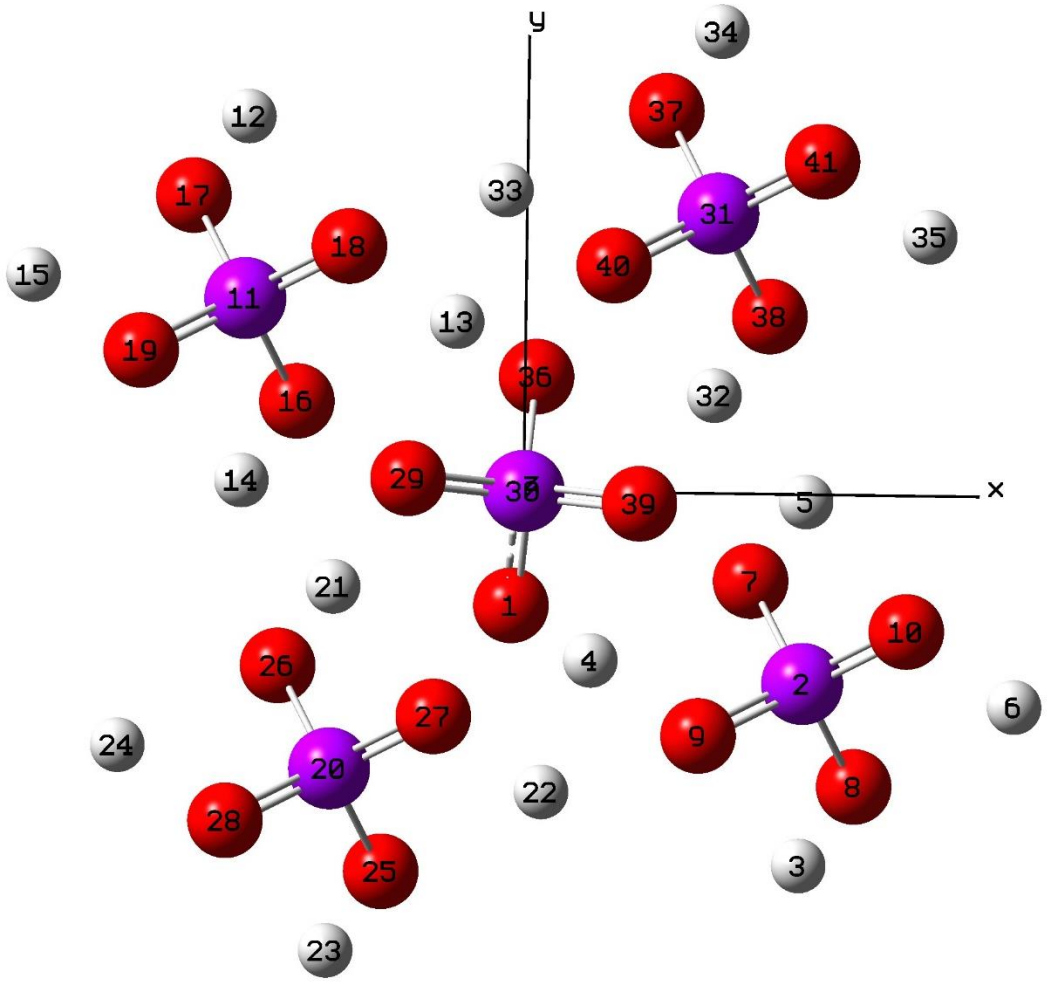

Figure 4.4. The 41-atom orthorhombic structure after trimming away the extra atoms in the larger structure created in GaussView.

4.2.1 Results from 41-atom using UMP2/6-31++G(d,p) without Potassium Ions

The methods described in the previous section were utilized in order to generate structures for the remainder of this research project. In this section, the orthorhombic 41-atom structure was submitted as an optimization run in Gaussian to examine the self-trapped hole defect, and all nine atoms in the central unit were allowed to move while keeping the other atoms in the cluster fixed. In reference to Figure 4.4, the atoms that were allowed to move were H4, O1, O36, H13, H32, O39, P30, H21, and O29. The method and

basis set that were chosen after having explored UHF for the optimization were UMP2/6-31++G(d,p). The UHF method had been producing hyperfine results that indicated an equally shared spin density on two hydrogen atoms and equally shared between their two respective oxygen atoms, as had been demonstrated for the tetragonal simulations in Section 4.1.1. However, it does not produce hyperfine results that are as close to EPR experiment as the UMP2 method. Additionally, once hours were granted on the HPC, it became possible to use the more computationally expensive UMP2 method in order to generate results that were closer to EPR measurements, in particular with larger clusters.

The hyperfine results for the 41-atom cluster were compared to experimental EPR results [19, 20], in addition to comparisons with the isotropic and anisotropic outputs from Wells *et al.* who conducted ENDOR and ESR experiments on the self-trapped hole in KDP at 4.2 K [82]. The resulting combination of hyperfine results are compared with Wells *et al.* for a large 129-atom structure in Section 4.1.7 of this dissertation. This comparison with Wells *et al.* was made because the EPR results published by Garces and Stevens only contained the combined hyperfine splittings along the c-axis of the magnetic field, which are a combination of isotropic and anisotropic parameters. The Wells paper refers to the self-trapped hole as the "4.2 K defect" and provides a complete description of the g matrix and the anisotropic matrices for the hydrogen ions that share the hole as well as for the phosphorus ion.

The results of the orthorhombic 41-atom structure simulation conducted with UMP2/6-31++G(d,p) after optimization are shown in Table 4.4, alongside the values obtained from experiments [19, 20 ,82]. The anisotropic hyperfine results are listed for the Baa, Bbb, and Bcc principal axes components. The calculated hyperfine values are on the

same order of magnitude as the EPR hyperfine results, which were 31.0 Gauss for the phosphorus ions and 3.2 Gauss for the two hydrogen ions that shared the self-trapped hole [19, 20]. Table 4.4 also demonstrates that there is comparatively little spin density on hydrogen number 4 and hydrogen number 13, which are the opposing pair of hydrogen ions of the same PO_4H_4 unit.

The separated isotropic and anisotropic hyperfine results in Table 4.5 are given in units of MHz for ease of comparison with the published isotropic and anisotropic ENDOR values [82]. The experimental values from the EPR experiments were converted from units of Gauss to MHz in order to include the results on the same table for comparison purposes. The conversion between Gauss and MHz may approximately be done by multiplying the value in Gauss by a factor of 2.8. According to the Gaussian results, the two hydrogen ions with the hole (H21 and H32) both have an isotropic value of –3.35 MHz and anisotropic values of $\mathrm{Baa} = -11.122, \mathrm{Bbb} = -8.195, \text{and } \mathrm{Bcc} = 19.317$ MHz, in the diagonalized form of the anisotropic matrix.

The hyperfine values for the four oxygen ions are also shown in Table 4.4 in a similar manner as was presented in Table 4.1 in order to understand the distribution of spin density among atoms in the central PO_4H_4 unit. The pair of oxygen ions that are paired with hydrogen number 21 and 32 (oxygen number 29 and number 39 respectively), have relatively large hyperfine values compared with the pair of oxygen ions that are paired with hydrogen number 4 and 13 (oxygen number 1 and number 35, respectively).

Table 4.4. UMP2/6-31++G(d,p) isotropic and anisotropic (along the principal axes) hyperfine values for the 41-atom cluster after allowing all nine ions in the central PO_4H_4 unit of the orthorhombic KDP structure to move, compared with results from ENDOR and EPR experiments [19, 20, 82].

Atom	Isotropic Results (MHz)	Anisotropic (MHz)	Isotropic ENDOR [82] (MHz)	Anisotropic ENDOR [82] (MHz)	EPR, Combined Hyperfine [19, 20] (MHz)
Hydrogen 21 and 32	-3.35	-11.12 -8.2 19.32	-1.03	14.17 -8.15 -6.02	6.4
Hydrogen 4 and 13	1.46	-3.31 -1.52 4.83			
Phosphorus 35	-34.05	-3.75 -1.67 5.41	-82.21	-3.31 -0.23 3.54	62.0
Oxygen 29 and 39	-50.66	70.12 67.93 -138.04			
Oxygen 1 and 36	1.33	1.73 1.33 -3.06			

The central PO_4 unit seen in Figure 4.5 is surrounded by four hydrogen ions; two are relatively closer to the unit and two are relatively farther away, as was introduced in Chapter 2. After optimization, the self-trapped hole is primarily interacting with O39 and O29, which have the far hydrogen ions, H32 and H21. These oxygen and hydrogen ions are separated by a distance of 1.44359 Angstroms. This is in contrast to previous research by Stevens *et al.*, which suggested that the self-trapped hole defect was on O1, O35, and the near hydrogen ions, H4 and H13 [20]. The distance between these oxygen and hydrogen ions are 1.0598 Angstroms, per pair. A zoomed in and rotated image of the ions without the hole are shown in Figure 4.6, and an image with the self-trapped hole are shown in Figure 4.7.

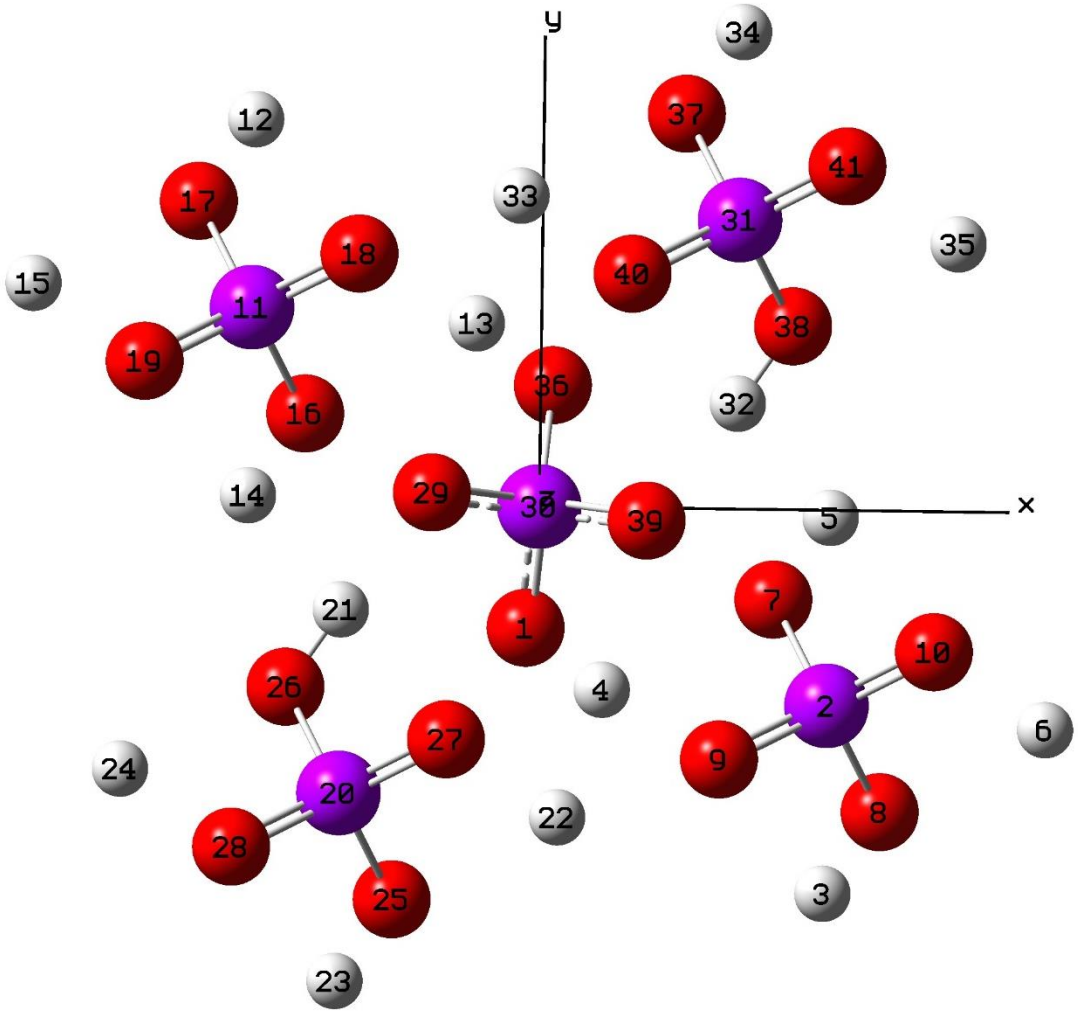

Figure 4.5. The 41-atom orthorhombic KDP structure after optimization which was conducted with UMP2/6-31++G(d,p). The central nine atoms were allowed to move (H4, O1, O36, H13, H32, O39, P30, H21, and O29). The two "near" hydrogen ions are H4 and H13, and the two "far" hydrogen ions are H21 and H32. The z-axis is pointing out of the page, the y-axis is pointing up, and the x-axis is pointing right.

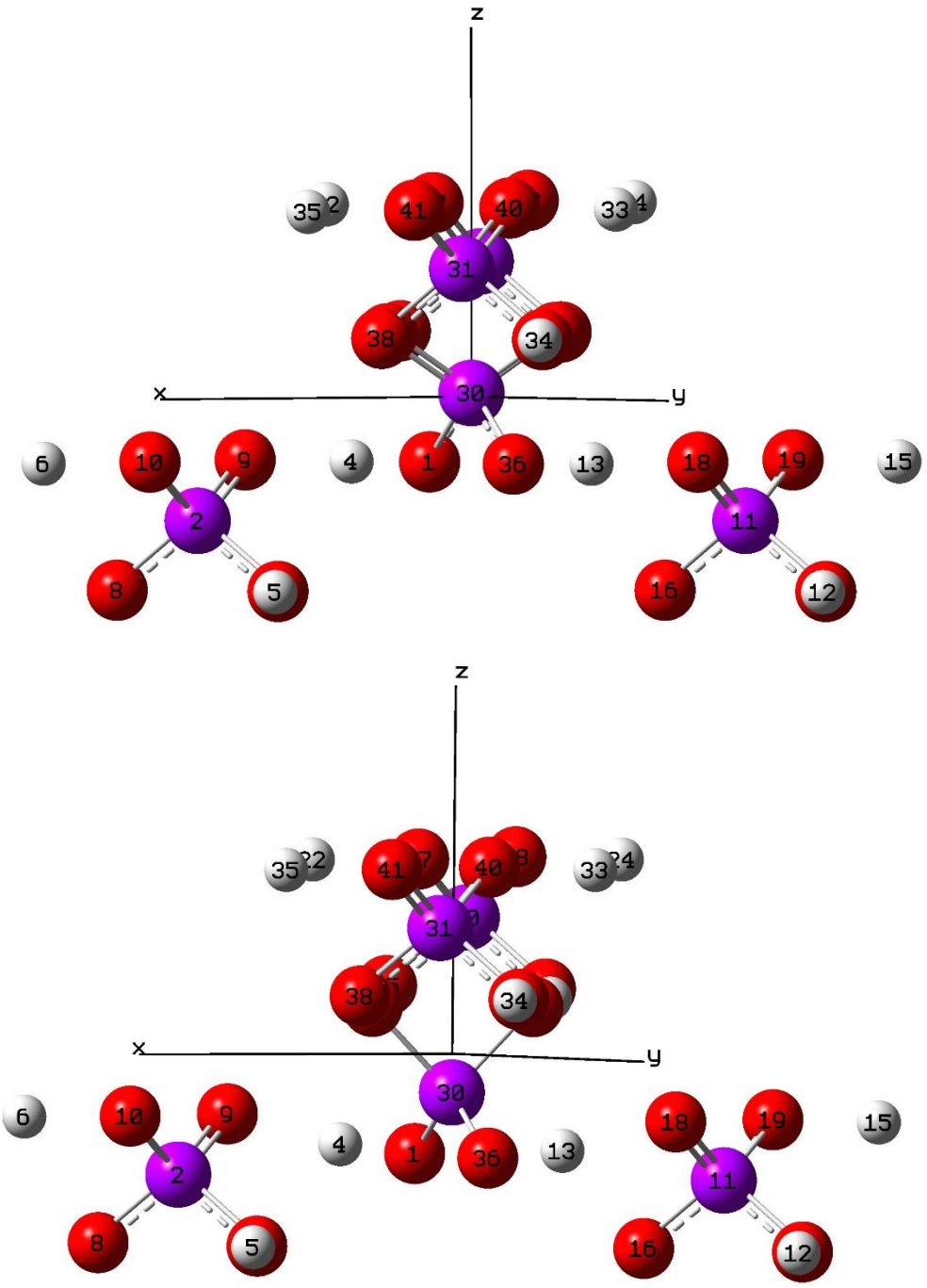

Figure 4.6. The view of the atoms in the central part of the 41-atom orthorhombic structure that do not have the hole (H13, O36, O1, and H4) with z-axis pointing up. The image on the top is before optimization, and the image on the bottom is after optimization. The quantitative changes in the relative distances between the atoms that took place during optimization are shown in Table 4.6.

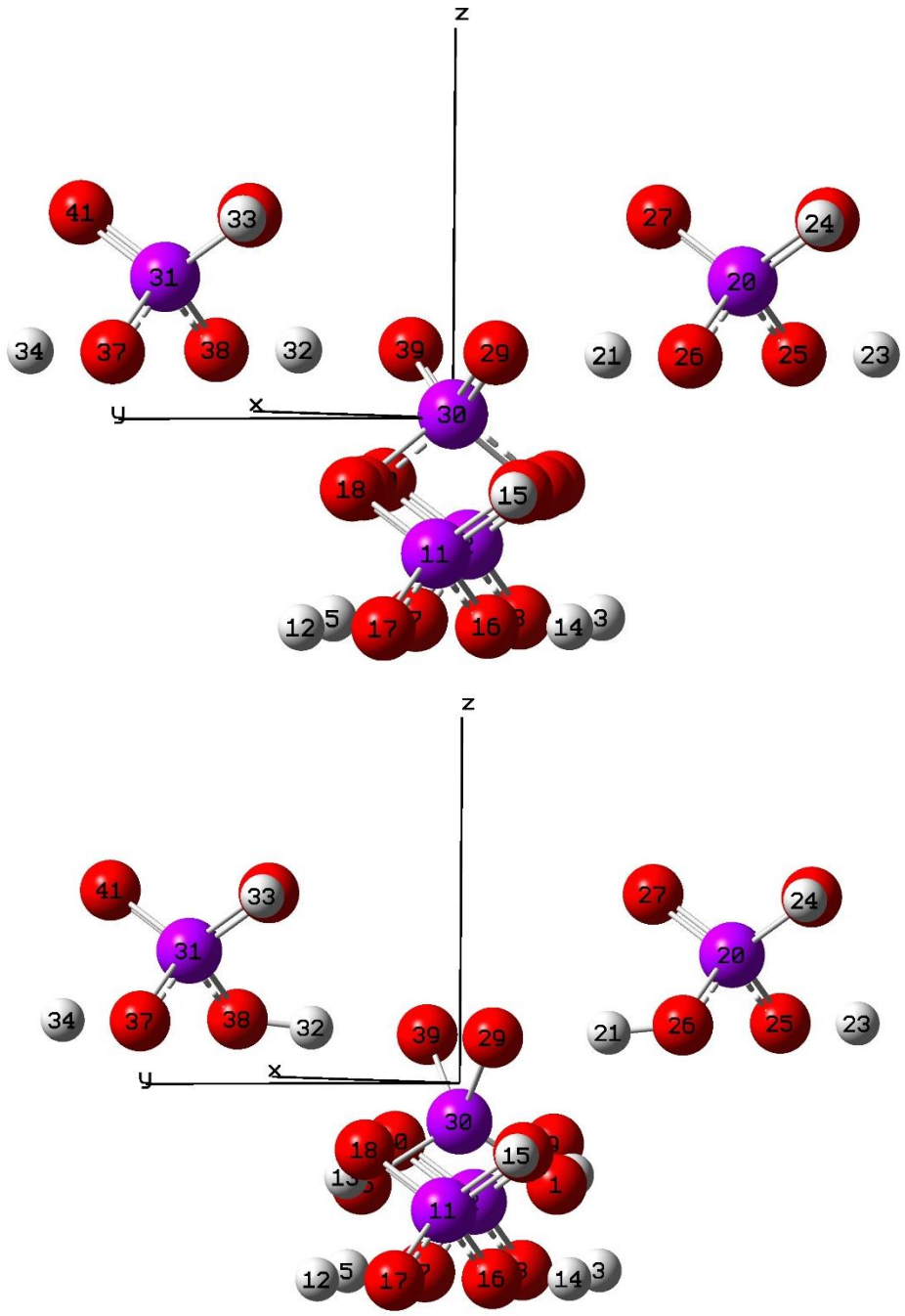

Figure 4.7. The view of the atoms in the central part of the orthorhombic structure that have the hole with z-axis pointing up in both images. The hole is shared between H32, O39, O29, and H21. The figure on the top is before optimization, and the figure on the bottom is after optimization. The quantitative changes in the relative distances between the atoms that took place during optimization are shown in Table 4.6.

In addition to the hyperfine values, the coordinates of the ions that were allowed to move during the geometry optimization were compared to those of the perfect crystal obtained from the x-ray and neutron diffraction experiments. The bond distances shown in Table 4.6 and displayed in Figures 4.6 and 4.7 demonstrate that the atoms in the PO_4 unit that are opposite from the oxygen atoms where the unpaired electron localizes moved relatively little in comparison with the atoms that host the unpaired electron. The angle between the two oxygen ions that have the hole (O29, P30, O39) was reduced from 115 degrees to 94 degrees, and these two oxygen ions moved farther away from the central phosphorus and their respective hydrogen ions. This is indicated by the increase in the P30-29 and P30-O39 distance from 1.412 to 1.57 Angstroms and an increase in the H21-O29 and H32-O39 distances from 1.44 to 1.58 Angstroms. As seen in Table 4.6, the OPO (oxygen-phosphorus-oxygen) angle for the trio that includes the two oxygen ions without the hole increased from 106 degrees to 112 degrees (O36, P30, O1). The distances between P30-O36 and P-30-O1 reduced very slightly, from 1.58 to 1.56 Angstroms, and the distances between H13-O36 and O1-H4 also changed slightly, from 1.06 to 1.05 Angstroms. Figure 4.6 presents a good view of the central phosphorus ion as it changes its position along the z-axis before and after optimization. The relative difference in location of phosphorus number 30 in the top image of Figure 4.6 compared to the bottom image in Figure 4.6, shows that it moves downwards along the z-axis during optimization, away from O29 and O39 and towards O1 and O36 and off of the origin of the Cartesian axis.

Table 4.6. Distances and angles, before and after geometry optimization, for the 41-atom orthorhombic structure. The unpaired electron is localized on O1-H4 and O36-H13 of the central PO_4 unit, while O29-H32 and O39-H21 are on the opposite side of the phosphorus atom and do not share the hole.

Atoms	Bond Distances (Å)		Angles (degrees)	
	Before opt.	After opt.	Before optimization	After optimization
R(H13-O36), R(O1-H4)	1.06	1.05		
R(P30-O36), R(P30-O1)	1.58	1.56		
R(H21-O29), R(H32-O39)	1.44	1.58		
R(P30-O29),R(P30-O39)	1.51	1.57		
A(O36-P30-O1)			106.22	112.72
A(O29-P30-O39)			115.28	94.55

The relative placement of the self-trapped hole within the KDP crystal can be explained by a simple electrostatics argument. The hole that is self-trapped represents a positive charge, thus it will primarily localize on one or more negatively charged oxygen ions. Furthermore, the positive hole will want to be far away from the positive hydrogen ions, i.e., due to electrostatic repulsion. This makes the preferred location of the hole on the oxygen ion pair that is farther from hydrogen ions. This electrostatic behavior is also seen when allowing the oxygen ions with the hole to move relative to the central phosphorus ion, which has a +5 charge. The positive hole wants to move away from the positive phosphorus ion. This process is explored in the context of a larger cluster which includes potassium ions, in Section 4.1.7.

4.2.2 Methods for Combining Hyperfine Values

The UMP2/6-31++G(d,p) simulation described in Section 4.2.1, both before and after optimization, gave results that were not as close to the experimental EPR results as the UMP/6-31++G simulation with no optimization. Table 4.7 below shows the results

generated using UMP2/6-31++G with no optimization, specifically listing the hydrogen and phosphorus anisotropic hyperfine values and their respective sets of direction cosines, along with a comparison to the results from experiment [19, 20]. The direction cosines are needed to combine isotropic and anisotropic hyperfine values. The phosphorus ion's Bcc anisotropic component lies exactly along the z direction, since alpha and beta are both equal to zero and gamma equals one. This means that the isotropic Fermi contact term can be added directly to the Bcc anisotropic term to obtain a value that can be compared to the EPR splitting experimentally measured when the applied magnetic field is along the z-axis (corresponding to the c-axis). This gives a value of -41.46 Gauss, which is closer to the EPR experiment value of 31 Gauss than the UMP2/6-31++G(d,p) results.

However, the hydrogen ion does not lie along the gamma direction, and so methods were explored to combine the isotropic and anisotropic hyperfine values, besides directly adding the Fermi contact term to the gamma direction of the Bcc principal component. The first method that was pursued was to use rotational operators. These operators were employed to extract the c-axis component of the anisotropic hyperfine matrix from the Gaussian output. This method is described in Appendix B.1, and the MATLAB code used to conduct the operations is in Appendix B.2. After converting the directional cosines into Euler angles and conducting these rotational operations, the predicted c-axis hyperfine value for the hydrogen ion is -5.334 Gauss, which is closer in magnitude than the UMP2/6-3++G(d,p) results to the experimental EPR value of 3.2 Gauss.

Table 4.7. A section of the "Anisotropic Spin Dipole Couplings in Principal Axis System" output from Gaussian for the UMP2/6-31++G run with no optimization, which has been formatted into a table. These results are for the central phosphorus (P30) and one of the hydrogen (H21) ions that have the hole. Results are compared to experiment [19, 20], using the rotation matrix method of combining the hyperfine values.

Atom	Principal Values (Gauss)		Direction Cosines			Combined (Iso+Aniso)	Garces, Stevens [19, 20]
H21	Baa	-4.473	-0.4806	0.3687	0.7957	-5.334 Gauss	3.2 Gauss
	Bbb	-3.145	0.6906	-0.4001	0.6025		
	Bcc	7.618	0.5404	0.8391	-0.0623		
P30	Baa	-4.572	0.9993	0.0366	0.0000	-41.46 Gauss	31 Gauss
	Bbb	-1.066	-0.0366	0.9993	0.0000		
	Bcc	5.638	0.0000	0.0000	1.0000		

The "Anisotropic Spin Dipole Couplings in Principal Axis System" section of the Gaussian output file will also display units of MHz and cm^{-1}, but in Table 4.7, only the units of Gauss are displayed for comparison purposes to the experiments conducted by Garces and Stevens [19, 20].

The next method to be explored within the course of this dissertation research, was to simulate the EPR spectrum using the open-source code EasySpin [83]. In order to use EasySpin to simulate EPR spectra, the anisotropic part of the **A** matrix, $\boldsymbol{A_{aniso} = T_{abc}}$, in the crystal coordinate system was first calculated using the outputs from a Gaussian simulation. The $\boldsymbol{T_{abc}}$ matrix was constructed by multiplying the transpose of the direction cosine matrix $\boldsymbol{R^T}$, by $\boldsymbol{T_{ABC}}$, the principal values multiplied by the identity matrix, and the matrix of direction cosines $\boldsymbol{R}$. This is expressed by Equation 4.1 and Equation 4.2.

$$\boldsymbol{T_{ABC}} = \begin{bmatrix} B_{aa} & 0 & 0 \\ 0 & B_{bb} & 0 \\ 0 & 0 & B_{cc} \end{bmatrix} \qquad \textit{Eq. 4.1.}$$

$$\boldsymbol{A_{aniso} = T_{abc} = R^T T_{ABC} R} \qquad \textit{Eq. 4.2.}$$

Once the $\boldsymbol{A_{aniso}}$ matrix was calculated, then the Fermi contact terms are added to the diagonal part of this matrix, such that: $\boldsymbol{A = a_{iso}I + A_{aniso}}$ (from Chapter 3, Equation 3.4). This **A** matrix and the specification of the frequency that was used during the experiment along with a range of magnetic field values are programmed into EasySpin. A complete description of this code is provided in Appendix B.3.

Simulated EPR spectra generated by EasySpin is shown in Figure 4.8 for the hydrogen ion, using the results from the UMP/6-31++G optimization for the 41-atom cluster. These results are not optimal and are only presented here in order to illustrate the EasySpin method. In Section 4.1.7, spectra are again simulated for a large 129-atom cluster, which provided the most optimal results.

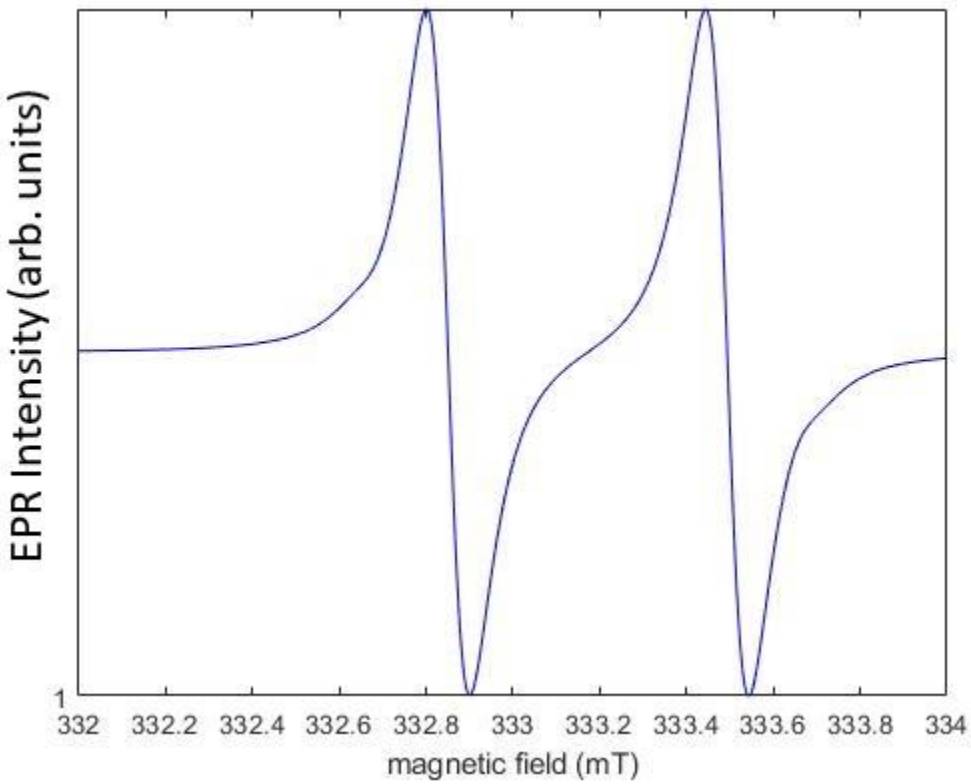

Figure 4.8. Simulated spectra from EasySpin for hydrogen number 21 in the 41-atom cluster for the self-trapped hole defect.

Finally, the combined hyperfine value is obtained from these simulated spectra the same way as they would be obtained from the experimental EPR spectra. This is done by centering a data cursor on the middle of each data peak and then measuring the separation between them. In the case of Figure 4.8, the hyperfine separation is approximately 333.5 mT minus 332.8 mT, which is 0.7 mT or approximately 7 Gauss.

4.2.3 Discrete Atom Movement for "Coordinate Scans"

Results from Table 4.4 show that the geometry optimization which allowed nine atoms to move with the UMP2/6-31++G(d,p) method and basis set gives a central phosphorus hyperfine value of −10.21 Gauss (after conversion from MHz). The optimization performed by Gaussian using UMP2/6-31++G also does not calculate the hyperfine values exactly as they are measured by EPR experiments, with a central phosphorus hyperfine value at 41.46 Gauss before optimization and a hyperfine value of 91.53 Gauss after optimization. In order to better understand the effect of the geometry on the calculated hyperfine values, the optimization process was examined in greater detail. Furthermore, Gaussian does not provide an incremental output for hyperfine values per optimization step, and therefore, this procedure was helpful to see how the hyperfine values may change during each optimization step.

An optimization of the cluster moves the oxygen ions inwards, such that the distance between the oxygen ions and their nearby hydrogen ions are increased to 1.55529 Angstroms, which might be farther than what may be realistically occurring. It should be assumed that in a real cluster, the ions effected by the defect have not moved more than a fraction of an Angstrom from their perfect lattice position. Therefore, a different technique

was pursued in order to further understand the Gaussian optimization and how it affects the hyperfine values. Optimization is conducted in Gaussian to find an energy minimum for the structure by moving atoms by a fraction of an Angstrom per step until an energy minimum is reached. For the self-trapped hole defect, a hole is expected to become trapped in KDP when the oxygen ions of the PO_4H_4 unit move closer to one another, thus "trapping" the defect. The two oxygen ions sharing the hole were manually moved by increments of degrees for the angle formed between the two oxygen ions and the central phosphorus ions, in a similar manner that Gaussian moves the oxygen ions. This is because it is known that the unpaired electron is shared between two oxygen ions, and that the two oxygen ions are closer together in this case than they are in the perfect crystal. The hyperfine values were also analyzed per step, as seen in Table 4.8.

Table 4.8. Hyperfine terms and total energy computed at various OPO angles of the PO_2 fragment that contains the unpaired electron.

	Phosphorus Hyperfine			
Angle (degree) OPO separation	Isotropic (Gauss)	Anisotropic (Gauss)	Total Hyperfine (Gauss)	Total Energy (Hartrees)
No optimization, 115.28	35.83	5.64	41.47	-3210.942
113.88	33.72	5.56	39.28	-3210.944
110.2	27.87	5.31	33.18	-3210.948
109.15	26.14	5.23	31.37	-3210.948
106.01	20.85	4.97	25.82	-3210.951
97	5.26	11.68	16.94	-3210.953
95	1.86	11.19	13.05	-3210.952
90	-6.18	10.03	3.85	-3210.949

As the results in Table 4.8 demonstrate, an energy minimum is reached near 97 degrees separation for the OPO angle, but the best hyperfine value occurs between 109.15 and 110.2 degrees, 31.37 Gauss and 33.18 Gauss respectively, compared to 31 Gauss from

EPR experiments [19, 20, 21]. The total energy is highest for the unaltered structure, at -3210.942 Hartrees. Each iteration that moves the two oxygen atoms closer together brings the energy down to the minimum and then up again, but the hyperfine value starts to diverge from the value measured in EPR experiment after the ions begin to close in at angles smaller than 109.15 degrees. The method described in Appendix B was used to combine and calculate the hyperfine value for the hydrogen atom, since the anisotropic values for Bcc did not lie exactly along the gamma direction. The hyperfine value for the hydrogen ion was calculated to be 5.814 Gauss, which is closer to the value obtained in the EPR experiment, of 3.2 Gauss. It is important to keep in mind that these manual angle scans were conducted with the 41-atom cluster that does not have any potassium ions. The influence that the potassium ions have on the hyperfine parameters is explained in "Section 4.1.3. Large Orthorhombic Clusters."

Another coordinate scan was performed for UMP2/6-31++G, by moving the two oxygen ions inwards and outwards, along the line that connects them. The results for those trials are seen in Table 4.9. Here, the results in Table 4.9 show that the moving the two oxygen ions in closer along their bond also brings them closer to the central phosphorus ion, which drives up the total energy of the cluster. Although the hyperfine value is closer to the value obtained in the EPR experiment (31 Gauss) between an O-O distance of 2.53 and 2.50 Angstroms (28.71 and 35.65 Gauss, respectively), the energy is higher than that of the structure before any geometric alteration has taken place. The energy begins to decrease when the two oxygen ions are separated farther from one another which also increase their distance from the central phosphorus. Therefore, this may indicate that for

the hole to be properly formed in this particular 41-atom structure, the oxygen ions need to come closer together while also moving away from the central phosphorus ion.

Table 4.9. Hyperfine terms (in Gauss) and total energy (in Hartrees) computed at various O-O distance of the PO_2 fragment that contains the self-trapped hole.

	Phosphorus Hyperfine				
O-O Distance Å	Isotropic	Anisotropic	Total	P-O distance, Å	Energy
2.4	5.33	3.17	8.5	1.447	-3210.902
2.45	14.14	3.90	18.04	1.468	-3210.918
2.5	24.00	4.70	28.71	1.489	-3210.931
2.53	30.43	5.21	35.65	1.502	-3210.937
2.54	32.65	5.39	38.40	1.506	-3210.939
2.55 (Before Moving)	35.83	5.64	41.47	1.512	-3210.942
2.57	39.48	5.92	44.40	1.519	-3210.945
2.59	44.17	6.28	50.35	1.521	-3210.948
2.62	51.33	6.81	58.14	1.540	-3210.952
2.7	70.22	8.10	78.32	1.574	-3210.960

For comparison with Table 4.9, the final results for the Gaussian optimization job described previously gave a distance between the two oxygen ions of 2.388 Angstroms with hyperfine of 91.535 Gauss, a phosphorus-oxygen distance of 1.657 Angstroms, and an energy of -3210.988 Hartrees. It is important to include an analysis of the estimated minimum energy of the structure, because it is well-defined and represents the most probably geometry for a given ground state wave function. However, unlike Table 4.8 which was able to demonstrate an energy minimum, the results seen in Table 4.9 have a diverging energy.

4.2.4 Layers of Interest and Atom Links

In order to tackle the challenge of modeling the self-trapped hole defect in a large KDP cluster that contained potassium ions, a variety of Gaussian techniques were utilized

to see if they could assist in producing a realistic computational result. The following information is meant to be instructive and potentially beneficial to a project that might need to utilize these methods for KDP. Multi-layered optimization calculations can be carried out using ONIOM [83] ("Our own N-layered Integrated molecular Orbital and Molecular mechanics"). The ONIOM method works by assigning the area of interest – in the case of KDP the central PO_4 cluster that has the self-trapped hole – as the "high" layer, and the rest of the structure as the "low" layer. The high layer is typically assigned a more complex quantum method and a larger basis set, while the low layer is assigned a quantum method that is less computationally intensive. A common assignment for the low layer is UFF (universal force field), but it can be changed by the user to a different method and basis set.

The results from the single point energy calculations can be applied to the ONIOM calculations, by knowing where the defect is localized and knowing which atoms to assign to the high layer and the low layer, and by studying the HOMO (highest occupied molecular orbital) and LUMO (lowest unoccupied molecular orbital) of the alpha and beta electrons. This method has been applied by previous computational physicists in the study of defects [84]. After an optimization, the ONIOM job will display updated Fermi contact terms and anisotropic spin dipole couplings for the atoms in the high layer of interest, omitting the atoms in the low layer. Therefore, the choice of atoms in the high and low layer needed to be done in such a way as to retain all nine of the atoms in the central unit. Appendix A.2 describes the progress made in exploring the ONIOM method along with a table of preliminary results for the self-trapped hole in KDP, although it was not utilized for the remaining simulations described in Chapters 4 – 6 of this dissertation.

4.3 Orthorhombic Clusters including Potassium Ions

4.3.1 Results from a 149-atom Cluster with +38 Charge

The functional ωB97XD was utilized in simulations for a variety of large KDP clusters. As had been the case previously in attempts to conduct self-trapped hole simulations for the tetragonal cluster, initial simulations for the large orthorhombic cluster were also incorrectly localizing the hole to the outer part of the cluster. In other words, the hole was not being assigned to atoms located in the symmetrically "middle region" with respect to the other atoms. Again, the main issue appeared to be the nearest potassium ion to the central PO_4 cluster (i.e., the potassium ion that was located along the same axis as the self-trapped hole), and the removal of that potassium ion would then give the excess spin density an unoccupied region to localize in the absence of the potassium ion. Two combined methods were attempted in order to explore this phenomenon, and a large cluster was created which placed the nearest potassium ion in the geometric and symmetric "middle" of the cluster, assuming that the self-trapped hole region extended along the z-axis, beyond the two oxygen atoms and hydrogen atoms. This is in contrast to the previous clusters, which had placed the entire PO_4 unit in the center of the cluster.

As seen in Figure 4.9, this axis extends from left to right, and the nearest potassium ion in the symmetric center of the cluster, is marked in yellow. The nearest potassium ion to the central PO_4 cluster was removed in the first method and is indicated by the yellow circle in Figure 4.9. The simulation was also conducted by retaining a large number of potassium ions arranged around the outer perimeter of the cluster. The reasoning behind retaining the large number of potassium ions on the outside of the cluster was in order to see if this would prevent the self-trapped hole from localizing in the outer regions of the

cluster. However, even with the excess potassium ions on the outer part of the cluster, the self-trapped hole would still tend to avoid the middle PO_4 unit - highlighted in teal in Figure 4.9. The removal or displacement of the potassium ion nearest to the unit was a successful method for localizing the defect on the nearby PO_4 unit. This provided a path forward in getting the self-trapped hole to not go on the outer part of the cluster and to localize on the middle PO_4 unit, and this was the second method that was explored for the +38-charge (149-atom) cluster. Unfortunately, the removal of the potassium ion would indicate that the defect is not a self-trapped hole but instead a hole trapped next to a potassium ion vacancy.

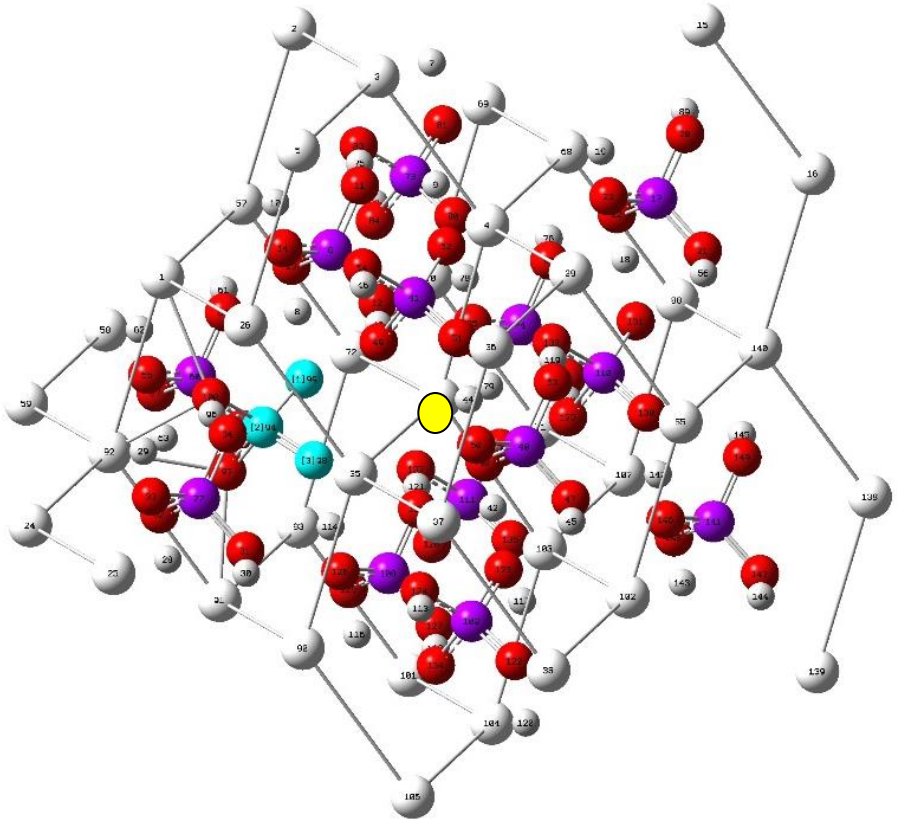

Figure 4.9. The 149-atom cluster which retains the potassium ions that surround the large orthorhombic cluster. The yellow circle indicates the area where the closest potassium ion resides. This potassium ion was removed in one instance.

The simulations for the large clusters were conducted in multiple steps and input files, as depicted in Appendix C.2, which has a “Link” to a second job after the first one is completed. First, a single point energy calculation is conducted for the entire cluster, utilizing the keyword and option scf=(xqc,maxconventionalcycles=150,maxcycles=300). This dictates quadratic convergence to an energy minima after 150 conventional linear steps, and it instructs Gaussian to stop attempts to converge the cluster to a solution after 300 cycles.

The method which resulted in the modeling of the self-trapped hole defect began by taking the final geometry results from the 41-atom cluster’s optimization job and applying them to the large cluster in attempts to localize the self-trapped hole on the pair of oxygen ions located in the middle of the cluster and to have the self-trapped hole localized for a PO_4 unit with a potassium ion nearby. Specifically, the angle between the central phosphorus ion and its two oxygen atoms was minimized in the large cluster similar to how the two oxygen atoms are drawn closer to one another during the optimization in the small 41-atom cluster. This adjustment of the coordinates for the optimization starting guess was also done for the distance along the bond between the central phosphorus and its nearest potassium ion. This negated the need to completely remove the potassium ion. Figure 4.10 depicts a series of orientations for the large cluster with the surrounding potassium ions that was utilized in this section of simulations. The results for the cluster below had 149-atoms with a stoichiometry of $H_{40}K_{39}O_{56}P_{14}$. Due to the excess number of potassium ions, this cluster had a total charge of +38, as was presented in Figure 4.9 previously.

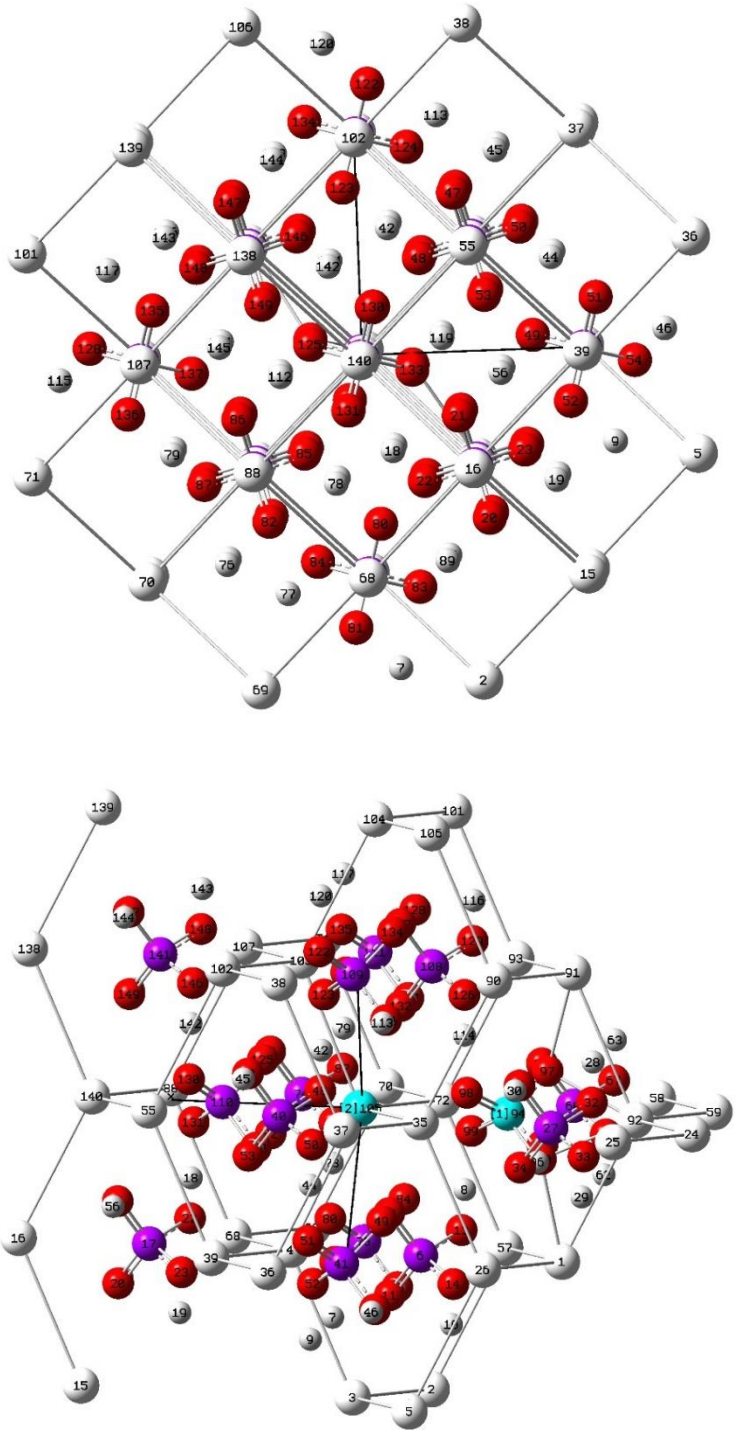

Figure 4.10. These two panels depict the 149-atom orthorhombic cluster. This particular cluster retains an excess amount of potassium ions around the outer part of the cluster for +38 charge. The top image has the z-axis pointing out of the page, and the bottom image shows phosphorus 94 and potassium 105 highlighted in teal, with the z-axis pointing left.

The simulation started by utilizing the keyword and option guess=fragment=2 in order to obtain convergence and a new energy for the large cluster. Utilizing the guess keyword, there were two fragments under consideration, with the central $(PO_4H_4)^{2+}$ being the second fragment. Charge and multiplicity are divided with the two fragments and are presented in the header of the input file as 38 2 36 1 2 2. This first pair in this line of numbers indicates that the total charge and multiplicity for the entire cluster are 38 2, while the second pair corresponds to the larger cluster's charge and multiplicity 36 1, and the second fragment, which is expected to have the self-trapped hole, has a charge and multiplicity of 2 2. A tool in GaussView known as "Atom Groups" was utilized to divide the cluster into fragments after specific atoms were highlighted.

The second part of the job was a full DFT SCF allowing relaxation of all orbital rotations. This step utilized the results from the guess=fragment job. The final part of this guess-method was to utilize the results from the second step in an optimization job. This is done by using the checkpoint file from the second step in the input file for Gaussian and re-specifying guess=read, to instruct Gaussian to read the inputs from the checkpoint file. Since the two oxygen ions and the potassium ion were manually moved at the beginning of the first simulation, they were un-frozen for the optimization job. The optimization then would move the two oxygen atoms and the potassium to where Gaussian determined was best in terms of lowest energy for the cluster. Upon analyzing the final geometric position of the cluster, these three ions did not move a significant distance away from where they were originally assigned.

Table 4.10. The hyperfine results from the large orthorhombic cluster with a total charge of +38 and a multiplicity of 2.

Atom	Isotropic (Gauss)	Anisotropic (Gauss)	Direction Cosines		
H8	-0.895	-3.60	0.8823	-0.4112	0.2293
		-2.60	0.4476	0.5818	0.6791
		6.20	0.1458	0.7017	-0.6973
H114	-1.147	-3.75	-3.506	0.4345	0.2264
		-2.78	-0.4652	0.5893	0.6606
		6.53	0.1536	-0.6812	0.7158
P94	-35.050	-1.93	1.0	0.0084	-0.0023
		0.35	0.0036	0.1613	0.9869
		1.56	0.0079	0.9869	-0.1613
O98	-11.319				
O99	-11.294				

It seemed that Gaussian had consistently rotated the guess-basis for the DFT simulations, such that the magnetic field was along the "x" axis. This is what this section of the Gaussian output seems to indicate:

```
B after Tr=     0.000000    0.000000    0.000000
       Rot=     1.000000    0.000663   -0.000009   -0.000006 Ang=   0.08 deg.
Guess basis will be translated and rotated to current coordinates.
```

For this reason, it is assumed that the isotropic hyperfine value may be added to the Baa principal axis value for the phosphorus ion, assuming that the other values are approximately zero, and that the magnetic field would be applied along the x-axis (also known as a-axis). This is in contrast to the UMP2 output, where the isotropic hyperfine value was added directly to the Bcc anisotropic component for the central phosphorus ion. In this case, the total hyperfine value is approximately -36.95 Gauss. The hydrogen ions also give values that are approximately -4 Gauss. Both of these values approach the EPR

experiment which measured 31 Gauss for the phosphorus and 3.2 Gauss for the two hydrogen ions. Table 4.11 below shows a summary of the distances for the atoms that were manually adjusted and then optimized.

Table 4.11. Distances between atoms from the PO_4 unit of interest for the 149-atom cluster before and after optimization. All distances are in Angstrom and angles are in degrees.

	K-P distance (Angstom)	OPO angle (degrees)	O-O distance (Angstom)	O-P distance (Angstom)
Before alteration	3.35	115.27		1.51
After manual change	3.86	97.30	2.58	1.53
After optimization (K and two O atoms move)	3.99	95.87	2.30	1.55

This table of values shows that the angle between the two oxygen ions became even smaller, from 97.30 degrees to 95.87 degrees, while subsequently pushing the potassium ion further away from the phosphorus ion, from 3.8626 Angstroms to 3.993 Angstroms. The two oxygen ions also moved further away from the central phosphorus ion, from 1.52983 Angstrom to 1.55491 Angstrom.

4.3.2 Self-Trapped Hole Simulations with +16 and +4 Charge

It was not optimal that the isotropic hyperfine values for the two hydrogen ions that shared the self-trapped hole were not equal (-0.90 Gauss versus -1.17 Gauss), as introduced in Table 4.10, and therefore the Miyoshi cluster was revisited in order to see if the issue resided in the crystal geometry. This was supposed, because the 149-atom cluster depicted in the preceding paragraphs was created using a unit cell from the Materials Project Database of DFT structures [85]. The next change that was performed for the results described in this section, involved the removal of the excess potassium ions from the outer

perimeter of the cluster. This was done for two reasons. First, it was suspected that the success of the localization for the self-trapped hole was due to the manual adjustment of the atoms before the Gaussian simulations took place, and therefore "manual optimization" procedure should at least be retained. Surrounding the large cluster with the excess potassium ions played a minimal role in localizing the self-trapped hole to the central part of the large cluster, as was demonstrated by the undesirable localization of the self-trapped hole to the outer part of the cluster in lieu of manual optimization. The second reason that the additional potassium ions were removed from the large cluster, was in an attempt to bring the total charge closer to zero, down from the +38 charge.

The first cluster reduced the excess charge by half to +16, rather than the +38 as it had been in the 149 atom cluster discussed in the preceding paragraphs. This new cluster with a total of 127 atoms is seen below in Figure 4.11.

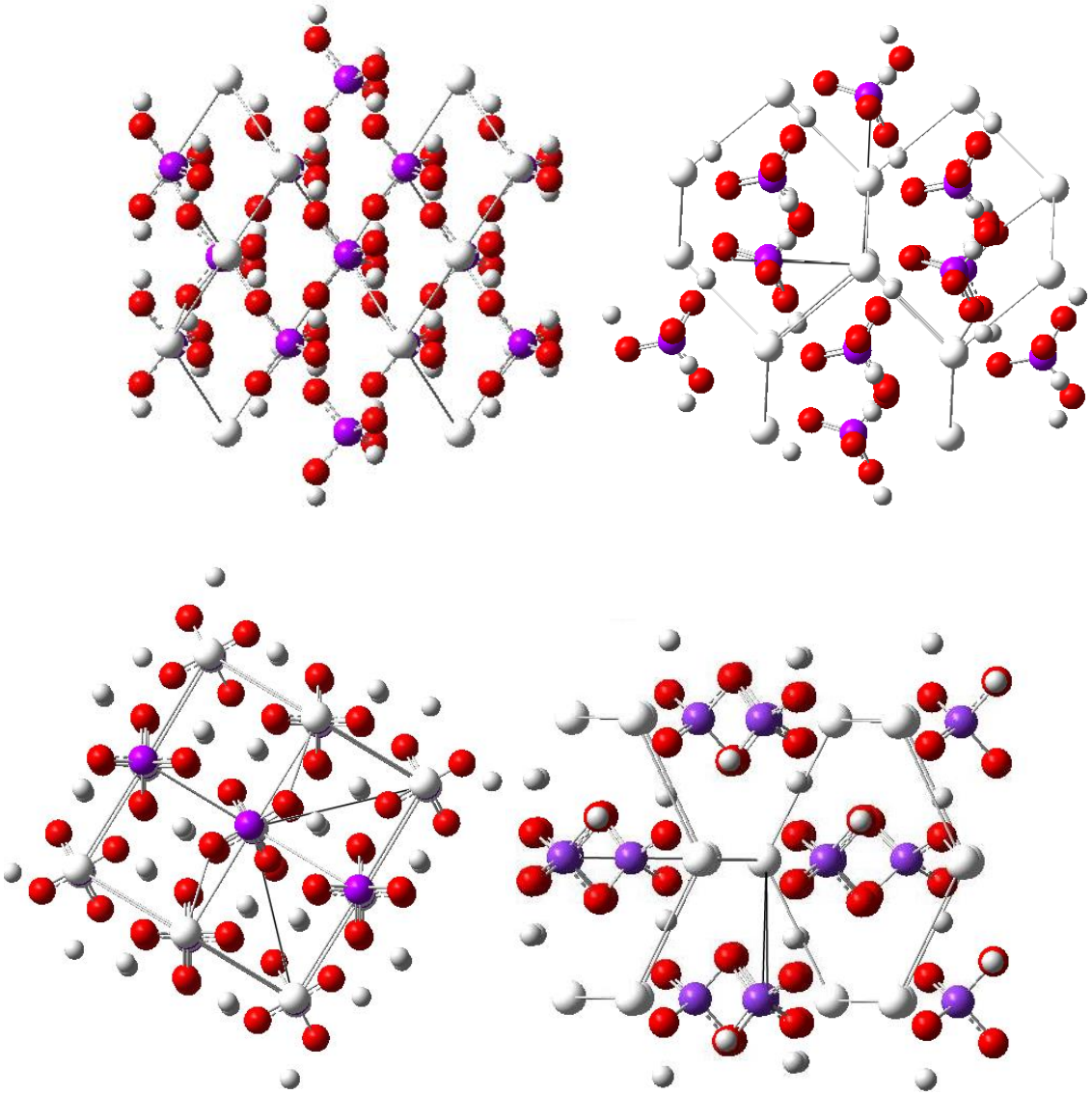

Figure 4.11. The second iteration of the large orthorhombic cluster utilizing the manual optimization method to examine the self-trapped hole, with an excess charge of +16 and a total of 127 atoms.

The pictures of the cluster in Figure 4.12 are after the manual alteration of the OPO angle and the P-K distance. Table 4.12 lists these angles and distances. The angle between oxygen 86, oxygen 120, and phosphorus 92 were also manually changed from 115.275 degrees before the manual change to 97.2 degrees after the manual change. As seen in the

figure, the two atoms highlighted in teal on the right side of the figure are the oxygen ions which were drawn in closer to one another, and the potassium ion that is nearest to it is located to the left.

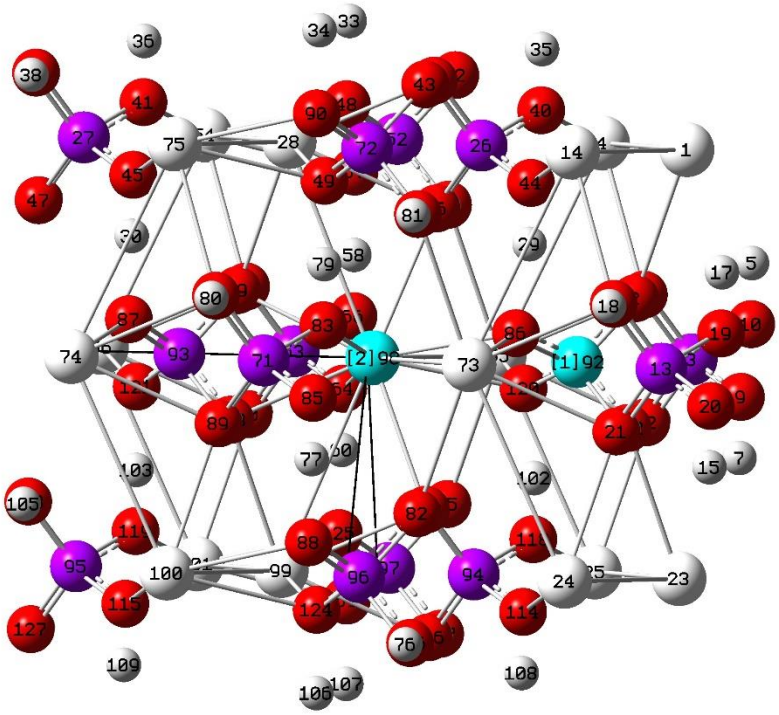

Figure 4.12. The 127-atom cluster, with the nearest potassium ion moved from the PO_4 unit, and the OPO angle of the unit decreased. Phosphorus 92 and potassium 98 are highlighted in teal.

Potassium ion number 98 (the nearest potassium to the self-trapped hole) directly to the left of the oxygen pair, was manually moved before the single point energy calculation. The P-K distance was changed from 3.35 to 3.86 Angstroms.

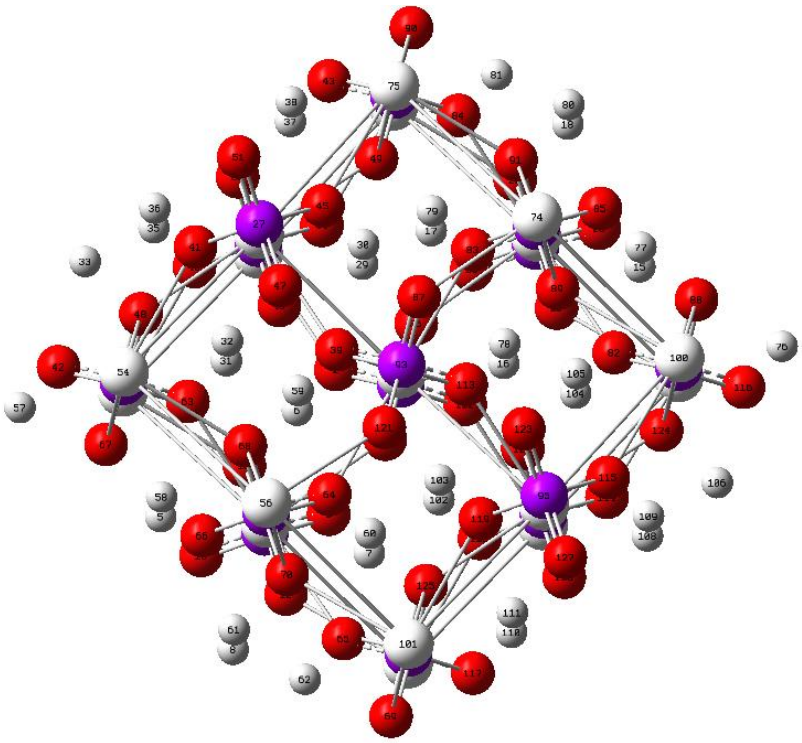

Figure 4.13. Looking down along “x” (x-axis in and out of page). Notice before, this axis was designated as the z-axis for the non-DFT jobs.

The results in Table 4.12 show that the geometry decreased the K-P distance from 3.86 to 3.56 Angstroms, increased the OPO angle from 97.2 to 99.68 degrees, and drove the OP distance from 1.51 to 1.55 Angstroms.

Table 4.12. Distances between atoms from the PO_4 unit of interest for the 127-atom cluster before and after optimization. All distances are in units of Angstrom, and the angles are in degrees.

	K-P distance	OPO angle	O-P distance
Before alteration	3.35	115.28	1.51189
After manual change	3.86	97.2	1.5119
After optimization (K and two O atoms move)	3.56	99.68	1.547

The full set of Fermi contact values and Anisotropic values from the Gaussian output are in Appendix D.3, and a subset of values for the atoms of interest are shown in Table 4.13 and 4.14. These values are in close agreement with experiment.

Table 4.13. Isotropic hyperfine values for the central KH_2PO_4 unit after optimization in units of Gauss for the 127 atom cluster.

Ion	After Optimization	EPR (combined hyperfine) [19-21]
P92	-33.53	31.0
O120, O86	-9.55	
H102, H29	-2.29	3.2

Table 4.14. Anisotropic hyperfine values for the ions that share the self-trapped hole for the 127 atom cluster.

Ion	Principal Value (Gauss)	Principal Axis Directions
P92	-2.159	0.0011 0.0040 1.0000
	0.685	0.9098 -0.4150 0.0006
	1.474	0.4150 0.9098 -0.0041
H29, H102	-3.923	0.3439 -0.2821 0.8956
	-3.038	-0.6146 0.6535 0.4419
	6.961	0.7099 0.7024 -0.0514

In an effort to reduce the total charge on the cluster, the size of the cluster was decreased to 115 atoms and had a total charge of +3 which became +4 with the defect. This cluster was adapted from the same cluster discussed in the preceding paragraphs with the nearest potassium ion being the “middle” of the cluster, and the total charge was lowered by removing 12 potassium ions from the 127-atom cluster. The stoichiometry of the 115-atom cluster was: $H_{40}K_5O_{56}P_{14}$, and the simulations all used the method and basis set ωB97XD/6-31+G(d). The simulations were conducted in the same manner as was

previously done, by starting with guess=fragment=2 and finishing with an optimization using the wavefunction from the fragment guess procedure.

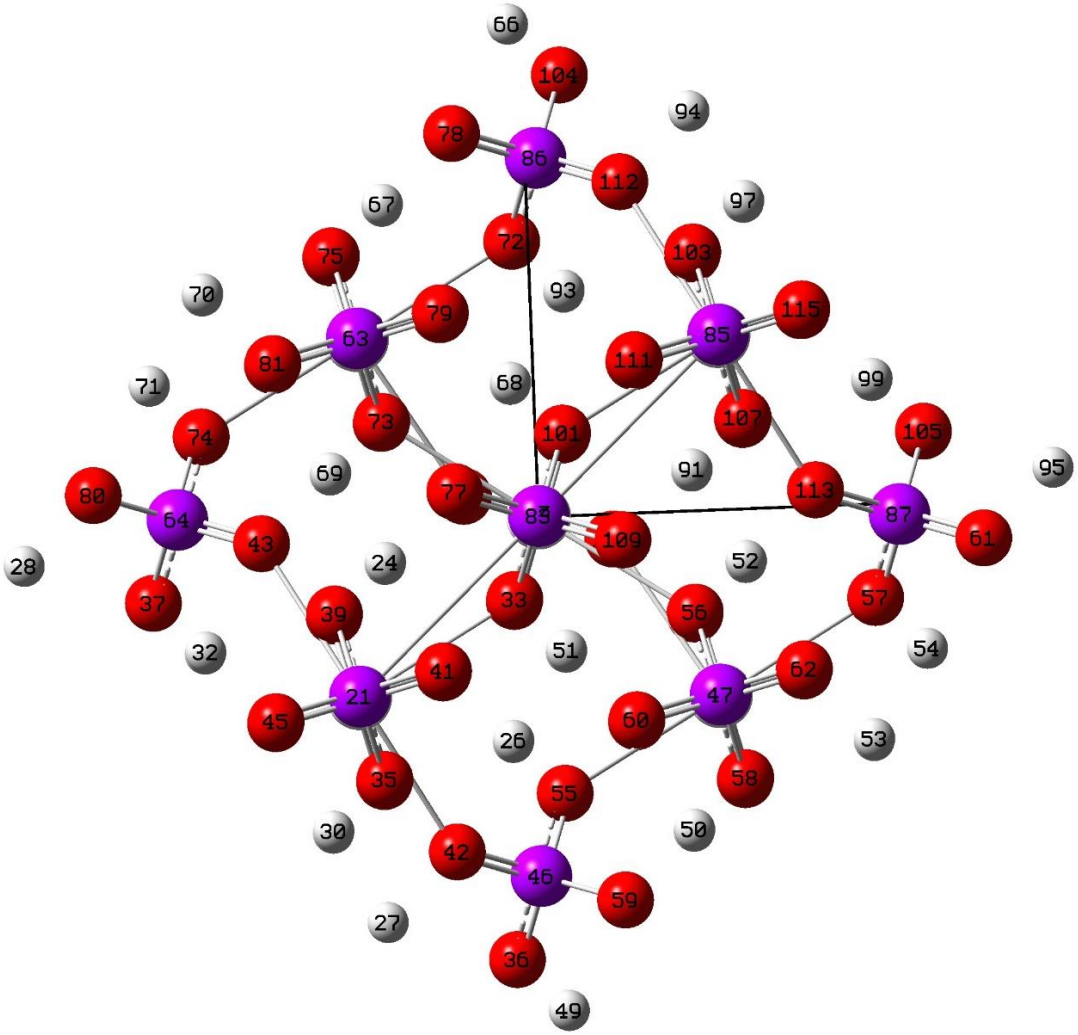

(a).

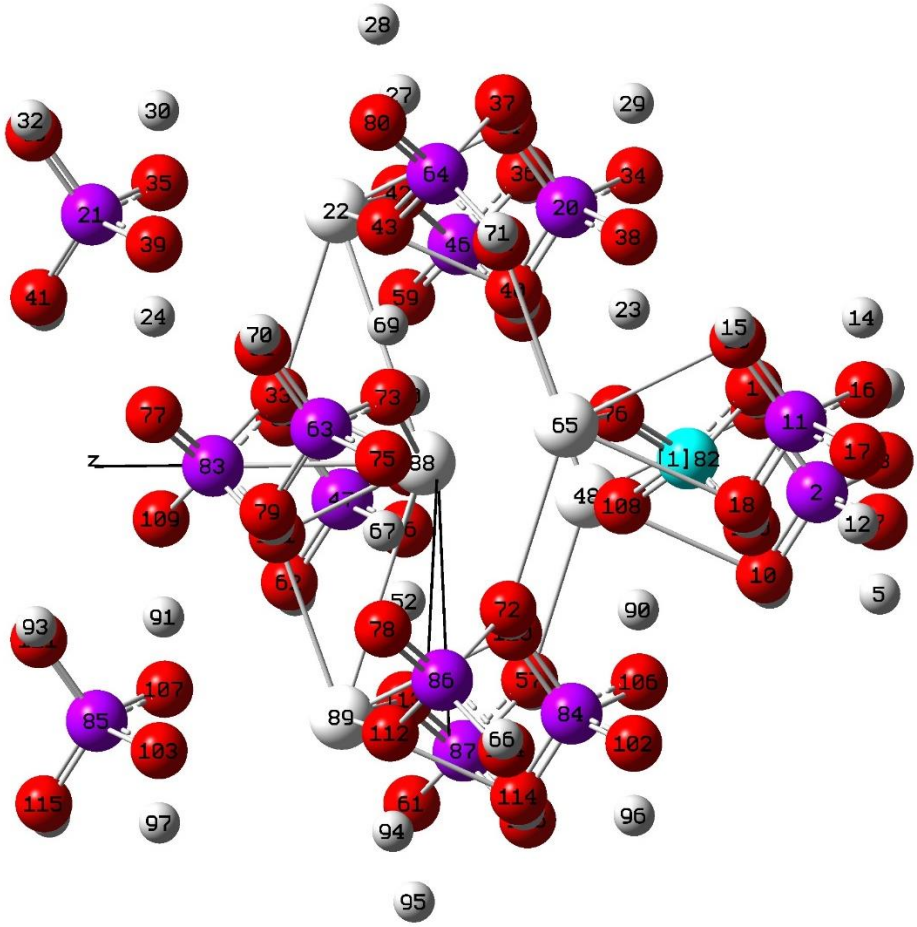

(b).

Figure 4.14. Two images (a and b) of the 115-atom cluster resulting from the ωB97XD/6-31+G(d) optimization, after allowing the two oxygen atoms and potassium atom to move.

As seen in Figure 4.14, the atom that is highlighted in teal is the central phosphorus of interest. Oxygen ions #76 and #108 were moved prior to the simulations began. Hydrogen ions number 23 and 90 are the neighboring ions of interest, as well. Again, the nearest potassium ion is located in the "middle" of the cluster. The distance of the central potassium relative to the nearby phosphorus of the PO_4 unit of interest was adjusted and allowed to move during optimization along with the two oxygen atoms. The values in Table 4.15 are

similar to 4.13, before and after the manual geometry change. After optimization, the KP distance went from 3.86 to 3.57 Angstroms as before, and the OP distance similarly repeated going from 1.51 to 1.55 Angstroms. However, in the 115 atom cluster, the OPO angle remained relatively close to its pre-optimization value of 97.2 degrees, becoming 97.89 degrees. The O-H distance went up, from 1.53 to 1.59 Angstroms.

Table 4.15. Distances between atoms from the PO_4 unit of interest for the 115-atom cluster before and after optimization. All distances are in Angstrom, and angles are in degrees.

	K-P distance	OPO angle	O-H distance	O-P distance
Before alteration	3.35	115.28	1.44	1.5119
After manual change	3.86	97.2	1.53	1.5119
After optimization (K and two O atoms move)	3.57	97.89	1.59	1.5493

The resultant isotropic Fermi contact value for phosphorus was –34.81 Gauss and the Fermi contact values for the hydrogen atoms that shared the self-trapped hole were –2.21 Gauss. The full list of isotropic and anisotropic values for the 115-atom cluster is seen in Appendix D.4, and an excerpt of the ions of interest are shown in Tables 4.16 and 4.17.

Table 4.16. Isotropic hyperfine values for the central KH_2PO_4 unit before and after optimization in units of Gauss for the 115 atom cluster.

Ion	After Optimization [Gauss]
P82	34.81
O76, O108	-10.34
H23, H90	-2.07
O38,O106	0.69
H4,H13	0.58

Table 4.17. Anisotropic hyperfine values for the ions that share the self-trapped hole for the 115 atom cluster.

Ion	Principal Value	Principal Axis Directions
P82	-2.042	-1.909 0.0014 0.0040 1.0000
	0.390	0.365 0.9529 -0.3032 -0.0001
	1.653	1.545 0.3032 0.9529 -0.0042
H23 and H90	-3.921	-3.665 -0.3196 0.2645 0.9099
	-3.102	-2.900 -0.6245 0.6634 -0.4122
	7.023	6.565 0.7126 0.7000 0.0468

4.3.3 Understanding Energy Minimization during Optimization

There is a tool in GaussView that allows the user to inspect the total energy of the cluster for each step in the optimization. This tool is useful for monitoring how the energy changes as a function of each optimization step, and the changes in energy can also be viewed while the optimization is in progress. This allows the user to monitor whether a job is likely to converge or diverge from a solution before the optimization finishes.

There were nine steps in the optimization job for the 115-atom cluster, and the energy is seen to reach a minimum at the ninth step, as seen in Table 4.18. At the ninth and final optimization step, the total energy of the cluster is -12,013.3286 Hartrees. Upon inspecting the significant digits, this is a reduction from step one, which was -12,013.31438 Hartrees at the beginning of the simulation. This data is also plotted in Figure 4.15.

Table 4.18. Angle between the OPO ions (in degrees), versus energy (Hartrees) for the nine steps that Gaussian conducted the geometry optimization for the 115-atom cluster.

Step number	OPO angle (deg)	Energy (Hartrees)
1	97.2	-12013.31438
2	97.67	-12013.31954
3	98.35	-12013.32387
4	98.33	-12013.3256
5	97.82	-12013.32817
6	97.67	-12013.3285
7	97.86	-12013.3286
8	97.88	-12013.3286
9	97.89	-12013.3286

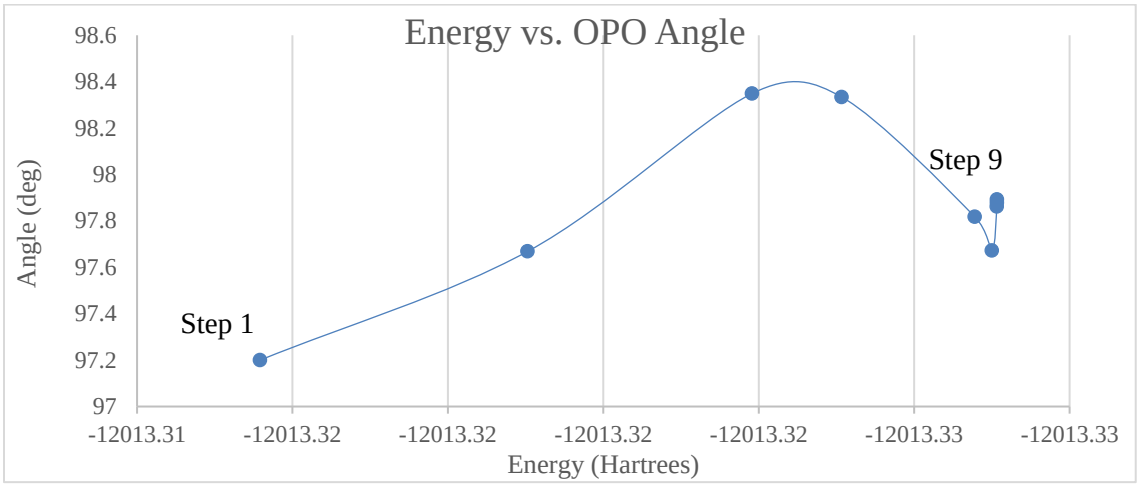

Figure 4.15. Angle (y-axis of the plot) between the OPO atoms in the central unit of the 115-atom cluster, which were allowed to move during the geometry optimization, versus energy (x-axis). This particular optimization took nine steps to complete and correlates with Table 4.18.

As seen in Figure 4.15, the angle between the two oxygen atoms and the central phosphorus atom gradually increased from the initial guess of 97.2 degrees, up to approximately 98.3 degrees. Gaussian finally settles on an angle which is 97.8921 degrees at step nine.

The results of these simulations with the large clusters demonstrated that making the OPO angle smaller (for the two oxygen atoms that were expected to share the hole) and increasing the KP distance were two keys to getting the wave function to converge to the two oxygen atoms with the self-trapped hole.

4.3.4 Examining a 47-Atom Cluster with Potassium Ions

The 41-atom cluster was revisited in order to more closely examine the interaction between the self-trapped hole and the six-nearest potassium ions (see Figures 4.16 and 4.17), but this time the ions' positions were adjusted manually, pre-optimization, for a small 47-atom cluster (unlike the 41-atom job, in which ions were not manually adjusted). Three optimization jobs utilizing the ωB97XD/6-31+G(d) theory and basis set were performed. The first job changed the OPO angle but held the position of the potassium ion fixed. The optimization for the first job allowed the two oxygen atoms that were moved pre-optimization to move again during optimization in order to observe how much more they'd move while Gaussian searched for the minimum energy of the cluster. The second and third job changed the angle between the central phosphorus and the two oxygen atoms that were suspected of having the hole, and the nearest potassium ion was moved away as had been done in Sections 4.3.1 and 4.3.2 of this dissertation for the large clusters to approximately 3.8 Angstroms. The optimization for the second job allowed the two oxygen atoms and the potassium ion to move, while the optimization for the third job only allowed the two oxygen atoms to move and held the nearest potassium ion frozen. A coordinate scan was conducted for the 47-atom cluster, in order to study the variance in the hyperfine values by changing the distance along the bond between the phosphorus ion and the nearest

potassium ion. The results of these simulations are shown in Table 4.19. This analysis explored values for the K-P distance between 3.85 to 3.34 Angstroms.

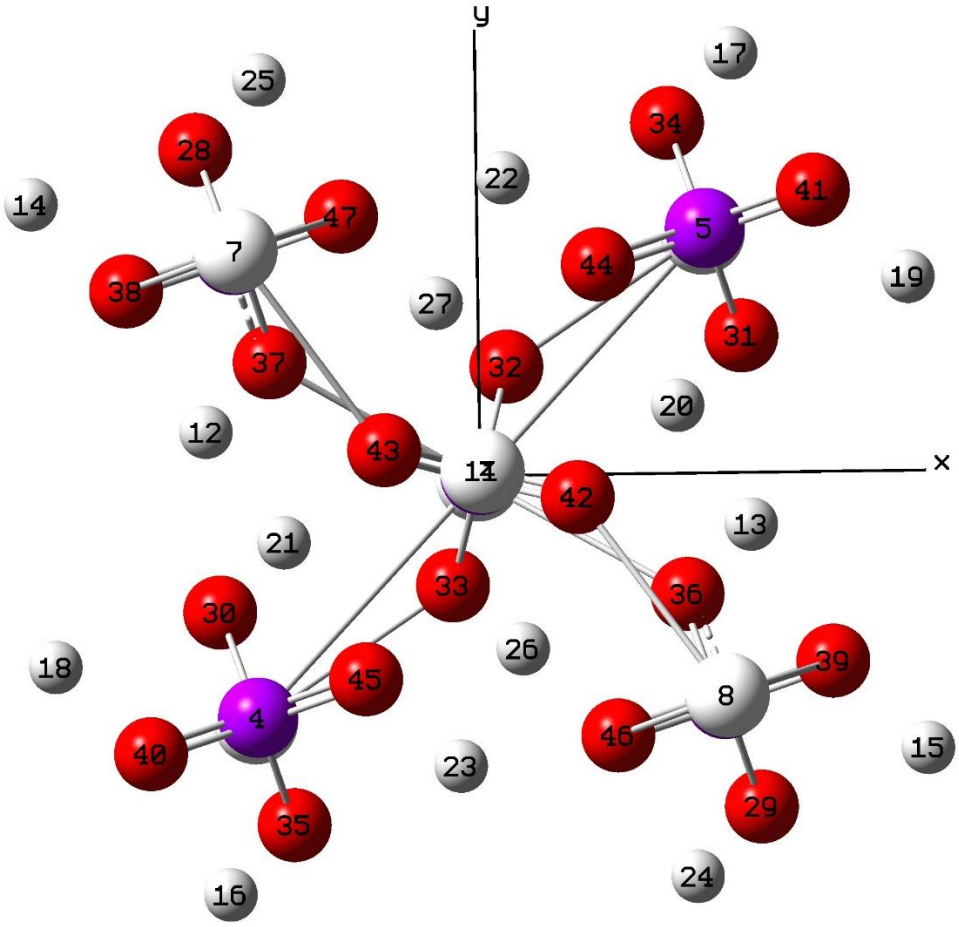

Figure 4.16. Left: The 47-atom cluster that moved the OPO angle but kept KP distance fixed with z-axis pointed up. Potassium number 11 is the closest potassium to the self-trapped hole. Right: The cluster that moved the OPO angle but kept KP distance fixed with z-axis pointed out.

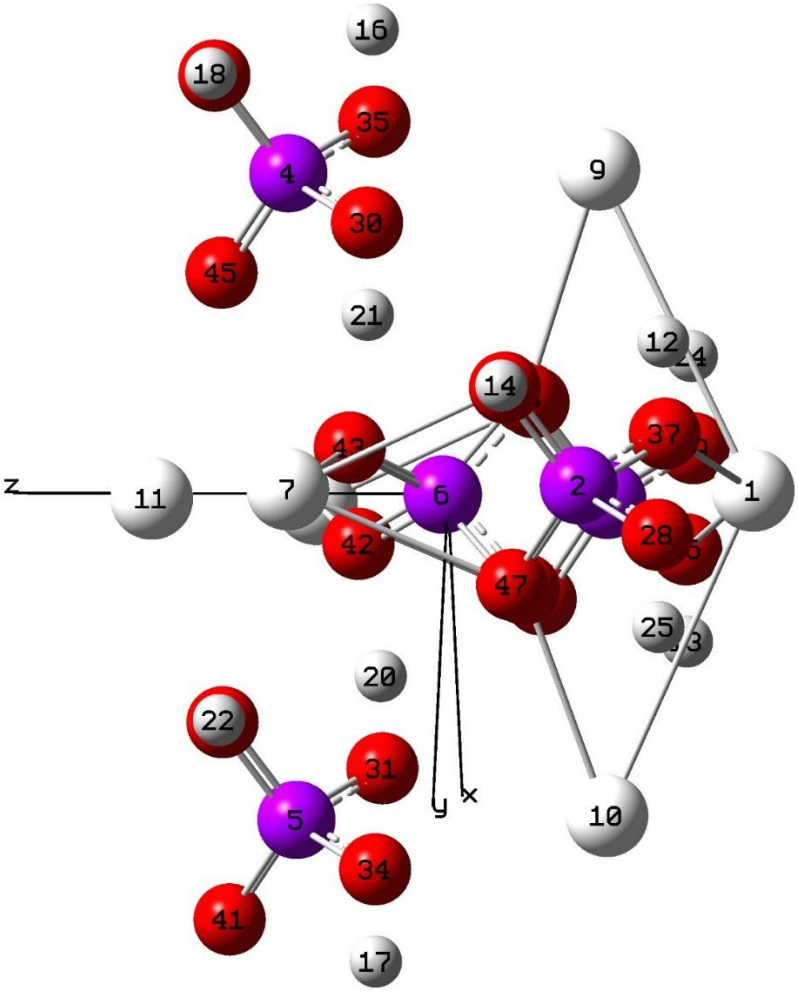

Figure 4.17. The cluster from the previous figure, that moved the OPO angle but kept the KP distance fixed with z-axis pointed left.

Table 4.19. Fermi contact values for the central phosphorus ion, two nearby phosphorus ions, and the hydrogen ions with the self-trapped hole defect at various KP distances in a 47-atom cluster with the OPO angle fixed at 90 degrees.

KP Distance (Å)	Fermi Contact Values (Gauss)		
	P1	P2 and P3	Hydrogen ions
Fixed, 3.34779	-3.25	-19.95	-0.02, -0.02
KP 3.45	-3.378	-19.99	-0.026, -0.027
KP 3.55	-3.5	-19.99	-0.033, -0.033
KP 3.65	-3.63	-19.92	-0.04, -0.04
KP 3.75	-33.64	-3.1	-1.65, -1.65
KP 3.85	-34.92	-1.92	-1.8,-1.8

As seen in Table 4.19, the hyperfine value is delocalized for distances that are lower than 3.75 Angstroms, and the hyperfine value improves once the distance is increased to 3.75 Angstroms. The Fermi contact value results were best before optimization for the first job, and thus the post-optimization results are not presented here. The 47-atom cluster results for the first job are displayed in Appendix D.5. The Fermi contact value for the central phosphorus ion was −30.2 Gauss, and the Fermi value for the two hydrogen atoms were approximately −4 Gauss. The Fermi contact values for the two hydrogen ions are equal for all cases except when the KP distance is 3.45 Angstroms. These results are in close agreement with the hyperfine values measured during the EPR experiment and are an improvement over the small 41-atom clusters that did not contain potassium ions.

Utilizing all 36 processors on one node, the job that did not alter the position of the nearest potassium ion finished in 2.5 hours, and the job that allowed the potassium ion to move during optimization took 15.5 hours. The result of this calculation was that the potassium ion moved 78 Angstroms away from the phosphorus atom, which is 26 times greater than the perfect lattice position of 3.34779 Angstroms. This job required forced convergence utilizing "scf=(xqc,maxconventionalcycles =150,maxcycles=300)". The third optimization variant which had changed the OPO angle and the distance between the potassium and phosphorus initially, froze the position of the potassium but allowed the two oxygen atoms to move. After this optimization, the Fermi contact values were −35 Gauss for the central phosphorus and −1.8 Gauss for the hydrogen atoms that shared the holes.

4.4 Results from a 129-atom Cluster: Anisotropy Analysis

A 129-atom cluster was optimized after reducing the angle between the central phosphorus (P1) and the two oxygen ions (O34, O35) that share the self-trapped hole from 115.3 to 90 degrees. The distance between the central phosphorus and the nearest potassium ion (K15) was increased from 3.347 to 3.650 Angstroms. As shown in Section 4.3, modifying the lattice in this way helps to trap and localize the hole, before an optimization is conducted. This cluster is shown in three different orientations, in Figure 4.18.

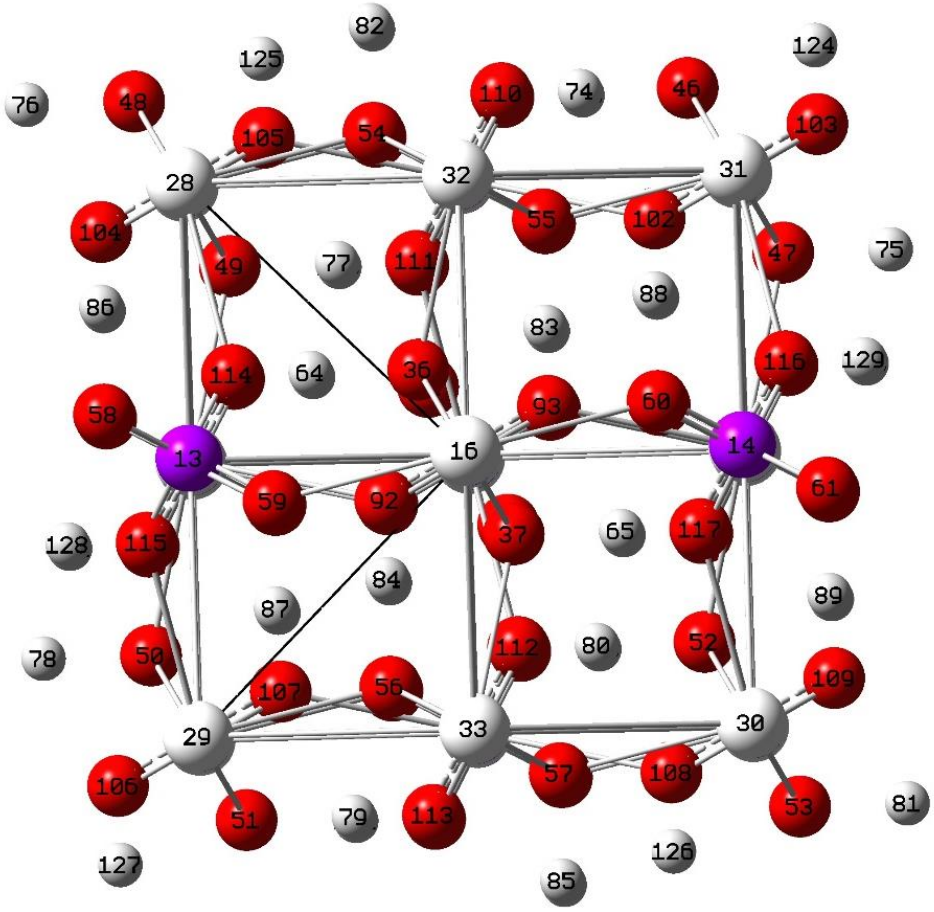

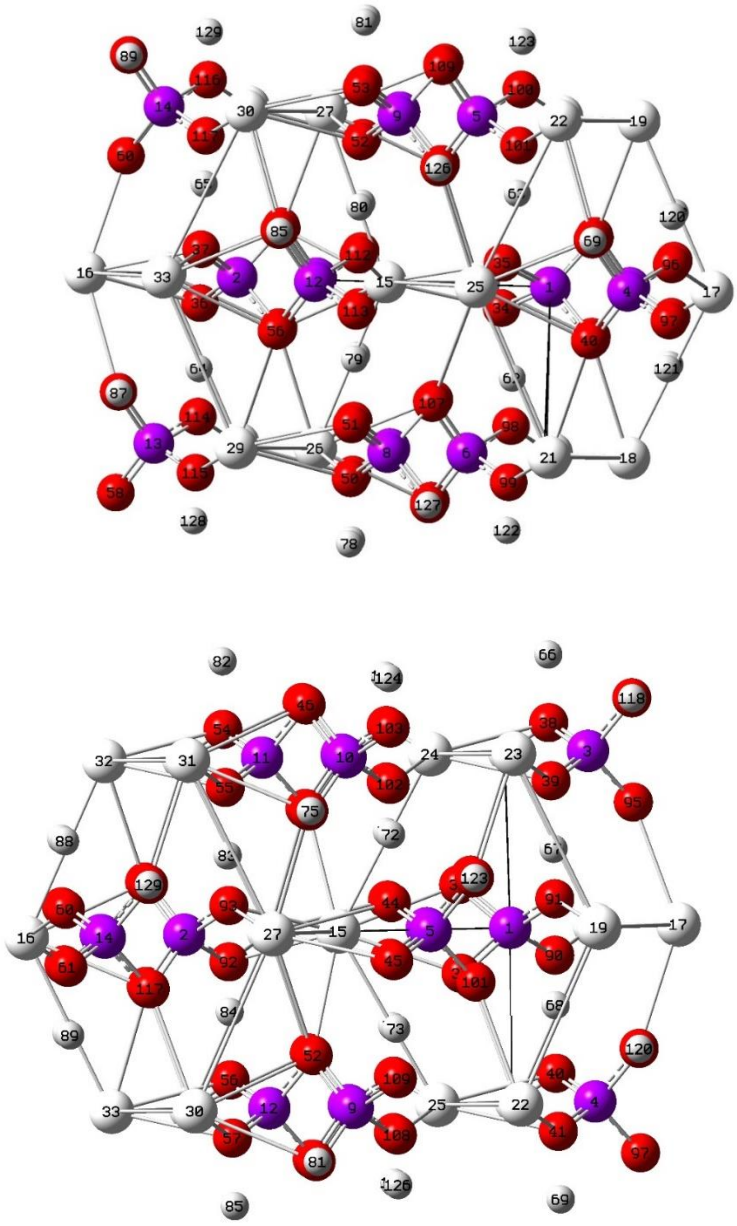

Figure 4.18. The 129 atom cluster. The top image is the x-y plane of the cluster with the z-axis out. The middle image has the z-axis pointing to the left and is rotated to show potassium #15 in the middle, phosphorus #1 to the right, and the oxygen ions that share the hole #35 and #34. The third image has the z-axis pointed to the left and is rotated to show the opposing oxygen pair #90 and #91 which does not share the self-trapped hole.

Table 4.20 shows the comparison between the distances before and after optimization, allowing ten ions in the central KH_2PO_4 unit to move. After optimization, the two oxygen ions O34 and O35 moved farther away from P1, from 1.512 to 1.573 Angstroms, and closer together to one another along O34-O35, from 2.554 to 2.318 Angstroms. All four hydrogen ions in the central KH_2PO_4 unit move away from their respective oxygen ions after optimization. The distance between the hydrogen-oxygen pairs that share the self-trapped hole, both O35-H63 and O34-H62, increased from 1.578 to 1.672 Angstroms. Similarly, the hydrogen-oxygen pairs without the self-trapped hole, both O90-H68 and O91-H67, increase from 1.060 to 1.515 Angstroms. From these movements, the self-trapped hole is seen to affect all four of the central PO_4 unit's surrounding hydrogen ions. This is because the two hydrogen ions (H67 and H68) that are nearest to the two oxygen ions (O90 and O91) without the self-trapped hole become repulsed by the oxygen ions after they have become slightly less negative. This drives the two hydrogen ions to the oxygen ions of their secondary neighboring PO_4 units, which had previously been "far pairs" to the hydrogen ions.

Table 4.20. Distances between ions in the KH_2PO_4 unit for the 129 atom cluster, before and after optimization.

Ion Pairs	Perfect Lattice	Before Optimization (Å)	After Optimization (Å)
O34-O35	2.554	2.138	2.317
O34-H63, O35-H62	1.443	1.578	1.672
P1-O34, P1-O35	1.512	1.512	1.573
P1-K15	3.347	3.650	3.660
O90-O91	2.525	2.525	2.571
O90-H68, O91-H67	1.060	1.060	1.515
P1-O90, P1-O91	1.578	1.578	1.527
P1-K15	3.573	3.573	3.349

Table 4.21 displays the isotropic hyperfine values for the 129 atom cluster before and after optimization in units of MegaHertz in order to conduct a direct comparison with the results from Wells. The anisotropic hyperfine values for the ions that share the hole are displayed in Table 4.22.

Table 4.21. Isotropic hyperfine values for the central KH_2PO_4 unit in the 129 atom cluster before and after optimization in units of MegaHertz.

Ion	Before Optimization [MHz]	After Optimization [MHz]
P1	-93.885	-83.406
O34, O35	-38.896	-33.662
H63, H62	-13.152	-1.515
O90,O91	1.819	0.818
H68,H67	1.179	0.226
K15	-1.116	-1.890

Table 4.22. Anisotropic hyperfine values for the ions that share the self-trapped hole for the 129-atom cluster in units of MHz.

Ion	Principal Value	Principal Axis Directions		
P1	-3.988	0.0000	0.0000	1.0000
	-0.333	0.9491	–0.3150	0.0000
	4.321	0.3150	0.9491	0.0000
H62, H63	–8.950	–0.2544	0.3125	0.9152
	–6.667	0.6652	–0.6304	0.4001
	15.616	0.7020	0.7106	–0.0475
O34, O35	71.176	–0.5688	0.1436	0.8098
	69.702	0.3516	0.9326	0.0816
	–140.877	0.7435	–0.3311	0.5810

The isotropic hyperfine values were combined with the anisotropic values aligned with the c-axis using the EasySpin method described in Section 4.2.2 and utilizing the code in Appendix B.2. As Table 4.23 indicates, the calculated values are in very good agreement with the results from Wells. The total hyperfine value for the central phosphorus atom was

calculated to be -86.79 MHz, and the value obtained from the ENDOR experiment was measured to be -85.49 MHz [82]. The two hydrogen atoms that shared the self-trapped hole each had hyperfine values of -9.95 MHz, calculated by Gaussian, and -8.82 MHz as measured by the ENDOR experiment [82]. The oxygen ions were not measured in experiment, but their values have been combined as well and are presented in Table 4.23.

Table 4.23. Comparison of hyperfine values from the 129 atom cluster with the hyperfine values from the paper from Wells *et al.* [82].

Ion	Isotropic [MHz]	Anisotropic B||c component [MHz]	Combined [MHz]	Wells [MHz] [82] B||c
P1	-83.406	-3.988	-86.788	-85.49
H62, H63	-1.515	-8.282	-9.949	-8.82
O34, O35	-33.662	-68.731	-105.206	--

4.4.1 Computationally Simulated EPR Spectra using Gaussian Results

Utilizing the isotropic and anisotropic results generated by Gaussian in Table 4.21 and 4.22, EPR spectra were simulated using EasySpin in the same manner that was used to generate the spectra Figure 4.9. These spectra are shown in Figure 4.19 – 4.21, for the hydrogen ion, oxygen ion, and phosphorus ion, respectively, and the combined spectra is shown in Figure 4.22. The isotope abundance for O^{17} is small (0.038%), so the intensity of the oxygen hyperfine is negligible and not observed.

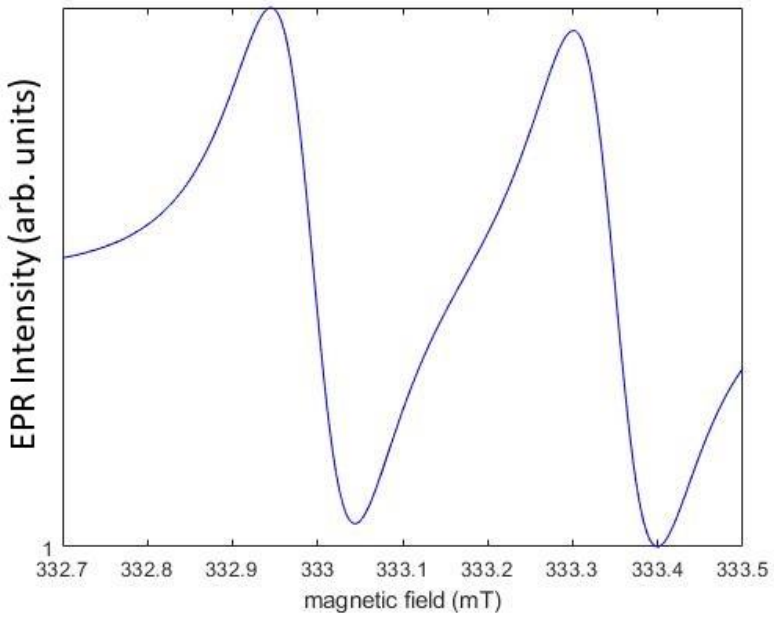

Figure 4.19. EPR spectra generated in EasySpin for the hydrogen ion for the 129-atom cluster, self-trapped hole defect simulation with inputs from the results from Gaussian.

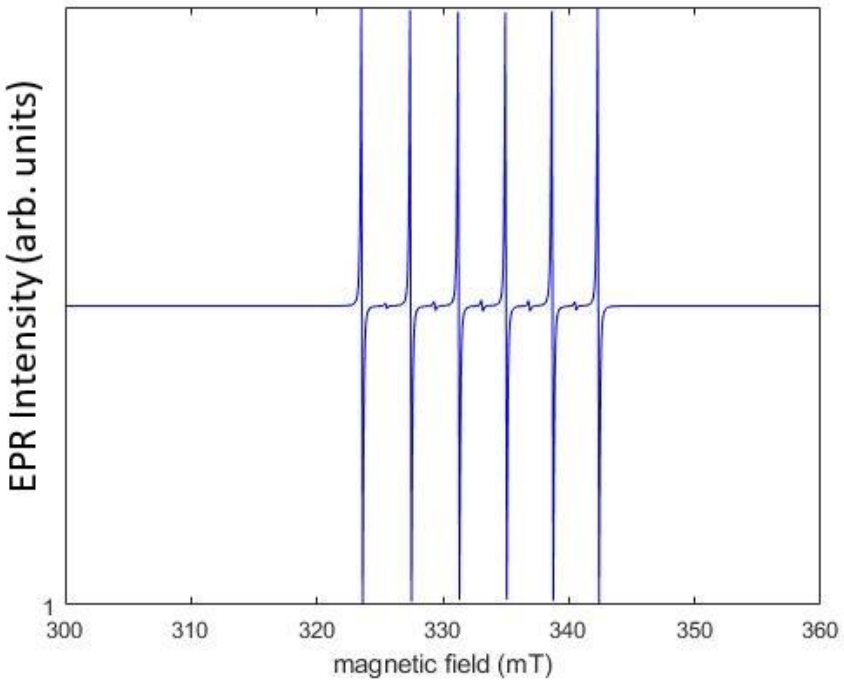

Figure 4.20. EPR spectra generated in EasySpin for the oxygen ion for the 129-atom cluster, self-trapped hole defect simulation using results from Gaussian.

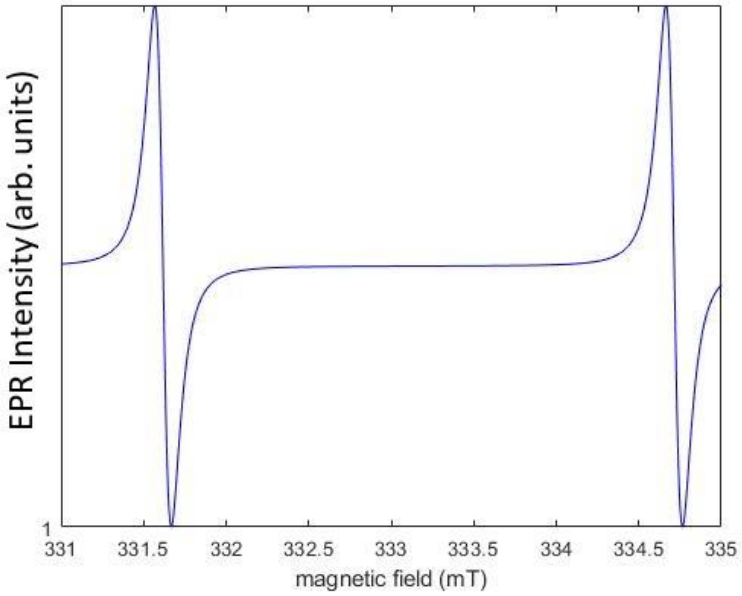

Figure 4.21. EPR spectra generated in EasySpin for the phosphorus ion for the 129-atom cluster, self-trapped hole defect simulation using results from Gaussian.

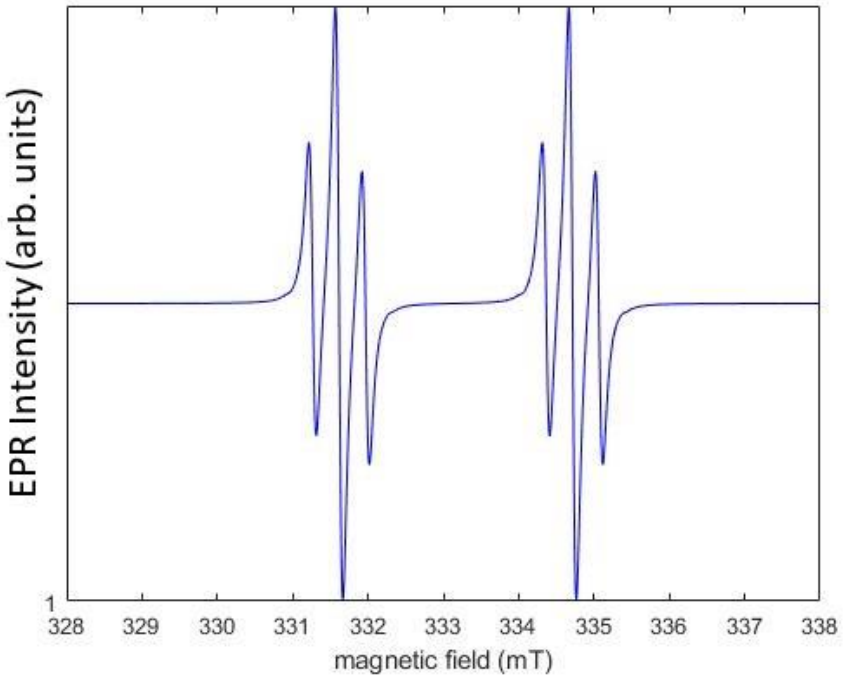

Figure 4.22. EPR spectra generated in EasySpin for the combined hydrogen, oxygen, and phosphorus signatures (seen in Figures 4.19-4.21), for the 129-atom cluster, using the 129-atom cluster self-trapped hole defect simulation results from Gaussian.

It is important to recognize that the spectra in Figure 4.22 is not exactly the same as the spectra from the EPR experiment, as presented in Figure 2.3. This is because Figure 4.22 does not yet include the results from the hydrogen vacancy defect simulation. Chapter 6 describes preliminary efforts to model the hydrogen vacancy, and incorporating this spectra into the combined simulated spectra will be part of future research.

4.4.2 Spin Density Distribution among Orbitals

The output from these calculations helps to understand the relative localization of the spin density outside of the central phosphorus ion's *3s* shell. As introduced in Chapter 2, previous researchers had postulated, using EPR on x-ray irradiated KDP, that approximately 0.9%-1% of the spin density for the phosphorus ion affected by a hole defect was in its *3s* orbital [33, 34]. This was deduced from the amount of spin density in the Fermi contact term compared to the anisotropic values. Using the results discussed in this chapter, the same ratio may be calculated. According to previously published literature, if 100% of the electron density were located in the *3s* orbital of the phosphorus ion, then the expected isotropic hyperfine value would be 10201 MHz [86]. By dividing the ratio between what was calculated in this research, specifically -83.406 MHz from Table 4.23 divided by 10201 MHz, the ratio turns out to be 0.8%, thus supporting previous claims on the insignificant localization of the spin density in the *3s* orbital [33, 34]. This supports the theory that the dominant contributor to the isotropic hyperfine term is from exchange core polarization, between *s*-type (core) orbitals and the orbitals of neighboring atoms [87].

Similar observations are made for the oxygen ions. Previously published literature states that for oxygen, an isotropic hyperfine value of -4623 MHz would indicate that 100%

of the spin density is located within an oxygen ion's *2s* orbital [86]. However, the calculations presented in Table 4.23 show that the calculated isotropic hyperfine values are -33.662 MHz for the two oxygen ions. Additional literature exists to help confirm that the placement of the unpaired spin on the two oxygen ions is in *p*-type orbitals versus *s*-type. The atomic value published by Fitzpatrick [86] for oxygen is -372.18 MHz (this is an updated value from the Morton and Preston value of -421 MHz [88]). By using the method in Reference [88], this number is divided by two (since ½ of the unpaired spin is in the *2p* orbital of a given oxygen ion) and multiplied by the angular factor of 4/5. This will give the expected result for the unique principal value of -148 MHz, which is very close to the result for the unique principal value of either oxygen ion predicted in the Gaussian calculations of -140.88 MHz, as presented in Table 4.22. There are no experimental EPR or ENDOR values to confirm this measurement for the oxygen ions, due to their low natural abundance. These *p*-type orbitals from the self-trapped hole, along with a variety of molecular orbitals, are illustrated in Chapter 5 to be localized on these two oxygen ions for a variety of large and small KDP clusters. There is little physical overlap from the *p*-type orbitals on the neighboring two hydrogen ions, which indicates that the anisotropic hyperfine values for the two hydrogens are due to point dipole-dipole interaction with the oxygen ions.

A further indicator that exchange core polarization is taking place between the central phosphorus ion and the two hydrogen ions that share the self-trapped, are the fact that their isotropic values are negative [89]. From previously published data, the nuclear magnetic moments of phosphorus and hydrogen nuclei are expected to have positive signs of 2.2632 and 5.585694 respectively, and the oxygen ions are expected to be negative, at

-0.757516 [90]. The use of the nuclear g-values in calculating the hyperfine terms was introduced in Chapter 3 of this dissertation, and their use was illustrated in Equation 3.3, Equation 3.5, and Equation 3.6, for computing the total Hamiltonian, the Fermi contact term, and the anisotropic component of the ***A*** matrix, respectively. The anisotropic results for the 129-atom cluster presented in Table 4.22 further indicate that the unique principal axis values had been calculated with the magnetic moments of the nuclei with the respective atoms' nuclear signs in accordance with the literature. The unique principal value for the phosphorus ion was calculated to be positive, at 4.321 MHz. Similarly, the unique principal value for the two hydrogen ions with the spin density were also positive, at 15.616 MHz. Lastly, the unique principal value for the two oxygen ions that share the defect are both negative, at -140.877 MHz.

V. Spin Density and Electronic Structure

5.1 Molecular Orbitals

This chapter consists of exploratory efforts to understand molecular orbitals and their role in the formation of the spin density, using the graphics software known as GaussView. GaussView allows the user to visualize HOMO, LUMO, and spin density iso surfaces. The combination of spatially distributed electron orbitals per atom can lead to a variety of molecular orbital shapes. Figure 5.1 demonstrates the association between orbital shapes and the σ, π naming convention for covalent bonds from p-type atomic orbitals, and the two colors are meant to indicate the phase of the orbital. The phase is a positive or negative probability amplitude for a given electron's orbital, and this sign difference is due to the wavelike nature of an electron orbital. When p-type atomic orbitals lie mostly horizontal to one another and have the same phase, they will fuse together, and σ-type orbitals are formed. If the electrons have a likelihood of being in the middle of their two positions, the orbital is considered σ-bonded. Molecular σ-type orbitals that have nodes in between them are referred to as anti-bonding σ^* orbitals. This results from the cancellation of the phase from the different orbitals. The π-type orbitals are formed from atomic orbitals that lie mostly parallel to one another. As seen in Figure 5.1, the π^* antibonding orbitals are similar in their naming convention to the σ^* antibonding orbitals, in that they demonstrate a repulsive behavior between the orbitals, thus creating a gap between them. The π-type bonding orbital demonstrates the combination of orbitals into two spherically shaped lobes, with no gaps.

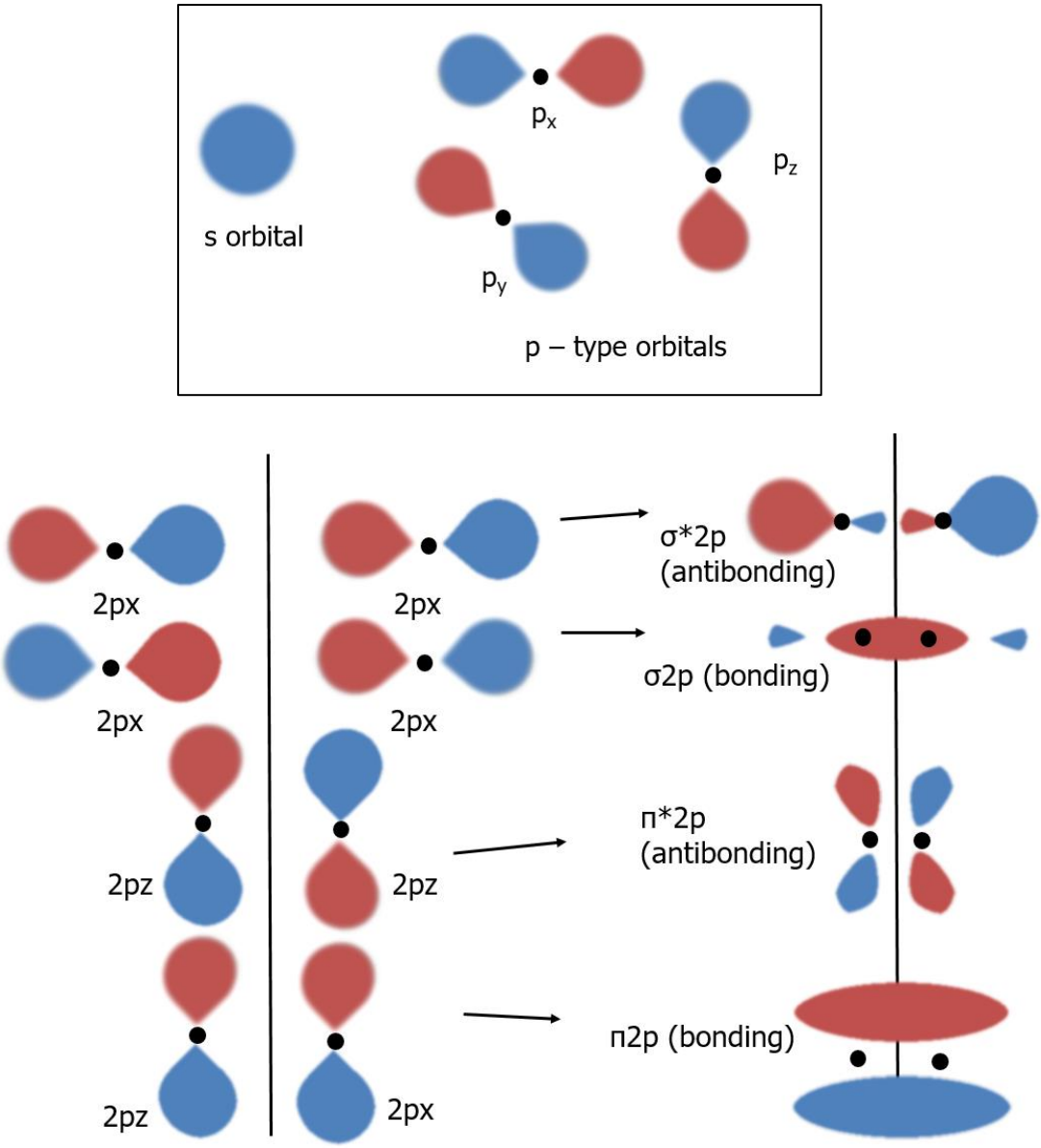

Figure 5.1. The top graphic shows the general shape of s orbitals and p orbitals, p_x, p_y, and p_z, and the two colors indicate two different phases. The bottom graphic shows different ways that atomic p-type orbitals can combine to create $\boldsymbol{\sigma}$ or $\boldsymbol{\pi}$ molecular orbitals.

The Gaussian output file contains the values for the alpha and beta (spin up and spin down) distribution per electron orbital, per atom, and the final output at the end of the calculations is titled “Gross orbital populations.” An example for the values for alpha, beta, and spin

density for each orbital per atom is listed below, for a UMP2 job. Notice how the column for Spin is correlated to the Alpha – Beta quantity. Ultimately, the hyperfine parameters are determined by the spin density $\rho^{\alpha-\beta}$, as described in Section 3.1, and are based on the cumulative difference of all spatially distributed alpha and beta orbitals that contribute to the molecular-level excess spin density.

Gross orbital populations:

			Total	Alpha	Beta	Spin
193	21	H 1S	0.39774	0.19819	0.19954	-0.00135
194		2S	0.03407	0.00788	0.02619	-0.01830
195		3S	-0.05369	-0.02888	-0.02481	-0.00406
257	29	O 1S	1.99810	0.99905	0.99905	0.00001
258		2S	0.91109	0.46379	0.44730	0.01648
259		2PX	0.83907	0.49151	0.34756	0.14396
260		2PY	1.05901	0.54260	0.51642	0.02618
261		2PZ	0.90784	0.54341	0.36443	0.17898
262		3S	1.09404	0.54539	0.54865	-0.00327
263		3PX	0.49208	0.28299	0.20909	0.07389
264		3PY	0.75421	0.37988	0.37433	0.00555
265		3PZ	0.58328	0.33389	0.24939	0.08450
266		4S	-0.08514	-0.03331	-0.05183	0.01851
267		4PX	0.02798	0.01251	0.01546	-0.00295
268		4PY	-0.04818	-0.02738	-0.02079	-0.00659
269		4PZ	0.02532	0.00128	0.02404	-0.02276
270	30	P 1S	1.99958	0.99979	0.99979	0.00000
271		2S	1.99919	0.99960	0.99959	0.00001
272		2PX	1.99244	0.99615	0.99629	-0.00014
273		2PY	1.99244	0.99621	0.99624	-0.00003
274		2PZ	1.99235	0.99617	0.99617	0.00000
275		3S	1.17339	0.58795	0.58543	0.00252
276		3PX	0.71691	0.34787	0.36904	-0.02117
277		3PY	0.73507	0.36539	0.36968	-0.00430
278		3PZ	0.71077	0.35531	0.35547	-0.00016
279		4S	-0.72967	-0.36604	-0.36363	-0.00241
280		4PX	0.17111	0.09067	0.08044	0.01022
281		4PY	0.16434	0.08152	0.08282	-0.00130
282		4PZ	0.21188	0.09001	0.12187	-0.03186
283		5S	0.17145	0.08833	0.08312	0.00521
284		5PX	0.28085	0.14486	0.13598	0.00888

285	5PY	0.29437	0.14417	0.15020	-0.00603
286	5PZ	0.08676	0.04082	0.04594	-0.00512

As seen above, the highest values for spin density for the three atoms are located on: the 2S orbital for the H21 hydrogen atom, the 2PZ orbital for the O29 oxygen atom, and the 4PZ orbital of the P30 phosphorus atom. These three atoms are where the highest hyperfine values are concentrated for this particular 41-atom cluster, self-trapped hole simulation.

There is one last point to be made about the spin density calculations conducted by Gaussian, in particular as it pertains to UMP2 simulations. Spin contamination can be an issue in simulations utilizing UMP2. This is when the total "S" value for the spin is greater than the prescribed value. In our case, S=1, and if there were spin contamination, it would be greater than one. However, Gaussian includes an annihilation step which eliminates higher order spin contaminants. As seen in the data below, the total Mulliken spin density sums to one, as it should. This spin density data is from a UMP2/6-31++G simulation – column two shows the spin densities, with the highest spin densities localized on the atoms where the hole is calculated to be. Namely, P(30), H(32), H(21), O(29), and O(39).

Mulliken charges and spin densities:

		1	2
1	O	-0.735944	0.023264
2	P	1.838118	0.001558
3	H	0.508711	0.000217
4	H	0.642901	-0.000692
5	H	0.490313	-0.000072
6	H	0.466990	0.000698
7	O	-0.764344	-0.001260
8	O	-0.795175	0.000541
9	O	-0.979338	0.002579
10	O	-0.652272	0.001943
11	P	1.838118	0.001558
12	H	0.508711	0.000217
13	H	0.642901	-0.000692

14	H	0.490313	-0.000072
15	H	0.466991	0.000698
16	O	-0.764344	-0.001260
17	O	-0.795174	0.000541
18	O	-0.979338	0.002579
19	O	-0.652272	0.001943
20	P	1.875443	0.001675
21	H	0.621879	-0.023715
22	H	0.486157	-0.000330
23	H	0.506344	-0.000021
24	H	0.505294	0.000189
25	O	-0.776497	0.000299
26	O	-0.880663	0.002125
27	O	-0.663909	0.001024
28	O	-0.653694	0.000315
29	O	-0.558704	0.512496
30	P	1.036779	-0.045661
31	P	1.875443	0.001675
32	H	0.621880	-0.023715
33	H	0.486157	-0.000330
34	H	0.506344	-0.000021
35	H	0.505294	0.000189
36	O	-0.735944	0.023265
37	O	-0.776497	0.000299
38	O	-0.880664	0.002125
39	O	-0.558706	0.512493
40	O	-0.663909	0.001024
41	O	-0.653694	0.000315

Sum of Mulliken charges = 2.00000 1.00000

Mulliken analysis is based on the linear combination of atomic orbitals (LCAO) and assigns the spin density based on the distribution of electrons across the molecule. The Mulliken spin density can be compared to the value obtained by manually performing a LCAO by utilizing the gross orbital population output from Gaussian. The values listed in the Mulliken spin density column are approximately equal to the values listed under the Spin column in the Gross Orbital Populations section of Gaussian output, on the previous

page. For instance, adding the three values under the Spin column for H21 gives a total of -0.02371, which is approximately equal to the Mulliken spin density of -0.023715.

5.2 Using GaussView to Visualize Molecular Orbitals: HOMO, LUMO, and Spin Density

The HOMO, LUMO, and electron density from the spin SCF density may be visualized using GaussView with "isosurfaces". The isosurface values, in units of electrons/Angstrom^3 for spin density or the square root of electrons/Angstrom^3 for the molecular orbital, are chosen by the user and may be changed from the default. Changing the isovalues to be larger values will make the size of the displayed orbitals smaller. The following graphics utilize the default values for the isosurfaces – this isosurface size maintains the electron cloud size to be relatively localized while at the same time allowing the viewer the ability to see areas where bonding occurs between atoms.

As seen in Figures 5.2-5.3, hovering over the isosurfaces for the spin density of the 47-atom simulation, which used the post-optimization ωB97XD/6-31+G(d) job that held the PK distance at 3.75 Angstrom and the OPO angle at 90 degrees, shows the blue surface at 0.0004, and green at -0.0004, and the HOMO and LUMO molecular orbitals for the alpha and beta are 0.02 for the red surface and -0.02 in green. The positive and negative values that are reported by the isosurface represent the amplitudes of the electron's probability distribution for a particular molecular orbital. The HOMO and LUMO for alpha are depicted below in Figure 5.2, and the structure is rotated in order to show that the HOMO and LUMO for the alpha molecular orbital are not located on the atoms with the highest hyperfine values. Similarly, the HOMO for the beta molecular orbital is not located on the PO_4 unit with the self-trapped hole, but the LUMO for the beta molecular orbital is

relatively localized on the atoms with the excess spin density. The HOMO and LUMO beta molecular orbitals are shown in Figure 5.3.

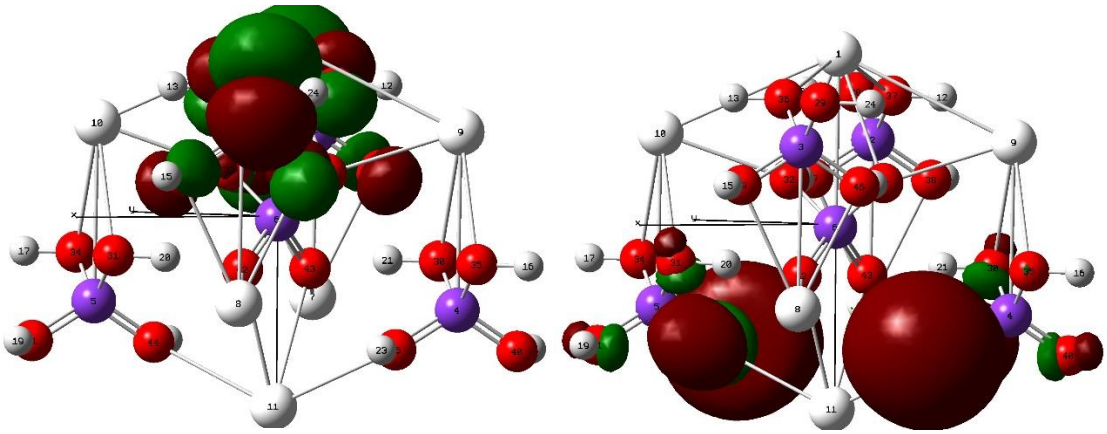

Figure 5.2. Graphics depicting the HOMO (left, z-axis down) and LUMO (right, z-axis down) for the alpha molecular orbital for the 47-atom cluster, after a ωB97XD/6-31+G(d) optimization. The atoms that have the highest hyperfine values are displayed in the middle of the cluster: P6, O43, O42, H21, and H20.

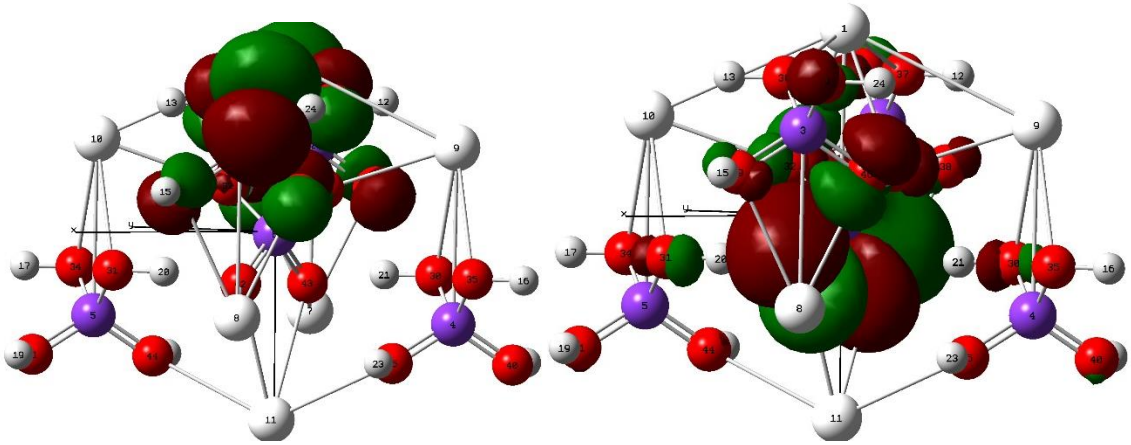

Figure 5.3. The HOMO (left) and LUMO (right), for the beta molecular orbital, displaying the same cluster and orientation as displayed in Figure 5.2. The beta LUMO is spatially located over the atoms that have the hole, O42, O43, and P6, unlike the HOMO for the beta molecular orbital.

The spin density graphic is shown below, in Figure 5.4, for the same post-optimization job as displayed in Figures 5.2-5.3. GaussView labels the spin density plot as "Electron density from SCF (or UMP2) Spin Density", depending on if UMP2 was used and is selected by the user for viewing.

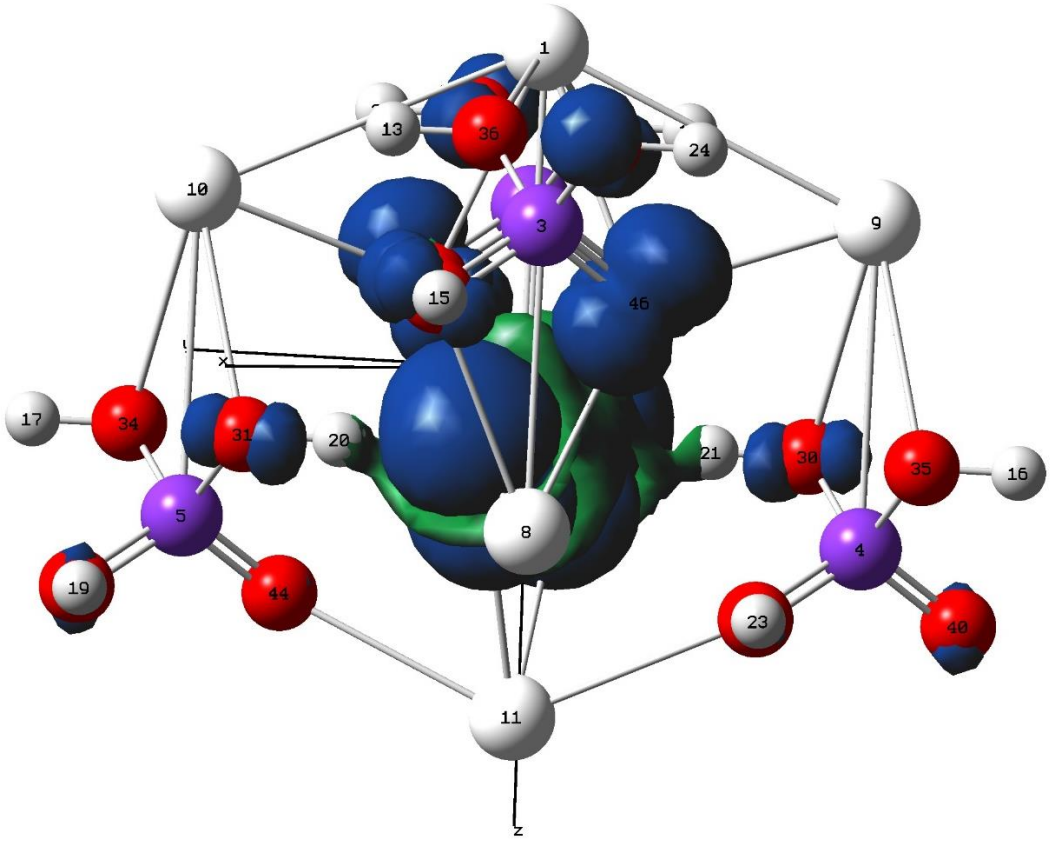

Figure 5.4. The spin density created by subtracting the alpha and beta molecular orbitals, such as those that were displayed in Figures 5.2-5.3. The z-axis is pointed down. The phosphorus and the two oxygen ions with the highest amount of spin density, P6, O43, and O42, are obscured by the lobes, and the H20 and H21 ions that partially share the hole are partially covered by the green part of the spin density lobes.

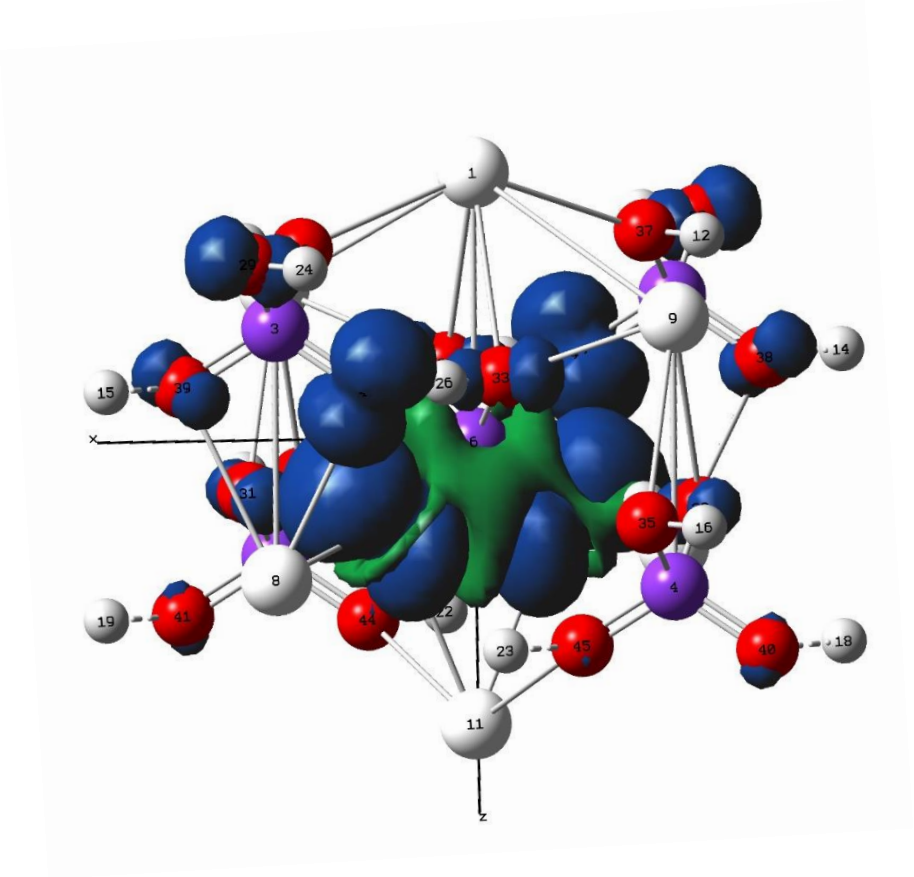

Figure 5.5. A slightly rotated view of the 47-atom cluster seen in Figure 5.4. This orientation shows the features of the four large, blue lobes that are distributed above the central phosphorus ion and over the two oxygen ions that share the self-trapped hole, O42, and O43, which are not visible in Figure 5.4.

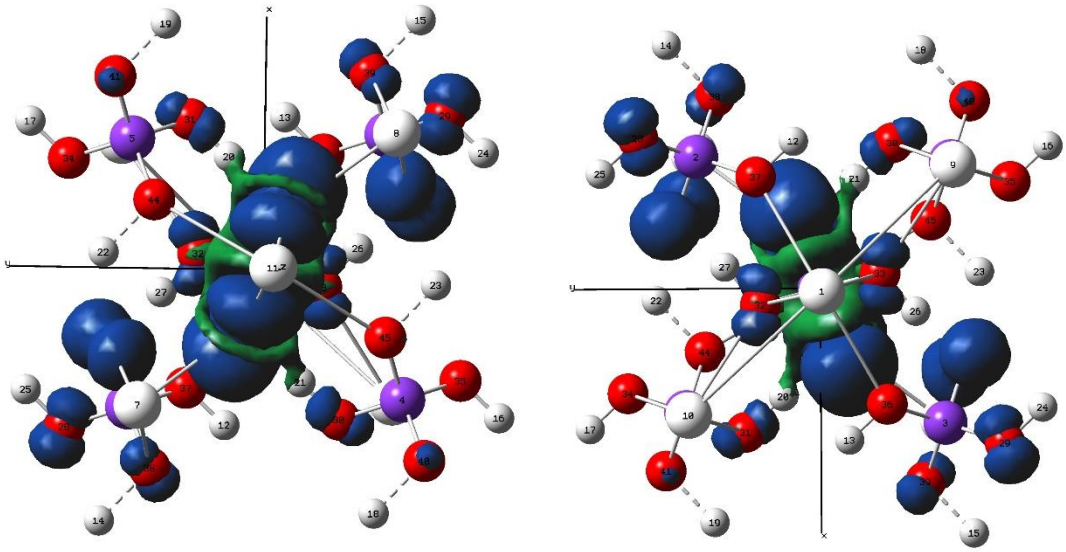

Figure 5.6. Two different orientations of the electron density form the spin SCF density, z-axis out (left image) and z-axis in (right), of the cluster shown in Figure 5.4 and Figure 5.5.

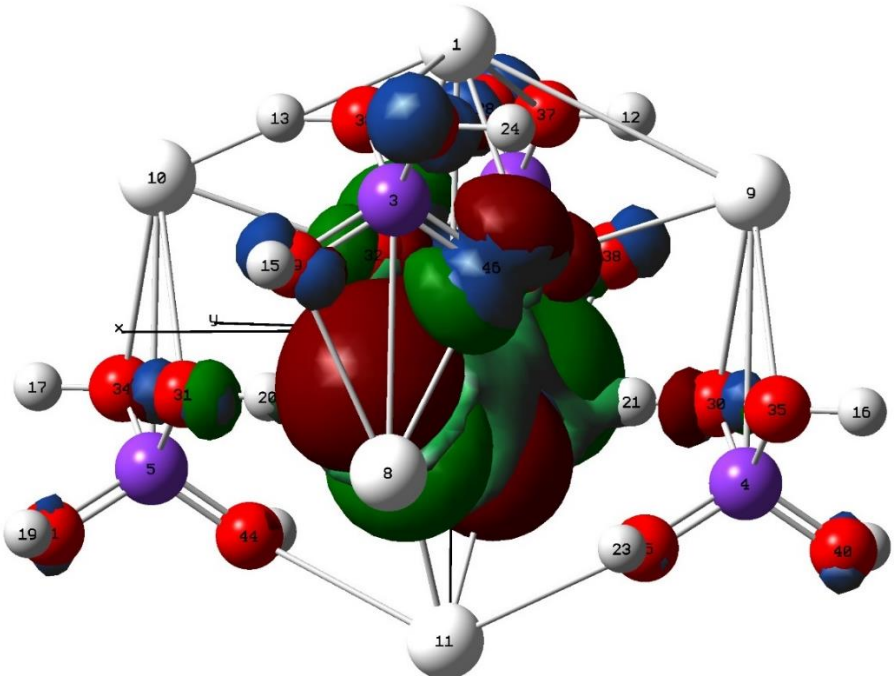

Figure 5.7. This image depicts the relationship between the spin density over-plotted with the beta LUMO. The large blue lobes which were localized on the central PO_4 unit for the electron density from the SCF spin density (seen in Figure 5.5) are obscured under the beta LUMO's blue and green lobes.

The positive-valued spin density lobes (in blue) are due to the subtraction of negative beta regions and the addition of positive alpha molecular orbitals. The resultant hyperfine measurements are from the spin density, localized on the five atoms that had come into existence due to the pre-established addition of the self-trapped hole via the addition of an extra charge.

GaussView will plot the spin density and spin density-squared values, after performing post-processing on the checkpoint file produced by Gaussian. This image makes it easier to visualize the localization of the excess spin density on the two oxygen ions, since the area covered by the isosurface is smaller and more confined to the two oxygen ions of interest versus the spin density isosurfaces in Figure 5.4 through Figure 5.6, and to see the relative shape and physical location of the orbitals, as seen in Figure 5.8.

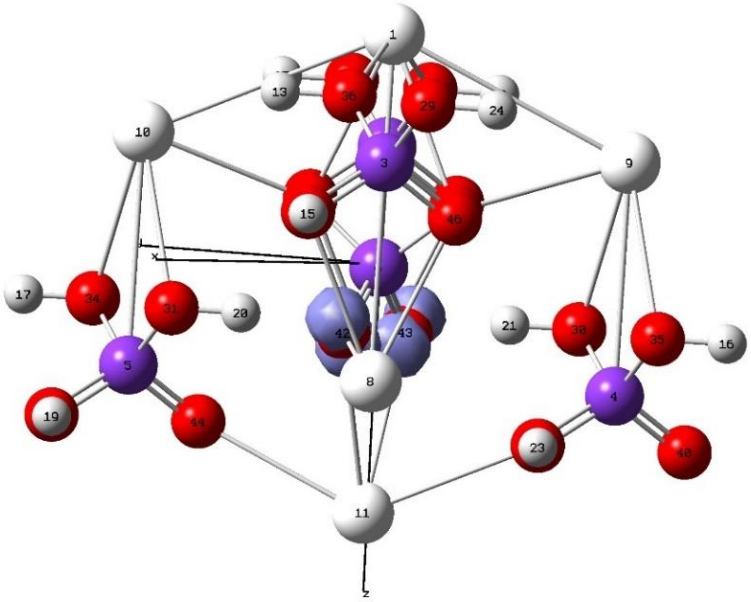

Figure 5.8. Spin density squared graphic for the same 47-atom cluster as depicted in the previous figures. This image makes it easier to visualize the shape and physical location of the spin density orbitals on the two oxygen ions.

5.2.1 Molecular Orbitals and Electron Density for 115-Atom Cluster

The following series of figures depicts the electron density from the spin SCF density along with a variety of different molecular orbitals for the 115-atom cluster which was explained in Section 4.3.2. In general, the orbitals are almost identical in shape and composition to the 47-atom cluster self-trapped hole simulations.

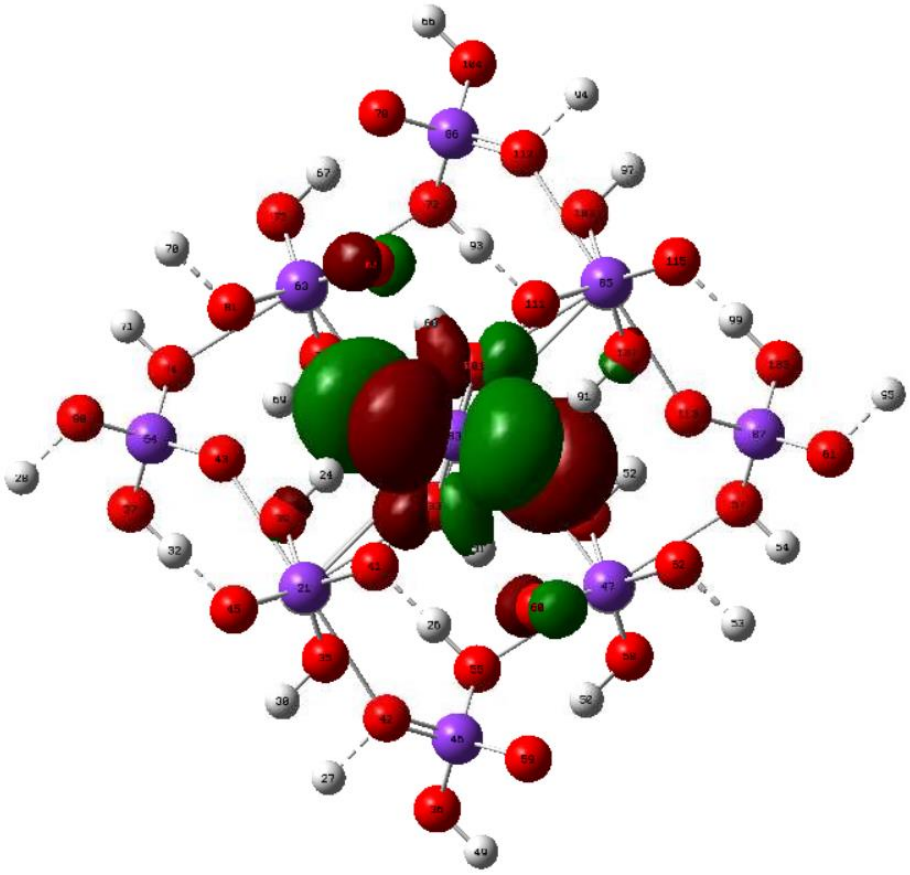

Figure 5.9. This is the beta HOMO for the 115- atom cluster. This graphic was generated from the cluster that is described in Section 4.3.2 of this dissertation.

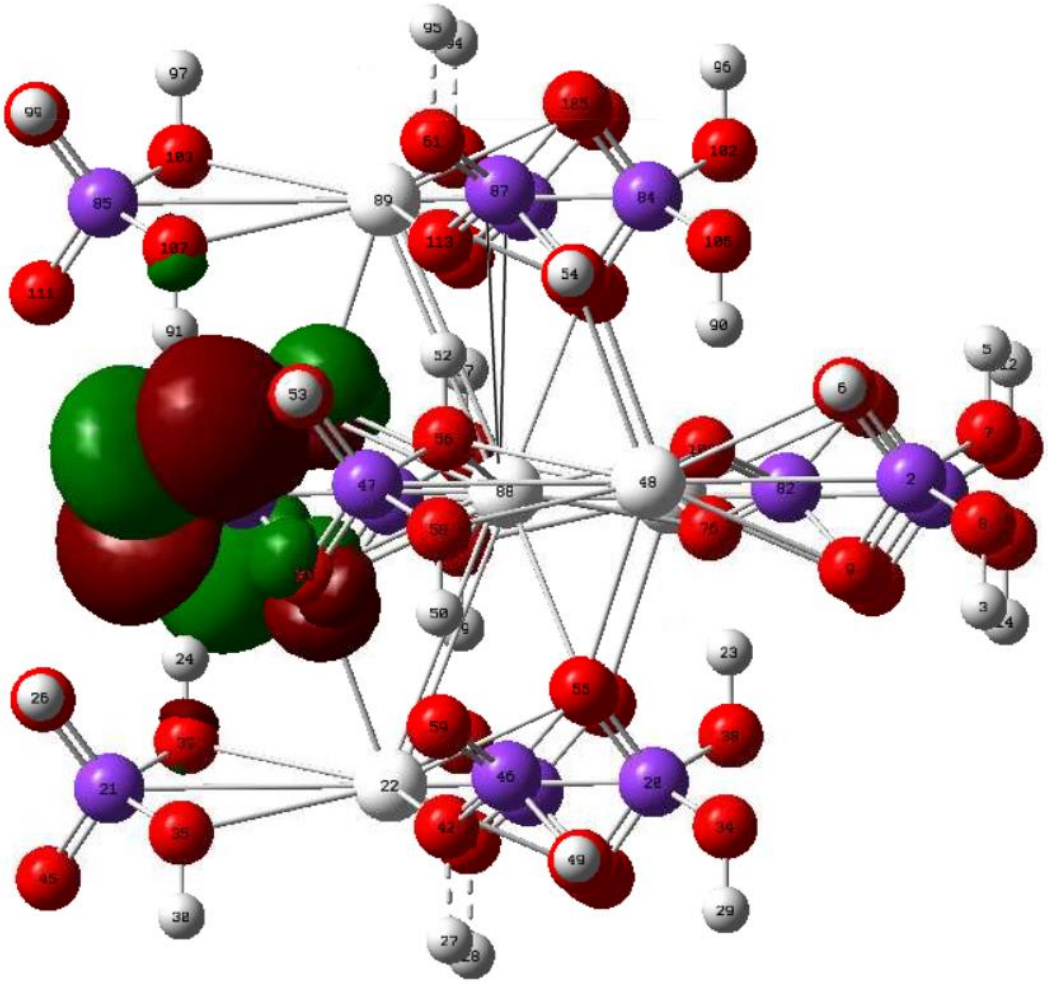

Figure 5.10. 115-atom cluster HOMO for beta. Note that the PO_4 unit of interest is to the far right of the central potassium ion (centralized around phosphorus number 82), and the beta HOMO is to the far left.

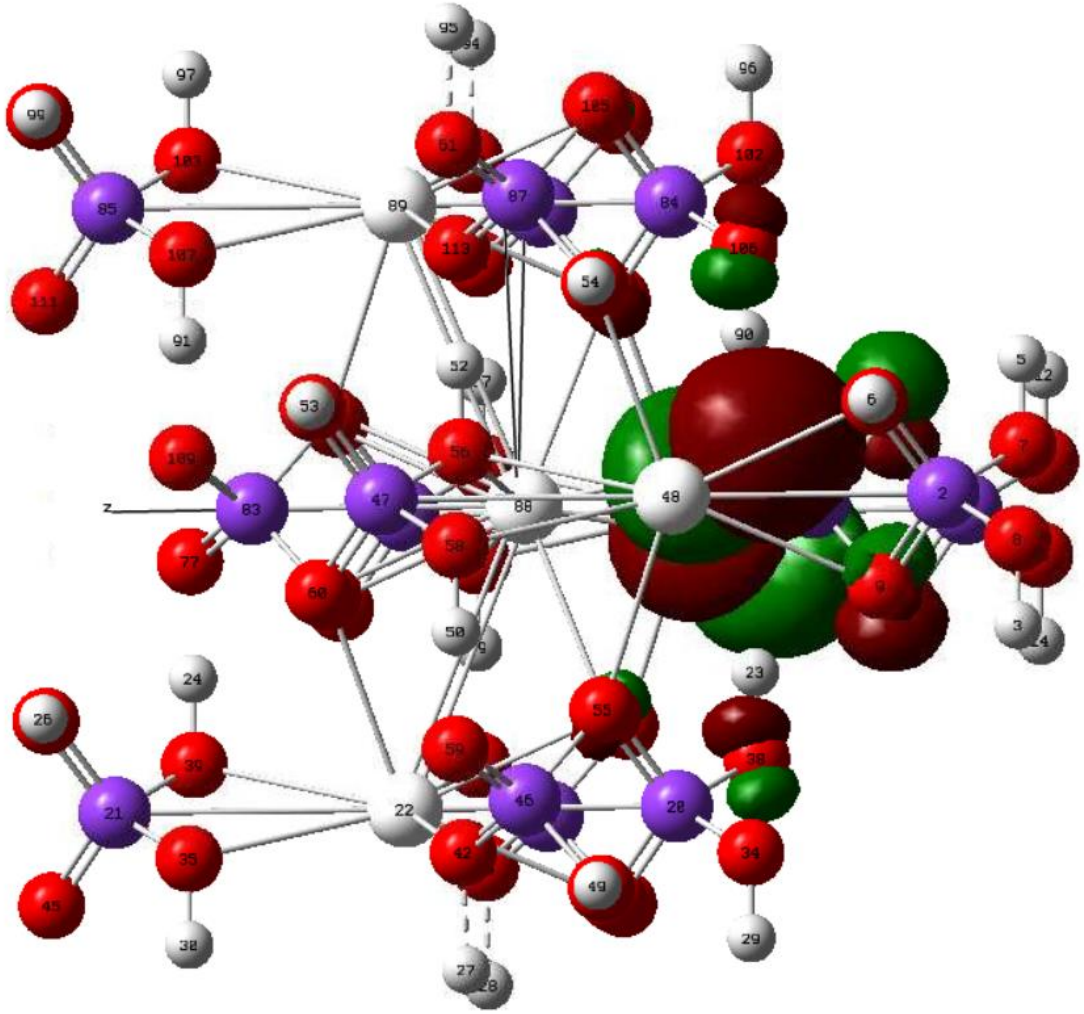

Figure 5.11. 115-atom cluster molecular orbital beta LUMO. Here, the orbitals are localized on the self-trapped hole.

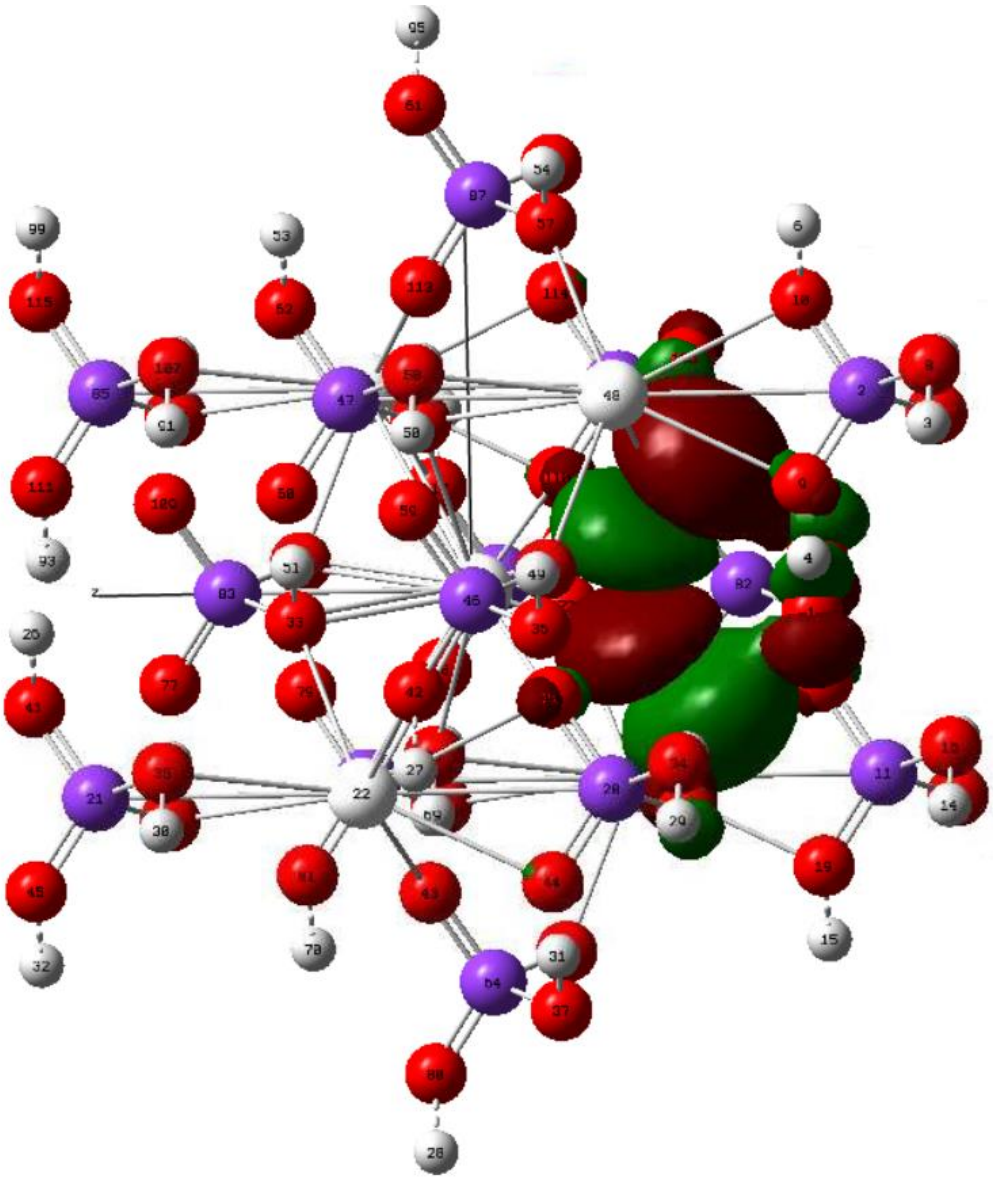

Figure 5.12. The same 115-atom cluster as displayed in the previous figure, for the beta LUMO. This image is rotated about the z-axis to show the four distinct, red and green anti-bonded lobes.

The electron density plots of the spin SCF density were plotted for the 115-atom cluster in Figures 5.13 and 5.14, along with the electron density for the spin SCF density squared in Figure 5.15. These graphics are shown in the following series of figures. As seen in the

figures, the relative shape and orientation of the electron density in the 115-atom cluster resembles the 47-atom cluster, as was described in the previous section.

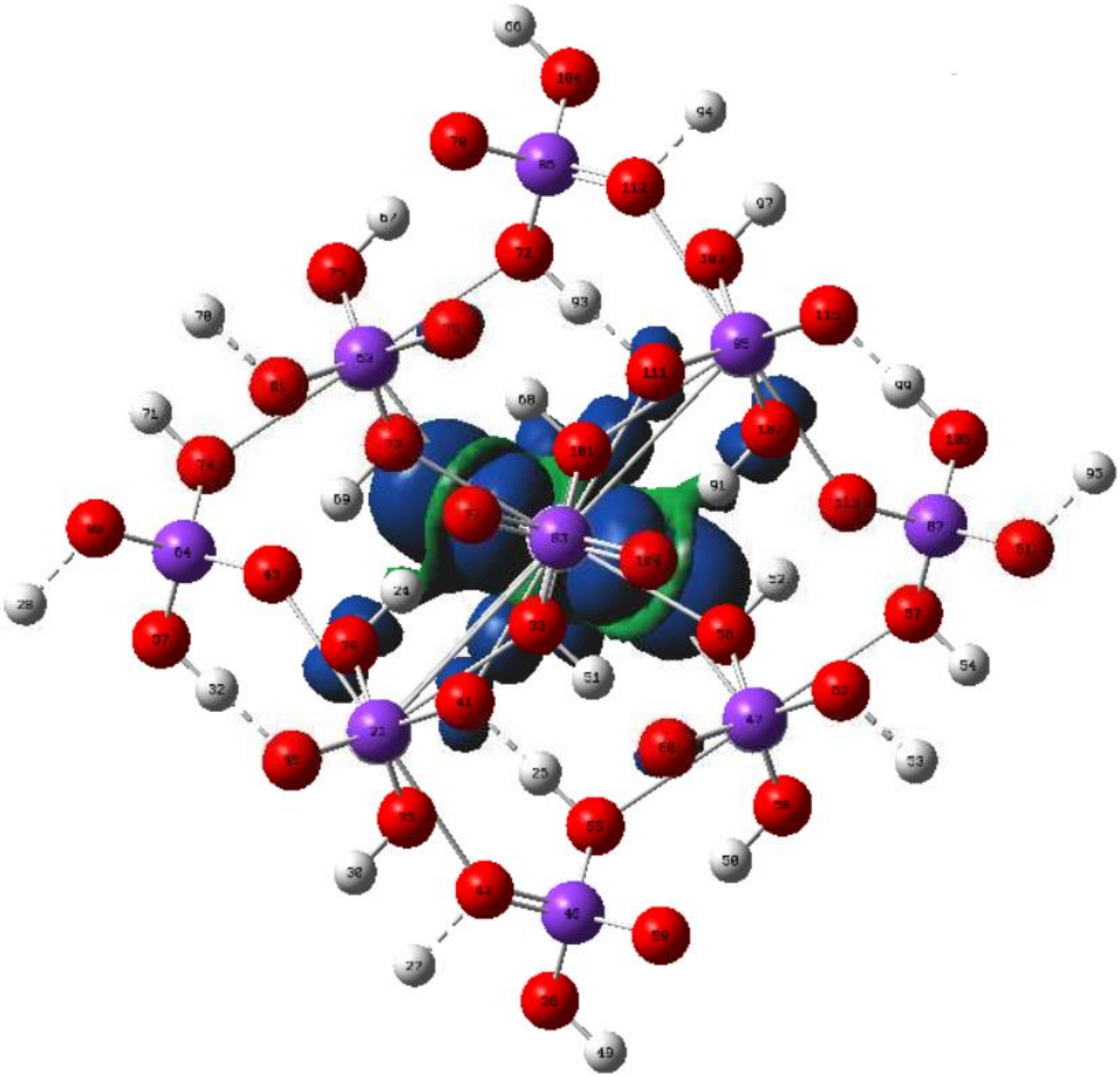

Figure 5.13. The x-y plane of the 115-atom cluster with the "z-axis" coming out, displaying the electron density plot of the spin SCF density, post-geometry optimization.

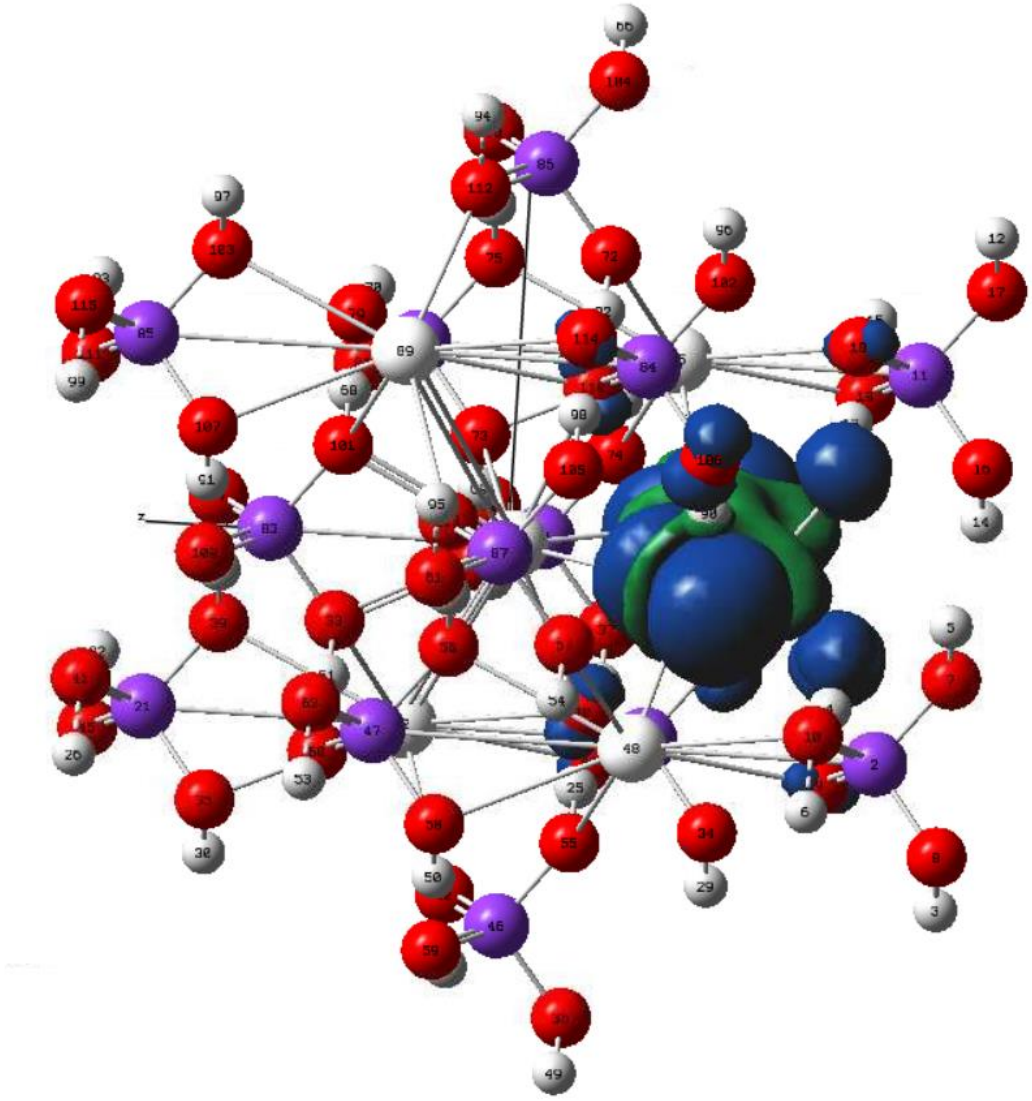

Figure 5.14. The electron density plot of the spin SCF density for the 115-atom cluster, post-optimization. This is the same image as seen in the previous figure, rotated while maintaining the “z-axis” pointing to the left**.**

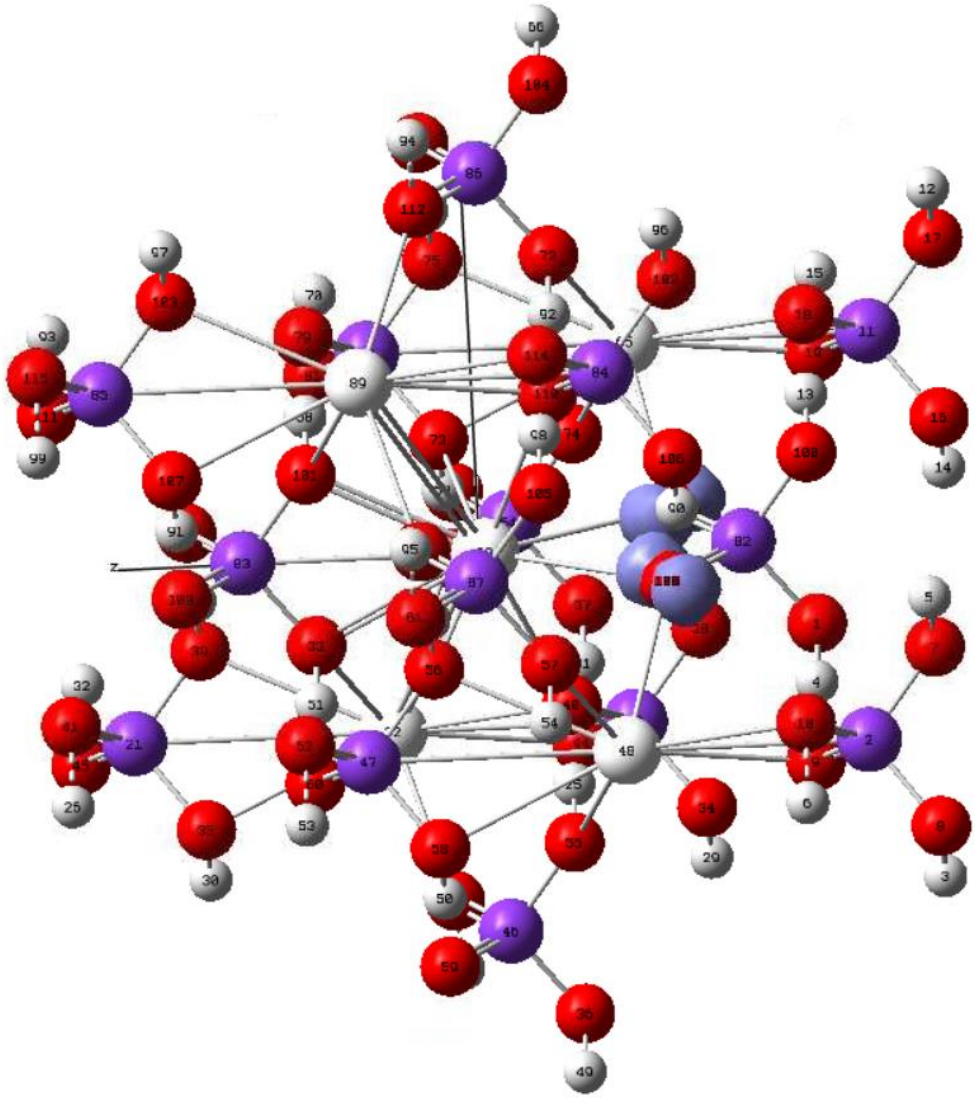

Figure 5.15. 115 atom cluster and the “Electron density from Spin SCF Density Squared” with the “z-axis” pointed to the left (same orientation as previous figure).

These molecular orbital and spin density plots for the larger 115-atom cluster are preliminary indications that a smaller, 47-atom cluster is sufficient for modeling and calculating the orbitals of the self-trapped hole defect.

5.2.2 Energy Gap Calculations

Energy gap calculations were not explored in great detail for the course of this dissertation, but they are occasionally studied in *ab initio* calculations for defects, and therefore were preliminarily explored here. Pacchioni [71] has compiled density of state (dos) data, concluding that the relative location of the conduction and valence bands – and the correct electron correlation calculations as they relate to polaronic distortions - are important indicators for successful EPR simulations. He references several papers, which explore the validity of quantum theories by calculating the dos data for the oxygen vacancies in MgO, AlO_4, TiO_2, and NiO. Valentin's [91] paper also contains a discussion of the importance of performing the dos calculation for a more precise polaronic structure in estimating the localization of holes.

The LUMO and HOMO are highlighted in Figure 5.16, for both the restricted (alpha molecular orbitals (MOs)) and unrestricted (split alpha and beta MOs). The energy gap E_g is calculated by subtracting LUMO from HOMO energy values. The following calculations demonstrate an energy gap of 4.4 eV for the alpha MO (1.42 beta MO) for the DFT calculations (tetragonal results were at 5.5 eV), versus UMP2 and UHF, which were 12.55 eV and 12.26 eV alpha MO, compared to 10.33 eV and 10.33 eV for the beta MO. The energy gap of KDP is generally known in the literature to be around 5.9 eV, with no defects. Literature also exists for the calculation of interstitial hydrogen and the hydrogen vacancy defects' energy gaps in the KDP crystal. However, only the self-trapped hole is presented below.

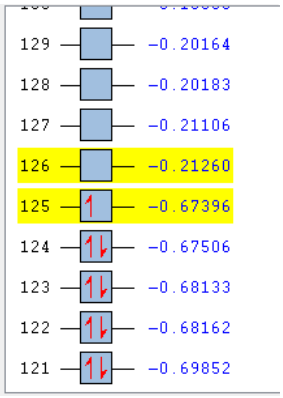

Figure 5.16. Results from the UMP2 calculation showing the highlighted restricted, alpha molecular orbitals.

The calculations are conducted in the following way. The highlighted values seen in Figure 63 are -0.212 Hartrees, or -5.785 eV, and -0.673 Hartrees, or -18.339 eV, giving a band gap of

$$\text{Eg} = \text{LUMO} - \text{HOMO} = -5.785 - (-18.339) = 12.554 \text{ eV}.$$

The red up and down arrows are in reference to the electrons occupying either a spin up or down position and can be broken into two separate columns as seen in Figure 5.17. This is a decent example of an output that unrestricted molecular orbit theory calculations can provide, as discussed earlier in this dissertation. For the unrestricted MOs (alpha MO and beta MO (2nd column)), the calculation is conducted in the following way:

$$-0.211 \text{ Hartrees} = -5.754 \text{ eV} - 0.591 \text{ Hartrees} = -16.088 \text{ eV}$$

$$\text{Eg (2nd column)} = \text{LUMO} - \text{HOMO} = -5.754 - (-16.088)$$

$$\text{Eg} = 10.334 \text{ eV}.$$

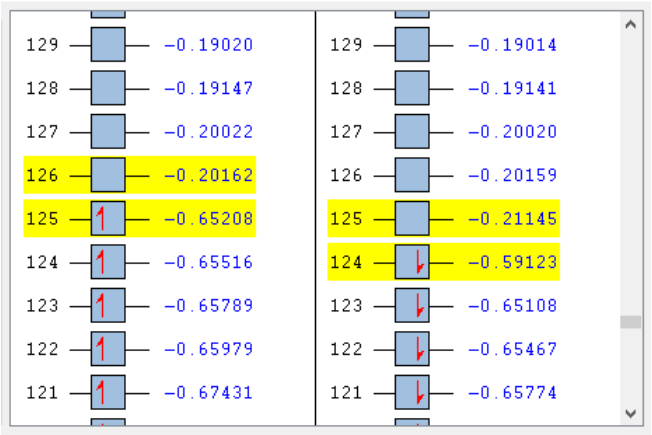

Figure 5.17. The unrestricted molecular orbitals split into alpha (spin up) and beta (spin down) values.

Lastly, the UHF Calculation for restricted MO (alpha MO) give

$$-0.201 \text{ Hartrees} = -5.486 \text{ eV} - (-0.652 \text{ Hartrees}) = -17.744 \text{ eV}$$

for a band gap energy of

$$\text{Eg} = -5.486 - (-17.744) = 12.258 \text{ eV}.$$

And the unrestricted (alpha and beta MOs) data gives

-0.2115 Hartrees $= -5.754$ eV minus -0.5912 Hartrees $= -16.088$ for a band gap of

$$\text{Eg} = -5.754 - (-16.088) = 10.334 \text{ eV}.$$

VI. KDP Hydrogen and Oxygen Vacancy Simulations

6.1 Hydrogen Vacancy

The hydrogen vacancy is a common defect experimentally observed in KDP crystals [11, 19, 36, 37]. The EPR spectra for the hydrogen vacancy overlaps the self-trapped hole spectra, as seen in Figure 2.3. The model proposed to explain the EPR spectrum of the hydrogen vacancy consists of a hole trapped on one oxygen atom adjacent to a missing hydrogen ion. The cluster used in this simulation, shown in Figure 6.1, is an orthorhombic KDP structure with 40 atoms. The hydrogen-vacancy defect occurs when a hydrogen atom is removed from a regular $(H_2PO_4)^-$ unit, and it becomes $(HPO_4)^{2-}$, which then stabilizes into a $(HPO_4)^-$ unit when the hole is included. Similar to the procedure outline for the self-trapped hole in Chapter 4 Section 4.1, prior research was first verified by utilizing the UHF and UMP2 method and the basis set 6-31++G [22]. However, unlike Chapter 4, which began by duplicating results from previous research for the self-trapped hole, this chapter does not duplicate the tetragonal simulations that had been conducted in prior research for the hydrogen vacancy [22].

The calculated Fermi contact values indicate that the highest spin density is on the nearby oxygen ion, as was expected by prior research [19, 22]. This is the O28 oxygen in the cluster in Figure 6.1. After geometry optimization, allowing only the central eight PO_4H_3 atoms to move, the Fermi contact value for the O28 oxygen went from −51.2 to −48.9 Gauss, and the central phosphorus went from −35.75 to −30.44 Gauss. This is in good agreement with the hyperfine value measured by an EPR experiment, which was 31.0 Gauss for the central phosphorus [19].

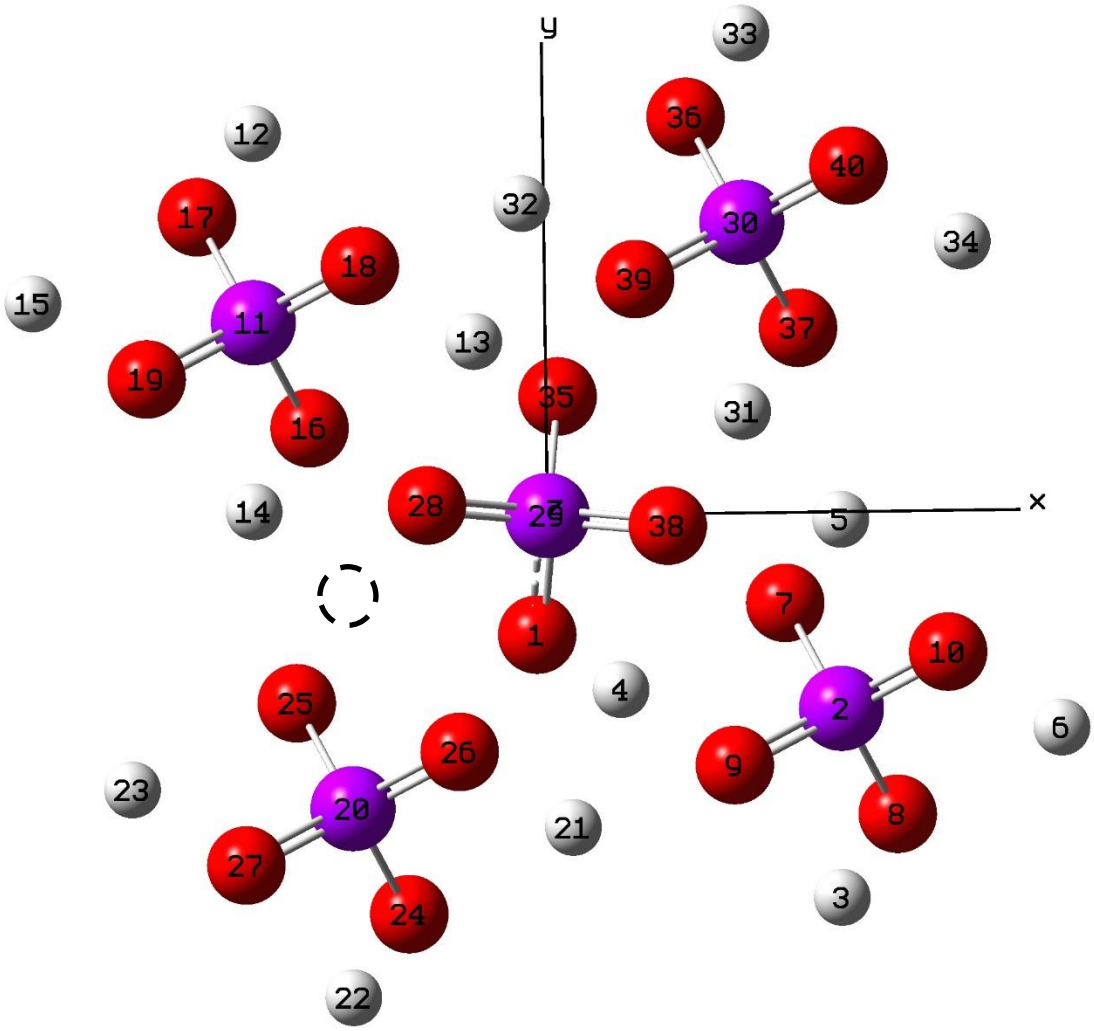

Figure 6.1. 40-atom cluster used in modeling of the hydrogen-vacancy trapped-hole defect in a KDP crystal. The hydrogen vacancy is between oxygen ions O28 and O25 and is indicated by the circle with a dashed outline.

The hydrogen vacancy defect was then simulated for the same cluster but with the ωB97XD/6-31+G(d) method and basis set. The Fermi contact values and anisotropic hyperfine values are presented below in Table 6.1 and compared to the EPR results from previous research [19, 20]. An interesting result of this simulation was the movement of

the atoms surrounding the central PO_4 unit. The geometry changes from this simulation are presented in Table 6.2.

Table 6.1 Hydrogen vacancy results for the 40-atom, orthorhombic cluster portrayed in Figure 6.1 compared to previously measured EPR data [19, 20].

Atom	Isotropic Results (Gauss)	Anisotropic (Gauss)	Directional Cosine Matrix			EPR, Hyperfine [19, 20] (Gauss)
P29	-27.95	-1.63	0.1649	0.9471	-0.2753	31.0
		-0.31	0.7209	0.0747	0.6890	
		1.93	0.6732	-0.3121	-0.6704	
O28	-25.05	34.76				
		33.79				
		-68.54				
O25	-22.58	12.24				
		11.80				
		-24.04				
H21	-3.38					
P20	-8.19					

Table 6.2 Distances and angles, before and after geometry optimization, for the 40-atom orthorhombic structure, hydrogen vacancy defect simulation. The unpaired electron is primarily localized on P29 and O28.

Atoms	Bond Distances (Å)		Angles (degrees)	
	Before opt.	After opt.	Before optimization	After optimization
R(H13-O35), R(O1-H4)	1.06	1.02		
R(P29-O35), R(P29-O1)	1.58	1.55		
R(H31-O38)	1.44	1.04		
R(P29-O38)	1.512	1.56		
R(P29-O28)	1.512	1.58		
A(O35-P29-O1)			106.22	114.93
A(O28-P29-O38)			115.28	115.90

The most noticeable geometry change that occurred in this simulation was the decrease in distance between H31 (a normally “far” hydrogen) and O38. The distance between these

two atoms decreased from 1.44 to 1.04 Angstroms, essentially placing H31 in the "near" position. This dramatic geometry change is also seen graphically in Figure 6.2, which shows the same cluster, post-geometry optimization.

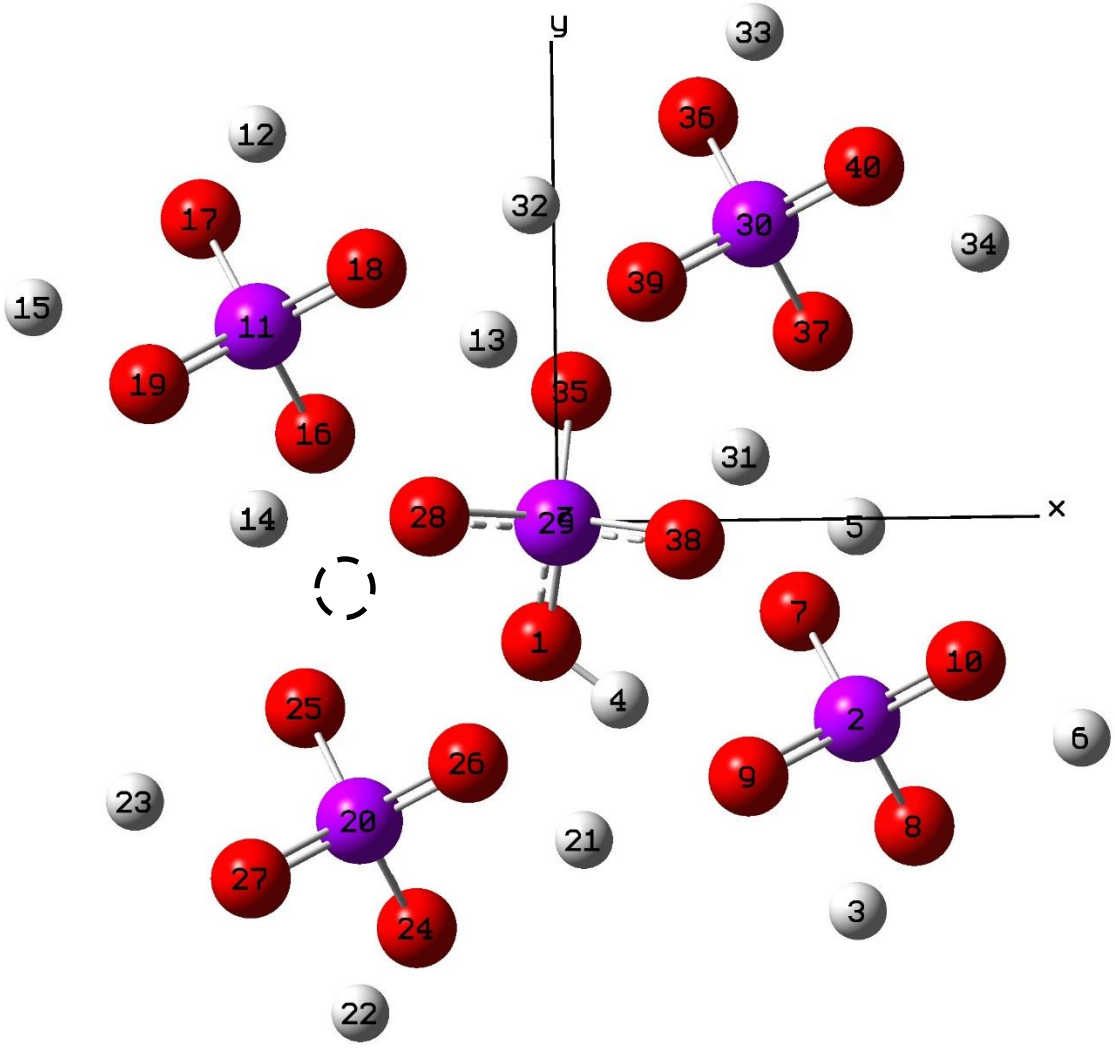

Figure 6.2. Post-optimization 41-atom cluster for the hydrogen vacancy defect. Hydrogen 31 had been a "far" hydrogen pre-optimization, but it moved closer to O38 post-optimization. The hydrogen vacancy is indicated by the circle with the dashed line.

Another interesting geometry change to note, is that unlike the self-trapped hole, in which the OPO angle between O29, P29, and O38 decreased, in the hydrogen vacancy defect

simulation, this angle did not change significantly. The change that occurred was for the O35-P29-O1 angle. This angle increased from 106.22 degrees to 114.9 degrees.

6.2 Oxygen Vacancy

As stated in Chapter 2, five different oxygen vacancies were measured by EPR experiment with the hyperfine splittings ranging from approximately 552 to 757 Gauss [20]. Since there are five different hyperfine values, it was hypothesized that the variance in these defect states were due to a variety of potassium vacancies surrounding the respective PO_3 unit with the missing oxygen ion. It was also suggested that one of the five hyperfine splitting values could be due to an oxygen plus a hydrogen vacancy. The same procedure was carried out in this chapter for the oxygen vacancy simulations as had been done by the self-trapped hole and hydrogen vacancy. The simulations started out by using the less computationally intensive UHF methods, and once the results seemed to have some level of validity in terms of hyperfine spectra and spin density localization, the more computationally intensive methods were employed. The results of these simulations supported previous research, which attributed the hyperfine splitting values in this range to $(PO_3)^{2-}$ units, with a 100% abundant I=1/2 phosphorus nucleus, with an electron trapped at one of the nearby oxygen divacancies [20]. Additional research is necessary in order to understand the underlying electronic structure, as had been done for the self-trapped hole.

6.2.1 Oxygen Vacancy using UHF

The oxygen vacancy simulations described here were successfully conducted for a larger cluster of 185 atoms, which become a cluster of 184 atoms upon removal of an oxygen ion. This cluster contains all six potassium ions that surround the central PO_4 unit.

This cluster is displayed in Figures 6.3, and a zoomed in and rotated view of the cluster with the oxygen vacancy visible is seen in Figure 6.4. The simulation results presented below were conducted before discovering the correct way to utilize all 36 processors, and the simulations took longer than what was reasonable. Additionally for this reason, the larger cluster meant that the simulations would have to use a simpler quantum chemistry approach and smaller basis set, so the job could finish in a timely manner. If the cluster was simulated with the UMP2 theory, the job time would have been over a week, and it would not finish (the limit on the duration of run-time for jobs on the HPC was one week). Initially, with no optimization, the job's CPU time was 0 days 2 hours 59 minutes 22.7 seconds with an elapsed time of 0 days 2 hours 59 minutes 33.1 seconds. The optimization CPU time was 1 day 16 hours 51 minutes with an elapsed time of 1 day 16 hours and 53 minutes, across two nodes sharing memory across all 72 processors. Thus, the jobs can finish in a relatively timely fashion, albeit the results are not as accurate due to the lack of electron correlation and smaller basis set.

An important realization occurred prior to conducting the oxygen vacancy simulations using ωB97XD/6-31+G(d). The previous oxygen vacancy simulations did not seem to be utilizing all 36 processors correctly, and this may have accounted for the simulations taking far longer than necessary. A small script was utilized that ensured that the input file was launched while utilizing all 36 cores. Additionally, another important piece of information to include in the input file was the following line:

%CPU=0,1,2,3,4,5,6,7,8,9,10,11,12,13,14,15,16,17,18,19,20,21,22,23,24,25,26,27,2
8,29,30,31,32,33,34,35

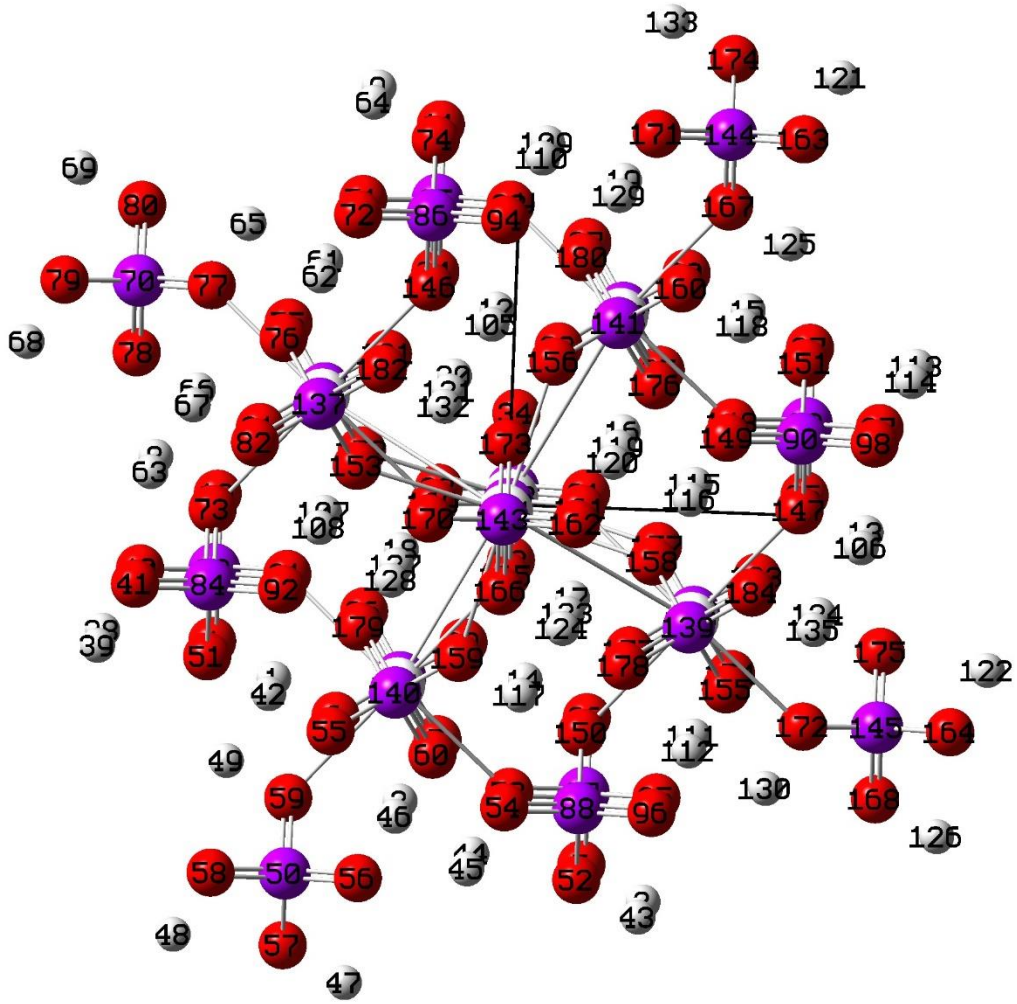

Figure 6.3. The y, z plane of the 184-atom cluster with an oxygen vacancy on the central PO_4 unit. In this orientation, all six potassium ions are visible (large white spheres).

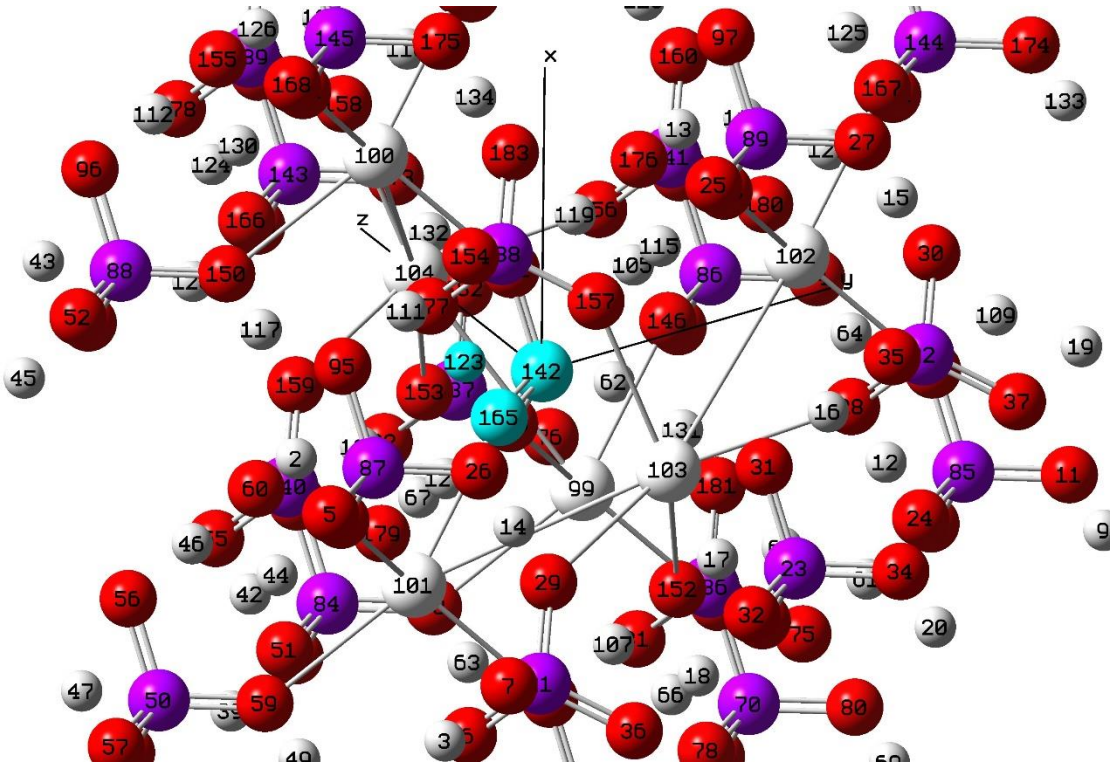

Figure 6.4. The central phosphorus unit located next to the oxygen vacancy. The teal atoms are the central phosphorus atom P142, a nearby oxygen O165, and its associated hydrogen H123. The hydrogen on the other side of the oxygen vacancy is H131, located up along the y-axis.

Table 6.3. Fermi contact terms and the central phosphorus anisotropic values for the oxygen vacancy simulation with 184 atoms.

Atom	Fermi value (Gauss)	Anisotropic values (Gauss)
Phosphorus(142)	324.74	-60.48 -54.81 115.29
Oxygen(165)	18.28	
Oxygen(161)	-8.85	
Oxygen(169)	-22.90	
Hydrogen(123)	1.98	
Hydrogen(131)	23.39	

Since only the phosphorus hyperfine value was measured during the EPR experiment for the oxygen vacancy defects, combining the hyperfine values for the other atoms was not the focus of this research; therefore, only the phosphorus anisotropic values are combined in this chapter. Combined with the Fermi term, the hyperfine value for c-axis EPR spectra is around 450 Gauss, which is lower than the lowest measured EPR value at 552 Gauss. The Fermi contact values are listed for nearby atoms to get an idea of where the defect is localized, with respect to the central phosphorus atom. The results in Table 6.3 show the excess spin density located on a region spanned by the oxygen vacancy, including its associated hydrogen atom. This asymmetric placement (versus equal sharing of the defect, as was done in the self-trapped hole) of the oxygen vacancy defect matches expectations set by previous research [20]. The hyperfine splitting value is not quite as high as seen in the EPR experiment, although, it is on the same order of magnitude.

6.2.1.1 Oxygen and Hydrogen Vacancy

Larger hyperfine results are seen after removing the nearby hydrogen and after conducting the geometry optimization. The optimization was conducted after removing the nearby hydrogen atom, as seen in Figure 6.5, which indicates the vacancy located to the right side of the central phosphorus atom. Both vacancies are indicated by circles made of dashed black lines. The three remaining oxygen atoms of the PO_4 unit were allowed to move during the optimization. The Fermi contact values were increased with the removal of the nearby hydrogen atom, as seen in Table 6.4, bringing the Fermi contact term for the phosphorus ion up to 587 Gauss and anisotropic values to –72.983, –67.593, and 140.576

Gauss before the geometry optimization and up to 602.63 Gauss and –77.398, –69.288, 146.686 Gauss after the geometry optimization.

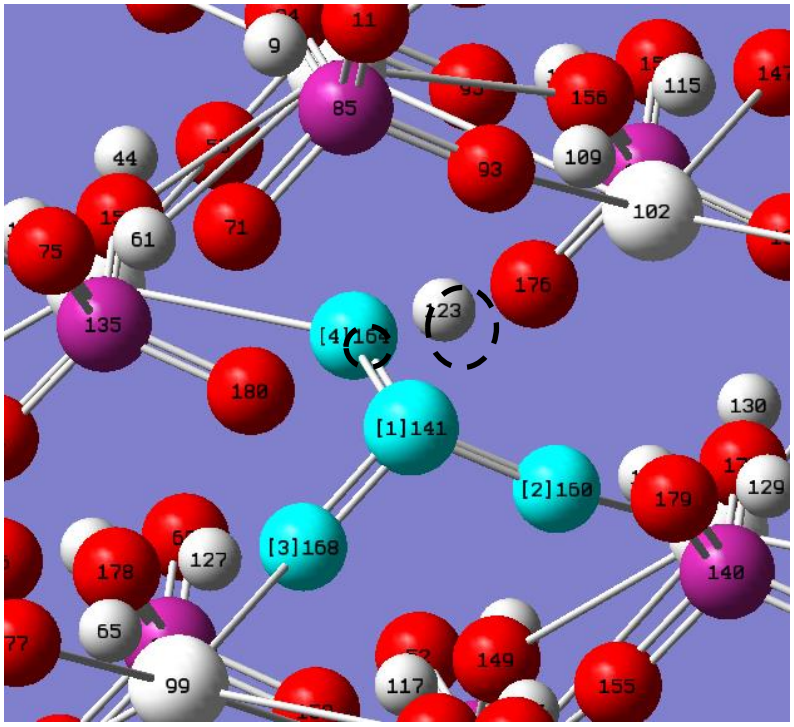

Figure 6.5. The central unit, P141, O164, O160, and O168 is highlighted in teal with a missing oxygen and its missing respective hydrogen. This is the structure after optimization. The atoms in the central unit were allowed to move during the optimization.

Table 6.4. Fermi contact and anisotropic values after conducting the oxygen vacancy simulation with its associated hydrogen atom removed.

Atom	Fermi value (before opt)	Anisotropic value (before opt)	Fermi value (after opt)	Anisotropic value (after opt)
Phosphorus	587.66	-72.98 -67.59 140.59	602.63	-77.40 -69.29 146.69
Oxygen(160)	-14.68		-9.92	
Oxygen(164)	-21.72		-19.18	
Oxygen(168)	-22.46		-19.06	

These values are an improvement over the simulations described previously, in which the crystal had only the oxygen vacancy, because they were in better agreement with the range of phosphorus hyperfine splitting values measured by EPR experiment, which ranged between 552 to 757 Gauss [20]. These encouraging results from the UHF simulations led to the focus on the oxygen and hydrogen vacancy simulations described in Section 6.2.2, utilizing the ωB97XD and 6-31+G(d) method and basis set.

6.2.1.2 Oxygen and Potassium Vacancy

Since there are six potassium ions around the central $(PO_3)^{2-}$ unit, it is reasonable to surmise that the results from these simulations could match the five EPR values measured by Garces *et al.*, which varied between 552 and 757 Gauss [20]. Table 6.5 lists isotropic and anisotropic values for these six simulations, before and after optimization, using UHF/6-31G theory and basis set. The highest hyperfine values are associated with vacancy number four which has a potassium vacancy along the y-axis. Job number four calculated a Fermi value of 415.05 Gauss and anisotropic values -71.10, -63.145, and 134.240 Gauss before optimization and a Fermi value of 416.79 Gauss and anisotropic values -71.10, -63.15, and 134.24 Gauss after optimization. The second highest hyperfine values are for job number five which had a potassium cation vacancy along the z-axis. Its hyperfine values are 391.73 Gauss before optimization and 382.42 Gauss after optimization. Job number five's hyperfine values are the only values that decreased after optimization, as seen at the bottom of Table 6.5.

Table 6.5. Isotropic and anisotropic hyperfine values, before and after optimization, for the oxygen vacancy plus six different potassium cation vacancies, using UHF/6-31G.

Atoms	Isotropic values (Gauss) (before opt)	Isotropic values (Gauss) (after opt)	Anisotropic values (Gauss) (before opt)	Anisotropic values (Gauss) (after opt)
Job 1				
P141	333.086	347.14	-62.13	-68.59
			-53.44	-56.06
			115.57	124.64
H130		-32.64		
O164		-16.70		
O168		-23.17		
O160		-7.74		
Job 2				
P141	208.856	239.44	-60.65	-66.87
			-45.68	-51.67
			106.33	118.54
H130		-20.48		
O164		-16.61		
O168		-20.01		
O160		-4.96		
Job 3				
P141	256.24	300.16	-55.35	-62.30
			-51.03	-57.29
			106.38	119.59
H130		-21.90		
O164		-18.54		
O168		-20.96		
O160		-6.79		
Job 4				
P141	415.05	416.79	-71.10	-71.10
			-63.15	-63.15
			134.24	134.24
H130		-20.32381		
O164		-17.37343		
O168		-22.10241		
O160		-7.17229		

Job 5				
P141	391.73	382.42	-61.66	-67.47
			-58.80	-61.49
			120.46	128.96
H130		-20.68		
O164		-17.98		
O168		-20.34		
O160		-7.87		
Job 6				
P141	-231.62	289.19	-59.47	-67.87
			-44.74	-50.84
			104.22	118.71
H130		-18.56		
O164		-15.77		
O168		-22.24		
O160		-6.44		

6.2.2 Oxygen Vacancy using ωB97XD/6-31+G(d)

Preliminary oxygen vacancy simulations were conducted using the ωB97XD and 6-31+G(d) method and basis set. Unlike the self-trapped hole, the oxygen vacancy simulations described in this chapter go immediately from the UHF method (described in Section 6.2.1) to the range-separated DFT method (in this section). The focus for these simulations was on the oxygen vacancy, with no additional vacancies, and the oxygen plus hydrogen vacancy. The hyperfine spectra for the phosphorus was simulated using EasySpin. This research sets the stage for ongoing and future research to generate a combined spectra for all five oxygen vacancy defects and to specifically identify what is causing the five different hyperfine splittings.

6.2.2.1 Oxygen Vacancy Simulations: Allowing Three Oxygen Ions to Move

The two oxygen vacancy simulations described in this section utilized guess=fragment=2, setting the central PO_3H_4 cluster as the second fragment and the rest of

the cluster as the first fragment. Utilizing GaussView, Figure 6.6 was created after hiding the atoms that make up the first fragment of the cluster, while making the atoms that make up the second fragment of the cluster visible.

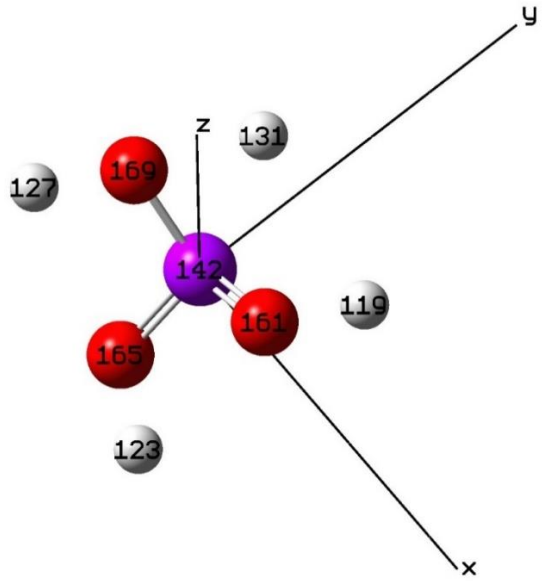

Figure 6.6. The central fragment for the oxygen vacancy simulations using fragments.

Table 6.6. Oxygen vacancy results using the method and basis set ωB97XD/6-31+G(d). These results may be correlated by referring to the numbering of the atoms seen in the previous figure. H131 is the hydrogen atom nearest to the oxygen vacancy.

Atom	Fermi contact (Gauss)	Anisotropic value (Gauss)	Directional cosines
Phosphorus(142)	321.27	-43.25	0.86 0.51 -0.03
		-41.86	-0.26 0.48 0.84
		85.12	-0.44 0.71 -0.55
Oxygen(165)	-10.69		
Oxygen(161)	-5.41		
Oxygen(169)	-15.31		
Hydrogen(123)	-0.36		
Hydrogen(131)	-4.39		

Referencing Table 6.3 and 6.6, the isotropic and anisotropic hyperfine values for P142 seem to be on the same order of magnitude as the UHF simulation described in the previous section. The other atoms of interest however have lower values, in particular for the hydrogen atoms: H131 has approximately –4 Gauss for the DFT simulation versus –23 Gauss for the UHF simulation. These results using the DFT method are an improvement over the UHF method. Hyperfine values were not measured during the experiment for the remaining oxygen ions associated with the oxygen vacancy, but the relative placement and anti-symmetry of the hyperfine values agrees with the assessment in the prior publication, which assumed that the excess spin density assigns itself to one oxygen and hydrogen pair more so than the other oxygen and hydrogen atoms [20]. As shown in Table 6.7, the three oxygen ions surrounding the central phosphorus moved away from the central phosphorus, by about a hundredth of an Angstrom. This is not a significant change in geometry, and this negligible change may be attributed to the fact that the remaining there oxygen ions have strong covalent bonds with the phosphorus.

Table 6.7. Distances between the central phosphorus and its remaining three oxygen ions, before and after optimization, for the oxygen vacancy job.

Atom Pair	Distance before optimization	Distance after optimization
P142-O161	1.53585	1.54173
P142-O165	1.53585	1.54487
P142-O169	1.53585	1.54797

The 185-atom cluster was then used in Gaussian to simulation an oxygen vacancy combined with a hydrogen atom vacancy. This particular oxygen vacancy defect variant was the focus in this section, because it had the best hyperfine splitting values as compared

to the relatively lower oxygen plus potassium vacancy variants. The Fermi contact and anisotropic results are shown in Table 6.8 below. With the oxygen plus hydrogen vacancy, the central phosphorus is renumbered to be phosphorus 141. After optimization with ωB97XD/6-31+G(d), this oxygen vacancy simulation with the hydrogen vacancy increased the isotropic hyperfine value by approximately 100 Gauss, from 429.08 Gauss to 563.04 Gauss. This value is still at the lower end of the range of values measured by EPR, which were 552 to 757 Gauss [20]. These calculations are also lower than the values calculated in Table 6.4, which range from 587.66 Gauss to 602.63 Gauss.

Table 6.8. Oxygen vacancy and hydrogen vacancy using the ωB97XD/6-31+G(d) method and basis set. The units are in Gauss.

Atom	Fermi contact (before opt)	Fermi contact (after opt)	Aniso value (before opt)	Directional Cosines (Before opt)			Aniso value (after opt)	Directional Cosines (After opt)		
P141	429.08	563.04	-39.20	0.9141	0.3450	-0.2128	-57.21	0.2232	0.9745	0.0221
			-39.11	-0.0492	0.6155	0.7866	-55.73	0.7911	-0.1944	0.5800
			78.31	-0.4024	0.7086	-0.5796	112.94	-0.5695	0.1120	0.8140
O160	-12.10	-10.05								
O164	-13.81	-14.62								
O168	-16.66	-16.44								

However, the hyperfine values for the surrounding oxygen ions are higher in Table 6.4 than those in Table 6.8. Specifically, the Fermi contact values for O160, O164, and O168 were -10.05, -14.62, and -16.44 Gauss after optimization for the DFT job, and they were -9.92, -19.18, and -19.06 Gauss respectively for the UHF job.

6.2.2.2 Oxygen Vacancy Simulations: Allowing Four Oxygen Ions to Move

A second oxygen vacancy plus hydrogen vacancy simulation was conducted. This time “fragments” were not used, and the oxygen ion nearest the hydrogen vacancy was allowed to move during the geometry optimization. This caused the hyperfine values for the central phosphorus ion to increase relative to the previous optimization job, with the

results depicted in Table 6.9. The Fermi contact term went from 563 Gauss post-optimization, from Section 6.2.2.1, to 597 Gauss post-optimization in this section. The value for the unique principal anisotropic value also increased to 113.93 Gauss compared to 78 Gauss from Section 6.2.2.1. The hyperfine splitting was computationally simulated in EasySpin, as had been demonstrated in Chapter 4 for the self-trapped hole, and the two peaks are shown in Figure 6.7 for the oxygen plus hydrogen defect simulated in this section. Since the hyperfine splitting is so large, two separate plots were generated in order to zoom in on each peak. The splitting between the two peaks is approximately 60.25 mT or 602.5 Gauss. This is compared to experiment in Table 6.10.

Table 6.9. Fermi contact values and anisotropic values of the oxygen vacancy plus hydrogen vacancy after geometry optimization, allowing four of the surrounding oxygen ions to move.

Atom	Fermi contact (before opt)	Fermi contact (after opt)	Aniso value (before opt)	Directional Cosines (Before opt)	Aniso value (after opt)	Directional Cosines (After opt)
P141	563.00	597.04	-57.21	0.7692 0.5986 0.2237	-57.714	0.7550 0.6314 0.1770
			-55.73	-0.5046 0.3541 0.7874	-56.211	-0.4871 0.3593 0.7960
			112.94	-0.3921 0.7185 -0.5745	113.925	-0.4391 0.6872 -0.5788
O160	-10.05	-9.41				
O164	-14.62	-15.16				
O168	-16.44	-15.38				
O180	-3.01	-3.44				

Table 6.10. Comparison between the computed value for the hydrogen plus oxygen vacancy and the range of hyperfine values measured by EPR experiment.

Ion	Computed [Gauss]	EPR Experiment [Gauss] [20] B‖c
P141	602.5	Five values ranging from 552 to 757

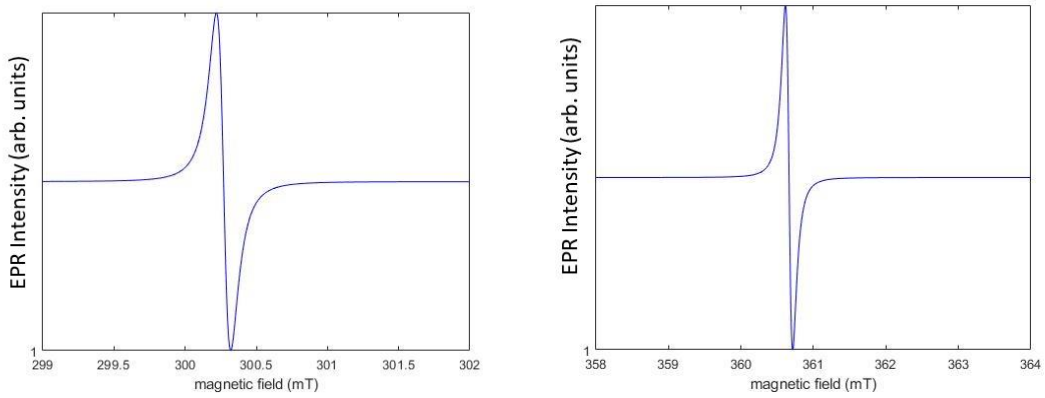

Figure 6.7. Hyperfine splitting for the oxygen plus hydrogen vacancy after geometry optimization, using the values listed in Table 6.9. This splitting is approximately 602.5 Gauss and is broken into two resolved plots, in order to show the definition of the peaks (the full splitting on one plot would not fit properly on this page).

The relative distances between P141 and the four oxygen ions that were allowed to move are shown in Table 6.11, and an image of the cluster after geometry optimization is seen in Figure 6.8, with the ions of interest highlighted in yellow.

Table 6.11. Distances between the central phosphorus, its remaining three oxygen ions, and O180 before and after optimization, for the oxygen plus hydrogen vacancy job.

Atom Pair	Distance before optimization	Distance after optimization
P141-O160	1.53585	1.57079
P141-O164	1.53585	1.56728
P141-O168	1.53585	1.55092
P141-O180	3.40272	3.37709

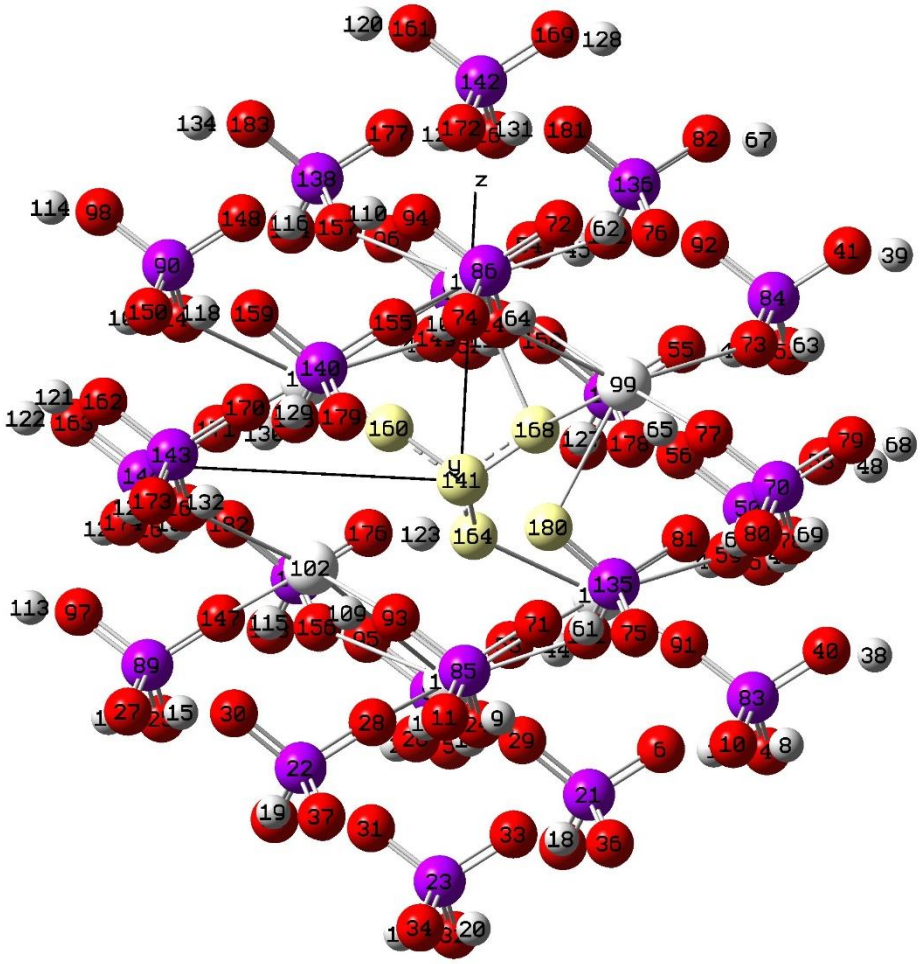

Figure 6.8. Oxygen plus hydrogen vacancy, with P141, O160, O164, O168, and O180 highlighted in yellow post geometry optimization. The hydrogen vacancy is between O180 and O164.

After geometry optimization (corresponding to the hyperfine splitting seen in Table 6.10 and Figure 6.7), the three oxygen ions that make up the remainder of the PO_3 unit moved only slightly farther away from the central phosphorus, while the oxygen ion that was on the other side of the hydrogen vacancy on a neighboring PO_4 unit moved slightly closer to the PO_3 unit with the vacancy, from 3.403 to 3.38 Angstroms.

VII. Summary

EPR provides insights into the location and nature of defects within a variety of materials, and there is a wealth of experimental data for point defects in nonlinear optical crystals like KDP. Utilizing the results from the EPR experiments on defects in KDP, a variety of Gaussian simulations were carried out for this dissertation in order to further understand and validate the experimental results that were obtained for this crystal. The present research will contribute to the on-going efforts of quantum chemists that conduct computational simulations with software such as Gaussian to better model defects in ever-more-complex materials.

In summary, the first part of this research examined a variety of quantum methods and basis sets in order to explore the best and most accurate options, based on the outputs from Gaussian runs. These theories and basis sets were selected based on their ability to achieve geometric localization of the self-trapped hole defect and provide quantitative estimation of the hyperfine values in agreement with experiment. It was found that methods that were progressively more complex tended to produce the more accurate results, and the more complex UMP2 method was a viable option once access to HPC resources was granted and parallel computing was possible. The work started where Chirila [22] had left off with the 41-atom tetragonal cluster, which had indicated that Gaussian could replicate the EPR results and place the self-trapped hole on two oxygen atoms and their respective hydrogen atoms. An orthorhombic unit cell of KDP was created in order to more accurately model the self-trapped hole defect, as it is only stable in the low-temperature orthorhombic phase. The results of most of the simulations (for a variety of methods and basis sets)

demonstrated the self-trapped hole localizing on two oxygen atoms and their adjoining hydrogen atoms.

There were a few interesting observations made after the 41-atom cluster runs were completed. First, the hole was localized on the oxygen-hydrogen atom pairs that had the hydrogen atoms further away from their respective oxygen atoms. Second, the angle between the two oxygen atoms and the central phosphorus atom became smaller, thus demonstrating the mechanism of lattice relaxation leading to the "self-trapping" of a hole. Third, the two oxygen atoms and the nearest potassium ion moved further away from the adjacent central phosphorus atom. After exploring two methods for combining the isotropic and anisotropic hyperfine values, the EasySpin method was chosen going forward. EasySpin successfully simulated EPR hyperfine spectra using output from Gaussian such that it could be directly compared to data from EPR experiment.

This post-optimization, geometric configuration from the 41-atom cluster was utilized for the larger orthorhombic clusters which incorporated the potassium ions. This meant that the angle between the two oxygen atoms and the phosphorus was carried into the large clusters, and the existence of this enhanced potential well was important for localizing the hole for the large cluster. Second, it was shown to be important to move the nearest potassium ion slightly away from the self-trapped hole region. This was one of the more crucial elements to having a successful simulation for the large clusters. The hyperfine values were found to be fairly consistent with the EPR experiments, and the method and basis set ωB97XD/6-31+G(d) were used towards the end of the self-trapped hole research. The 47-atom cluster was used to explore the optimal distance between the phosphorus ion and its nearest potassium, as well.

In-depth analysis of the 129-atom cluster provided insight into the distribution of the spin-density among the atomic and molecular orbitals. Inspection of the isotropic and anisotropic values of the phosphorus ion and comparison to previously published data, indicated that approximately 0.9% of the spin density from the self-trapped hole was situated in the phosphorus's *3s* orbital. A similar inspection was conducted for the two oxygen ions with the self-trapped hole, placing the spin density on the $2p_z$ orbital, which was further validated by inspecting spin density graphics generated using GaussView. The theory that exchange core polarization was occurring between the orbitals was validated by inspecting the signs (whether positive or negative) of the hyperfine values of the atoms that had the self-trapped hole spin distributed within their orbitals.

Molecular orbitals and a visualization of the electron density from the spin SCF density were used in GaussView in order to visually inspect the physical ways in which the defects were localizing and what the shapes of their orbitals might look like, according to how they were distributed within the cluster. Most of the focus was on the self-trapped hole, and the self-trapped hole consistently was aligned outwards from the central PO_4 unit, usually outwards along the "z-axis" depending on how Gaussian had defined the coordinate system. This had been problematic when the nearest potassium ion was present and also located along the z-axis. Eliminating the nearby potassium ion and moving the nearest potassium ion away from the self-trapped hole region along the z-axis enforced this idea, when altering the geometry in this way caused the hyperfine values to properly localize in response.

Preliminary work was done on the hydrogen and oxygen vacancy, and the oxygen vacancy combined with the vacancy of nearby potassium or hydrogen ions. These vacancy

simulations started off by utilizing small methods and basis sets in order to validate previous research and also to assess the viability of a given geometry. The hydrogen vacancy was successful in generating hyperfine values that were on the same order as EPR experiment. A variety of oxygen vacancy simulations were completed for large tetragonal clusters. These simulations used UHF before parallel computing was utilized and used UMP2 and ωB97XD/6-31+G(d) after parallel computing was available. Each of the oxygen vacancy simulations produced encouraging hyperfine values and defect localization that compared favorably with the EPR experiments.

Appendix A

A.1 DFT Comparisons

Table A.1. Results that compare the hole localization abilities of UHF, UMP2, and DFT.

41-atoms (orthorhombic) UMP2/631++G				
	before opt P-O dist	before opt O-H dist		Fermi values (after opt)
O(1)	1.57864	1.05980 (H(4))		0.34957
O(36)	1.57864	1.05980 (H13))		0.34957
O(29)	1.51189	1.44359 (H(21))		-31.9317
O(39)	1.51189	1.44359 (H(32))		-31.9317
			H(4)	0.19232
			H(13)	0.19232
			H(21)	-1.42217
			H(32)	-1.42217
			P(30)	35.82866

41-atoms (orthorhombic) UHF/6-31++G(d,p)				
	before opt P-O dist	before opt O-H dist		Fermi values (after opt)
O(1)	1.57864	1.05980 (H(4))		1.51847
O(36)	1.57864	1.05980 (H13))		1.71044
O(29)	1.51189	1.44359 (H(21))		-27.7596
O(39)	1.51189	1.44359 (H(32))		-27.6504
			H(4)	0.31283
			H(13)	0.2776
			H(21)	-1.01215
			H(32)	-0.83763
			P(30)	-87.1958

Inputs: nosymmetry and broken symmetry (Quadratic convergence, and stability run first before optimization) UHF/6-31++G(d,p)				
	before opt P-O dist	before opt O-H dist		Fermi values (after opt)
O(1)	1.57864	1.05980 (H(4))		-0.68206
O(36)	1.57864	1.05980 (H13))		1.09232
O(29)	1.51189	1.44359 (H(21))		-3.31442
O(39)	1.51189	1.44359 (H(32))		-36.0299
			H(4)	0.12692
			H(13)	-0.33131
			H(21)	-0.42285
			H(32)	-0.29919
			P(30)	-36.0299

Inputs: nosymmetry and broken symmetry , DFT (Stability run first before optimization) UB3LYP/6-31++G(d,p) (DFT)				
	before opt P-O dist	before opt O-H dist		Fermi values (after opt)
O(1)	1.57864	1.05980 (H(4))		-2.69801
O(36)	1.57864	1.05980 (H13))		-2.69799
O(29)	1.51189	1.44359 (H(21))		-10.2035
O(39)	1.51189	1.44359 (H(32))		-10.2035
			H(4)	-1.26565
			H(13)	-1.26565
			H(21)	-1.12956
			H(32)	-1.12956
			P(30)	-33.2442

Table A.2. Additional results for the DFT method UB3LYP/6-31++G(d,p) that show the delocalization of the hole, including the anisotropic value output.

Atom	Isotropic (Gauss)	Anisotropic (Gauss units)
H(21)	-1.42692	-3.198, -3.095, 6.293
H(4) and H(13)	-2.30038	-3.195, -2.614, 5.810
P(30)	-31.84743	-3.092, 1.416, 1.675

A.2 ONIOM Results

A job was attempted by specifying "ONIOM(ωB97XD/N07D:UHF/6-31+G(d))" in the input file. The secondary layer incorporated UHF instead of UFF in an attempt to have more accurate results. All nine of the central atoms were designated as high layer atoms, and they were unfrozen. One of the features of ONIOM is to automatically cap dangling bonds with hydrogen ions, but this is something that is not needed for the present situation, because hydrogen ions are already next to all of the oxygen ions. KDP is an unusual oxide compared to other crystals, in that each oxygen on one PO_4 unit has a hydrogen that links it to an oxygen on a neighboring PO_4 unit. Thus, the outer units do not require any dangling bonds to be capped by additional hydrogen ions. A variety of tests were conducted that attempted to avoid having the central PO_4 unit capped by additional hydrogen atoms while at the same time including all four hydrogen atoms in the hyperfine analysis Gaussian automatically made two of the atoms "link atoms" and instead of O26 and O38, included H26 and H38 in the hyperfine output. This additionally distorted the location of the hole. Therefore, various attempts were made to circumvent this automatic link creation process, because only the hyperfine values from the nine atoms of interest were needed. The output file specifically stated that: "Atom O26 in layer R is bonded to H21 in layer M and was made a link atom replaced by H. Atom O38 in layer R is bonded to H32 in layer M and was made a link atom replaced by H."

Table A.3 presents results from an ONIOM(ωB97XD/N07D:UHF/6-31++G(d,p)) simulation. A simulation using ONOIM(ωB97XD/N07D:UHF/6-31+G(d)) had failed to converge. Compared to the single point energy calculation, the results below show a much

higher ratio of hyperfine values for the hydrogen oxygen pairs with the self-trapped hole compared to the hydrogen oxygen pairs without the self-trapped hole.

Table A.3. The Fermi contact and Anisotropic results for the ONIOM(ωB97XD/N07D: UHF/6-31++G(d,p)) simulation. Each atom in the central PO_4 unit along with two outer hydrogen ions were placed in the high level, and the two hydrogen ions with the hole were placed at the low level linked to the high level. The two oxygen ions that shared the hole were allowed to move during the optimization.

High layer, **Low layer**	**Atom**	**Fermi (Gauss)**	**Aniso (Gauss)**	**Anisotropic Directional Cosines**	**Total Hyperfine**
ωB97XD/N07D, UHF/6-31++G(d,p)	H4, H13 (high level, frozen)	-0.04695	-1.828 -0.200 2.027	-0.3025 -0.6260 0.7188 0.9252 -0.0113 0.3794 -0.2293 0.7798 0.5825	0.6072
	H21, H32 (low level linked to high level)	-37.57419	-5.613 -4.133 9.745	-0.5263 0.3622 0.7693 0.6606 -0.3955 0.6381 0.5354 0.8440 -0.0311	28.6342
	O1, O36 (high level, frozen)	1.93857	2.509 1.463 -3.972	0.4407 0.4860 0.7547 -0.4891 0.8350 -0.2521 0.7527 0.2580 -0.6057	
	O29, O39 (high level, unfrozen)	-31.52009	35.230 25.698 -60.929	-0.6314 0.2853 0.7211 0.4248 0.9052 0.0139 0.6487 -0.3151 0.6927	
	P30 (high level, frozen)	-128.47504	-18.410 8.094 10.316	0.0000 0.0000 1.0000 -0.2191 0.9757 0.0000 0.9757 0.2191 0.0000	36.0387

A similar run was conducted in which the exact same methods and basis sets were used as before, except the high and low-level atoms of interest were reversed for the four hydrogen

atoms. This meant that the H4, H13 ions were assigned at the low level, linked to high level, and the H21, H32 ions were at the high level. However, this run was not successful.

The success of the small 41-atom cluster using ONIOM motivated attempts to use ONOIM for a larger cluster with 182 atoms which included ten potassium ions. There were difficulties in setting the atoms in the central PO_4 unit as the high layer and the remainder of the cluster as the low layer, because Gaussian would cancel the simulation due to the bonds that it established between the potassium ions and the central unit. As mentioned, Gaussian will attempt to assign link atoms between the high-level and low-level atoms, and since Gaussian assigns bonds between the potassium ions and the central unit, it was becoming overwhelmed with the task of distributing link atoms between these groups. One work-around to this issue is to simply use "geom=connectivity" along with a manual assignment of bonds in the connectivity table in the input file. This way, Gaussian will not automatically assign bonds between the potassium ions and the central PO_4 unit.

Appendix B

B.1 MATLAB Eigenvalue Calculations from Gaussian Hyperfine Results

The EPR measurements that were taken by Stevens *et al.* were along the z-direction [20], and therefore the isotropic and anisotropic values computed by Gaussian need to be visualized as the crystal is rotated on its axes, with respect to the magnetic field axes, to estimate what the splitting is for a measurement taken along the co-aligned crystal and magnetic field z-axis. For the self-trapped hole results, anisotropic directional cosines that were calculated by Gaussian for the phosphorus atom for Bcc were calculated to be along directional cosines 0, 0, 1, and no further computation is needed. However, the Bcc vector of the hydrogen atom with the hole is along directional cosines 0.5404, 0.8391, and -0.0623 for alpha, beta, and gamma respectively; this is more ambiguous and requires further investigation as to how the dipole is oriented with respect to the magnetic field in the z-direction.

B.1.1 Axes Angles and Orientation

The post-analysis of the Gaussian results begins by assigning the spin-Hamiltonian parameters variables P1-P7, which represents the g-value and six **A** matrix values. Three of the values are principal values, adding together the Fermi contact term and each of the three anisotropic components, Baa, Bbb, and Bcc. The variables P5-P7 are the three Euler angles calculated from the directional cosines of the anisotropic hyperfine parameters and converted from degrees to radians. The principal axes of the $\boldsymbol{A}$ matrix uses the coordinates x_1, y_1, z_1 for a particular dipole, the crystal axes uses the coordinates x_c, y_c, z_c, and the magnetic field system for a magnetic field parallel to the z-axis uses the coordinates x, y, z.

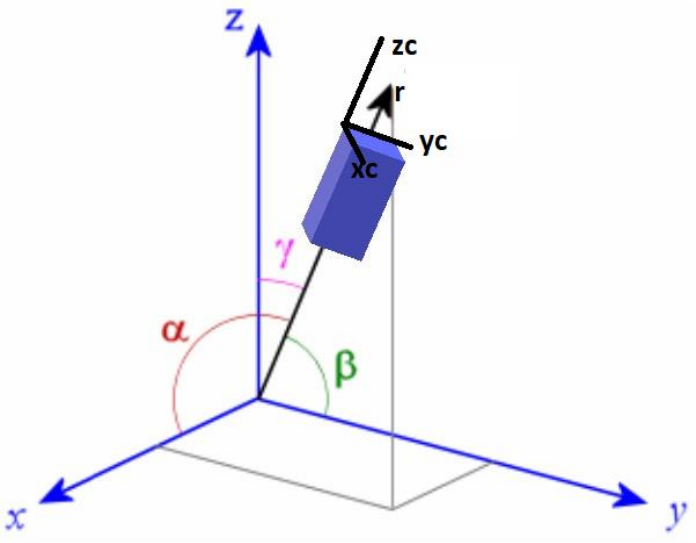

Figure B.1. The orientation of the crystal coordinate system with respect to the magnetic field coordinate system. The dipole coordinate axes are hidden in the crystal.

The vector r can be represented in terms of the directional cosine angles α, β, γ or in terms of the two angles, θ, ϕ which are relative only to the z-axis.

$$\vec{r} = \sin\theta\cos\phi\,\vec{\imath} + \sin\theta\sin\phi\,\vec{\jmath} + \cos\theta\,\vec{k}, \qquad \textit{Eq. B.24}$$

$$\vec{r} = \cos\alpha\,\vec{\imath} + \cos\beta\,\vec{\jmath} + \cos\gamma\,\vec{k}, \qquad \textit{Eq. B.25}$$

The conversion between the angles is done in the following way:

$$\cos\alpha = \sin\theta\cos\phi, \quad \cos\beta = \sin\theta\sin\phi, \qquad \textit{Eq. B.26}$$

$$\sin\theta = \frac{\cos\alpha}{\cos\phi} = \frac{\cos\beta}{\sin\phi'}, \qquad \textit{Eq. B.27}$$

$$\frac{\sin\phi}{\cos\phi} = \frac{\cos\beta}{\cos\alpha} = \tan\phi, \qquad \textit{Eq. B.28}$$

$$\theta = \gamma, \qquad \textit{Eq. B.29}$$

Now each row of alpha, beta, and gamma for Baa, Bbb, and Bcc (a 3x3 set of values) can be represented as three rows of theta and phi for Baa, Bbb, and Bcc (a 2x3 set of values, $\theta_{aa}\phi_{aa}, \theta_{bb}\phi_{bb}, \theta_{cc}\phi_{cc}$). The last step is to convert the pairs of theta and phi into a 1x3 set of Euler angles (Θ, Φ, Γ). This is done in the following way:

$$\boldsymbol{\Theta = \theta_{cc}}, \qquad \textit{Eq. B.30}$$

$$\boldsymbol{\Phi = \phi_{cc} - 270\left(\frac{\pi}{180}\right)}, \qquad \textit{Eq. B.31}$$

$$\boldsymbol{\sin\Phi = \left(\frac{\cos\theta_{aa}}{\sin\theta_{cc}}\right)}, \qquad \textit{Eq. B.32}$$

$$\boldsymbol{\Gamma = \begin{cases} \operatorname{acos}\left(\frac{\cos\theta_{bb}}{\sin\theta_{cc}}\right), & \sin\psi \geq 0 \\ 2\pi - \operatorname{acos}\left(\frac{\cos\theta_{bb}}{\sin\theta_{cc}}\right), & \sin\psi < 0 \end{cases}} \qquad \textit{Eq. B.33}$$

It is important when following this process to ensure that the three pairs of theta and phi are orthogonal to one another before proceeding to calculate the Euler angles.

B.1.2 Rotation Operations

Expanding Equation 3.3 using the notation given above introduces a Hamiltonian of the form:

$$\boldsymbol{H = g\beta BS_z + I_{x_1}A_xS_{x_1} + I_{y_1}A_yS_{y_1} + I_{z_1}A_zS_{z_1}}, \qquad \textit{Eq. B.34}$$

The g-value is isotropic, and **A** has at least six values with an Euler angle corresponding per row to α, β, γ. For **S** and **I** both equal to spin ½, the Hamiltonian will be transformed into a four by four matrix, and then the eigenvalues will be calculated in order to estimate the energy as a function of position. The transformation begins with the crystal axes being related to the principal axes of the hyperfine matrix in the following way:

$$\begin{bmatrix} \boldsymbol{x_1} \\ \boldsymbol{y_1} \\ \boldsymbol{z_1} \end{bmatrix} = [\boldsymbol{H}] \begin{bmatrix} \boldsymbol{x_c} \\ \boldsymbol{y_c} \\ \boldsymbol{z_c} \end{bmatrix}, \qquad \textit{Eq. B.35}$$

The 3x3 matrix **H** incorporates the three Euler angles θ, ϕ, ψ, represented below as P5, P6, and P7 in order to correspond with the notation in the MATLAB code:

$$\boldsymbol{H} = \begin{bmatrix} \cos P7 \cos P6 - \cos P5 \sin P6 \sin P7 & \cos P7 \sin P6 + \cos P5 \cos P6 \sin P7 & \sin P7 \sin P5 \\ -\sin P7 \cos P6 - \cos P5 \sin P6 \cos P7 & -\sin P7 \cos P6 + \cos P5 \sin P6 \cos P7 & \cos P7 \sin P5 \\ \sin P5 \sin P6 & -\sin P5 \cos P6 & \cos P5 \end{bmatrix},$$

Eq. B.36

This matrix was created using the convention from Goldstein's book, Classical Mechanics [92], which rotates along z (matrix **D**), ξ (matrix **C**), and ξ' (matrix **B**), such that **H=BCD**, and refers to its second rotation as similar to a rotation along an equivalent system's x-axis. Hence, this rotation is said to be done in the x-convention. It can be related to the magnetic field axis system by the rotation matrix, **R**. A rotation from x to y is calculated as:

$$\boldsymbol{R} = \begin{bmatrix} \cos\alpha & -\sin\alpha \sin\beta & \sin\alpha \cos\beta \\ 0 & \cos\beta & \sin\beta \\ -\sin\alpha & -\cos\alpha \sin\beta & \cos\alpha \cos\beta \end{bmatrix} \qquad \textit{Eq.B.14}$$

With $\alpha = \frac{\pi}{180} * 90, \beta = \frac{\pi}{180} * (n-1), 1 < n < 91$. A rotation from y to z is calculated using the same matrix, but with $\alpha = 0, \beta = 90 * \frac{\pi}{180} - \frac{\pi}{180} * (n-1), 1 < n < 91$. Lastly, a rotation from z to x is calculated with $\alpha = \frac{\pi}{180} * (n-1), \beta = 0, 1 < n < 91$. The indices "n" are increments of degrees.

$$\begin{bmatrix} \boldsymbol{x_c} \\ \boldsymbol{y_c} \\ \boldsymbol{z_c} \end{bmatrix} = [\boldsymbol{R}] \begin{bmatrix} \boldsymbol{x} \\ \boldsymbol{y} \\ \boldsymbol{z} \end{bmatrix} \qquad \textit{Eq.B.15}$$

$$[\boldsymbol{TH}] = [\boldsymbol{H}][\boldsymbol{R}] \qquad \textit{Eq.B.16}$$

$$\begin{bmatrix} \boldsymbol{x_1} \\ \boldsymbol{y_1} \\ \boldsymbol{z_1} \end{bmatrix} = [\boldsymbol{TH}] \begin{bmatrix} \boldsymbol{x} \\ \boldsymbol{y} \\ \boldsymbol{z} \end{bmatrix} \qquad \textit{Eq.B.17}$$

The I and S values in the hyperfine coordinate system can be written in terms of the magnetic field system as:

$$\boldsymbol{I_{x_1} = TH(1,1)I_x + TH(1,2)I_y + TH(1,3)I_z} \qquad \textit{Eq.B.18}$$

$$\boldsymbol{I_{y_1} = TH(2,1)I_x + TH(2,2)I_y + TH(2,3)I_z} \qquad \textit{Eq.B.19}$$

$$\boldsymbol{I_{z_1} = TH(3,1)I_x + TH(3,2)I_y + TH(3,3)I_z} \qquad \textit{Eq.B.20}$$

$$\boldsymbol{S_{x_1} = TH(1,1)S_x + TH(1,2)S_y + TH(1,3)S_z} \qquad \textit{Eq.B.21}$$

$$\boldsymbol{S_{y_1} = TH(2,1)S_x + TH(2,2)S_y + TH(2,3)S_z} \qquad \textit{Eq.B.22}$$

$$\boldsymbol{S_{z_1} = TH(3,1)S_x + TH(3,2)S_y + TH(3,3)S_z} \qquad \textit{Eq.B.23}$$

Equation B.11 is re-written as:

$$\begin{aligned} \boldsymbol{H = g\beta BS_z + A_x}\big[&\boldsymbol{TH(1,1)TH(1,1)I_xS_x + TH(1,1)TH(1,2)I_yS_x +} \\ &\boldsymbol{TH(1,1)TH(1,3)I_zS_x + TH(1,2)TH(1,1)I_xS_y + TH(1,2)TH(1,2)I_yS_y +} \\ &\boldsymbol{TH(1,3)TH(1,2)I_zS_y + TH(1,1)TH(1,3)I_xS_z + TH(1,2)TH(1,3)I_yS_z +} \\ &\boldsymbol{TH(1,3)TH(1,3)I_zS_z}\big] + \boldsymbol{A_y}\big[\boldsymbol{TH(2,1)TH(2,1)I_xS_x + TH(2,1)TH(2,2)I_yS_x +} \\ &\boldsymbol{TH(2,1)TH(2,3)I_zS_x + TH(2,2)TH(2,1)I_xS_y + TH(2,2)TH(2,2)I_yS_y +} \\ &\boldsymbol{TH(2,3)TH(2,2)I_zS_y + TH(2,1)TH(2,3)I_xS_z + TH(2,2)TH(2,3)I_yS_z +} \\ &\boldsymbol{TH(2,3)TH(2,3)I_zS_z}\big] + \boldsymbol{A_z}\big[\boldsymbol{TH(3,1)TH(3,1)I_xS_x + TH(3,1)TH(3,2)I_yS_x +} \\ &\boldsymbol{TH(3,1)TH(3,3)I_zS_x + TH(3,2)TH(3,1)I_xS_y + TH(3,2)TH(3,2)I_yS_y +} \\ &\boldsymbol{TH(3,3)TH(3,2)I_zS_y + TH(3,1)TH(3,3)I_xS_z + TH(3,2)TH(3,3)I_yS_z +} \\ &\boldsymbol{TH(3,3)TH(3,3)I_zS_z}\big] \end{aligned} \qquad \textit{Eq.B.24}$$

The A_x, A_y, A_z components can be grouped into six equations, **W1-W6**, that group respective pairs of **IS** according to their indices in the magnetic field axis system:

$$W1 = A_x TH(1,1)TH(1,1) + A_y TH(2,1)TH(2,1) + A_z TH(3,1)TH(3,1)$$ *Eq.B.25*

$$W2 = A_x TH(1,2)TH(1,1) + A_y TH(2,2)TH(2,1) + A_z TH(3,2)TH(3,1)$$ *Eq.B.26*

$$W3 = A_x TH(1,3)TH(1,1) + A_y TH(2,3)TH(2,1) + A_z TH(3,3)TH(3,1)$$ *Eq.B.27*

$$W4 = A_x TH(1,2)TH(1,2) + A_y TH(2,2)TH(2,2) + A_z TH(3,2)TH(3,2)$$ *Eq.B.28*

$$W5 = A_x TH(1,3)TH(1,2) + A_y TH(2,3)TH(2,2) + A_z TH(3,3)TH(3,2)$$ *Eq.B.29*

$$W6 = A_x TH(1,3)TH(1,3) + A_y TH(2,3)TH(2,3) + A_z TH(3,3)TH(3,3)$$ *Eq.B.30*

The spin Hamiltonian is re-written as:

$$H = g\beta BS_z + W1 I_x S_x + W2 I_y S_x + W3 I_z S_x + W2 I_x S_y + W4\, I_y S_y + W5 I_z S_y + W3 I_x S_z + W5 I_y S_z + W6 I_z S_z$$

Eq.B.31

Next, the operators along (x,y) may be replaced by the raising and lowering operators which are rewritten to be in terms of S_x, S_y, I_x, I_y:

$$S_+ = S_x + iS_y, \;\; S_- = S_x - iS_y$$ *Eq.B.32*

$$S_x = \frac{1}{2}(S_+ + S_-), \;\; S_y = \frac{1}{2i}(S_+ - S_-)$$ *Eq.B.33*

$$I_+ = I_x + iI_y, \;\; I_- = I_x - iI_y$$ *Eq.B.34*

$$I_x = \frac{1}{2}(I_+ + I_-), \;\; I_y = \frac{1}{2i}(I_+ - I_-)$$ *Eq.B.35*

To get the IS pairs, each configuration needs to be multiplied and expanded:

$$I_x S_x = \frac{1}{2}(I_+ + I_-) * \frac{1}{2}(S_+ + S_-) = \frac{1}{4}(I_+S_+ + I_+S_- + I_-S_+ + I_-S_-)$$ *Eq.B.36*

$$I_y S_x = \frac{1}{4i}(I_+S_+ + I_+S_- - I_-S_+ - I_-S_-)$$ *Eq.B.37*

$$I_x S_y = \frac{1}{4i}(I_+S_+ - I_+S_- + I_-S_+ - I_-S_-)$$ *Eq. B.38*

$$\boldsymbol{I_y S_y = \frac{-1}{4}(I_+ S_+ - I_+ S_- - I_- S_+ + I_- S_-)},$$ *Eq. B.39*

The operators along "z" commute with the raising and lowering operators and thus can remain in the form of I_z, S_z:

$$\boldsymbol{I_z S_x = \frac{1}{2}(I_z S_+ + I_z S_-)}$$ *Eq. B.40*

$$\boldsymbol{I_z S_y = \frac{-i}{2}(I_z S_+ - I_z S_-)}$$ *Eq. B.41*

$$\boldsymbol{I_x S_z = \frac{1}{2}(I_+ S_z + I_- S_z)}$$ *Eq. B.42*

$$\boldsymbol{I_y S_z = \frac{-i}{2}(I_+ S_z - I_- S_z)}$$ *Eq. B.43*

Replacing the **IS** pairs with the raising and lowering operators gives the Hamiltonian in the following form:

$$\begin{aligned}\boldsymbol{H = g\beta B S_z + W6 I_z S_z + \frac{1}{4}(W1 - iW2 - iW2 - W4) I_+ S_+} \\ \boldsymbol{+ \frac{1}{4}(W1 - iW2 + iW2 + W4) I_+ S_-} \\ \boldsymbol{+ \frac{1}{4}(W1 + iW2 - iW2 + W4) I_- S_+} \\ \boldsymbol{+ \frac{1}{4}(W1 + iW2 + iW2 - W4) I_- S_- + \frac{1}{2}(W3 - iW5) I_+ S_z} \\ \boldsymbol{+ \frac{1}{2}(W3 + iW5) I_- S_z + \frac{1}{2}(W3 - iW5) I_z S_+ + \frac{1}{2}(W3 + iW3) I_z S_-},\end{aligned}$$

Eq. B.44

The last set of simplifications are:

$$\boldsymbol{Q1 = \frac{1}{4}(W1 - W4) + \frac{i}{2} W2},$$ *Equation 37*

$$\boldsymbol{Q2 = \frac{1}{4}(W1 + W4)},$$ *Equation 38*

$$\boldsymbol{Q3 = \frac{1}{2}(W3 + iW5)}, \textit{ Equation 39}$$

$$\boldsymbol{H = g\beta BS_z + W6I_zS_z + Q1^*I_+S_+ + Q2I_+S_- + Q2I_-S_+ + Q1I_-S_- + Q3I_zS_+ + Q3I_zS_-},$$

Equation 40

The first two terms are along the diagonal of the four by four matrix, A(1,1), A(2,2), A(3,3), and A(4,4):

	|1/2,1/2>	|1/2,1/2>	|1/2,1/2>	|1/2,1/2>
|1/2,1/2>	A(1,1)			
|1/2,1/2>		A(2,2)		
|1/2,1/2>			A(3,3)	
|1/2,1/2>				A(4,4)

Each operator $S_z$and I_z acting on the kets $|m_s, m_I>$ being:

$$\boldsymbol{A(1,1) = \frac{1}{2}g\beta B + \frac{1}{4}W6,\ \ A(2,2) = \frac{1}{2}g\beta B - \frac{1}{4}W6}$$

$$\boldsymbol{A(3,3) = -\frac{1}{2}g\beta B - \frac{1}{4}W6,\ A(4,4) = -\frac{1}{2}g\beta B + \frac{1}{4}W6} \qquad \textit{Eq. 41}$$

	|1/2,1/2>	|1/2,1/2>	|1/2,1/2>	|1/2,1/2>
|1/2,1/2>	A(1,1)			
|1/2,1/2>	½ Q3	A(2,2)		
|1/2,1/2>	½ Q3	Q2	A(3,3)	

|1/2,1/2>	Q1	- ½ Q3	- ½ Q3	A(4,4)

B.2 MATLAB Code

The following is the MATLAB code that performs these calculations. It was written by Dr. Larry Halliburton and reprinted with permission.

B.2.1 Main Code

```
%                                   KDP_STH_ENDORlines

% This main program calculates ENDOR line positions as a function of
% angle, using a g value and a hyperfine matrix, for the self-trapped hole
% in KH2PO4 crystals.  The input A matrix is taken from Gaussian output.

% This program uses a subroutine named KDP_STH_energylevels.

clear all
clf reset

% Constants:

h = 6.62606957;                 % Planck's constant
B = 9.27400968/h;               % Bohr magneton divided by Planck's constant
gbn = 0.004257748;      % gn*bn for hydrogen
CTR = pi/180;                   % Conversion constant, degrees to radians
FREQQ = 9400;                   % Measured microwave frequency (in MHz)
HH = 3377;              % Magnetic field (in gauss)

% Spin-Hamiltonian parameters:
% One for the g matrix and six for the A matrix (three principal
% values and three Euler angles).

P(1) = 2.01;
P(2) = -5.895*2.8;      % P(2) trough P(7) values obtained
P(3) = -4.567*2.8;      % from Gaussian output for atom 21 (hydrogen).
P(4) = 6.196*2.8;
P(5) = 93.57*CTR;
```

```
P(6) = -212.78*CTR;
P(7) = 52.8659*CTR;

% H is the 3x3 rotation matrix which takes the principal
% axes of the A matrix into the crystal coordinate system.

% R is the 3x3 rotation matrix which takes the crystal coordinate
% system into the magnetic field coordinate system.

H(1,1) = cos(P(7))*cos(P(6)) - cos(P(5))*sin(P(6))*sin(P(7));
H(1,2) = cos(P(7))*sin(P(6)) + cos(P(5))*cos(P(6))*sin(P(7));
H(1,3) = sin(P(7))*sin(P(5));
H(2,1) = -sin(P(7))*cos(P(6)) - cos(P(5))*sin(P(6))*cos(P(7));
H(2,2) = -sin(P(7))*sin(P(6)) + cos(P(5))*cos(P(6))*cos(P(7));
H(2,3) = cos(P(7))*sin(P(5));
H(3,1) = sin(P(5))*sin(P(6));
H(3,2) = -sin(P(5))*cos(P(6));
H(3,3) = cos(P(5));

% Select a plane of rotation before running the program.

% Plane = 1 corresponds to rotation from x to y
% Plane = 2 corresponds to rotation from y to z
% Plane = 3 corresponds to rotation from z to x

% Enter the number below for the plane to be used.

Plane = 3;

if Plane==1            % Rotation from x to y.

for n=1:91             % Rotation increment is one degree.
   Alpha = 90*CTR;
   Beta = (n-1)*CTR;
   N(n) = n-1;

   R(1,1) = cos(Alpha);
   R(1,2) = -sin(Alpha)*sin(Beta);
   R(1,3) = sin(Alpha)*cos(Beta);
   R(2,1) = 0;
   R(2,2) = cos(Beta);
   R(2,3) = sin(Beta);
   R(3,1) = -sin(Alpha);
   R(3,2) = -cos(Alpha)*sin(Beta);
   R(3,3) = cos(Alpha)*cos(Beta);
```

```
   TH = H * R;

   EE = KDP_STH_energylevels(TH,HH,P,B,gbn);
      E(n,1) = EE(4)-EE(3);
      E(n,2) = EE(2)-EE(1);

end

elseif Plane==2        % Rotation from y to z.

for n=1:91             % Rotation increment is one degree.
   Alpha = 0*CTR;
   Beta = 90*CTR - (n-1)*CTR;
   N(n) = n-1;

   R(1,1) = cos(Alpha);
   R(1,2) = -sin(Alpha)*sin(Beta);
   R(1,3) = sin(Alpha)*cos(Beta);
   R(2,1) = 0;
   R(2,2) = cos(Beta);
   R(2,3) = sin(Beta);
   R(3,1) = -sin(Alpha);
   R(3,2) = -cos(Alpha)*sin(Beta);
   R(3,3) = cos(Alpha)*cos(Beta);

   TH = H * R;

   EE = KDP_STH_energylevels(TH,HH,P,B,gbn);
      E(n,1) = EE(4)-EE(3);
      E(n,2) = EE(2)-EE(1);

end

elseif Plane==3        % Rotation from z to x.

for n=1:91             % Rotation increment is one degree.
   Alpha = (n-1)*CTR;
   Beta = 0*CTR;
   N(n) = n-1;

   R(1,1) = cos(Alpha);
   R(1,2) = -sin(Alpha)*sin(Beta);
   R(1,3) = sin(Alpha)*cos(Beta);
   R(2,1) = 0;
```

```
   R(2,2) = cos(Beta);
   R(2,3) = sin(Beta);
   R(3,1) = -sin(Alpha);
   R(3,2) = -cos(Alpha)*sin(Beta);
   R(3,3) = cos(Alpha)*cos(Beta);

   TH = H * R;

   EE = KDP_STH_energylevels(TH,HH,P,B,gbn);
      E(n,1) = EE(4)-EE(3);
      E(n,2) = EE(2)-EE(1);

end

end

plot(N,E)
ylabel('ENDOR frequency (MHz)')
xlabel('Angle (degrees)')
```

B.2.2 Subroutine

```
%KDP_STH_energylevels
% This subroutine is used in conjunction with KDP_STH_linepositions.
% That main program determines the line positions as a function of
% angle for the self-trapped hole in KH2PO4 crystals.

% This subroutine calculates the eigenvalues and returns them to the
% main program.

function EE = KDP_STH_energylevels(TH,HH,P,B,gbn)

W1 = P(2)*TH(1,1)*TH(1,1)+P(3)*TH(2,1)*TH(2,1)+P(4)*TH(3,1)*TH(3,1);
W2 = P(2)*TH(1,1)*TH(1,2)+P(3)*TH(2,1)*TH(2,2)+P(4)*TH(3,1)*TH(3,2);
W3 = P(2)*TH(1,1)*TH(1,3)+P(3)*TH(2,1)*TH(2,3)+P(4)*TH(3,1)*TH(3,3);
W4 = P(2)*TH(1,2)*TH(1,2)+P(3)*TH(2,2)*TH(2,2)+P(4)*TH(3,2)*TH(3,2);
W5 = P(2)*TH(1,2)*TH(1,3)+P(3)*TH(2,2)*TH(2,3)+P(4)*TH(3,2)*TH(3,3);
W6 = P(2)*TH(1,3)*TH(1,3)+P(3)*TH(2,3)*TH(2,3)+P(4)*TH(3,3)*TH(3,3);

Q1 = 0.25*(W1-W4)+0.5*i*W2;
Q2 = 0.25*(W1+W4);
Q3 = 0.5*(W3+i*W5);

% Ham is the matrix representing the spin-Hamiltonian.
```

```
Ham = zeros(4);
Ham(1,1) = 0.5*P(1)*B*HH + 0.25*W6 - 0.5*gbn*HH;
Ham(2,2) = 0.5*P(1)*B*HH - 0.25*W6 + 0.5*gbn*HH;
Ham(3,3) = -0.5*P(1)*B*HH - 0.25*W6 - 0.5*gbn*HH;
Ham(4,4) = -0.5*P(1)*B*HH + 0.25*W6 + 0.5*gbn*HH;

Ham(2,1) = 0.5*Q3;
Ham(3,1) = 0.5*Q3;
Ham(3,2) = Q2;
Ham(4,1) = Q1;
Ham(4,2) = -0.5*Q3;
Ham(4,3) = -0.5*Q3;

Ham(1,2) = conj(Ham(2,1));
Ham(1,3) = conj(Ham(3,1));
Ham(2,3) = conj(Ham(3,2));
Ham(1,4) = conj(Ham(4,1));
Ham(2,4) = conj(Ham(4,2));
Ham(3,4) = conj(Ham(4,3));

EE = sort(real(eig(Ham)));
```

B.3 EasySpin Method to Generate Simulated Hyperfine Spectra

EasySpin is an open source software available for download and editing, and it runs in MATLAB. The user must provide spin parameter inputs “Sys.S” and “Sys.g”, nuclear specifications per atom such as “1H” for hydrogen, “17O” for oxygen, and “31P” for potassium, and inputs for the computationally generated hyperfine parameters for “Sys.A”. The method for combining the anisotropic values into a readable matrix format that is easily discernable by EasySpin is described in Chapter 4, Section 4.2.2, and simulated spectra are presented in Section 4.4.2 and Chapter 6 Section 6.2.2.2. Furthermore, the user must specify the conditions for the fictitious EPR conditions. The variable “Exp.mwFreq” is the microwave spectrometer frequency in units of GHz. In the example below, it is set to 9.4 GHz. The program also expects and input for the magnetic field range in

"Exp.Range", and this range will vary depending on the expected size of the hyperfine splitting, on a per-atom basis.

B.3.1 EasySpin MATLAB Code with Self-Trapped Hole Inputs

```
% testing EasySpin (EPR spectra of the self-trapped hole in KDP)
%============================================================

clear, clf

% Spin parameters
Sys.S = 1/2;
Sys.g = 2.0158;
Sys.lwpp = [0 0.1];    % units of mT

Sys.Nucs ='1H,1H,31P';
Sys.A = [[2.651 11.297 -0.211; 11.297 2.847 -1.405; -0.211 -1.405 -10.043]; [2.651 11.297 -
0.211; 11.297 2.847 -1.405; -0.211 -1.405 -10.043]; [-83.277 1.391 0; 1.391 -79.547 0; 0 0 -
87.394]];
Exp.Range = [328 338];

%Sys.Nucs = '1H';
%Sys.A = [2.651 11.297 -0.211; 11.297 2.847 -1.405; -0.211 -1.405 -10.043];
%Exp.Range = [332.7 333.5];

%Sys.Nucs ='31P';
%Sys.A = [-83.277 1.391 0; 1.391 -79.547 0; 0 0 -87.394];
%Exp.Range = [331 335];

%Sys.Nucs ='17O';
%Sys.A = [-79.893 51.722 -91.640; 51.722 12.985 40.682; -91.640 40.682 -34.077];
%Exp.Range = [300 360];

% Experimental parameters
Exp.mwFreq = 9.4;
Exp.CrystalSymmetry = 'Fdd2';

% Generate orientations in a single rotation plane
rotN = [1 0 0];  % rotation axis  (starts at c direction and goes to b direction)
N = 1;
[phi,theta] = rotplane(rotN,[0 pi],N);
chi = zeros(N,1);
Exp.CrystalOrientation = [phi(:) theta(:) chi];

% Simulate spectra
Opt.Output = 'separate';  % make sure spectra are not added up
Bres = resfields(Sys,Exp,Opt);
```

```
[B,spc] = pepper(Sys,Exp,Opt);
stackplot(B,spc);

% plotting
%plot(Bres,theta*180/pi);
xlabel('magnetic field (mT)');
ylabel('theta (°)');
```

Appendix C

C.1 Example Gaussian Input: 41-atom Self-Trapped Hole

```
%mem=5GB
#p density=current UMP2/6-31++G nosymm pop=full

ortho self trapped hole no opt

2 2
O      -1   -0.12415097   -1.25646485   -0.89861414
P      -1    3.08241621   -2.07716757   -1.68111914
H      -1    3.06496500   -4.07392108   -2.62327614
H      -1    0.75469833   -1.84871836   -0.89315114
H      -1    3.09986742   -0.08041406   -2.62327614
H      -1    5.41013409   -2.30561678   -0.89315114
O      -1    2.50237401   -0.95570940   -2.62873914
O      -1    3.66245840   -3.19862574   -2.62873914
O      -1    1.94716553   -2.66205439   -0.87183614
O      -1    4.21766689   -1.49228074   -0.87183614
P      -1   -3.08241621    2.07716757   -1.68111914
H      -1   -3.06496500    4.07392108   -2.62327614
H      -1   -0.75469833    1.84871836   -0.89315114
H      -1   -3.09986742    0.08041406   -2.62327614
H      -1   -5.41013409    2.30561678   -0.89315114
O      -1   -2.50237401    0.95570940   -2.62873914
O      -1   -3.66245840    3.19862574   -2.62873914
O      -1   -1.94716553    2.66205439   -0.87183614
O      -1   -4.21766689    1.49228074   -0.87183614
P      -1   -2.09563067   -3.06989363    1.77913086
H      -1   -2.07817946   -1.07314011    0.83697386
H      -1    0.23208721   -3.29834284    2.56709886
H      -1   -2.11308188   -5.06664714    0.83697386
H      -1   -4.42334855   -2.84144442    2.56709886
O      -1   -1.51558848   -4.19135180    0.83151086
O      -1   -2.67567287   -1.94843545    0.83151086
O      -1   -0.96037999   -2.48500680    2.58841386
O      -1   -3.23088135   -3.65478045    2.58841386
O      -1   -1.27107114    0.12355103    0.85828886
P      -1    0.00000000    0.00000000    0.04900586
P      -1    2.09563067    3.06989363    1.77913086
H      -1    2.07817946    1.07314011    0.83697386
H      -1   -0.23208721    3.29834284    2.56709886
H      -1    2.11308188    5.06664714    0.83697386
H      -1    4.42334855    2.84144442    2.56709886
O      -1    0.12415097    1.25646485   -0.89861414
```

O	-1	1.51558848	4.19135180	0.83151086
O	-1	2.67567287	1.94843545	0.83151086
O	-1	1.27107114	-0.12355103	0.85828886
O	-1	0.96037999	2.48500680	2.58841386
O	-1	3.23088135	3.65478045	2.58841386

C.2 Example Gaussian Input: 115-Atom Orthorhombic Cluster Self-Trapped Hole

```
%chk=115.chk
%mem=96GB
%CPU=0,1,2,3,4,5,6,7,8,9,10,11,12,13,14,15,16,17,18,19,20,21,22,23,24,25,26,27,28,29,30,31,3
2,33,34,35
%LindaWorkers=r16i6n11,
#p wb97xd/6-31+g(d) nosymm guess=fragment=2 iop(6/82=1,10/47=1)
scf=(xqc,maxconventionalcycles=150,maxcycles=300)

115 atom cluster

4 2 2 1 2 2
O(Fragment=2)  -1  -0.40240020  -1.21773255  -4.58796516
P(Fragment=1)  -1   2.54575070  -2.72352401  -5.36831023
H(Fragment=1)  -1   2.09044414  -4.67191323  -6.30183278
H(Fragment=2)  -1   0.32553620  -1.98794057  -4.58032689
H(Fragment=1)  -1   2.99848059  -0.78289167  -6.31908396
H(Fragment=1)  -1   4.76812018  -3.45262004  -4.58037240
O(Fragment=1)  -1   2.22390582  -1.50621872  -6.32051019
O(Fragment=1)  -1   2.86500397  -3.94863115  -6.31133245
O(Fragment=1)  -1   1.31112533  -3.04244094  -4.55601849
O(Fragment=1)  -1   3.78258934  -2.39794418  -4.56205120
P(Fragment=1)  -1  -2.56045329   2.67926297  -5.38356883
H(Fragment=1)  -1  -2.10772339   4.61989532  -6.33434255
H(Fragment=2)  -1  -0.33808381   1.95016695  -4.59563099
H(Fragment=1)  -1  -3.01575985   0.73087376  -6.31709137
H(Fragment=1)  -1  -4.78066778   3.41484642  -4.59558549
O(Fragment=1)  -1  -2.24120002   1.45415584  -6.32659104
O(Fragment=1)  -1  -2.88229816   3.89656826  -6.33576878
O(Fragment=1)  -1  -1.32361464   3.00484281  -4.57730980
O(Fragment=1)  -1  -3.79507865   2.36034605  -4.57127708
P(Fragment=1)  -1  -2.71929407  -2.54469415  -1.90156420
P(Fragment=1)  -1  -2.70983076  -2.51620558   5.01887070
K(Fragment=1)  -1  -2.71471619  -2.53091281   1.44619631
H(Fragment=2)  -1  -2.26656418  -0.60406180  -2.85233792
H(Fragment=1)  -1  -2.25710087  -0.57557323   4.06809697
H(Fragment=1)  -1  -0.49692459  -3.27379018  -1.11362636
H(Fragment=1)  -1  -0.48746128  -3.24530161   5.80680853
H(Fragment=1)  -1  -2.42540496  -5.82801893   0.62966671
H(Fragment=1)  -1  -7.53160894  -0.42523194   0.61440812
```

H(Fragment=1)	-1	-3.17460063	-4.49308337	-2.83508674
H(Fragment=1)	-1	-3.16513732	-4.46459480	4.08534815
H(Fragment=1)	-1	-4.93950857	-1.80911071	-1.11358086
H(Fragment=1)	-1	-4.93004526	-1.78062214	5.80685404
O(Fragment=1)	-1	-0.39293690	-1.18924398	2.33246973
O(Fragment=1)	-1	-2.40004080	-3.76980129	-2.84458641
O(Fragment=1)	-1	-2.39057749	-3.74131272	4.07584848
O(Fragment=1)	-1	-0.56124099	-6.44168968	-1.10596053
O(Fragment=1)	-1	-5.66744497	-1.03890269	-1.12121912
O(Fragment=1)	-1	-3.04113895	-1.32738886	-2.85376415
O(Fragment=1)	-1	-3.03167564	-1.29890029	4.06667074
O(Fragment=1)	-1	-1.48245543	-2.21911432	-1.09530517
O(Fragment=1)	-1	-1.47299212	-2.19062575	5.82512973
O(Fragment=1)	-1	-1.37593762	-4.83690010	0.64546680
O(Fragment=1)	-1	-4.05570558	-0.23158101	0.63017303
O(Fragment=1)	-1	-3.95391943	-2.86361108	-1.08927245
O(Fragment=1)	-1	-3.94445613	-2.83512251	5.83116244
P(Fragment=1)	-1	-0.16382625	-5.23896550	-0.16382618
P(Fragment=1)	-1	2.55521400	-2.69503545	1.55212466
K(Fragment=1)	-1	2.55032857	-2.70974267	-2.02054973
H(Fragment=1)	-1	0.16669542	-7.21189770	-1.09832226
H(Fragment=1)	-1	2.09990744	-4.64342466	0.61860211
H(Fragment=1)	-1	0.33499950	-1.95945200	2.34010800
H(Fragment=1)	-1	3.00794389	-0.75440310	0.60135093
H(Fragment=1)	-1	4.77758348	-3.42413147	2.34006249
H(Fragment=1)	-1	5.60004427	-2.13828186	-1.12663804
O(Fragment=1)	-1	0.23099687	-4.04404318	-1.11691399
O(Fragment=1)	-1	2.23336912	-1.47773016	0.59992471
O(Fragment=1)	-1	4.87210787	-1.36807384	-1.13427631
O(Fragment=1)	-1	2.87446727	-3.92014258	0.60910244
O(Fragment=1)	-1	1.05049840	-5.63436800	0.64543163
O(Fragment=1)	-1	1.32058864	-3.01395237	2.36441640
O(Fragment=1)	-1	6.48384725	-0.56075217	0.61711585
O(Fragment=1)	-1	3.79205264	-2.36945561	2.35838369
P(Fragment=1)	-1	-2.55098998	2.70775154	1.53686607
P(Fragment=1)	-1	-5.27003023	0.16382148	-0.17908477
K(Fragment=1)	-1	-2.55587541	2.69304432	-2.03580832
H(Fragment=1)	-1	-0.16977972	7.20261264	-1.15720073
H(Fragment=1)	-1	-2.09826009	4.64838389	0.58609234
H(Fragment=1)	-1	-0.32862050	1.97865552	2.32480390
H(Fragment=1)	-1	-3.00629654	0.75936233	0.60334352
H(Fragment=1)	-1	-4.77120448	3.44333499	2.32484940
H(Fragment=1)	-1	-5.60312857	2.12899681	-1.12888495
O(Fragment=1)	-1	-0.23409611	4.03471315	-1.14953490
O(Fragment=1)	-1	-2.23173671	1.48264441	0.59384385
O(Fragment=1)	-1	-4.87520711	1.35874381	-1.13217258
O(Fragment=1)	-1	-2.87283486	3.92505683	0.58466611
O(Fragment=2)	0	-1.08101110	0.34320139	-2.64599068
O(Fragment=1)	-1	-1.20763353	0.41554559	4.08389706

O(Fragment=1)	-1	-1.04879275	5.63950272	0.60189242
O(Fragment=1)	-1	-1.31415134	3.03333138	2.34312509
O(Fragment=1)	-1	-6.48214160	0.56588689	0.63020820
O(Fragment=1)	-1	-3.78561535	2.38883461	2.34915781
P(Fragment=2)	-1	-0.00498547	-0.01500838	-3.64583081
P(Fragment=1)	-1	0.00447784	0.01348019	3.27460409
P(Fragment=1)	-1	2.71405478	2.52892168	-1.92987997
P(Fragment=1)	-1	2.72351809	2.55741025	4.99055492
P(Fragment=1)	-1	0.16331862	5.23743732	-0.20740055
P(Fragment=1)	-1	5.26952260	-0.16534967	-0.19214195
K(Fragment=1)	0	0.00029282	0.00088150	0.21413288
K(Fragment=1)	-1	2.71863266	2.54270303	1.41788053
H(Fragment=2)	-1	2.25874822	0.58053246	-2.86340252
H(Fragment=1)	-1	2.26821153	0.60902103	4.05703238
H(Fragment=1)	-1	0.49384029	3.26450512	-1.14189663
H(Fragment=1)	-1	0.50330359	3.29299369	5.77853826
H(Fragment=1)	-1	2.42705231	5.83297816	0.57502774
H(Fragment=1)	-1	7.53325629	0.43019117	0.59028634
H(Fragment=1)	-1	3.16678468	4.46955403	-2.88065370
H(Fragment=1)	-1	3.17624798	4.49804260	4.03978119
H(Fragment=1)	-1	4.93642426	1.79982565	-1.14194214
H(Fragment=1)	-1	4.94588757	1.82831422	5.77849276
O(Fragment=2)	-1	0.38983766	1.17991395	-4.59891862
O(Fragment=1)	-1	0.39930096	1.20840252	2.32151627
O(Fragment=1)	-1	2.39220991	3.74622697	-2.88207993
O(Fragment=1)	-1	2.40167321	3.77471554	4.03835497
O(Fragment=1)	-1	0.55814174	6.43235964	-1.16048836
O(Fragment=1)	-1	5.66434573	1.02957265	-1.14522977
O(Fragment=1)	-1	3.03330805	1.30381454	-2.87290219
O(Fragment=1)	-1	3.04277136	1.33230311	4.04753270
O(Fragment=2)	0	1.07377457	-0.36498642	-2.64602190
O(Fragment=1)	-1	1.21880249	-0.38192231	4.08386189
O(Fragment=1)	-1	1.47942942	2.21000475	-1.11758823
O(Fragment=1)	-1	1.48889272	2.23849332	5.80284666
O(Fragment=1)	-1	1.37764327	4.84203482	0.60185726
O(Fragment=1)	-1	4.05741123	0.23671573	0.61715102
O(Fragment=1)	-1	3.95089343	2.85450151	-1.12362094
O(Fragment=1)	-1	3.96035673	2.88299008	5.79681395

--Link1--
%chk=115.chk
%mem=96GB
%CPU=0,1,2,3,4,5,6,7,8,9,10,11,12,13,14,15,16,17,18,19,20,21,22,23,24,25,26,27,28,29,30,31,32,33,34,35
%LindaWorkers=r16i6n11,

#p uwb97xd/6-31+g(d) nosymm guess=(read) Geom=AllCheckpoint Symmetry=None density=current pop=full prop=epr scf=(xqc,maxconventionalcycles=80,maxcycles=300)

After this job had completed, the resultant checkpoint file was then provided for the optimization job. The input file for the optimization job utilizes the same atom list as above, but the --Link1-- at the bottom of the input file is removed, and guess=fragment becomes guess=read. Last, the keyword “opt” is included. The results from the optimization are then used as the final results.

```
%chk=115.chk
%mem=96GB
%CPU=0,1,2,3,4,5,6,7,8,9,10,11,12,13,14,15,16,17,18,19,20,21,22,23,24,25,26,27,28,29,30,31,3
2,33,34,35
%LindaWorkers=r16i6n11,
#p opt wb97xd/6-31+g(d) nosymm guess=read iop(6/82=1,10/47=1)
scf=(xqc,maxconventionalcycles=150,maxcycles=300)

115 atom cluster

4 2 2 1 2 2
 O(Fragment=2)   -1   -0.40240020   -1.21773255   -4.58796516
 P(Fragment=1)   -1    2.54575070   -2.72352401   -5.36831023
 H(Fragment=1)   -1    2.09044414   -4.67191323   -6.30183278
 H(Fragment=2)   -1    0.32553620   -1.98794057   -4.58032689
 H(Fragment=1)   -1    2.99848059   -0.78289167   -6.31908396
 H(Fragment=1)   -1    4.76812018   -3.45262004   -4.58037240
 O(Fragment=1)   -1    2.22390582   -1.50621872   -6.32051019
 O(Fragment=1)   -1    2.86500397   -3.94863115   -6.31133245
 O(Fragment=1)   -1    1.31112533   -3.04244094   -4.55601849
 O(Fragment=1)   -1    3.78258934   -2.39794418   -4.56205120
 P(Fragment=1)   -1   -2.56045329    2.67926297   -5.38356883
 H(Fragment=1)   -1   -2.10772339    4.61989532   -6.33434255
 H(Fragment=2)   -1   -0.33808381    1.95016695   -4.59563099
 H(Fragment=1)   -1   -3.01575985    0.73087376   -6.31709137
 H(Fragment=1)   -1   -4.78066778    3.41484642   -4.59558549
 O(Fragment=1)   -1   -2.24120002    1.45415584   -6.32659104
 O(Fragment=1)   -1   -2.88229816    3.89656826   -6.33576878
 O(Fragment=1)   -1   -1.32361464    3.00484281   -4.57730980
 O(Fragment=1)   -1   -3.79507865    2.36034605   -4.57127708
 P(Fragment=1)   -1   -2.71929407   -2.54469415   -1.90156420
 P(Fragment=1)   -1   -2.70983076   -2.51620558    5.01887070
 K(Fragment=1)   -1   -2.71471619   -2.53091281    1.44619631
 H(Fragment=2)   -1   -2.26656418   -0.60406180   -2.85233792
 H(Fragment=1)   -1   -2.25710087   -0.57557323    4.06809697
 H(Fragment=1)   -1   -0.49692459   -3.27379018   -1.11362636
```

H(Fragment=1)	-1	-0.48746128	-3.24530161	5.80680853
H(Fragment=1)	-1	-2.42540496	-5.82801893	0.62966671
H(Fragment=1)	-1	-7.53160894	-0.42523194	0.61440812
H(Fragment=1)	-1	-3.17460063	-4.49308337	-2.83508674
H(Fragment=1)	-1	-3.16513732	-4.46459480	4.08534815
H(Fragment=1)	-1	-4.93950857	-1.80911071	-1.11358086
H(Fragment=1)	-1	-4.93004526	-1.78062214	5.80685404
O(Fragment=1)	-1	-0.39293690	-1.18924398	2.33246973
O(Fragment=1)	-1	-2.40004080	-3.76980129	-2.84458641
O(Fragment=1)	-1	-2.39057749	-3.74131272	4.07584848
O(Fragment=1)	-1	-0.56124099	-6.44168968	-1.10596053
O(Fragment=1)	-1	-5.66744497	-1.03890269	-1.12121912
O(Fragment=1)	-1	-3.04113895	-1.32738886	-2.85376415
O(Fragment=1)	-1	-3.03167564	-1.29890029	4.06667074
O(Fragment=1)	-1	-1.48245543	-2.21911432	-1.09530517
O(Fragment=1)	-1	-1.47299212	-2.19062575	5.82512973
O(Fragment=1)	-1	-1.37593762	-4.83690010	0.64546680
O(Fragment=1)	-1	-4.05570558	-0.23158101	0.63017303
O(Fragment=1)	-1	-3.95391943	-2.86361108	-1.08927245
O(Fragment=1)	-1	-3.94445613	-2.83512251	5.83116244
P(Fragment=1)	-1	-0.16382625	-5.23896550	-0.16382618
P(Fragment=1)	-1	2.55521400	-2.69503545	1.55212466
K(Fragment=1)	-1	2.55032857	-2.70974267	-2.02054973
H(Fragment=1)	-1	0.16669542	-7.21189770	-1.09832226
H(Fragment=1)	-1	2.09990744	-4.64342466	0.61860211
H(Fragment=1)	-1	0.33499950	-1.95945200	2.34010800
H(Fragment=1)	-1	3.00794389	-0.75440310	0.60135093
H(Fragment=1)	-1	4.77758348	-3.42413147	2.34006249
H(Fragment=1)	-1	5.60004427	-2.13828186	-1.12663804
O(Fragment=1)	-1	0.23099687	-4.04404318	-1.11691399
O(Fragment=1)	-1	2.23336912	-1.47773016	0.59992471
O(Fragment=1)	-1	4.87210787	-1.36807384	-1.13427631
O(Fragment=1)	-1	2.87446727	-3.92014258	0.60910244
O(Fragment=1)	-1	1.05049840	-5.63436800	0.64543163
O(Fragment=1)	-1	1.32058864	-3.01395237	2.36441640
O(Fragment=1)	-1	6.48384725	-0.56075217	0.61711585
O(Fragment=1)	-1	3.79205264	-2.36945561	2.35838369
P(Fragment=1)	-1	-2.55098998	2.70775154	1.53686607
P(Fragment=1)	-1	-5.27003023	0.16382148	-0.17908477
K(Fragment=1)	-1	-2.55587541	2.69304432	-2.03580832
H(Fragment=1)	-1	-0.16977972	7.20261264	-1.15720073
H(Fragment=1)	-1	-2.09826009	4.64838389	0.58609234
H(Fragment=1)	-1	-0.32862050	1.97865552	2.32480390
H(Fragment=1)	-1	-3.00629654	0.75936233	0.60334352
H(Fragment=1)	-1	-4.77120448	3.44333499	2.32484940
H(Fragment=1)	-1	-5.60312857	2.12899681	-1.12888495
O(Fragment=1)	-1	-0.23409611	4.03471315	-1.14953490
O(Fragment=1)	-1	-2.23173671	1.48264441	0.59384385
O(Fragment=1)	-1	-4.87520711	1.35874381	-1.13217258

O(Fragment=1)	-1	-2.87283486	3.92505683	0.58466611
O(Fragment=2)	0	-1.08101110	0.34320139	-2.64599068
O(Fragment=1)	-1	-1.20763353	0.41554559	4.08389706
O(Fragment=1)	-1	-1.04879275	5.63950272	0.60189242
O(Fragment=1)	-1	-1.31415134	3.03333138	2.34312509
O(Fragment=1)	-1	-6.48214160	0.56588689	0.63020820
O(Fragment=1)	-1	-3.78561535	2.38883461	2.34915781
P(Fragment=2)	-1	-0.00498547	-0.01500838	-3.64583081
P(Fragment=1)	-1	0.00447784	0.01348019	3.27460409
P(Fragment=1)	-1	2.71405478	2.52892168	-1.92987997
P(Fragment=1)	-1	2.72351809	2.55741025	4.99055492
P(Fragment=1)	-1	0.16331862	5.23743732	-0.20740055
P(Fragment=1)	-1	5.26952260	-0.16534967	-0.19214195
K(Fragment=1)	0	0.00029282	0.00088150	0.21413288
K(Fragment=1)	-1	2.71863266	2.54270303	1.41788053
H(Fragment=2)	-1	2.25874822	0.58053246	-2.86340252
H(Fragment=1)	-1	2.26821153	0.60902103	4.05703238
H(Fragment=1)	-1	0.49384029	3.26450512	-1.14189663
H(Fragment=1)	-1	0.50330359	3.29299369	5.77853826
H(Fragment=1)	-1	2.42705231	5.83297816	0.57502774
H(Fragment=1)	-1	7.53325629	0.43019117	0.59028634
H(Fragment=1)	-1	3.16678468	4.46955403	-2.88065370
H(Fragment=1)	-1	3.17624798	4.49804260	4.03978119
H(Fragment=1)	-1	4.93642426	1.79982565	-1.14194214
H(Fragment=1)	-1	4.94588757	1.82831422	5.77849276
O(Fragment=2)	-1	0.38983766	1.17991395	-4.59891862
O(Fragment=1)	-1	0.39930096	1.20840252	2.32151627
O(Fragment=1)	-1	2.39220991	3.74622697	-2.88207993
O(Fragment=1)	-1	2.40167321	3.77471554	4.03835497
O(Fragment=1)	-1	0.55814174	6.43235964	-1.16048836
O(Fragment=1)	-1	5.66434573	1.02957265	-1.14522977
O(Fragment=1)	-1	3.03330805	1.30381454	-2.87290219
O(Fragment=1)	-1	3.04277136	1.33230311	4.04753270
O(Fragment=2)	0	1.07377457	-0.36498642	-2.64602190
O(Fragment=1)	-1	1.21880249	-0.38192231	4.08386189
O(Fragment=1)	-1	1.47942942	2.21000475	-1.11758823
O(Fragment=1)	-1	1.48889272	2.23849332	5.80284666
O(Fragment=1)	-1	1.37764327	4.84203482	0.60185726
O(Fragment=1)	-1	4.05741123	0.23671573	0.61715102
O(Fragment=1)	-1	3.95089343	2.85450151	-1.12362094
O(Fragment=1)	-1	3.96035673	2.88299008	5.79681395

C.3 Example Gaussian Input: 183 Atom Oxygen and Hydrogen Vacancy Optimization

%chk=ovachvac.chk

%mem=96GB
%CPU=0,1,2,3,4,5,6,7,8,9,10,11,12,13,14,15,16,17,18,19,20,21,22,23,24,25,26,27,28,29,30,31,32,33,34,35
%LindaWorkers=1,
#p ωB97XD/6-31+g(d) nosymm guess=read opt iop(6/82=1,10/47=1) scf=(xqc,maxconventionalcycles=150,maxcycles=300)

tetrag ovac hvac opt

1 2 0 1 1 2

h(fragment=1)	-1	9.28300000	6.31741569	6.06462500
h(fragment=1)	-1	16.70940000	6.31741569	6.06462500
h(fragment=1)	-1	12.24858431	5.56980000	4.33187500
o(fragment=1)	-1	8.04152871	6.31741569	6.06462500
o(fragment=1)	-1	15.46792871	6.31741569	6.06462500
o(fragment=1)	-1	10.52447129	6.31741569	6.06462500
o(fragment=1)	-1	12.24858431	6.81127129	4.33187500
h(fragment=1)	-1	5.56980000	8.53538431	6.06462500
h(fragment=1)	-1	5.56980000	15.96178431	6.06462500
o(fragment=1)	-1	6.81127129	8.53538431	6.06462500
o(fragment=1)	-1	6.81127129	15.96178431	6.06462500
h(fragment=1)	-1	9.28300000	13.74381569	6.06462500
h(fragment=1)	-1	16.70940000	13.74381569	6.06462500
h(fragment=1)	-1	12.99620000	8.53538431	6.06462500
h(fragment=1)	-1	12.99620000	15.96178431	6.06462500
h(fragment=1)	-1	12.24858431	12.99620000	4.33187500
h(fragment=1)	-1	12.99620000	10.03061569	2.59912500
h(fragment=1)	-1	10.03061569	9.28300000	4.33187500
h(fragment=1)	-1	10.03061569	16.70940000	4.33187500
h(fragment=1)	-1	9.28300000	12.24858431	2.59912500
p(fragment=1)	-1	11.13960000	7.42640000	5.19825000
p(fragment=1)	-1	11.13960000	14.85280000	5.19825000
p(fragment=1)	-1	11.13960000	11.13960000	3.46550000
o(fragment=1)	-1	8.04152871	13.74381569	6.06462500
o(fragment=1)	-1	15.46792871	13.74381569	6.06462500
o(fragment=1)	-1	14.23767129	8.53538431	6.06462500
o(fragment=1)	-1	14.23767129	15.96178431	6.06462500
o(fragment=1)	-1	10.52447129	13.74381569	6.06462500
o(fragment=1)	-1	11.75472871	8.53538431	6.06462500
o(fragment=1)	-1	11.75472871	15.96178431	6.06462500
o(fragment=1)	-1	12.24858431	11.75472871	4.33187500
o(fragment=1)	-1	11.75472871	10.03061569	2.59912500
o(fragment=1)	-1	10.03061569	10.52447129	4.33187500
o(fragment=1)	-1	10.52447129	12.24858431	2.59912500
o(fragment=1)	-1	12.24858431	14.23767129	4.33187500

o(fragment=1) -1 10.03061569 8.04152871 4.33187500
o(fragment=1) -1 10.03061569 15.46792871 4.33187500
h(fragment=1) -1 6.31741569 5.56980000 7.79737500
h(fragment=1) -1 6.31741569 5.56980000 14.72837500
o(fragment=1) -1 6.31741569 6.81127129 7.79737500
o(fragment=1) -1 6.31741569 6.81127129 14.72837500
h(fragment=1) -1 9.28300000 6.31741569 12.99562500
h(fragment=1) -1 16.70940000 6.31741569 12.99562500
h(fragment=1) -1 13.74381569 5.56980000 7.79737500
h(fragment=1) -1 13.74381569 5.56980000 14.72837500
h(fragment=1) -1 12.24858431 5.56980000 11.26287500
h(fragment=1) -1 12.99620000 2.60421569 9.53012500
h(fragment=1) -1 10.03061569 1.85660000 11.26287500
h(fragment=1) -1 9.28300000 4.82218431 9.53012500
p(fragment=1) -1 11.13960000 3.71320000 10.39650000
o(fragment=1) -1 8.04152871 6.31741569 12.99562500
o(fragment=1) -1 15.46792871 6.31741569 12.99562500
o(fragment=1) -1 13.74381569 6.81127129 7.79737500
o(fragment=1) -1 13.74381569 6.81127129 14.72837500
o(fragment=1) -1 10.52447129 6.31741569 12.99562500
o(fragment=1) -1 12.24858431 4.32832871 11.26287500
o(fragment=1) -1 11.75472871 2.60421569 9.53012500
o(fragment=1) -1 10.03061569 3.09807129 11.26287500
o(fragment=1) -1 10.52447129 4.82218431 9.53012500
o(fragment=1) -1 12.24858431 6.81127129 11.26287500
h(fragment=1) -1 6.31741569 12.99620000 7.79737500
h(fragment=1) -1 6.31741569 12.99620000 14.72837500
h(fragment=1) -1 5.56980000 8.53538431 12.99562500
h(fragment=1) -1 5.56980000 15.96178431 12.99562500
h(fragment=1) -1 4.82218431 12.99620000 11.26287500
h(fragment=1) -1 5.56980000 10.03061569 9.53012500
h(fragment=1) -1 5.56980000 10.03061569 16.46112500
h(fragment=1) -1 2.60421569 9.28300000 11.26287500
h(fragment=1) -1 1.85660000 12.24858431 9.53012500
p(fragment=1) -1 3.71320000 11.13960000 10.39650000
o(fragment=1) -1 6.31741569 14.23767129 7.79737500
o(fragment=1) -1 6.31741569 14.23767129 14.72837500
o(fragment=1) -1 6.81127129 8.53538431 12.99562500
o(fragment=1) -1 6.81127129 15.96178431 12.99562500
o(fragment=1) -1 6.31741569 11.75472871 7.79737500
o(fragment=1) -1 6.31741569 11.75472871 14.72837500
o(fragment=1) -1 4.82218431 11.75472871 11.26287500
o(fragment=1) -1 4.32832871 10.03061569 9.53012500
o(fragment=1) -1 2.60421569 10.52447129 11.26287500
o(fragment=1) -1 3.09807129 12.24858431 9.53012500

o(fragment=1)	-1	6.81127129	10.03061569	9.53012500
o(fragment=1)	-1	6.81127129	10.03061569	16.46112500
p(fragment=1)	-1	7.42640000	7.42640000	6.93100000
p(fragment=1)	-1	7.42640000	7.42640000	13.86200000
p(fragment=1)	-1	7.42640000	14.85280000	6.93100000
p(fragment=1)	-1	7.42640000	14.85280000	13.86200000
p(fragment=1)	-1	14.85280000	7.42640000	6.93100000
p(fragment=1)	-1	14.85280000	7.42640000	13.86200000
p(fragment=1)	-1	14.85280000	14.85280000	6.93100000
p(fragment=1)	-1	14.85280000	14.85280000	13.86200000
o(fragment=1)	-1	8.53538431	8.04152871	7.79737500
o(fragment=1)	-1	8.53538431	8.04152871	14.72837500
o(fragment=1)	-1	8.53538431	15.46792871	7.79737500
o(fragment=1)	-1	8.53538431	15.46792871	14.72837500
o(fragment=1)	-1	15.96178431	8.04152871	7.79737500
o(fragment=1)	-1	15.96178431	8.04152871	14.72837500
o(fragment=1)	-1	15.96178431	15.46792871	7.79737500
o(fragment=1)	-1	15.96178431	15.46792871	14.72837500
k(fragment=1)	-1	7.42640000	11.13960000	12.12925000
k(fragment=1)	-1	14.85280000	11.13960000	12.12925000
k(fragment=1)	-1	11.13960000	7.42640000	8.66375000
k(fragment=1)	-1	11.13960000	14.85280000	8.66375000
k(fragment=1)	-1	11.13960000	11.13960000	6.93100000
k(fragment=1)	-1	11.13960000	11.13960000	13.86200000
h(fragment=1)	-1	9.28300000	13.74381569	12.99562500
h(fragment=1)	-1	16.70940000	13.74381569	12.99562500
h(fragment=1)	-1	8.53538431	9.28300000	7.79737500
h(fragment=1)	-1	8.53538431	9.28300000	14.72837500
h(fragment=1)	-1	8.53538431	16.70940000	7.79737500
h(fragment=1)	-1	8.53538431	16.70940000	14.72837500
h(fragment=1)	-1	15.96178431	9.28300000	7.79737500
h(fragment=1)	-1	15.96178431	9.28300000	14.72837500
h(fragment=1)	-1	15.96178431	16.70940000	7.79737500
h(fragment=1)	-1	15.96178431	16.70940000	14.72837500
h(fragment=1)	-1	13.74381569	12.99620000	7.79737500
h(fragment=1)	-1	13.74381569	12.99620000	14.72837500
h(fragment=1)	-1	12.99620000	8.53538431	12.99562500
h(fragment=1)	-1	12.99620000	15.96178431	12.99562500
h(fragment=2)	-1	12.24858431	12.99620000	11.26287500
h(fragment=1)	-1	12.24858431	12.99620000	18.19387500
h(fragment=1)	-1	12.24858431	20.42260000	11.26287500
h(fragment=1)	-1	19.67498431	12.99620000	11.26287500
h(fragment=2)	-1	12.99620000	10.03061569	9.53012500
h(fragment=1)	-1	12.99620000	10.03061569	16.46112500
h(fragment=1)	-1	12.99620000	17.45701569	9.53012500

h(fragment=1)	-1	20.42260000	10.03061569	9.53012500
h(fragment=2)	-1	10.03061569	9.28300000	11.26287500
h(fragment=1)	-1	10.03061569	9.28300000	18.19387500
h(fragment=1)	-1	10.03061569	16.70940000	11.26287500
h(fragment=1)	-1	17.45701569	9.28300000	11.26287500
h(fragment=1)	-1	9.28300000	12.24858431	16.46112500
h(fragment=1)	-1	9.28300000	19.67498431	9.53012500
h(fragment=1)	-1	16.70940000	12.24858431	9.53012500
h(fragment=1)	-1	16.70940000	12.24858431	16.46112500
p(fragment=1)	-1	7.42640000	11.13960000	8.66375000
p(fragment=1)	-1	7.42640000	11.13960000	15.59475000
p(fragment=1)	-1	14.85280000	11.13960000	8.66375000
p(fragment=1)	-1	14.85280000	11.13960000	15.59475000
p(fragment=1)	-1	11.13960000	7.42640000	12.12925000
p(fragment=1)	-1	11.13960000	14.85280000	12.12925000
p(fragment=2)	-1	11.13960000	11.13960000	10.39650000
p(fragment=1)	-1	11.13960000	11.13960000	17.32750000
p(fragment=1)	-1	11.13960000	18.56600000	10.39650000
p(fragment=1)	-1	18.56600000	11.13960000	10.39650000
o(fragment=1)	-1	8.04152871	13.74381569	12.99562500
o(fragment=1)	-1	15.46792871	13.74381569	12.99562500
o(fragment=1)	-1	13.74381569	14.23767129	7.79737500
o(fragment=1)	-1	13.74381569	14.23767129	14.72837500
o(fragment=1)	-1	14.23767129	8.53538431	12.99562500
o(fragment=1)	-1	14.23767129	15.96178431	12.99562500
o(fragment=1)	-1	8.53538431	10.52447129	7.79737500
o(fragment=1)	-1	8.53538431	10.52447129	14.72837500
o(fragment=1)	-1	15.96178431	10.52447129	7.79737500
o(fragment=1)	-1	15.96178431	10.52447129	14.72837500
o(fragment=1)	-1	10.52447129	13.74381569	12.99562500
o(fragment=1)	-1	13.74381569	11.75472871	7.79737500
o(fragment=1)	-1	13.74381569	11.75472871	14.72837500
o(fragment=1)	-1	11.75472871	8.53538431	12.99562500
o(fragment=1)	-1	11.75472871	15.96178431	12.99562500
o(fragment=2)	0	12.24858431	11.75472871	11.26287500
o(fragment=1)	-1	12.24858431	11.75472871	18.19387500
o(fragment=1)	-1	12.24858431	19.18112871	11.26287500
o(fragment=1)	-1	19.67498431	11.75472871	11.26287500
o(fragment=2)	0	11.75472871	10.03061569	9.53012500
o(fragment=1)	-1	11.75472871	10.03061569	16.46112500
o(fragment=1)	-1	11.75472871	17.45701569	9.53012500
o(fragment=1)	-1	19.18112871	10.03061569	9.53012500
o(fragment=2)	0	10.03061569	10.52447129	11.26287500
o(fragment=1)	-1	10.03061569	10.52447129	18.19387500
o(fragment=1)	-1	10.03061569	17.95087129	11.26287500

o(fragment=1)	-1	17.45701569	10.52447129	11.26287500
o(fragment=1)	-1	10.52447129	12.24858431	16.46112500
o(fragment=1)	-1	10.52447129	19.67498431	9.53012500
o(fragment=1)	-1	17.95087129	12.24858431	9.53012500
o(fragment=1)	-1	12.24858431	14.23767129	11.26287500
o(fragment=1)	-1	14.23767129	10.03061569	9.53012500
o(fragment=1)	-1	14.23767129	10.03061569	16.46112500
o(fragment=1)	-1	10.03061569	8.04152871	11.26287500
o(fragment=1)	-1	10.03061569	15.46792871	11.26287500
o(fragment=1)	-1	8.04152871	12.24858431	9.53012500
o(fragment=1)	-1	8.04152871	12.24858431	16.46112500
o(fragment=1)	-1	15.46792871	12.24858431	9.53012500
o(fragment=1)	-1	15.46792871	12.24858431	16.46112500

Appendix D

D.1 41-Atom Self Trapped Hole Hyperfine Results using Miyoshi Coordinates

Isotropic Fermi Contact Couplings

	Atom	a.u.	MegaHertz	Gauss	10(-4) cm-1
1	O(17)	-0.00591	3.58178	1.27807	1.19475
2	P(31)	-0.00009	-0.15414	-0.05500	-0.05141
3	H(1)	0.00000	0.00107	0.00038	0.00036
4	H(1)	-0.00034	-1.53861	-0.54902	-0.51323
5	H(1)	0.00000	-0.00319	-0.00114	-0.00106
6	H(1)	0.00007	0.30595	0.10917	0.10205
7	O(17)	0.00001	-0.00355	-0.00127	-0.00119
8	O(17)	-0.00002	0.01133	0.00404	0.00378
9	O(17)	-0.00087	0.52489	0.18729	0.17508
10	O(17)	-0.00021	0.12811	0.04571	0.04273
11	P(31)	-0.00008	-0.15386	-0.05490	-0.05132
12	H(1)	0.00000	0.00108	0.00038	0.00036
13	H(1)	-0.00034	-1.53871	-0.54905	-0.51326
14	H(1)	0.00000	-0.00318	-0.00113	-0.00106
15	H(1)	0.00007	0.30559	0.10904	0.10193
16	O(17)	0.00001	-0.00359	-0.00128	-0.00120
17	O(17)	-0.00002	0.01134	0.00405	0.00378
18	O(17)	-0.00087	0.52537	0.18747	0.17525
19	O(17)	-0.00021	0.12805	0.04569	0.04271
20	P(31)	0.00027	0.49227	0.17566	0.16420
21	H(1)	-0.00161	-7.19876	-2.56870	-2.40125
22	H(1)	-0.00008	-0.35428	-0.12641	-0.11817
23	H(1)	-0.00001	-0.04113	-0.01468	-0.01372
24	H(1)	0.00006	0.27244	0.09721	0.09088
25	O(17)	0.00005	-0.03317	-0.01184	-0.01107
26	O(17)	0.00172	-1.03996	-0.37108	-0.34689
27	O(17)	-0.00138	0.83739	0.29880	0.27932
28	O(17)	-0.00025	0.14981	0.05346	0.04997
29	O(17)	0.17151	-103.96595	-37.09763	-34.67931
30	P(31)	0.12268	222.18562	79.28135	74.11314
31	P(31)	0.00027	0.49264	0.17578	0.16433
32	H(1)	-0.00161	-7.20143	-2.56965	-2.40214
33	H(1)	-0.00008	-0.35495	-0.12665	-0.11840
34	H(1)	-0.00001	-0.04112	-0.01467	-0.01372
35	H(1)	0.00006	0.27201	0.09706	0.09073
36	O(17)	-0.00591	3.58280	1.27843	1.19509

37	O(17)	0.00005	-0.03315	-0.01183	-0.01106
38	O(17)	0.00171	-1.03904	-0.37076	-0.34659
39	O(17)	0.17153	-103.98117	-37.10307	-34.68439
40	O(17)	-0.00138	0.83683	0.29860	0.27914
41	O(17)	-0.00025	0.14970	0.05342	0.04994

Anisotropic Spin Dipole Couplings in Principal Axis System

Atom		a.u.	MegaHertz	Gauss	10(-4) cm-1	Axes		
	Baa	-0.0233	-12.408	-4.428	-4.139	-0.3470	0.0512	0.9365
21 H(1)	Bbb	-0.0180	-9.587	-3.421	-3.198	0.7786	-0.5410	0.3181
	Bcc	0.0412	21.995	7.849	7.337	0.5229	0.8395	0.1479
	Baa	-0.1503	-32.490	-11.593	-10.838	0.9988	-0.0498	-0.0001
30 P(31)	Bbb	-0.0086	-1.851	-0.660	-0.617	0.0498	0.9988	0.0000
	Bcc	0.1589	34.341	12.254	11.455	0.0001	0.0000	1.0000
	Baa	-0.0233	-12.411	-4.429	-4.140	0.3471	-0.0510	0.9364
32 H(1)	Bbb	-0.0180	-9.589	-3.421	-3.198	0.7787	-0.5408	-0.3181
	Bcc	0.0412	22.000	7.850	7.338	0.5226	0.8396	-0.1479

D.2 149-Atom Self Trapped Hole Hyperfine Results using Miyoshi Coordinates

Isotropic Fermi Contact Couplings

Atom		a.u.	MegaHertz	Gauss	10(-4) cm-1
1	K(39)	0.00011	0.02339	0.00835	0.00780
2	K(39)	0.00000	-0.00003	-0.00001	-0.00001
3	K(39)	0.00000	0.00077	0.00028	0.00026
4	K(39)	-0.00002	-0.00332	-0.00118	-0.00111
5	K(39)	0.00000	0.00000	0.00000	0.00000
6	P(31)	-0.00007	-0.12443	-0.04440	-0.04150
7	H(1)	0.00000	0.00077	0.00027	0.00026
8	H(1)	-0.00056	-2.50927	-0.89537	-0.83700
9	H(1)	0.00000	-0.00076	-0.00027	-0.00025
10	H(1)	0.00000	-0.01638	-0.00584	-0.00546
11	O(17)	0.00002	-0.01510	-0.00539	-0.00504
12	O(17)	-0.00036	0.21612	0.07712	0.07209
13	O(17)	-0.00168	1.02043	0.36411	0.34038
14	O(17)	0.00002	-0.01472	-0.00525	-0.00491
15	K(39)	0.00000	0.00001	0.00000	0.00000

16	K(39)	0.00000	-0.00001	0.00000	0.00000
17	P(31)	0.00000	0.00003	0.00001	0.00001
18	H(1)	0.00000	0.00004	0.00001	0.00001
19	H(1)	0.00000	0.00000	0.00000	0.00000
20	O(17)	0.00000	0.00000	0.00000	0.00000
21	O(17)	0.00000	0.00000	0.00000	0.00000
22	O(17)	0.00000	-0.00002	-0.00001	-0.00001
23	O(17)	0.00000	-0.00001	0.00000	0.00000
24	K(39)	0.00000	-0.00022	-0.00008	-0.00007
25	K(39)	0.00001	0.00197	0.00070	0.00066
26	K(39)	-0.00005	-0.00956	-0.00341	-0.00319
27	P(31)	-0.00110	-1.98947	-0.70989	-0.66361
28	H(1)	-0.00003	-0.13036	-0.04652	-0.04348
29	H(1)	-0.00003	-0.13448	-0.04799	-0.04486
30	H(1)	-0.00009	-0.38806	-0.13847	-0.12944
31	O(17)	-0.00044	0.26384	0.09414	0.08801
32	O(17)	-0.00020	0.12121	0.04325	0.04043
33	O(17)	-0.00020	0.11851	0.04229	0.03953
34	O(17)	0.00128	-0.77440	-0.27633	-0.25831
35	K(39)	-0.00113	-0.23620	-0.08428	-0.07879
36	K(39)	0.00000	0.00000	0.00000	0.00000
37	K(39)	0.00000	0.00009	0.00003	0.00003
38	K(39)	0.00000	0.00002	0.00001	0.00001
39	K(39)	0.00000	0.00008	0.00003	0.00003
40	P(31)	0.00000	-0.00776	-0.00277	-0.00259
41	P(31)	0.00000	0.00082	0.00029	0.00027
42	H(1)	0.00000	0.00137	0.00049	0.00046
43	H(1)	0.00000	-0.00569	-0.00203	-0.00190
44	H(1)	0.00000	-0.00030	-0.00011	-0.00010
45	H(1)	0.00000	-0.00108	-0.00039	-0.00036
46	H(1)	0.00000	0.00008	0.00003	0.00003
47	O(17)	0.00000	0.00120	0.00043	0.00040
48	O(17)	-0.00005	0.03308	0.01180	0.01103
49	O(17)	-0.00002	0.01319	0.00471	0.00440
50	O(17)	0.00000	-0.00112	-0.00040	-0.00037
51	O(17)	0.00000	-0.00018	-0.00006	-0.00006
52	O(17)	-0.00001	0.00372	0.00133	0.00124
53	O(17)	0.00000	-0.00023	-0.00008	-0.00008
54	O(17)	0.00000	-0.00005	-0.00002	-0.00002
55	K(39)	0.00000	-0.00001	0.00000	0.00000
56	H(1)	0.00000	0.00001	0.00000	0.00000
57	K(39)	-0.00005	-0.01104	-0.00394	-0.00368
58	K(39)	0.00001	0.00184	0.00066	0.00061
59	K(39)	0.00000	-0.00029	-0.00010	-0.00010
60	P(31)	-0.00098	-1.77922	-0.63487	-0.59348

61	H(1)	-0.00008	-0.37862	-0.13510	-0.12629
62	H(1)	-0.00003	-0.14076	-0.05023	-0.04695
63	H(1)	-0.00003	-0.13031	-0.04650	-0.04347
64	O(17)	-0.00037	0.22434	0.08005	0.07483
65	O(17)	-0.00018	0.11097	0.03960	0.03702
66	O(17)	0.00119	-0.72329	-0.25809	-0.24126
67	O(17)	-0.00020	0.11834	0.04223	0.03947
68	K(39)	0.00000	0.00025	0.00009	0.00008
69	K(39)	0.00000	0.00002	0.00001	0.00001
70	K(39)	0.00000	0.00007	0.00002	0.00002
71	K(39)	0.00000	0.00000	0.00000	0.00000
72	K(39)	-0.00118	-0.24546	-0.08759	-0.08188
73	P(31)	0.00000	-0.00449	-0.00160	-0.00150
74	P(31)	0.00000	-0.00882	-0.00315	-0.00294
75	H(1)	0.00000	-0.01916	-0.00684	-0.00639
76	H(1)	0.00000	-0.00106	-0.00038	-0.00036
77	H(1)	0.00000	0.00026	0.00009	0.00009
78	H(1)	0.00000	0.00130	0.00046	0.00043
79	H(1)	0.00000	-0.00044	-0.00016	-0.00015
80	O(17)	0.00000	0.00132	0.00047	0.00044
81	O(17)	0.00000	0.00041	0.00015	0.00014
82	O(17)	0.00000	0.00130	0.00046	0.00043
83	O(17)	-0.00001	0.00396	0.00141	0.00132
84	O(17)	-0.00001	0.00333	0.00119	0.00111
85	O(17)	-0.00006	0.03398	0.01212	0.01133
86	O(17)	0.00000	-0.00027	-0.00010	-0.00009
87	O(17)	0.00000	-0.00198	-0.00071	-0.00066
88	K(39)	0.00000	-0.00001	-0.00001	0.00000
89	H(1)	0.00000	0.00000	0.00000	0.00000
90	K(39)	-0.00005	-0.00991	-0.00354	-0.00330
91	K(39)	0.00012	0.02444	0.00872	0.00815
92	K(39)	-0.00016	-0.03352	-0.01196	-0.01118
93	K(39)	-0.00004	-0.00924	-0.00330	-0.00308
94	P(31)	-0.05424	-98.22884	-35.05049	-32.76562
95	H(1)	0.00029	1.30120	0.46430	0.43403
96	H(1)	0.00035	1.54987	0.55303	0.51698
97	O(17)	-0.00269	1.62877	0.58119	0.54330
98	O(17)	0.05233	-31.72256	-11.31940	-10.58151
99	O(17)	0.05221	-31.65068	-11.29375	-10.55753
100	O(17)	-0.00281	1.70385	0.60798	0.56834
101	K(39)	0.00000	0.00000	0.00000	0.00000
102	K(39)	0.00000	0.00025	0.00009	0.00008
103	K(39)	-0.00002	-0.00456	-0.00163	-0.00152
104	K(39)	0.00000	0.00101	0.00036	0.00034
105	K(39)	-0.00339	-0.70876	-0.25290	-0.23642

106	K(39)	0.00000	-0.00004	-0.00001	-0.00001
107	K(39)	0.00000	0.00006	0.00002	0.00002
108	P(31)	-0.00014	-0.25542	-0.09114	-0.08520
109	P(31)	0.00000	-0.00529	-0.00189	-0.00176
110	P(31)	0.00000	0.00136	0.00049	0.00045
111	P(31)	0.00000	0.00106	0.00038	0.00035
112	H(1)	0.00000	0.00027	0.00009	0.00009
113	H(1)	0.00000	0.00019	0.00007	0.00006
114	H(1)	-0.00072	-3.21382	-1.14677	-1.07201
115	H(1)	0.00000	0.00010	0.00003	0.00003
116	H(1)	0.00000	-0.01983	-0.00708	-0.00662
117	H(1)	0.00000	-0.00091	-0.00033	-0.00030
118	H(1)	-0.00001	-0.02410	-0.00860	-0.00804
119	H(1)	0.00000	0.00034	0.00012	0.00011
120	H(1)	0.00000	0.00083	0.00030	0.00028
121	H(1)	0.00000	-0.00787	-0.00281	-0.00262
122	O(17)	0.00000	0.00050	0.00018	0.00017
123	O(17)	0.00000	0.00114	0.00041	0.00038
124	O(17)	-0.00001	0.00385	0.00137	0.00128
125	O(17)	-0.00001	0.00386	0.00138	0.00129
126	O(17)	-0.00154	0.93171	0.33246	0.31079
127	O(17)	0.00005	-0.03023	-0.01079	-0.01008
128	O(17)	0.00000	0.00001	0.00000	0.00000
129	O(17)	0.00002	-0.01232	-0.00440	-0.00411
130	O(17)	0.00000	0.00026	0.00009	0.00009
131	O(17)	0.00000	0.00024	0.00008	0.00008
132	O(17)	-0.00034	0.20619	0.07357	0.06878
133	O(17)	-0.00001	0.00421	0.00150	0.00141
134	O(17)	-0.00001	0.00689	0.00246	0.00230
135	O(17)	-0.00001	0.00446	0.00159	0.00149
136	O(17)	0.00000	-0.00019	-0.00007	-0.00006
137	O(17)	-0.00003	0.01603	0.00572	0.00535
138	K(39)	0.00000	-0.00001	0.00000	0.00000
139	K(39)	0.00000	0.00001	0.00000	0.00000
140	K(39)	0.00000	-0.00001	0.00000	0.00000
141	P(31)	0.00000	0.00003	0.00001	0.00001
142	H(1)	0.00000	0.00004	0.00001	0.00001
143	H(1)	0.00000	0.00000	0.00000	0.00000
144	H(1)	0.00000	0.00000	0.00000	0.00000
145	H(1)	0.00000	0.00001	0.00000	0.00000
146	O(17)	0.00000	-0.00002	-0.00001	-0.00001
147	O(17)	0.00000	0.00000	0.00000	0.00000
148	O(17)	0.00000	0.00000	0.00000	0.00000
149	O(17)	0.00000	0.00000	0.00000	0.00000

Anisotropic Spin Dipole Couplings in Principal Axis System

Atom		a.u.	MegaHertz	Gauss	10(-4) cm-1	Axes		
	Baa	-0.0189	-10.090	-3.601	-3.366	0.8823	-0.4112	-0.2293
8 H(1)	Bbb	-0.0137	-7.292	-2.602	-2.432	0.4476	0.5818	0.6791
	Bcc	0.0326	17.382	6.202	5.798	0.1458	0.7017	-0.6973
	Baa	-0.0250	-5.398	-1.926	-1.801	1.0000	-0.0084	-0.0023
94 P(31)	Bbb	0.0048	1.038	0.370	0.346	0.0036	0.1613	0.9869
	Bcc	0.0202	4.360	1.556	1.454	0.0079	0.9869	-0.1613
	Baa	-0.0197	-10.511	-3.750	-3.506	0.8718	0.4345	0.2264
114 H(1)	Bbb	-0.0146	-7.787	-2.779	-2.597	-0.4652	0.5893	0.6606
	Bcc	0.0343	18.297	6.529	6.103	0.1536	-0.6812	0.7158

D.3 127-Atom Self Trapped Hole Hyperfine Results using Miyoshi Coordinates

Isotropic Fermi Contact Couplings

Atom		a.u.	MegaHertz	Gauss	10(-4) cm-1
1	K(39)	0.00016	0.03344	0.01193	0.01115
2	O(17)	-0.00159	0.96307	0.34365	0.32124
3	P(31)	-0.00082	-1.48565	-0.53012	-0.49556
4	K(39)	-0.00006	-0.01310	-0.00467	-0.00437
5	H(1)	-0.00007	-0.29280	-0.10448	-0.09767
6	H(1)	0.00024	1.07335	0.38300	0.35803
7	H(1)	-0.00008	-0.35842	-0.12789	-0.11956
8	H(1)	-0.00008	-0.36140	-0.12896	-0.12055
9	O(17)	0.00011	-0.06474	-0.02310	-0.02159
10	O(17)	0.00047	-0.28339	-0.10112	-0.09453
11	O(17)	0.00063	-0.38190	-0.13627	-0.12739
12	O(17)	-0.00044	0.26862	0.09585	0.08960
13	P(31)	-0.00082	-1.49339	-0.53288	-0.49814
14	K(39)	-0.00001	-0.00240	-0.00086	-0.00080
15	H(1)	-0.00007	-0.29418	-0.10497	-0.09813
16	H(1)	0.00024	1.07675	0.38421	0.35916
17	H(1)	-0.00008	-0.35981	-0.12839	-0.12002
18	H(1)	-0.00008	-0.36266	-0.12941	-0.12097
19	O(17)	0.00011	-0.06516	-0.02325	-0.02173
20	O(17)	0.00047	-0.28416	-0.10139	-0.09478

21	O(17)	0.00064	-0.38601	-0.13774	-0.12876
22	O(17)	-0.00045	0.26984	0.09629	0.09001
23	K(39)	0.00016	0.03254	0.01161	0.01086
24	K(39)	-0.00006	-0.01316	-0.00470	-0.00439
25	K(39)	-0.00001	-0.00240	-0.00086	-0.00080
26	P(31)	-0.00136	-2.45732	-0.87683	-0.81967
27	P(31)	0.00000	0.00009	0.00003	0.00003
28	K(39)	-0.00015	-0.03152	-0.01125	-0.01051
29	H(1)	-0.00143	-6.39634	-2.28237	-2.13359
30	H(1)	0.00000	-0.00002	-0.00001	-0.00001
31	H(1)	-0.00004	-0.16544	-0.05903	-0.05518
32	H(1)	0.00000	0.00002	0.00001	0.00001
33	H(1)	0.00000	-0.00263	-0.00094	-0.00088
34	H(1)	0.00000	0.00540	0.00193	0.00180
35	H(1)	-0.00001	-0.05808	-0.02072	-0.01937
36	H(1)	0.00000	0.00000	0.00000	0.00000
37	H(1)	-0.00006	-0.28943	-0.10328	-0.09654
38	H(1)	0.00000	0.00001	0.00000	0.00000
39	O(17)	-0.00002	0.01363	0.00486	0.00455
40	O(17)	-0.00011	0.06812	0.02431	0.02272
41	O(17)	0.00000	0.00024	0.00009	0.00008
41	O(17)	0.00000	0.00024	0.00009	0.00008
42	O(17)	0.00000	0.00071	0.00025	0.00024
43	O(17)	-0.00006	0.03892	0.01389	0.01298
44	O(17)	-0.00372	2.25753	0.80554	0.75303
45	O(17)	0.00000	0.00034	0.00012	0.00011
46	O(17)	0.00072	-0.43496	-0.15521	-0.14509
47	O(17)	0.00000	-0.00006	-0.00002	-0.00002
48	O(17)	-0.00003	0.02067	0.00738	0.00690
49	O(17)	-0.00001	0.00616	0.00220	0.00205
50	O(17)	0.00076	-0.46024	-0.16423	-0.15352
51	O(17)	0.00000	0.00001	0.00000	0.00000
52	P(31)	-0.00001	-0.01037	-0.00370	-0.00346
53	P(31)	-0.00003	-0.05365	-0.01914	-0.01790
54	K(39)	0.00000	0.00005	0.00002	0.00002
55	K(39)	-0.00052	-0.10804	-0.03855	-0.03604
56	K(39)	0.00000	-0.00012	-0.00004	-0.00004
57	H(1)	0.00000	0.00042	0.00015	0.00014
58	H(1)	0.00000	-0.00552	-0.00197	-0.00184
59	H(1)	0.00000	-0.00107	-0.00038	-0.00036
60	H(1)	0.00000	-0.00232	-0.00083	-0.00077
61	H(1)	0.00000	-0.00378	-0.00135	-0.00126
62	H(1)	0.00000	-0.00101	-0.00036	-0.00034
63	O(17)	-0.00014	0.08647	0.03086	0.02884
64	O(17)	-0.00017	0.10394	0.03709	0.03467

65	O(17)	0.00000	0.00176	0.00063	0.00059
66	O(17)	0.00003	-0.01530	-0.00546	-0.00510
67	O(17)	0.00000	-0.00091	-0.00032	-0.00030
68	O(17)	0.00000	-0.00050	-0.00018	-0.00017
69	O(17)	0.00000	0.00241	0.00086	0.00080
70	O(17)	-0.00001	0.00615	0.00219	0.00205
71	P(31)	-0.00003	-0.05163	-0.01842	-0.01722
72	P(31)	-0.00004	-0.06918	-0.02469	-0.02308
73	K(39)	-0.00053	-0.11038	-0.03939	-0.03682
74	K(39)	0.00000	-0.00012	-0.00004	-0.00004
75	K(39)	0.00000	-0.00003	-0.00001	-0.00001
76	H(1)	0.00000	0.00041	0.00015	0.00014
77	H(1)	0.00000	-0.00553	-0.00197	-0.00184
78	H(1)	0.00000	-0.00109	-0.00039	-0.00036
79	H(1)	0.00000	-0.00269	-0.00096	-0.00090
80	H(1)	0.00000	-0.00355	-0.00127	-0.00118
81	H(1)	0.00000	-0.00101	-0.00036	-0.00034
82	O(17)	-0.00015	0.08957	0.03196	0.02988
83	O(17)	-0.00016	0.09617	0.03432	0.03208
84	O(17)	0.00000	0.00159	0.00057	0.00053
85	O(17)	0.00003	-0.01529	-0.00546	-0.00510
86	O(17)	0.04418	-26.78299	-9.55684	-8.93384
87	O(17)	0.00000	-0.00035	-0.00012	-0.00012
88	O(17)	0.00000	-0.00093	-0.00033	-0.00031
89	O(17)	0.00000	-0.00055	-0.00020	-0.00018
90	O(17)	0.00000	0.00242	0.00086	0.00081
91	O(17)	-0.00001	0.00583	0.00208	0.00194
92	P(31)	-0.05189	-93.97310	-33.53194	-31.34605
93	P(31)	0.00000	-0.00114	-0.00041	-0.00038
94	P(31)	-0.00136	-2.45743	-0.87687	-0.81971
95	P(31)	0.00000	0.00009	0.00003	0.00003
96	P(31)	-0.00001	-0.01095	-0.00391	-0.00365
97	P(31)	-0.00004	-0.06914	-0.02467	-0.02306
98	K(39)	-0.00835	-1.74468	-0.62254	-0.58196
99	K(39)	-0.00015	-0.03149	-0.01124	-0.01050
100	K(39)	0.00000	0.00005	0.00002	0.00002
101	K(39)	0.00000	-0.00002	-0.00001	-0.00001
102	H(1)	-0.00143	-6.40489	-2.28543	-2.13644
103	H(1)	0.00000	-0.00002	-0.00001	-0.00001
104	H(1)	-0.00004	-0.16584	-0.05918	-0.05532
105	H(1)	0.00000	0.00002	0.00001	0.00001
106	H(1)	0.00000	-0.00266	-0.00095	-0.00089
107	H(1)	0.00000	0.00541	0.00193	0.00180
108	H(1)	-0.00001	-0.05812	-0.02074	-0.01939
109	H(1)	0.00000	0.00000	0.00000	0.00000

110	H(1)	-0.00006	-0.28919	-0.10319	-0.09646
111	H(1)	0.00000	0.00001	0.00000	0.00000
112	O(17)	-0.00159	0.96144	0.34306	0.32070
113	O(17)	-0.00002	0.01364	0.00487	0.00455
114	O(17)	-0.00011	0.06805	0.02428	0.02270
115	O(17)	0.00000	0.00024	0.00009	0.00008
116	O(17)	0.00000	0.00077	0.00027	0.00026
117	O(17)	-0.00006	0.03890	0.01388	0.01298
118	O(17)	-0.00372	2.25632	0.80511	0.75263
119	O(17)	0.00000	0.00034	0.00012	0.00011
120	O(17)	0.04414	-26.76028	-9.54873	-8.92627
121	O(17)	0.00000	-0.00035	-0.00012	-0.00012
122	O(17)	0.00071	-0.43269	-0.15439	-0.14433
123	O(17)	0.00000	-0.00006	-0.00002	-0.00002
124	O(17)	-0.00003	0.02076	0.00741	0.00692
125	O(17)	-0.00001	0.00595	0.00212	0.00199
126	O(17)	0.00076	-0.46014	-0.16419	-0.15348
127	O(17)	0.00000	0.00002	0.00001	0.00001

Anisotropic Spin Dipole Couplings in Principal Axis System

Atom		a.u.	MegaHertz	Gauss	10(-4) cm-1	Axes		
	Baa	-0.0206	-10.995	-3.923	-3.667	-0.3421	0.2902	0.8937
29 H(1)	Bbb	-0.0160	-8.514	-3.038	-2.840	-0.6157	0.6493	-0.4465
	Bcc	0.0366	19.509	6.961	6.507	0.7099	0.7030	0.0435
	Baa	-0.0206	-10.986	-3.920	-3.665	0.3439	-0.2821	0.8956
102 H(1)	Bbb	-0.0159	-8.510	-3.036	-2.838	-0.6146	0.6535	0.4419
	Bcc	0.0365	19.496	6.957	6.503	0.7099	0.7024	-0.0514
	Baa	-0.0280	-6.051	-2.159	-2.018	0.0011	0.0040	1.0000
92 P(31)	Bbb	0.0089	1.920	0.685	0.640	0.9098	-0.4150	0.0006
	Bcc	0.0191	4.131	1.474	1.378	0.4150	0.9098	-0.0041

D.4 115-Atom Self Trapped Hole Hyperfine Results using Miyoshi Coordinates

Isotropic Fermi Contact Couplings

Atom		a.u.	MegaHertz	Gauss	10(-4) cm-1
1	O(17)	0.00050	-0.30163	-0.10763	-0.10061

2	P(31)	-0.00013	-0.22737	-0.08113	-0.07584
3	H(1)	0.00000	-0.00212	-0.00076	-0.00071
4	H(1)	0.00036	1.61157	0.57505	0.53756
5	H(1)	0.00000	-0.01547	-0.00552	-0.00516
6	H(1)	-0.00003	-0.15335	-0.05472	-0.05115
7	O(17)	-0.00009	0.05301	0.01891	0.01768
8	O(17)	-0.00003	0.01736	0.00619	0.00579
9	O(17)	-0.00064	0.38631	0.13785	0.12886
10	O(17)	-0.00014	0.08519	0.03040	0.02842
11	P(31)	-0.00013	-0.22825	-0.08145	-0.07614
12	H(1)	0.00000	-0.00216	-0.00077	-0.00072
13	H(1)	0.00036	1.61558	0.57648	0.53890
14	H(1)	0.00000	-0.01550	-0.00553	-0.00517
15	H(1)	-0.00003	-0.15361	-0.05481	-0.05124
16	O(17)	-0.00009	0.05303	0.01892	0.01769
17	O(17)	-0.00003	0.01734	0.00619	0.00578
18	O(17)	-0.00063	0.38405	0.13704	0.12811
19	O(17)	-0.00014	0.08528	0.03043	0.02845
20	P(31)	-0.00069	-1.25027	-0.44613	-0.41705
21	P(31)	0.00000	0.00006	0.00002	0.00002
22	K(39)	-0.00007	-0.01385	-0.00494	-0.00462
23	H(1)	-0.00139	-6.19536	-2.21066	-2.06655
24	H(1)	0.00000	0.00000	0.00000	0.00000
25	H(1)	-0.00002	-0.10083	-0.03598	-0.03363
26	H(1)	0.00000	0.00002	0.00001	0.00001
27	H(1)	0.00000	-0.00366	-0.00131	-0.00122
28	H(1)	0.00000	0.00255	0.00091	0.00085
29	H(1)	-0.00002	-0.10659	-0.03803	-0.03555
30	H(1)	0.00000	0.00000	0.00000	0.00000
31	H(1)	-0.00001	-0.04782	-0.01706	-0.01595
32	H(1)	0.00000	0.00001	0.00000	0.00000
33	O(17)	-0.00002	0.01363	0.00487	0.00455
34	O(17)	0.00006	-0.03766	-0.01344	-0.01256
35	O(17)	0.00000	0.00010	0.00004	0.00003
36	O(17)	0.00000	0.00064	0.00023	0.00021
37	O(17)	-0.00001	0.00655	0.00234	0.00218
38	O(17)	-0.00320	1.93868	0.69177	0.64667
39	O(17)	0.00000	0.00026	0.00009	0.00009
40	O(17)	0.00021	-0.12561	-0.04482	-0.04190
41	O(17)	0.00000	-0.00001	0.00000	0.00000
42	O(17)	-0.00002	0.01109	0.00396	0.00370
43	O(17)	-0.00001	0.00512	0.00183	0.00171
44	O(17)	0.00011	-0.06715	-0.02396	-0.02240
45	O(17)	0.00000	0.00000	0.00000	0.00000
46	P(31)	-0.00001	-0.01876	-0.00670	-0.00626

47	P(31)	-0.00002	-0.03480	-0.01242	-0.01161
48	K(39)	0.00063	0.13054	0.04658	0.04354
49	H(1)	0.00000	0.00028	0.00010	0.00009
50	H(1)	0.00000	-0.00348	-0.00124	-0.00116
51	H(1)	0.00000	-0.00106	-0.00038	-0.00035
52	H(1)	0.00000	-0.00085	-0.00030	-0.00028
53	H(1)	0.00000	-0.00426	-0.00152	-0.00142
54	H(1)	0.00000	-0.00151	-0.00054	-0.00050
55	O(17)	-0.00006	0.03675	0.01311	0.01226
56	O(17)	-0.00011	0.06482	0.02313	0.02162
57	O(17)	-0.00001	0.00857	0.00306	0.00286
58	O(17)	0.00002	-0.01470	-0.00525	-0.00491
59	O(17)	0.00000	0.00018	0.00006	0.00006
60	O(17)	0.00000	-0.00147	-0.00052	-0.00049
61	O(17)	0.00000	0.00166	0.00059	0.00055
62	O(17)	-0.00001	0.00342	0.00122	0.00114
63	P(31)	-0.00002	-0.03977	-0.01419	-0.01327
64	P(31)	-0.00001	-0.01285	-0.00459	-0.00429
65	K(39)	0.00062	0.12907	0.04605	0.04305
66	H(1)	0.00000	0.00028	0.00010	0.00009
67	H(1)	0.00000	-0.00347	-0.00124	-0.00116
68	H(1)	0.00000	-0.00106	-0.00038	-0.00035
69	H(1)	0.00000	-0.00019	-0.00007	-0.00006
70	H(1)	0.00000	-0.00506	-0.00180	-0.00169
71	H(1)	0.00000	-0.00151	-0.00054	-0.00050
72	O(17)	-0.00006	0.03645	0.01301	0.01216
73	O(17)	-0.00014	0.08406	0.02999	0.02804
74	O(17)	-0.00001	0.00852	0.00304	0.00284
75	O(17)	0.00002	-0.01478	-0.00527	-0.00493
76	O(17)	0.04780	-28.97759	-10.33992	-9.66588
77	O(17)	0.00000	-0.00037	-0.00013	-0.00012
78	O(17)	0.00000	0.00019	0.00007	0.00006
79	O(17)	0.00000	-0.00142	-0.00051	-0.00047
80	O(17)	0.00000	0.00166	0.00059	0.00055
81	O(17)	-0.00001	0.00421	0.00150	0.00141
82	P(31)	-0.05386	-97.55206	-34.80900	-32.53987
83	P(31)	0.00000	-0.00022	-0.00008	-0.00007
84	P(31)	-0.00069	-1.25215	-0.44680	-0.41767
85	P(31)	0.00000	0.00006	0.00002	0.00002
86	P(31)	-0.00001	-0.01868	-0.00667	-0.00623
87	P(31)	-0.00001	-0.01293	-0.00461	-0.00431
88	K(39)	-0.00875	-1.82745	-0.65208	-0.60957
89	K(39)	-0.00007	-0.01385	-0.00494	-0.00462
90	H(1)	-0.00139	-6.19950	-2.21214	-2.06793
91	H(1)	0.00000	0.00000	0.00000	0.00000

92	H(1)	-0.00002	-0.10081	-0.03597	-0.03363
93	H(1)	0.00000	0.00002	0.00001	0.00001
94	H(1)	0.00000	-0.00367	-0.00131	-0.00122
95	H(1)	0.00000	0.00255	0.00091	0.00085
96	H(1)	-0.00002	-0.10664	-0.03805	-0.03557
97	H(1)	0.00000	0.00000	0.00000	0.00000
98	H(1)	-0.00001	-0.04781	-0.01706	-0.01595
99	H(1)	0.00000	0.00001	0.00000	0.00000
100	O(17)	0.00050	-0.30321	-0.10819	-0.10114
101	O(17)	-0.00002	0.01358	0.00484	0.00453
102	O(17)	0.00006	-0.03765	-0.01343	-0.01256
103	O(17)	0.00000	0.00010	0.00004	0.00003
104	O(17)	0.00000	0.00063	0.00023	0.00021
105	O(17)	-0.00001	0.00655	0.00234	0.00218
106	O(17)	-0.00320	1.93908	0.69191	0.64681
107	O(17)	0.00000	0.00026	0.00009	0.00009
108	O(17)	0.04773	-28.93606	-10.32511	-9.65203
109	O(17)	0.00000	-0.00036	-0.00013	-0.00012
110	O(17)	0.00020	-0.12304	-0.04390	-0.04104
111	O(17)	0.00000	-0.00001	-0.00001	0.00000
112	O(17)	-0.00002	0.01110	0.00396	0.00370
113	O(17)	-0.00001	0.00510	0.00182	0.00170
114	O(17)	0.00011	-0.06715	-0.02396	-0.02240
115	O(17)	0.00000	0.00000	0.00000	0.00000

Anisotropic Spin Dipole Couplings in Principal Axis System

Atom		a.u.	MegaHertz	Gauss	10(-4) cm-1	Axes		
	Baa	-0.0206	-10.988	-3.921	-3.665	-0.3196	0.2645	0.9099
23 H(1)	Bbb	-0.0163	-8.693	-3.102	-2.900	-0.6245	0.6634	-0.4122
	Bcc	0.0369	19.681	7.023	6.565	0.7126	0.7000	0.0468
	Baa	-0.0265	-5.724	-2.042	-1.909	0.0014	0.0040	1.0000
82 P(31)	Bbb	0.0051	1.093	0.390	0.365	0.9529	-0.3032	-0.0001
	Bcc	0.0214	4.631	1.653	1.545	0.3032	0.9529	-0.0042
	Baa	-0.0206	-10.983	-3.919	-3.663	0.3217	-0.2566	0.9114
90 H(1)	Bbb	-0.0163	-8.691	-3.101	-2.899	-0.6235	0.6671	0.4078
	Bcc	0.0369	19.673	7.020	6.562	0.7126	0.6994	-0.0546

D.5 47-Atom Self-Trapped Hole Results

Isotropic Fermi Contact Couplings (Before optimization)

	Atom	a.u.	MegaHertz	Gauss	10(-4) cm-1
1	K(39)	-0.00015	-0.03094	-0.01104	-0.01032
2	P(31)	-0.00358	-6.49166	-2.31639	-2.16538
3	P(31)	-0.00359	-6.49375	-2.31713	-2.16608
4	P(31)	-0.00194	-3.51730	-1.25506	-1.17325
5	P(31)	-0.00194	-3.51751	-1.25513	-1.17331
6	P(31)	-0.04784	-86.64115	-30.91572	-28.90038
7	K(39)	-0.00256	-0.53562	-0.19112	-0.17866
8	K(39)	-0.00257	-0.53575	-0.19117	-0.17871
9	K(39)	-0.00004	-0.00848	-0.00303	-0.00283
10	K(39)	-0.00004	-0.00872	-0.00311	-0.00291
11	K(39)	-0.01050	-2.19242	-0.78231	-0.73131
12	H(1)	-0.00008	-0.37914	-0.13529	-0.12647
13	H(1)	-0.00008	-0.37917	-0.13530	-0.12648
14	H(1)	-0.00023	-1.04927	-0.37441	-0.35000
15	H(1)	-0.00023	-1.04982	-0.37460	-0.35018
16	H(1)	-0.00003	-0.11425	-0.04077	-0.03811
17	H(1)	-0.00003	-0.11427	-0.04077	-0.03812
18	H(1)	-0.00008	-0.33904	-0.12098	-0.11309
19	H(1)	-0.00008	-0.33919	-0.12103	-0.11314
20	H(1)	-0.00257	-11.49187	-4.10059	-3.83328
21	H(1)	-0.00257	-11.48569	-4.09838	-3.83121
22	H(1)	-0.00007	-0.32020	-0.11426	-0.10681
23	H(1)	-0.00007	-0.31901	-0.11383	-0.10641
24	H(1)	-0.00010	-0.43717	-0.15599	-0.14582
25	H(1)	-0.00010	-0.43703	-0.15594	-0.14578
26	H(1)	-0.00006	-0.26220	-0.09356	-0.08746
27	H(1)	-0.00006	-0.26299	-0.09384	-0.08772
28	O(17)	0.00137	-0.82805	-0.29547	-0.27621
29	O(17)	0.00137	-0.82793	-0.29543	-0.27617
30	O(17)	-0.00409	2.48055	0.88512	0.82742
31	O(17)	-0.00409	2.48038	0.88506	0.82736
32	O(17)	-0.00342	2.07522	0.74049	0.69222
33	O(17)	-0.00342	2.07568	0.74065	0.69237
34	O(17)	0.00013	-0.07665	-0.02735	-0.02557
35	O(17)	0.00013	-0.07668	-0.02736	-0.02558
36	O(17)	-0.00083	0.50265	0.17936	0.16767
37	O(17)	-0.00083	0.50291	0.17945	0.16775
38	O(17)	-0.00058	0.35193	0.12558	0.11739
39	O(17)	-0.00058	0.35308	0.12599	0.11777
40	O(17)	0.00071	-0.43125	-0.15388	-0.14385

41	O(17)	0.00071	-0.43154	-0.15398	-0.14395
42	O(17)	0.04174	-25.30207	-9.02841	-8.43986
43	O(17)	0.04175	-25.31041	-9.03138	-8.44265
44	O(17)	-0.00011	0.06667	0.02379	0.02224
45	O(17)	-0.00011	0.06758	0.02411	0.02254
46	O(17)	0.00484	-2.93593	-1.04761	-0.97932
47	O(17)	0.00484	-2.93150	-1.04603	-0.97784

Anisotropic Spin Dipole Couplings in Principal Axis System (before optimization)

Atom		a.u.	MegaHertz	Gauss	10(-4) cm-1	Axes		
	Baa	-0.0173	-3.746	-1.337	-1.250	0.0070	0.0135	0.9999
6 P(31)	Bbb	0.0053	1.141	0.407	0.381	0.9491	-0.3149	-0.0024
	Bcc	0.0120	2.605	0.930	0.869	0.3148	0.9490	-0.0151
	Baa	-0.0237	-12.623	-4.504	-4.211	0.3220	-0.2231	0.9201
20 H(1)	Bbb	-0.0198	-10.542	-3.762	-3.516	0.6596	-0.6443	-0.3871
	Bcc	0.0434	23.165	8.266	7.727	0.6792	0.7315	-0.0603
	Baa	-0.0237	-12.622	-4.504	-4.210	-0.3084	0.2478	0.9184
21 H(1)	Bbb	-0.0198	-10.541	-3.761	-3.516	0.6654	-0.6338	0.3944
	Bcc	0.0434	23.163	8.265	7.726	0.6799	0.7327	0.0306

D.6 Oxygen Vacancy Hyperfine Results

This cluster was formed from a 185 atom cluster. After removing one oxygen atom it became a 184 atom cluster, with Stoichiometry H64K6O91P23 and Charge and multiplicity (2+,2). Before optimization, the central phosphorus Fermi value was 311.62984 Gauss. And before optimization, central phosphorus' anisotropic values were:

Anisotropic Spin Dipole Couplings in Principal Axis System

Atom		a.u.	MegaHertz	Gauss	10(-4) cm-1	Axes		
	Baa	-0.5560	-120.188	-42.886	-40.090	0.8360	0.5465	0.0499
142 P(31)	Bbb	-0.5386	-116.433	-41.546	-38.838	-0.3436	0.4504	0.8241
	Bcc	1.0945	236.621	84.432	78.928	-0.4279	0.7060	-0.5643

Post-optimization results. The optimization allowed three oxygen atoms around central potassium to move.

Isotropic Fermi Contact Couplings

	Atom	a.u.	MegaHertz	Gauss	10(-4) cm-1
1	H(1)	0.00000	-0.00014	-0.00005	-0.00005
2	H(1)	0.00000	0.00078	0.00028	0.00026
3	H(1)	0.00000	-0.00085	-0.00030	-0.00028
4	O(17)	0.00000	0.00047	0.00017	0.00016
5	O(17)	0.00000	0.00000	0.00000	0.00000
6	O(17)	0.00002	-0.01362	-0.00486	-0.00454
7	O(17)	0.00000	0.00125	0.00045	0.00042
8	H(1)	0.00000	-0.00205	-0.00073	-0.00068
9	H(1)	0.00000	0.00224	0.00080	0.00075
10	O(17)	0.00003	-0.01709	-0.00610	-0.00570
11	O(17)	-0.00001	0.00348	0.00124	0.00116
12	H(1)	0.00000	-0.01047	-0.00374	-0.00349
13	H(1)	0.00000	0.00015	0.00005	0.00005
14	H(1)	0.00000	-0.00016	-0.00006	-0.00005
15	H(1)	0.00000	-0.00073	-0.00026	-0.00024
16	H(1)	0.00000	-0.00142	-0.00051	-0.00047
17	H(1)	0.00000	-0.00005	-0.00002	-0.00002
18	H(1)	0.00000	-0.00027	-0.00010	-0.00009
19	H(1)	0.00000	0.00748	0.00267	0.00250
20	H(1)	0.00000	-0.00009	-0.00003	-0.00003
21	P(31)	0.00000	0.00132	0.00047	0.00044
22	P(31)	0.00002	0.03734	0.01332	0.01246
23	P(31)	0.00000	-0.00287	-0.00102	-0.00096
24	O(17)	0.00001	-0.00652	-0.00233	-0.00218
25	O(17)	0.00001	-0.00385	-0.00137	-0.00128
26	O(17)	0.00000	-0.00039	-0.00014	-0.00013
27	O(17)	0.00000	0.00140	0.00050	0.00047
28	O(17)	0.00016	-0.09652	-0.03444	-0.03219
29	O(17)	0.00000	0.00103	0.00037	0.00034
30	O(17)	0.00000	-0.00179	-0.00064	-0.00060
31	O(17)	-0.00001	0.00471	0.00168	0.00157
32	O(17)	0.00000	0.00134	0.00048	0.00045
33	O(17)	0.00000	0.00169	0.00060	0.00056
34	O(17)	0.00000	0.00084	0.00030	0.00028
35	O(17)	0.00000	0.00055	0.00020	0.00018
36	O(17)	0.00000	-0.00060	-0.00021	-0.00020

37	O(17)	0.00000	-0.00201	-0.00072	-0.00067
38	H(1)	0.00000	-0.00084	-0.00030	-0.00028
39	H(1)	0.00000	0.00020	0.00007	0.00007
40	O(17)	0.00000	0.00098	0.00035	0.00033
41	O(17)	0.00000	-0.00063	-0.00023	-0.00021
42	H(1)	-0.00001	-0.03677	-0.01312	-0.01226
43	H(1)	0.00000	-0.00012	-0.00004	-0.00004
44	H(1)	0.00000	0.00282	0.00101	0.00094
45	H(1)	0.00000	0.00009	0.00003	0.00003
46	H(1)	0.00000	-0.01242	-0.00443	-0.00414
47	H(1)	0.00000	-0.00056	-0.00020	-0.00019
48	H(1)	0.00000	-0.00030	-0.00011	-0.00010
49	H(1)	0.00000	-0.00374	-0.00134	-0.00125
50	P(31)	0.00002	0.02734	0.00976	0.00912
51	O(17)	-0.00002	0.01172	0.00418	0.00391
52	O(17)	0.00000	0.00036	0.00013	0.00012
53	O(17)	0.00003	-0.01910	-0.00682	-0.00637
54	O(17)	0.00002	-0.01369	-0.00489	-0.00457
55	O(17)	0.00011	-0.06907	-0.02465	-0.02304
56	O(17)	0.00001	-0.00552	-0.00197	-0.00184
57	O(17)	0.00000	-0.00176	-0.00063	-0.00059
58	O(17)	0.00000	-0.00001	-0.00001	0.00000
59	O(17)	0.00004	-0.02721	-0.00971	-0.00908
60	O(17)	0.00035	-0.21108	-0.07532	-0.07041
61	H(1)	-0.00002	-0.07330	-0.02615	-0.02445
62	H(1)	0.00000	-0.00007	-0.00003	-0.00002
63	H(1)	0.00000	0.00054	0.00019	0.00018
64	H(1)	0.00000	-0.00028	-0.00010	-0.00009
65	H(1)	0.00000	-0.00731	-0.00261	-0.00244
66	H(1)	-0.00002	-0.09077	-0.03239	-0.03028
67	H(1)	0.00000	0.00333	0.00119	0.00111
68	H(1)	0.00000	0.00025	0.00009	0.00008
69	H(1)	0.00000	-0.00117	-0.00042	-0.00039
70	P(31)	0.00001	0.01904	0.00679	0.00635
71	O(17)	-0.00019	0.11283	0.04026	0.03764
72	O(17)	0.00000	0.00060	0.00022	0.00020
73	O(17)	0.00001	-0.00388	-0.00138	-0.00129
74	O(17)	0.00000	0.00260	0.00093	0.00087
75	O(17)	-0.00008	0.04706	0.01679	0.01570
76	O(17)	0.00000	0.00074	0.00026	0.00025
77	O(17)	0.00003	-0.01840	-0.00656	-0.00614
78	O(17)	-0.00005	0.03210	0.01145	0.01071
79	O(17)	0.00000	0.00001	0.00000	0.00000
80	O(17)	0.00000	0.00286	0.00102	0.00095
81	O(17)	-0.00007	0.04137	0.01476	0.01380

82	O(17)	0.00000	-0.00231	-0.00082	-0.00077
83	P(31)	0.00000	-0.00611	-0.00218	-0.00204
84	P(31)	0.00000	-0.00330	-0.00118	-0.00110
85	P(31)	-0.00001	-0.02017	-0.00720	-0.00673
86	P(31)	-0.00001	-0.01211	-0.00432	-0.00404
87	P(31)	0.00000	-0.00236	-0.00084	-0.00079
88	P(31)	0.00000	0.00454	0.00162	0.00152
89	P(31)	0.00000	0.00760	0.00271	0.00254
90	P(31)	0.00000	-0.00031	-0.00011	-0.00010
91	O(17)	-0.00008	0.04573	0.01632	0.01525
92	O(17)	0.00001	-0.00670	-0.00239	-0.00223
93	O(17)	0.00002	-0.01172	-0.00418	-0.00391
94	O(17)	0.00001	-0.00575	-0.00205	-0.00192
95	O(17)	-0.00002	0.01296	0.00463	0.00432
96	O(17)	0.00000	0.00002	0.00001	0.00001
97	O(17)	0.00000	-0.00009	-0.00003	-0.00003
98	O(17)	0.00001	-0.00340	-0.00121	-0.00114
99	K(39)	-0.00093	-0.19477	-0.06950	-0.06497
100	K(39)	0.00397	0.82814	0.29550	0.27624
101	K(39)	0.00167	0.34807	0.12420	0.11610
102	K(39)	0.00413	0.86349	0.30811	0.28803
103	K(39)	-0.00075	-0.15716	-0.05608	-0.05242
104	K(39)	0.00224	0.46825	0.16708	0.15619
105	H(1)	-0.00001	-0.04832	-0.01724	-0.01612
106	H(1)	0.00000	0.00381	0.00136	0.00127
107	H(1)	-0.00002	-0.10728	-0.03828	-0.03579
108	H(1)	0.00000	-0.00284	-0.00101	-0.00095
109	H(1)	0.00000	0.00099	0.00035	0.00033
110	H(1)	0.00000	0.00128	0.00046	0.00043
111	H(1)	0.00000	-0.01673	-0.00597	-0.00558
112	H(1)	0.00000	-0.00042	-0.00015	-0.00014
113	H(1)	0.00000	0.00078	0.00028	0.00026
114	H(1)	0.00000	-0.00018	-0.00006	-0.00006
115	H(1)	0.00001	0.03295	0.01176	0.01099
116	H(1)	0.00000	-0.00490	-0.00175	-0.00164
117	H(1)	-0.00001	-0.04732	-0.01688	-0.01578
118	H(1)	0.00000	-0.00148	-0.00053	-0.00049
119	H(1)	0.00022	0.99584	0.35534	0.33218
120	H(1)	0.00000	-0.00019	-0.00007	-0.00006
121	H(1)	0.00000	0.00038	0.00013	0.00013
122	H(1)	0.00000	-0.00019	-0.00007	-0.00006
123	H(1)	-0.00023	-1.00903	-0.36005	-0.33658
124	H(1)	0.00000	-0.00041	-0.00015	-0.00014
125	H(1)	0.00000	0.00004	0.00001	0.00001
126	H(1)	0.00000	0.00055	0.00020	0.00018

127	H(1)	0.00011	0.48787	0.17409	0.16274
128	H(1)	0.00000	0.00022	0.00008	0.00007
129	H(1)	0.00000	0.00579	0.00207	0.00193
130	H(1)	0.00000	-0.00082	-0.00029	-0.00027
131	H(1)	-0.00275	-12.31118	-4.39294	-4.10657
132	H(1)	0.00000	-0.00058	-0.00021	-0.00019
133	H(1)	0.00000	-0.00053	-0.00019	-0.00018
134	H(1)	0.00000	-0.01343	-0.00479	-0.00448
135	H(1)	0.00000	0.00499	0.00178	0.00167
136	P(31)	-0.00309	-5.58982	-1.99459	-1.86456
137	P(31)	0.00002	0.03051	0.01089	0.01018
138	P(31)	0.00018	0.33261	0.11868	0.11095
139	P(31)	0.00003	0.05565	0.01986	0.01856
140	P(31)	-0.00102	-1.85325	-0.66128	-0.61818
141	P(31)	-0.00011	-0.20064	-0.07159	-0.06693
142	P(31)	0.49713	900.34828	321.26666	300.32386
143	P(31)	0.00000	-0.00148	-0.00053	-0.00049
144	P(31)	0.00000	0.00156	0.00056	0.00052
145	P(31)	0.00001	0.02447	0.00873	0.00816
146	O(17)	0.00000	-0.00263	-0.00094	-0.00088
147	O(17)	0.00005	-0.03111	-0.01110	-0.01038
148	O(17)	-0.00002	0.01298	0.00463	0.00433
149	O(17)	0.00000	-0.00246	-0.00088	-0.00082
150	O(17)	0.00002	-0.01228	-0.00438	-0.00410
151	O(17)	0.00003	-0.01770	-0.00632	-0.00591
152	O(17)	-0.00013	0.07957	0.02839	0.02654
153	O(17)	0.00016	-0.09470	-0.03379	-0.03159
154	O(17)	0.00001	-0.00488	-0.00174	-0.00163
155	O(17)	0.00001	-0.00785	-0.00280	-0.00262
156	O(17)	0.00042	-0.25612	-0.09139	-0.08543
157	O(17)	-0.00029	0.17360	0.06194	0.05791
158	O(17)	0.00028	-0.16762	-0.05981	-0.05591
159	O(17)	0.00038	-0.22742	-0.08115	-0.07586
160	O(17)	0.00004	-0.02274	-0.00811	-0.00758
161	O(17)	0.02503	-15.17521	-5.41489	-5.06191
162	O(17)	0.00000	-0.00038	-0.00014	-0.00013
163	O(17)	0.00000	-0.00133	-0.00048	-0.00044
164	O(17)	0.00000	-0.00029	-0.00010	-0.00010
165	O(17)	0.04941	-29.95468	-10.68858	-9.99181
166	O(17)	0.00000	-0.00145	-0.00052	-0.00048
167	O(17)	0.00003	-0.01552	-0.00554	-0.00518
168	O(17)	0.00000	-0.00136	-0.00048	-0.00045
169	O(17)	0.07080	-42.91915	-15.31462	-14.31629
170	O(17)	0.00000	-0.00081	-0.00029	-0.00027
171	O(17)	0.00002	-0.01398	-0.00499	-0.00466

172	O(17)	0.00004	-0.02473	-0.00882	-0.00825
173	O(17)	0.00001	-0.00719	-0.00257	-0.00240
174	O(17)	0.00000	0.00107	0.00038	0.00036
175	O(17)	0.00000	0.00005	0.00002	0.00002
176	O(17)	-0.00257	1.55566	0.55510	0.51891
177	O(17)	0.00584	-3.54225	-1.26396	-1.18157
178	O(17)	0.00000	-0.00034	-0.00012	-0.00011
179	O(17)	0.00928	-5.62597	-2.00748	-1.87662
180	O(17)	0.00035	-0.21302	-0.07601	-0.07106
181	O(17)	0.03247	-19.68101	-7.02267	-6.56488
182	O(17)	0.00000	-0.00004	-0.00002	-0.00001
183	O(17)	0.00011	-0.06823	-0.02435	-0.02276
184	O(17)	0.00001	-0.00700	-0.00250	-0.00233

Bibliography

[1] M. J. Frisch, A. Frisch, and J. B. Foresman. *Gaussian 94 User's Reference*. Gaussian, 1996.

[2] V. G. Dmitriev, G. G. Gurzadyan, and D. N. Nikogosyan, "Handbook of Nonlinear Optical Crystals," Springer Series in Optical Sciences, vol 64 Springer-Verlag, Berlin Heidelberg, 1991.

[3] D. Bruneau, A. M. Tournade, and E. Fabre. "Fourth harmonic generation of a large-aperture Nd:glass laser," *Applied Optics* **24**, 3740 (1985).

[4] G. J. Linford, B. C. Johnson, J. S. Hildum, W. E. Martin, K. Snyder, R. D. Boyd, W. L. Smith, C. L. Vercimak, D. Eimerl, and J. T. Hunt, "Large aperture harmonic conversion experiments at Lawrence Livermore National Laboratory," *Applied Optics* **21,** 3633 (1982).

[5] R. S. Craxton, S. D. Jacobs, J. E. Rizzo, and R. Boni, "Basic properties of KDP related to the frequency conversion of 1 μm laser radiation," *IEEE Journal of Quantum Electronics* **17,** 1782 (1981).

[6] D. Eimerl, "Electrooptic, linear, and nonlinear optical-properties of KDP and its isomorphs," *Ferroelectrics* **72,** 397 (1987).

[7] V. G. Dmitriev, G. G. Gurzadyan, and D. N. Nikogosyan, "Handbook of nonlinear optical crystals," Springer Series in Optical Sciences, vol 64, 3rd edition, Springer-Verlag Berlin, 1999.

[8] N. Zaitseva and L. Carman, "Rapid growth of KDP-type crystals," *Progress in Crystal Growth and Characterization of Materials* **43,** 1 (2001).

[9] J. J. De Yoreo, A. K. Burnham, and P. K. Whitman, "Developing KH_2PO_4 and KD_2PO_4 crystals for the world's most powerful laser," *International Materials Reviews* **47,** 113 (2002).

[10] P. A. Baisden, L. J. Atherton, R. A. Hawley, T. A. Land, J. A. Menapace, P. E. Miller, M. J. Runkel, M. L. Spaeth, C. J. Stolz, T. I. Suratwala, P. J. Wegner, and L. L. Wong, "Large optics for the National Ignition Facility," *Fusion Science and Technology* **69,** 295 (2016).

[11] J. E. Davis, R. S. Hughes, and H. W. Lee, "Investigation of optically generated transient electronic defects and protonic transport in hydrogen-bonded molecular solids. Isomorphs of potassium dihydrogen phosphate," *Chemical Physics Letters* **207**, 540 (1993).

[12] M. C. Nadeau, G. Duchateau, M. Dumergue, N. Fedorov, D. Descamps, S. Petit, G. Geoffroy, and P. Martin, "Dynamics of laser-induced defects by multiple femtosecond pulses in potassium dihydrogen phosphate crystals," *Journal of the Optical Society of America B* **35,** 1119 (2018).

[13] F. Geng, Q. Xu, F. R. Wang, X. D. Xia, J. B. Wen, J. Huang, and X. D. Jiang, "Room-Temperature Transient Absorption in KDP Crystal Under Exposure to Nanosecond Laser at 355 nm," *IEEE Photonics Journal* **10**, 6400208 (2018).

[14] Y. B. Zheng, R. S. Ba, X. D. Zhou, L. Ding, J. Li, J. Yuan, H. L. Xu, J. Na, Y. Li, X. Y. Yang, B. Chen, and W. G. Zheng, "Characteristics of precursors responsible for bulk damage initiation in doubler KDP crystal at different wavelengths," *Optics and Laser Technology* **96**, 196 (2017).

[15] G. Duchateau, G. Geoffroy, A. Belsky, N. Fedorov, P. Martin, and S. Guizard, "Interaction of intense femtosecond laser pulses with KDP and DKDP crystals in the short wavelength regime," *Journal of Physics: Condensed Matter* **25,** 435501 (2013).

[16] G. Duchateau, G. Geoffroy, A. Dyan, H. Piombini, and S. Guizard, "Electron-hole dynamics in normal and deuterated KH_2PO_4 illuminated by intense femtosecond laser pulses," *Physical Review B* **83,** 075114 (2011).

[17] S. G. Demos, P. DeMange, R. A. Negres, M. D. and Feit "Investigation of the electronic and physical properties of defect structures responsible for laser-induced damage in DKDP crystals," *Optics Express* **18**, 13788 (2010).

[18] C. W. Carr, H. B. Radousky, and S. G. Demos, "Wavelength Dependence of Laser-Induced Damage: Determining the Damage Initiation Mechanisms," *Physical Review Letters* **91**, 127402 (2003).

[19] K. T. Stevens, N. Y. Garces, L. E. Halliburton, M. Yan, N. P. Zaitseva, J. J. de Yoreo, G. C. Catella, and J. R. Luken, "Identification of the intrinsic self-trapped hole center in KD_2PO_4." *Applied Physics Letters* **75**, 1503 (1999).

[20] N. Y. Garces, K. T. Stevens, L. E. Halliburton, S. G. Demos, H. B. Radousky, and N. P. Zaitseva, "Identification of electron and hole traps in KH_2PO_4 crystals," *Journal of Applied Physics* **89**, 47 (2001).

[21] Chirila, Madalina M. *Characterization of point defects in nonlinear optical materials,* PhD Dissertation, West Virginia University (2003).

[22] M. M. Chirila, N. Y. Garces, L. E. Halliburton, S. G. Demos, T. A. Land, and H. B. Radousky, "Production and thermal decay of radiation-induced point defects in KD_2PO_4 crystals," *Journal of Applied Physics* **94,** 6456 (2003).

[23] O. F. Schirmer, "O−bound small polarons in oxide materials," *Journal of Physics: Condensed Matter* **18**, R667 (2006).

[24] B. E. Kananen, N. C. Giles, L. E. Halliburton, G. K. Foundos, K. B. Chang, and K. T. Stevens, "Self-trapped holes in β-Ga_2O_3 crystals," *Journal of Applied Physics* **122**, 215703 (2017).

[25] V. V. Laguta, M. Nikl, J. Rosa, B. V. Grinyov, L. L. Nagornaya, and I. A. Tupitsina, "Electron spin resonance study of self-trapped holes in $CdWO_4$ scintillator crystals," *Journal of Applied Physics* **104,** 103525 (2008).

[26] S. Koval, J. Kohanoff, R. L. Migoni, and E. Tosatti, "Ferroelectricity and isotope effects in hydrogen-bonded KDP crystals," *Physical Review Letters* **89**, 187602 (2002).

[27] S. Koval, J. Lasave, R. L. Migoni, J. Kohanoff, and N. S. Dalal, *Ab initio studies of H-bonded systems: The cases of ferroelectric KH_2PO_4 and antiferroelectric $NH_4H_2PO_4$,* Chapter 21, Ferroelectrics-Characterization and Modeling, InTech Open Access (2011). http://cdn.intechweb.org/pdfs/16617.pdf

[28] C. S. Liu, N. Kioussis, S. G. Demos, and H. B. Radousky, "Electron-or hole-assisted reactions of H defects in hydrogen-bonded KDP," *Physical Review Letters* **91,** 015505 (2003).

[29] R. J. Nelmes, "Structural studies of KDP and the KDP-type transition by neutron and X-ray diffraction: 1970–1985," *Ferroelectrics* **71,** 87 (1987).

[30] R. J. Nelmes, W. F. Kuhs, C. J. Howard, J. E. Tibballs, and T. W. Ryan, "Structural ordering below Tc in KDP and DKDP," *Journal of Physics C: Solid State Physics* **18,** L711 (1985).

[31] J. E. Tibballs, R. J. Nelmes, and G. J. McIntyre. "The crystal structure of tetragonal KH_2PO_4 and KD_2PO_4 as a function of temperature and pressure." *Journal of Physics C: Solid State Physics* **15,** 37 (1982).

[32] W. E. Hughes and W. G. Moulton, "Electron spin resonance of irradiated KH_2PO_4 and KD_2PO_4," *Journal of Chemical Physics* **39**, 1359 (1963).

[33] R. C. DuVarney and R. P. Kohin, "Domain Switching in Irradiated Ferroelectric KH_2PO_4 Observed by Electron Spin Resonance," *Physical Review Letters* **20**, 259 (1968).

[34] J. A. McMillan and J. M. Clemens, "Paramagnetic and optical studies of radiation damage centers in $K(H_{1-x}D_x)_2PO_4$," *Journal of Chemical Physics* **68**, 3627 (1978).

[35] S. G. Demos, M. Yan, M. Staggs, J. J. de Yoreo, and H. B. Radousky, "Raman scattering investigation of KH_2PO_4 subsequent to high fluence laser irradiation," *Applied Physics Letters* **72**, 2367 (1998).

[36] C. D. Marshall, S. A. Payne, M. A. Henesian, J. A. Speth, and H. T. Powell, "Ultraviolet-induced transient absorption in potassium dihydrogen phosphate and its

influence on frequency conversion," *Journal of the Optical Society of America B* **11**, 774 (1994).

[37] E. Dieguez and J. M. Cabrera, "Optical absorption and thermoluminescence of X-irradiated KDP," *Journal of Physics D: Applied Physics* **14,** 91 (1981).

[38] N. P. Zaitseva, J. J. De Yoreo, M. R. DeHaven, R. L. Vital, K. E. Montgomery, M. Richardson, and L. J. Atherton, "Rapid growth of large-scale (40–55 cm) KH_2PO_4 crystals," *Journal of Crystal Growth* **180**, 255 (1997).

[39] S. D. Setzler, K. T. Stevens, L. E. Halliburton, M. Yan, N. P. Zaitseva, and J. J. DeYoreo, "Hydrogen atoms in KH_2PO_4 crystals," *Physical Review B* **57,** 2643 (1998).

[40] D. L. Griscom, "Self-trapped holes in pure-silica glass: A history of their discovery and characterization and an example of their critical significance to industry," *Journal of Non-Crystalline Solids* **352**, 2601 (2006).

[41] T. G. Castner and W. Känzig, "The electronic structure of V-centers," *Journal of Physics and Chemistry of Solids* **3**, 178 (1957).

[42] D.L. Griscom, "Electron spin resonance characterization of self-trapped holes in amorphous silicon dioxide," *Journal of Non-Crystalline Solids* **149,** 137 (1992).

[43] A. Szabo, and N. S. Ostlund. *Modern Quantum Chemistry: Introduction to Advanced Electronic Structure Theory*. McGraw-Hill, New York (1989); available in print by Dover Publications.

[44] W. J. Hehre, R. Ditchfield, and J. A. Pople, "Self-consistent molecular orbital methods. XII. Further extensions of Gaussian-type basis sets for use in molecular orbital studies of organic molecules," *The Journal of Chemical Physics **56,*** 2257 (1972).

[45] J. A. Pople, R. Krishnan, H. B. Schlegel, and J.S. Binkley, "Electron correlation theories and their application to the study of simple reaction potential surfaces," *International Journal of Quantum Chemistry* **14,** 545 (1987).

[46] T. Clark, J. Chandrasekhar, G.W. Spitznagel, and P.V.R. Schleyer, "Efficient diffuse function-augmented basis sets for anion calculations. III. The 3-21+ G basis set for first-row elements, Li–F," *Journal of Computational Chemistry* **4,** 294 (1983).

[47] R. H. Ditchfield, W. J., Hehre, and J. A. Pople, "Self-consistent molecular-orbital methods. IX. An extended Gaussian-type basis for molecular-orbital studies of organic molecules," *Journal of Chemical Physics* **54,** 724 (1971).

[48] G.W. Spitznagel, T. Clark, P. von Ragué Schleyer, and W.J. Hehre, "An evaluation of the performance of diffuse function-augmented basis sets for second row elements, Na-Cl," *Journal of Computational Chemistry* **8,** 1109 (1987).

[49] P. C. Hariharan and J. A. Pople, “Influence of polarization functions on molecular-orbital hydrogenation energies,” *Theoretica Chimica Acta* **28,** 213 (1973).

[50] M. M. Francl, W. J. Pietro, W. J. Hehre, J. S. Binkley, M. S. Gordon, D. J. DeFrees, and J. A. Pople, “Self-consistent molecular orbital methods. XXIII. A polarization-type basis set for second-row elements,” *Journal of Chemical Physics* **77,** 3654 (1982).

[51] V. A. Rassolov, M. A. Ratner, J. A. Pople, P. C. Redfern, and L. A. Curtiss, “6-31G* basis set for third-row atoms,” *Journal of Computational Chemistry* **22,** 976 (2001).

[52] V. A. Rassolov, J. A. Pople, M. A. Ratner, and T.L. Windus, “6-31G* basis set for atoms K through Zn,” *Journal of Chemical Physics* **109**, 1223 (1998).

[53] J. P. Blaudeau, M. P. McGrath, L. A. Curtiss, and L. Radom, “Extension of Gaussian-2 (G2) theory to molecules containing third-row atoms K and Ca,” *Journal of Chemical Physics* **107,** 5016 (1997).

[54] D.R. Hartree, W., Hartree, and B. Swirles, “Self-consistent field, including exchange and superposition of configurations, with some results for oxygen,” *Philosophical Transactions of the Royal Society of London. Series A, Mathematical and Physical Sciences* **238**, 229 (1939).

[55] C. Møller and M. S. Plesset, “Note on an approximation treatment for many-electron systems,” *Physical Review* **46**, 618 (1934).

[56] G. Berthier, “Extension de la methode du champ moleculaire self-consistent a l'etude des couches incompletes,” Comptes rendus hebdomadaires des séances de l'Académie des sciences **238**, 91 (1954).

[57] J. A. Pople, and R. K. Nesbet, "Self-consistent orbitals for radicals," *Journal of Chemical Physics* **22**, 571 (1954).

[58] M. Head-Gordon and T. Head-Gordon, "Analytic MP2 frequencies without fifth-order storage. Theory and application to bifurcated hydrogen bonds in the water hexamer," *Chemical Physics Letters* **220**, 122 (1994).

[59] X. Li and M. J. Frisch, “Energy-represented DISS with a hybrid geometry optimization method,” *Journal of Chemical Theory and Computation* **2**, 835 (2006)

[60] A. D. Becke, "Density-functional thermochemistry. III. The role of exact exchange," *Journal of Chemical Physics* **98**, 5648 (1993).

[61] J. Chai and M. Head-Gordon. "Long-range corrected hybrid density functionals with damped atom–atom dispersion corrections," *Physical Chemistry Chemical Physics* **10**, 6615 (2008).

[62] V. Barone, P. Cimino, and E. Stendardo, "Development and validation of the B3LYP/N07D computational model for structural parameter and magnetic tensors of large free radicals," *Journal of Chemical Theory and Computation* **4**, 751 (2008).

[63] R. A. Kendall, T. H. Dunning Jr, and R. J. Harrison, "Electron affinities of the first-row atoms revisited. Systematic basis sets and wave functions," *Journal of Chemical Physics* **96**, 6796 (1992).

[64] W. Zhu and S. B. Trickey, "Accurate and balanced anisotropic Gaussian type orbital basis sets for atoms in strong magnetic fields," *Journal of Chemical Physics* **147**, 244108 (2017).

[65] AFRL DSRC website, High Performance Computing Systems, https://www.afrl.hpc.mil/hardware/

[66] C. M. Aikens, and M. S. Gordon, "Parallel unrestricted MP2 analytic gradients using the distributed data interface," *Journal of Physical Chemistry A* **108**, (2004).

[67] J. Foresman, and AE. Frish, Exploring chemistry with Electronic Structure Methods 3rd ed. *Gaussian Inc., Pittsburg, PA* (2015).

[68] J. A. Weil and J. R. Bolton, "Electron Paramagnetic Resonance: Elementary Theory and Practical Applications Second Edition," *John Wiley & Sons, Inc., Hoboken, New Jersey* (2007).

[69] L. A. Eriksson, ESR Hyperfine Calculations, *Encyclopedia of Computational Chemistry*, John Wiley & Sons, Ltd, Hoboken, NJ (2002).

[70] H. C. Box, "Radiation effects: ESR and ENDOR Analysis," *Academic Press, New York* (1977).

[71] M. Pesci, F. Gallino, C. Di Valentin, and G. Pacchioni, "Nature of defect states in nitrogen-doped MgO," *Journal of Physical Chemistry C* **114,** 1350 (2009).

[72] G. Pacchioni, F. Frigoli, D. Ricci, and J. A. Weil, "Theoretical description of hole localization in a quartz Al center: The importance of exact electron exchange," *Physical Review B* **63,** 054102 (2000).

[73] G. Pacchioni, "Modeling doped and defective oxides in catalysis with density functional theory methods: Room for improvements," *Journal of Chemical Physics* **128,** 182505 (2008).

[74] M. V. Ganduglia-Pirovano, A. Hofmann, and J. Sauer, "Oxygen vacancies in transition metal and rare earth oxides: Current state of understanding and remaining challenges," *Surface Science Reports* **62,** 219-270 (2007).

[75] J. To, A. A. Sokol, S. A. French, N. Kaltsoyannis, and C. R. A. Catlow,"Hole localization in $[AlO_4]^0$ defects in silica materials," *Journal of Chemical Physics* **122,** 144704 (2005).

[76] F. Pilar, "Elementary Quantum Chemistry Second Edition," *Dover Books on Chemistry* (2001).

[77] K. Ruedenberg, "A Study of Two-center Integrals Useful in Calculations on Molecular Structure. II. The Two-center Exchange Integrals," *Journal of Chemical Physics* **19**, 1459 (1951).

[78] V. Hänninen, Introduction to Computational Chemistry, Lecture 4. Perturbation Theory, University of Helsinki, 2012. http://www.helsinki.fi/kemia/fysikaalinen/opetus/jlk/luennot/Lecture4.pdf

[79] J. Chai, and M. Head-Gordon, "Long-range corrected hybrid density functionals with damped atom–atom dispersion corrections," *Physical Chemistry Chemical Physics* **10**, 6615 (2008).

[80] R. J. Nelmes, Z. Tun, and W. F. Kuhs, "A compilation of accurate structural parameters for KDP and DKDP, and a users' guide to their crystal structures," *Ferroelectrics* **71,** 12 (1987).

[81] T. Miyoshi, H. Mashiyama, T. Asahi, H. Kimura, and Y. Noda, "Single-crystal neutron structural analyses of potassium dihydrogen phosphate and potassium dideuterium phosphate," *Journal of the Physical Society of Japan* **80,** 044709 (2011).

[82] J. W. Wells, E. Budzinski, and H. C. Box, "ESR and ENDOR studies of irradiated potassium dihydrogen phosphate," *Journal of Chemical Physics* **85,** 6340 (1986).

[83] S. Stoll and A. Schweiger, "EasySpin, a comprehensive software package for spectral simulation and analysis in EPR," *Journal of Magnetic Resonance* **178,** 42 (2006).

[84] L. V. Liu, Q. T. Wei, and Y. A. Wang, "Chemical reaction of nitric oxides with the 5-1DB defect of the single-walled carbon nanotube," *Journal of Physical Chemistry B* **110,** 1999 (2006).

[85] A. Jain, S. P. Ong, G. Hautier, W. Chen, W. D. Richards, S. Dacek, S. Cholia, D. Gunter, D. Skinner, G. Ceder, K.A. Persson, "*The Materials Project: A materials genome approach to accelerating materials innovation*,"*APL Materials* **1**, 011002 (2013)

[86] J. A. Fitzpatrick, F. R. Manby, and C. M. Western, "The interpretation of molecular magnetic hyperfine interactions," *Journal of Chemical Physics* **122**, 084312 (2005).

[87] O. F. Schirmer, "Model calculation on exchange core polarization in transferred hyperfine interaction," *Journal of Physics C: Solid State Physics* **6**, 300 (1973).

[88] J. R. Morton and K. F. Preston, “Atomic parameters for paramagnetic resonance,” *Journal of Magnetic Resonance* **30,** 577 (1969-1992).

[89] F. J. Adrian, A. N. Jette, J. M. and Spaeth, “Theory of indirect hyperfine interactions of oxygen-aluminum defects in ionic crystals,” *Physical Review B* **31**, 3923 (1985).

[90] N. J. Stone, “Table of nuclear magnetic dipole and electric quadrupole moments,” *Atomic Data and Nuclear Data Tables* **90**, 75 (2005).

[91] C. Di Valentin, G. Pacchioni, and A. Selloni, "Electronic structure of defect states in hydroxylated and reduced rutile TiO 2 (110) surfaces," *Physical review letters* **97,** 166803 (2006).

[92] H. Goldstein, C. Poole, and J. Safko. "Classical mechanics." (2002): 782-783.

REPORT DOCUMENTATION PAGE

Form Approved
OMB No. 0704-0188

1. REPORT DATE *(DD-MM-YYYY)*	**2. REPORT TYPE**	**3. DATES COVERED** *(From - To)*
12-09-2019	Doctoral Dissertation	August 2014-September 2019

4. TITLE AND SUBTITLE

Investigations of Point Defects in KH_2PO_4 Crystals Using Ab Initio Quantum Methods

5a. CONTRACT NUMBER

5b. GRANT NUMBER

5c. PROGRAM ELEMENT NUMBER

6. AUTHOR(S)

Dodson, Tabitha, E.R., PhD

5d. PROJECT NUMBER

5e. TASK NUMBER

5f. WORK UNIT NUMBER

7. PERFORMING ORGANIZATION NAME(S) AND ADDRESS(ES)

Air Force Institute of Technology
Graduate School of Engineering and Management (AFIT/EN)
2950 Hobson Way
Wright-Patterson AFB OH 45433-7765

8. PERFORMING ORGANIZATION REPORT NUMBER

AFIT-ENP-DS-19-S-021

9. SPONSORING / MONITORING AGENCY NAME(S) AND ADDRESS(ES)

Intentionally Left Blank

10. SPONSOR/MONITOR'S ACRONYM(S)

11. SPONSOR/MONITOR'S REPORT NUMBER(S)

12. DISTRIBUTION / AVAILABILITY STATEMENT

Distribution Statement A. Approved for Public Release; Distribution Unlimited

13. SUPPLEMENTARY NOTES

This work is declared a work of the U. S. Government and is not subject to copyright protection in the United States.

14. ABSTRACT

Potassium dihydrogen phosphate crystals can be grown to large sizes and are used for many important devices for high powered lasers. The nonlinear optical material has a wide intrinsic transparency range. Intrinsic point defects are responsible for several short-lived absorption bands in the visible and ultraviolet regions that affect operations. The primary intrinsic defects have been experimentally detected in KDP using electron paramagnetic resonance (EPR) experiments. The defect models established include (i) self-trapped holes, (ii) oxygen vacancies, and (iii) hydrogen vacancies. In this research, the quantum chemistry Gaussian software program was successfully used to establish the atomic displacements forming the potential well to "self-trap" the hole in an otherwise perfect region of the crystal. The Gaussian results provide isotropic and anisotropic hyperfine predictions for the self-trapped hole and simulated EPR spectra are in excellent agreement with prior experimental work. This research further develops the understanding of the overlap of spin density on neighboring ions in KDP and the resulting nuclear hyperfine values which can be compared to EPR data. The best approach determined by the modeling of self-trapped holes is also applied to the cation and anion vacancy problems. Work was performed on the DOD's High Performance Computer.

15. SUBJECT TERMS

Potassium dihydrogen phosphate, polaron, density functional theory, hyperfine, electron paramagnetic resonance

16. SECURITY CLASSIFICATION OF:			**17. LIMITATION OF ABSTRACT**	**18. NUMBER OF PAGES**	**19a. NAME OF RESPONSIBLE PERSON**
a. REPORT	**b. ABSTRACT**	**c. THIS PAGE**			Dr. Nancy C. Giles, AFIT/EN
U	U	U	UU	218	**19b. TELEPHONE NUMBER** *(include area code)* 937-255-3636, x4601 Nancy.Giles@afit.edu